Spring 5-15-2017

Stellar and Interstellar Origins of Meteoritic Nanodiamonds

Josiah Lewis
Washington University in St. Louis

WASHINGTON UNIVERSITY IN ST. LOUIS

Department of Physics

Dissertation Examination Committee:
Ryan Ogliore, Chair
Christine Floss, Co-Chair
Erik Henriksen
Dieter Isheim
Martin Israel
Rita Parai

Stellar and Interstellar Origins of Meteoritic Nanodiamonds

by

Josiah Benjamin Lewis

A dissertation presented to
The Graduate School
of Washington University in
partial fulfillment of the
requirements for the degree
of Doctor of Philosophy

May 2017
St. Louis, Missouri

Table of Contents

List of Figures

List of Tables

Acknowledgments

I express deep gratitude to Dr. Christine Floss for her role as my advisor in every practical and essential capacity. Her guidance, example, patience, quick weekend reviews of my written work, and always-open office door have without a doubt contributed more to my development as a scientist than any other individual. More than this, she created stability for me in a long uncertain season of my life.

Dr. Tom Bernatowicz carried the torch of the "4th floor" during the majority of my time in the Laboratory for Space Sciences, and it was a bright and encouraging light. I am indebted to many others for maintenance of that torch, particularly to three who are across the divide: To Dr. Robert Walker, who lit it in the first place; to Dr. Ernst Zinner, who fueled it with secondary ions and mediated so much of the history of the laboratory for me; and to Dr. Frank Stadermann, whose experimental insights carved out space for my atom-probe work, and the effects of whose loss I have felt even though we missed meeting as lab-mates by a few months. Dr. Ryan Ogliore has perceived the *zeitgeist* behind the 4th floor and continues to bring it into conversation with our ever-changing scientific context, with daily-refreshed scientific creativity and enthusiasm that has sparked many fruitful conversations in a short time.

Many others have poured years into keeping the Laboratory for Space Sciences alight: Technician Tim Smolar applied his patiently honed immense experience in the craft of diagnosing, fixing, and building scientific equipment to my needs, peppered with moments of conversation and coffee as a brother-in-arms. Dr. Frank Gyngard was selflessly attentive to maintaining the NanoSIMS and my sanity, and reached out as a deeply insightful friend and mentor. Dr. Pierre Haenecour was first an office-mate, and is now a friend and colleague,

consistently vibrant with philosophical and practical wisdom on surviving life, academia, and dissertation-writing. Wei Jia Ong brought an attitude of intense excellence in science, caring integrity as a community-member and thinker, and lively humor to the first half of my stint in the laboratory, and has supported me as a colleague and friend from afar. Dr. Evan Groopman was a faithful peer and office-mate; so much of my growth has been due to following in his footsteps. Linda Trower was my guide to the jungle of academic paperwork and policy, as well as to the art of St. Louis potlucks. There are others: Brendan Haas, Inga Koch, Dr. Kevin Croat, Dr. Brigitte Wopenka, Dr. Sachiko Amari, Dr. Alex Meshik, and Dr. Olga Pravdivtseva. Finally, Rhombus and Audrey have provided companionship, fun, and lower blood pressure as only dogs can.

At the Northwestern University Center for Atom-Probe Tomography, Dr. Dieter Isheim was a faithful instructor, colleague, and mentor, sharing from a deep store of wisdom on experimentation and scientific communication. Dr. David Seidman provided a foundation and framework for the lab, and helpful insight.

My broader scientific context is full of excellent minds and souls who have fulfilled their duties to the scientific community with care and zeal, creating space for me to thrive and contributing time and insight gladly when sought out. To name them all would be to name the members of the entire subfield that is presolar grains, and then some. Some specific contributions are named in the acknowledgement sections at the ends of the following chapters.

NASA provided substantial support, including the majority of research funding for overhead, equipment, and supplies, and, through the NASA Earth and Space Sciences Fellowship from 2014–2017, contributed substantially to my livelihood and travel to numerous conferences.

Turning to my personal life, many housemates, church family members, and friends have invested, taken time to understand, prayed, grieved, celebrated, and endured with me, in outpourings of support and service that have served as a gentle yet solid framework for life, as a part of a number of communities and life rhythms. Somewhat chronologically, I am deeply grateful to the hundreds of people who are Heritage Church, Covenant College, Resurrected Baptist Church, Manhouse, Hanley Road Baptist, physics ultimate Frisbee, physics book club, Nerd Movie Nights, the Pierce community group and coffees, International Friends, The Journey at Hanley Road, the Lodge, Graduate Christian Fellowship, Monday Nights, Christians in the Planetary Sciences, and the Maven Haven.

I am grateful to my high school physics instructor, Dawn Rhymer, for investing value in me through her gifts and faithful work as a teacher and scientist. She inspired me to have vision for science and for myself.

Sam Berning has been a constant friend in science, philosophy, and creativity for the past six years. I am deeply grateful for his sharp mind and kind heart, for his love of inquiry, and for hundreds of hours reviewing scientific material together. I so deeply needed the parts of himself he has shared. The Berning family coaxed me progressively into their lives and out of my shell: first to their home, then their dinner table, and then wholesale into their hearts and times of rest. I only aspire to exercise hospitality with such consideration and love (and Tom reminds me that I am free to rest from perfectionism).

My parents Ray and Donna Lewis, and my sisters Hope Beverly and Claire Lewis, have, first of all, *listened*, for a frightening number of hours as I piped my angst and frustrations out of state via the wireless networks. Their solidarity, prayer, words of encouragement, and cautious

exhortations have been the continuation of a labor of love. My appreciation for the pure gold that is my family continues to grow.

My girlfriend and now fiancée, Amber Mohrmann, has waited, cared, hoped, celebrated, endured, and worked on behalf of me and my scientific endeavors at a significant but gladly paid cost. Surely no dissertation-writer has ever been so well cared for and celebrated by someone who is also quietly accomplishing her own feat of graduate work, practicing rest, and being a source of wisdom, safety, and encouragement for many. I am amazed, and made at home wherever she is with me. Such love, and its expressions, could never be repaid, but the love is returned, and the expressions aspired to.

The contribution made by Jesus of Nazareth to my life and work is transcendent – to start by thanking him for a list of particulars might suggest he was not ultimately and divinely responsible for each bit, so I prefer to unpack my gratitude as an analogy: Jesus' activity as it relates to my dissertation has been that of a transcendent author, writing not only the biography that I live out, a smattering of which is evident from these acknowledgments, but also writing the cosmic tales of nucleosynthesis, presolar dust, and solar system formation. As a most excellent author, he has weaved together the personal and professional threads, from the great spans of scale in time and space, into an epic I hope someday to begin to understand, and am happily amazed to get to be a part of. But he has taken an active role in his own story; somehow in addition to sustaining the fundamental processes that govern the universe, he has found me, gently serving as my source of fuel for life, constantly loving me with immense patience and kindness, believing good into me and inviting me to look away from myself to take a long gaze at something greater and brighter.

Soli deo gloria.

Josiah Benjamin Lewis

Washington University in St. Louis

May 2017

ABSTRACT OF THE DISSERTATION

Stellar and Interstellar Origins of Meteoritic Nanodiamonds

by
Josiah Benjamin Lewis
Doctor of Philosophy in Physics
Washington University in St. Louis, 2017
Ryan Ogliore, Chair
Christine Floss, Co-Chair
Erik Henriksen
Dieter Isheim
Martin Israel
Rita Parai

In 1987 presolar grains were first isolated from meteorites, opening up a new line of data about the stars that produced them. Based on anomalies in isotopic ratios, identification and classification of presolar grains has borne great fruit in understanding nucleosynthesis, stellar evolution, and mass loss from the stellar objects in which these grains originated: primarily, but not exclusively, supernovae and asymptotic giant branch stars.

Meteoritic nanodiamonds were the first type of presolar grain identified, but more than three decades later, their origins remain unclear. Anomalies in the ratios of Xe isotopes carried by the nanodiamonds suggest the nanodiamonds formed from supernova material, but, measured in bulk, the ratios of $^{12}C/^{13}C$ and $^{14}N/^{15}N$ are consistent with formation in the solar system. Nanodiamonds are ~3 nm in diameter and contain only a few thousand atoms each, such that it is impossible to measure the isotopic ratios of single grains with traditional techniques.

A multi-part experimental approach has allowed me to investigate the origins of meteoritic nanodiamonds. I use statistical studies with nanoscale secondary ion mass spectrometry of thousands of small aggregates of nanodiamonds to put upper limits on the fraction of them that

can have non-solar ratios of the stable isotopes ^{12}C and ^{13}C and to detect isotopically anomalous statistical outliers. I also continue a collaborative work to measure the ratio of $^{12}C/^{13}C$ in individual nanodiamonds. This work adapts the experimental technique of atom-probe tomography from materials science to presolar grain research, and to that end my collaborators and I have worked extensively to mature the experimental procedures. I use focused ion beam sample preparation and correlated secondary and transmission electron microscopy to characterize samples before and after atom-probe isotopic analysis.

These studies characterize the likelihood of various origins for individual and small clusters of nanodiamonds and accompanying disordered C, based on ratios of $^{12}C/^{13}C$ isotopes. The results are consistent with solar system formation for most nanodiamonds, although they do not necessarily rule out a large fraction of supernova grains with isotopic anomalies averaging close to the solar system value. The data suggest that a small subset of nanodiamonds have large isotopic enrichments in ^{13}C relative to ^{12}C. Supernovae are favored due to their production of the Xe isotopes, although J-star or novae could also produce this isotopic anomaly.

Chapter 1: Introduction

This chapter outlines the scientific context for the subsequent chapters. Section 1.1 introduces presolar grain research, a subfield of space sciences, in the broader context of astrophysics and nucleosynthesis. Section 1.2 describes the current state of our knowledge of meteoritic nanodiamonds, one type of potential presolar grain, as well as its astrophysical and nucleosynthetic context. Particular attention is given to how the spatial resolution of mass-sensitive experimental techniques limits studies. Section 1.3 outlines the contents of the remaining chapters.

1.1 Presolar grains

Nucleogenesis, the creation of the chemical elements, takes place in a number of nucleosynthetic processes. Big Bang nucleosynthesis describes the production of H, He, and a small amount of Li as cooling nucleons confined to a small universe bond through the strong force. This accounts for only a small fraction of the atomic mass in the observable region of the universe. The remaining atomic matter, including *all* elements of atomic number six and higher, was produced by the fusion of nuclei inside stars (Burbidge et al. 1957). Supernova explosions and stellar winds – especially outflows from late-type stars – inject this material back into the interstellar medium. While most of the matter is in a gaseous state, a small fraction condenses into grains of dust as it moves through cooling, expanding regions of outflows and nebulae. These grains are subject to various alteration processes. Implantation of material by supernova shock can damage crystal structures, amorphize or ablate material, and may implant heterogeneously and preferentially based on grain size. At length these “presolar grains” form part of the protosolar nebula. During the formation of the solar system and subsequent planetary (parent-body) processes, the vast

majority of the gas and dust in the nebular cloud is homogenized at the atomic level, erasing the isotopic signatures of potentially millions of stars and replacing them with average ratios of stable isotopes similar to what we measure today on the earth, in the sun, and in the rest of the solar system. Later radioactive decay of unstable nuclides, mass dependent fractionation during physical and chemical processing, and irradiation, can modify the composition and distribution of isotopes in the solar system by a few parts per thousand. However, a few grains escape homogenization and maintain their original isotopic signatures, varying from the mean solar system isotopic ratios by up to four orders of magnitude (Zinner 2014). These presolar grains are represented in primitive materials such as comets and asteroids. Some of this material is recovered by meteorite searches and finds, interplanetary dust particle (IDP) collection in the Earth's stratosphere (Bradley et al. 1988), and extraterrestrial sample return missions such as NASA's Stardust mission to comet Wild 2 (Brownlee 2014). Thus, we have the unparalleled opportunity to study dust grains from distant stars in a laboratory environment.

The survival of presolar grains in material available on the Earth was first hypothesized as an explanation for the presence of isotopically anomalous trace elements, liberated from their meteoritic carrier phases during bulk stepped heating (Boato 1954). Isotopic anomalies were identified (e.g., Clayton 1963; Clayton et al. 1973) and traced through various subdivisions of meteoritic material using a complex regime of dissolution (crushing and freeze-thaw disaggregation) size, mass, and density separation by sieving, settling, ultracentrifugation, ultrasonication, and acid dissolution of all but the most refractory phases (Amari et al. 1994). Finally, a fraction composed of ~3 nm diamond crystals was separated as a colloid and identified by transmission electron microscopy (Lewis et al. 1987; Lewis et al. 1989). These meteoritic

nanodiamonds were the carrier of the isotopically anomalous component, Xe-HL, and were the first type of presolar grain identified.

A number of other presolar grain types have been subsequently separated and identified (Table 1.1). We briefly identify the major types here, although this is not an exhaustive list. For discussion and additional references see Zinner 2014. For compiled data on presolar grains see the presolar grain database (Hynes and Gyngard 2009, http://presolar.wustl.edu/Laboratory_for_Space_Sciences/Presolar_Grain_Database).

Table 1.1 Presolar grain types and basic features.[a]

Type	Abundance[b]	Identifying anomalies[c]	Size[d]	Stellar sources
Diamond	1400 ppm	Xe(HL)	2–3 nm	Supernovae?
Silicon carbide	150 ppm	Si, C, N, Al, O, Ne, Xe	0.1–20 μm	AGB, supernovae, J-stars, novae, born-again AGB
Graphite	1–2 ppm	C, Ne	1–20 μm	Supernovae, AGB, born-again AGB
Silicates in IDPs	> 1.5%	O	0.2–1 μm	Red giant, AGB, supernovae
Silicates in meteorites	> 220 ppm	O	0.2–0.9 μm	Red giant, AGB, supernovae
Oxides	> 80 ppm	O	0.15–3 μm	Red giant, AGB, supernovae, novae
Silicon nitride	~3 ppb	Si, N, Al	0.3–1 μm	Supernovae
Ti, Fe, Zr, Mo carbide subgrains	Very low	Condensation sequence	10–200 nm	AGB, supernovae
Kamacite, iron subgrains	Very low	Condensation sequence	~10–20 nm	Supernovae

[a] Adapted from Zinner (2014).

[b] Abundances vary by meteorite; the maximum observed value is given here.

[c] A non-exhaustive list of elements and noble gas components with anomalies that commonly demonstrate these grains are presolar. Subgrains within other presolar grains are identified as presolar primarily but not exclusively based on the inferred condensation sequence.

[d] The range of grain diameters commonly observed. There are some exceptional grains that lie outside of these ranges.

Presolar silicon carbide (SiC) is the best-studied type of presolar grain. These grains are separated from chondrites by acid dissolution or freeze-thaw disaggregation, or studied in situ in polished sections or by focused ion beam (FIB) liftout. Presolar SiC grains are the third most

abundant type of presolar grain, behind nanodiamonds and silicates. While they usually range in size from 0.1–20 μm (Zinner 2014 and references therein), they have been observed in sizes at least as small as meteoritic nanodiamonds (3 nm) (Lewis et al. 1989) and one grain, Bonanza, is roughly 30 μm across (Zinner et al. 2010). Presolar SiC grains are subdivided into a number of types, based on isotopic anomalies in Si, C, N, Al, and a host of trace element isotopes. Trace elements either co-condensed, were implanted later, or are hosted by a subgrain with a formation history of its own (Hynes et al. 2010). Different types of presolar SiC have been categorized based on their isotopic contents: Mainstream grains comprise the vast majority of SiC grains. They have $^{12}C/^{13}C$ ratios ranging from approximately 10–100, with a mean value near $^{12}C/^{13}C$ = 50, and are attributed to asymptotic giant branch (AGB) stars. A and B grains comprise roughly 5% of presolar SiC. With $^{12}C/^{13}C < 10$, they have traditionally been attributed to J-stars or born-again AGB stars, although it has more recently been suggested that they could have originated from supernovae (Liu et al. 2016; Nittler and Hoppe 2005). X grains comprise approximately 1% of the presolar SiC grains and are attributed to Type II supernovae due to various enrichments in isotopes such as N, Si, and Al. They have $^{12}C/^{13}C$ ratios that range roughly from 10–1000 (Amari et al. 1992; Besmehn and Hoppe 2003; Hoppe et al. 1996; Hoppe et al. 2000; Lin, Gyngard, and Zinner 2010; Nittler et al. 1996). Y grains (Amari et al. 2001a; Hoppe et al. 1994; Nittler and Alexander 2003) and Z grains (Hoppe et al. 1997; Nittler and Alexander 2003; O'D Alexander 1993) are from AGB stars and carry different anomalies in N, C, and Si. Each comprises roughly 1% of studied presolar SiC grains. N grains form a miniscule fraction of the presolar SiC inventory. With $^{12}C/^{13}C < 10$, they have been attributed to novae, but this has recently been challenged, with supernova origins being given as an alternative (Liu et al. 2016; Nittler and

Hoppe 2005). C grains are ^{13}C-depleted compared to the solar system and have a possible supernova origin. Only a few C grains have been identified.

Presolar graphite grains are one of the least abundant types by mass, 1000 times less abundant than nanodiamonds and 10 times less abundant than SiC. They are more refractory, i.e., more resistant to melting or chemical dissolution, than most chondrite matrix materials, such that they can be isolated by acid dissolution of less refractory materials, and they are larger than many presolar grain types. As a result, they are the second best studied type of presolar grain in spite of their low concentration compared to, for example, silicates, which are both too fragile and too small for many isolation and characterization techniques. Presolar graphite is found in two varieties, low-density and high-density, as well as in two general structure types, "onion" structure and "cauliflower" structure. Both low- and high-density graphite grains have been observed with a broad range of C isotopic ratios, but low-density grains are more often observed with ^{13}C enrichments relative to ^{12}C, and probably have a supernova origin (Zinner et al. 2006), while high density grains are more often observed with ^{13}C depletions relative to ^{12}C, with probable origins in low-metallicity AGB stars (Amari 2003; Amari et al. 2005; Jadhav et al. 2006, 2013). A small fraction of graphite grains may originate in novae (Amari et al. 2001b). ~40% of the presolar graphite grains in the presolar grains database are low-density, which may be used as a rough estimate of the fraction of presolar graphite that was created in supernova explosions.

Presolar silicates are the second most abundant presolar grain type, but they are smaller and more fragile than presolar graphite and SiC, and are hidden amongst an overwhelming majority of solar silicate material. As a result they were not discovered for almost two decades after the isolation of the first presolar grains in 1987; however, large numbers of silicates have been well-

characterized in the past decade after significant technical advances, most notably the NanoSIMS 50 nanoscale mass spectrometer. The ease of alteration of these grains means that, once presolar survivors are found, large amounts of information can be gained from studying the degree of alteration in their structural and compositional features. Presolar oxides are lower in concentration than the other types of presolar grain described thus far, but were discovered prior to the silicate grains. Presolar oxides (Nittler et al. 1997), and later silicates (Floss and Haenecour 2016), have been subdivided into the same four groups based primarily on O isotopic ratios. Three of the groups carry isotopic signatures from AGB or other red giant stars. The fourth carries evidence of supernova formation (Floss and Haenecour 2016; Nittler et al. 2008).

Several other types of presolar grains have been detected in very small numbers. Among these are kamacite and iron grains. Titanium, vanadium, aluminum, iron, zirconium, and molybdenum carbides have been found, often as subgrains in graphite (Hynes and Gyngard 2009; Zinner 2014) or SiC (Hynes et al. 2010) grains.

1.2 Nanodiamonds

Nanodiamonds are the primary type of presolar material studied in this dissertation, and therefore merit a more detailed discussion. Indeed, the lines of evidence for the grains' origins are complex, the strength of various arguments is subjective, and the implications of the nanodiamonds' origins could have a significant impact on our understanding of the early solar system, the interstellar medium, and/or supernovae explosions. It is the complex and potent nature of this question that motivated this research.

Studies have established that nanodiamonds are present in meteorites at levels up to 1400 ppm by mass, making them the most abundant type of presolar grain discovered (Zinner 2014).

Nanodiamonds have a log-normal size distribution with a median size of ~3 nm in several carbonaceous chondrite meteorites (Daulton et al. 1996). Daulton et al. (1996) also noted a high frequency occurrence of twinning, suggestive of formation by chemical vapor deposition, consistent with low pressure formation in a stellar atmosphere (Lewis et al. 1989). Model fitting of EELS data from the nanodiamonds predicted that on the order of half the carbonaceous acid residue is disordered C (Bernatowicz et al. 1990). Aberration corrected scanning transmission electron microscopy studies confirmed the presence of a significant amount of disordered C, specifically sp^2-bonded sheet fragments in which the nanodiamonds are embedded (Stroud et al. 2011). It is unknown if the nanodiamonds were associated with the sheets in situ in the host meteorites, or if the sheets were originally organized in layers or spheres and damaged by the separation process. It is possible that the disordered C sheets observed in the laboratory are fullerene shells that have been altered and damaged by solar system, parent body, and laboratory processing.

Nanodiamonds are the carrier of the Xe-H and Xe-L anomalous isotopic fractions, since dubbed Xe-HL (Figure 1.1). Xe-H is enriched in the heavy Xe isotopes ^{134}Xe and ^{136}Xe relative to solar system values. Xe-L, in turn, is enriched in the light Xe isotopes ^{124}Xe and ^{126}Xe. Xe-L is a predicted product of the *p*-process or proton capture nucleosynthetic process, while Xe-H is a product of the *r*-process or rapid neutron capture process. These processes both occur in supernovae, so it was believed that whatever meteoritic phase carried Xe-HL was presolar and had either condensed from, or been implanted by supernova material (Jorgensen 1988; Clayton 1989; see Section 1.2.2: Type II supernovae, for further discussion of this candidate for nanodiamond origins).

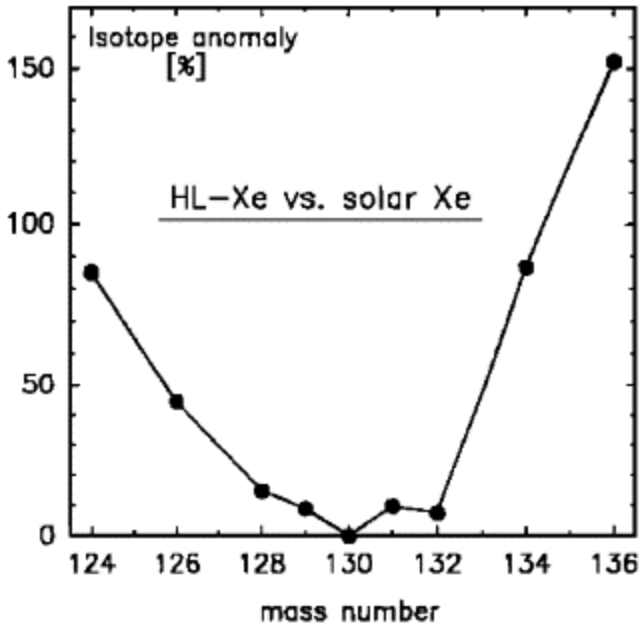

Figure 1.1 Xe-HL isotopic anomalies in nanodiamonds (Huss and Lewis 1995) relative to solar system abundances (Pepin et al. 1995). Normalization is to ^{130}Xe. Figure taken from Arnould and Goriely (2003) with permission.

Because the nanodiamonds are mixed with disordered, sp^2-bonded C in the acid residues, the interpretation of the Xe-HL component is complex. While Xe-HL might be evenly distributed throughout the carbonaceous residue, it might also be predominately or exclusively associated with the nanodiamonds or the disordered C.

A further complication is that the major element isotopic composition of the bulk nanodiamonds is normal, adding complexity to interpreting the isotopic evidence for their origins.

Since the isotopic anomalies encountered on Earth are usually very small fractional deviations from standard values, they are described as per mille or per mil (‰) deviations in the less abundant of the two stable isotopes in a ratio, called the deviation or “delta” value for a given isotope. Hence the deviation from the standard $^{12}C/^{13}C$ ratio is denoted as $\delta^{13}C$ and is calculated as

$$\delta^{13}C = \left(\frac{\left(\frac{^{13}C}{^{12}C}\right)_{sample}}{\left(\frac{^{13}C}{^{12}C}\right)_{reference}} - 1 \right) * 1000 \quad (1.1)$$

Positive delta values indicate a relative enrichment of the isotope in question and negative delta values represent a relative depletion. Note that the reference ratio must be known in order for this measure to be quantitatively useful.

Swart et al. (1983) measured the $\delta^{13}C$ of the carbonaceous Xe-HL carrier in Allende to be -32‰ to -38‰ from terrestrial. Verchovsky (1998) measured Efremovka (CV3) acid residues by stepped heating and detected delta values ranging from -26.0‰ to -36.8‰.

Nitrogen is the most common substitutionary element, >1% by weight (Russell, Arden, and Pillinger 1991; Russell, Arden, and Pillinger 1996). $\delta^{15}N$ has been measured to go as low as -350.4±1.0‰ to -247.4±2.3‰ in nanodiamond-containing carbonaceous residue from primitive chondrites (Russell, Arden, and Pillinger 1996). This is a significant anomaly from terrestrial values; however, it is close to values measured for Jupiter (-374±82‰, (Owen et al. 2001)), and, more recently, the solar wind ($\delta^{15}N$ = -407±7‰ from the Genesis spacecraft) and the bulk sun (-383±8‰, derived from the Genesis measurement (Marty et al. 2011)), where the reference is N_2 from Earth's atmosphere.

Therefore, it is apparent that both the C and N isotopic compositions of the nanodiamonds are consistent with those that are found in solar system material.

Isotopic anomalies in other trace elements in addition to Xe are present in the nanodiamond-containing acid residues. High-sensitivity pyrolysis has detected significant isotopic anomalies in the *r*-process isotopes ^{128}Te, ^{130}Te (Maas et al. 2001; Richter et al. 1998), and ^{110}Pd (Maas et al.

2001). Small enrichments have been reported in the *r*-process elements ^{135}Ba and ^{137}Ba, but low concentrations precluded measurement of the *p*-process elements ^{130}Ba and ^{132}Ba (Lewis et al. 1991). However, the same study found no enrichment of the *r*-process isotope ^{88}Sr, confounding the issue of whether all the trace elements were from an *r*-process source.

The abundance of Xe-HL in the nanodiamond-containing acid residues is such that only one in a million nanodiamonds would be required to host an atom from the Xe-HL reservoir. If ion implantation, rather than co-condensation, is the mechanism for trace element inclusion in the nanodiamonds, it is likely that not every nanodiamond was implanted by an ion, certainly not by many ions, as even the inclusion of one Xe atom in the diamond-bonded C structure will significantly destabilize such a small grain. Thus one expects the ratio of presolar nanodiamonds to trace element atoms to be significantly greater than one and the fraction of presolar nanodiamonds to be significantly greater than one in a million.

If all of the anomalous components are taken into account, the fraction of nanodiamonds required to be carriers rises to about one in ten (Huss and Lewis 1994a, 1994b, 1995; Huss et al. 2008; see Huss (2005) for an overview of the topic). The strength of the evidence for presolar production of the isotopic signatures of these trace element anomalies varies, that for Xe being the strongest.

Given the complexity of the nanodiamonds, and the lack of a single suggested origin that can explain all of their features, especially the isotopic signatures, researchers have put forward a number of origins, which are introduced in the following sections.

1.2.1 Stellar Evolution and the Nucleosynthesis of Carbon

To understand the isotopic composition of the types of stars that have been hypothesized to produce meteoritic nanodiamonds, it is necessary to explain the composition of these stars at the time that they either formed nanodiamonds or lost material, via explosion (for supernovae) or stellar winds (for AGB stars). And to understand how the stars arrived at these compositions, it is helpful to review some key points of stellar evolution.

Stars are formed by the gravitational collapse of a protostellar cloud, mostly composed of H. The collapse leads to thermodynamic conditions sufficient to fuse H nuclei into He. During H burning, a shell of unburned H surrounds a convective core, which contains circulating He along with additional H. When H burning is no longer able to support the mass of the star, the star compresses gravitationally until it begins to fuse He into C.

The only stable pathway for He burning in stars is the triple-alpha process, in which three alpha particles (^{4}He) combine in quick succession to form a ^{12}C atom. The first two ^{4}He atoms involved form ^{8}Be, a highly unstable isotope (half-life of roughly 7×10^{-17} s). There is a small probability that the ^{8}Be will combine with another ^{4}He to form a ^{12}C atom in an excited state. If this excited state of ^{12}C did not exist, stellar nucleosynthesis of stable isotopes above mass 4 would not occur. As He burns, a C core is formed at the center of the star.

The triple-alpha process is the only fusion process that creates ^{12}C in massive stars. ^{13}C is produced, but only from extant ^{12}C as one step in the CNO cycle. This occurs largely in the CN portion of the CNO bi-cycle, proceeding as $^{12}C + p \rightarrow {}^{13}N + \gamma$; $^{13}N \rightarrow {}^{13}C + e^+ + \nu$. ^{13}C can be lost again via $^{13}C + p \rightarrow {}^{14}N + \gamma$, so there is a source and a sink for this isotope. Given the proton fluxes expected, the triple-alpha process will proceed much more quickly than proton capture on ^{12}C once helium burning begins. However, for second or later generation stars, which contain ^{12}C

prior to helium burning, ^{13}C is created from the CNO cycle in the He shell prior to ignition of He burning. In this case a He/N zone rich in ^{13}C will form. The He zone is therefore subdivided into an earlier-forming, outer He/N shell and a later-forming, inner He/C shell.

Stars under 8 solar masses, cannot sustain the temperatures and pressures required to continue nuclear fusion beyond the CNO cycle. At this stage some of these become AGB stars.

For stars with more than 8 solar masses, similar fusion processes repeat: Fusion burning of a lighter element in the core produces a heavier element. → A shell of the lighter element remains around the heavier element core. →The core runs out of the lighter element fuel, fusion slows. → Gravitational compression occurs. → Heavier element fusion burning commences in the core, creating a new, even heavier element. The result is a star with a number of concentric shells, lighter elements at larger radii, heavier elements at smaller radii. Stars at or above roughly 8 solar masses continue this process until they produce ^{56}Fe in their cores by ^{28}Si burning (Figure 1.2).

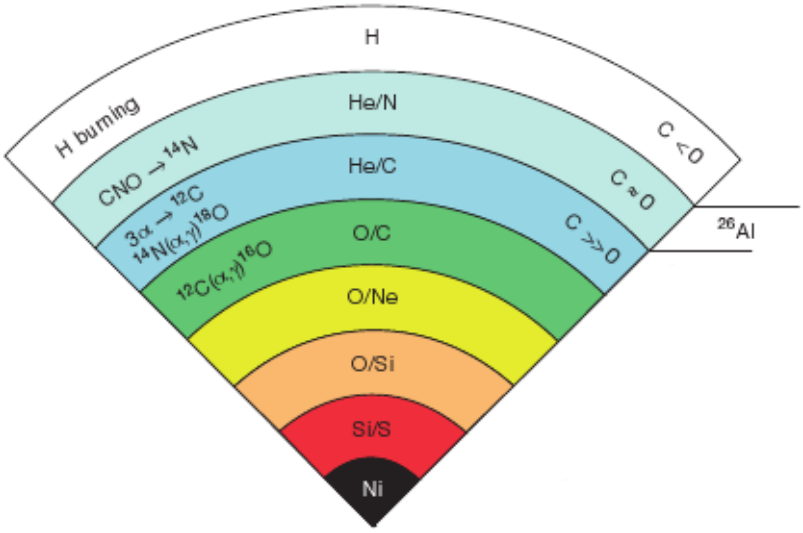

Figure 1.2 Shells of an evolved massive star, prior to core-collapse (Type II) supernova explosion. Some nucleosynthetic processes are highlighted on the left. Carbon and oxygen abundance are compared on the right. ^{26}Al is produced in the He/N zone. Fe is produced in the innermost region as well as Ni. Adapted with permission from Zinner (2014), who use data from Woosley and Weaver (1995).

1.2.2 Type II Supernovae

Type II supernovae are produced by the core collapse of stars massive enough to gravitationally compact their cores into neutron stars, at least ~8 solar masses. These stars must also be below ~50 solar masses, or else they will collapse into black holes without producing a supernova explosion. Late in the lifetime of such a massive star, Si begins to burn out and the star compresses once more with ^{56}Fe at the core. ^{56}Fe has no pathway for nuclear fusion burning due to the high binding energies of the heavier elements, so gravitational compression dominates the core, proceeding at a precipitous rate. The beta-minus reaction ($p + e^- = n + \bar{\nu}$) transforms the core into a neutron- and neutrino-rich region supported by neutron degeneracy pressure as material at higher radius collapses inward as a supersonic shockwave. Through a yet-to-be-determined mechanism, the extreme conditions where the infalling shockwave impacts the dense

neutron-and-neutrino core precipitate the expulsion of a large fraction of the outer radial mass of the star in a supernova shockwave.

Various supernova models exist, which model the star layers and contents for given masses of supernovae. Depending on the model and parameters, mixing between the He/C and He/N shells leads to predictions of a wide variety of $^{12}C/^{13}C$ ratios. For example, mixing material from different layers of the He/C shell in a 15 solar mass Rauscher model produces $^{12}C/^{13}C$ ratios ranging from 20–800, and $^{14}N/^{15}N$ ratios ranging from 6–500 (Fedkin et al. 2010). Therefore, while some of the mixed material from supernovae should contain the C and N isotopic signatures we see in meteoritic nanodiamonds, there is a wide range of isotopic signatures believed to be present in supernovae that are not represented in the nanodiamonds.

The presence of the Xe-HL anomalous component in the nanodiamonds is strong evidence of a supernova origin for some of material in the nanodiamond-containing acid residues. The nucleosynthetic *p*- and *r*-processes occur together only in supernovae, making these the only known synthesizers of Xe-HL. The *p*- or proton capture process occurs where thermally dissociated protons are abundant in the presence of heavy elements, near the neutron core. The *r*- or rapid neutron capture process takes place where heavy elements are surrounded by abundant neutrons, which is the case during supernova explosions.

Theoretical calculations of the production of isotopes in Type II supernovae are the best fit for the Xe-HL observed in the nanodiamonds (Clayton 1989; Richter, Ott, and Begemann 1998). Different authors have suggested that nanodiamonds formed in different regions of Type II supernovae through various processes. Clayton (1989) suggest chemical vapor deposition (CVD) formation in the He/C shell, Nuth and Allen (1992) argue for annealing by radiation, and Clayton

et al. (1999) and Deneault et al. (2006) suggest nanodiamonds could form in the C < O hydrogen shell. Depending on the formation mechanism, nanodiamonds may be able to form in regions with a range of $^{12}C/^{13}C$ isotopic ratios, or may be limited to a ratio occurring only in one shell.

A study of small enough aggregates of nanodiamonds should be able to distinguish between populations of nanodiamonds that formed from reservoirs of material with homogeneous or heterogeneous C isotopic signatures, by assessing whether the ratios of different aggregates vary more than expected based on the hypothesis of a single isotopic reservoir.

We do not understand supernovae well enough to know if they provide the exact conditions (radiation, pressure, temperature, C, N, H, and O concentrations and isotopes) required to grow the nanodiamonds we observe in meteorites, and not all predictions based on supernova formation are consistent with the data.

Therefore, while it is possible that nanodiamonds formed in supernovae either through CVD or radiation annealing, formation mechanisms in other environments have been studied as alternative explanations.

1.2.3 Other Presolar Source Candidates

If nanodiamonds were produced in any environment other than supernovae, the observed Xe-HL must have been implanted later in the form of energetic ions, since only supernovae produce Xe-HL. Several other sources have been considered in the literature.

It has been proposed that meteoritic nanodiamonds formed in binary star systems. In this model, nanodiamonds form in a carbon star, red giants with C/O>1, and were implanted with Xe-HL when companion white dwarfs exploded, a Type Ia supernova (Jorgensen 1988).

Verchovsky et al. (2006) report nanodiamonds with an asymptotic giant branch origin; however, their identification of the grains as nanodiamonds is inconclusive – it is possible that the isolated grains are actually SiC. Their evidence indicates <1% of nanodiamonds could be produced in asymptotic giant branch stars.

Supernova shock waves traveling through the interstellar medium have been suggested as a mechanism for the co-formation of nanodiamond and sp^2-bonded sheets (Stroud et al. 2011). In this scenario, trace elements would be implanted with low efficiency, explaining the low concentration of isotopically anomalous trace elements in the residues. Observation of graphitic carbon sheets in the interstellar medium, as predicted by this model, is tentative. A 2175 Å extinction feature in the interstellar medium can be matched in the laboratory by nanodiamonds encased in graphitic fullerene shells (Yastrebov and Smith, 2009).

1.2.4 Evidence for Solar System Formation of Nanodiamonds

Given the bulk solar value of the C and N isotopic ratios in meteoritic nanodiamonds, a solar system origin for these grains has been suggested, and there are several lines of evidence for this origin candidate. The lack of nanodiamonds in non-cluster IDPs (Dai et al. 2002) suggests they may not have been present in the early solar system, implying they are not presolar. Infrared radiation that may be from hydrogenated nanodiamond surfaces has been observed in the circumstellar disks around some young stars (Van Kerckhoven, Tielens, and Waelkens 2002), but there are other interpretations of these signals (Pirali et al. 2007). Elsewhere it has been proposed that nanodiamonds formed on the surfaces of iron grains, which could serve as substrates to catalyze formation (Meibom et al. 1999), or by shock transformation of sp^2-bonded C "onion shell" fullerene structures colliding with early solar system materials (Marks et al. 2012). A solar system origin is attractive due to its simplicity, but it cannot explain the formation

of all of the nanodiamonds without an explanation for the presence of Xe-HL and the other isotopically anomalous components carried by the nanodiamonds.

1.2.5 Experimental Considerations

The only signatures that conclusively distinguish presolar grains from all other material in the solar system (excepting some materials that can be synthesized by humans in small amounts in laboratory environments) are dramatic anomalies in stable isotopic ratios. Given the small size of nanodiamonds, the variety and complexity of their potential formation and alteration mechanisms, and because of the important implications of their potential origins, strong, direct evidence is required to establish those origins. In the three decades since their identification as the carrier of the Xe-HL anomaly by Lewis et al. (1987), only indirect evidence, requiring significant interpretation, has been acquired, through isotopic studies with stepped heating and mass spectrometry, which lack the spatial resolution to distinguish individual nanodiamonds, and techniques such as transmission electron microscopy, which do not possess the requisite mass sensitivity to distinguish isotopes of C.

Because of the small number of atoms in a nanodiamond (approximately 2000 for a 3 nm grain) and the low concentration of trace elements, isotopic ratios from single grains are, unfortunately, uninformative, with the exception of $^{12}C/^{13}C$, where, for the solar system ratio of 89/1, ~22 of 2000 atoms should be ^{13}C. Under ideal (i.e., unrealistic) measurement conditions this would give an isotopic ratio with 21% statistical uncertainty. Given this uncertainty, most grains that condensed from a reservoir with a $^{12}C/^{13}C$ ratio of 10/1 or 1000/1 would (under ideal measurement conditions) be easily detected.

Nitrogen, the second most abundant element, is present with order ~1% to 0.1% concentration (Russell, Arden, and Pillinger 1996). At 1% concentration the average nanodiamond would

contain 20 N atoms. For the solar system $^{14}N/^{15}N$ isotopic ratio, one would expect there to be a single ^{15}N atom in only one in ten nanodiamonds, and greater than 100% statistical uncertainty in the isotopic ratio. Thus, measurements of single nanodiamonds cannot, even with idealized instrumentation, yield statistically meaningful isotopic ratios of trace elements.

1.3 Outline of the Following Chapters

I studied the origins of nanodiamonds separated from the meteorite Allende (CV3) by measuring the $^{12}C/^{13}C$ ratios of individual and small aggregates of nanodiamonds, utilizing novel applications of two experimental techniques, atom-probe tomography and nanoscale secondary ion mass spectrometry (NanoSIMS).

In Chapter 2 I give an overview of my methods, including materials, sample preparation, equipment, data collection, reduction, and analysis.

In Chapter 3 I discuss the NanoSIMS studies of small-bulk measurements and statistical data for ensembles of small aggregates of nanodiamonds and the implications for the origins of the nanodiamonds.

In Chapters 4–6 I discuss the results and implications of multiple experimental runs using atom-probe tomography, as well as the correction of various instrumental artifacts.

In Chapter 7 I discuss a final round of atom-probe results, complemented by data from transmission electron microscopy, and present final corrections of previous data sets, comparing these to the NanoSIMS data and discussing the overall implications for potential presolar and solar origins of the nanodiamonds.

1.4 References

Amari S., Hoppe P., Zinner E., and Lewis R. S. 1992. Interstellar SiC with unusual isotopic compositions: Grains from supernova? *The Astrophysical Journal* 394:L43–L46.

Amari S., Lewis R. S., and Anders E. 1994. Interstellar grains in meteorites: I. Isolation of SiC, graphite and diamond; size distributions of SiC and graphite. *Geochimica et Cosmochimica Acta* 58:459–470.

Amari S., Nittler L. R., Zinner E., Gallino R., Lugaro M., and Lewis R. S. 2001a. Presolar SiC grains of type Y: Origin from low-metallicity asymptotic giant branch stars. *The Astrophysical Journal* 546:248–266.

Amari S., Gao X., Nittler L. R., Zinner E., José J., Hernanz M., and Lewis R. S. 2001b. Presolar grains from novae. *The Astrophysical Journal* 551:1065–1072.

Amari S. 2003. Presolar graphite: Noble gases and their origins. *Publications of the Astronomical Society of Australia* 20:378–381.

Amari S., Zinner E., and Lewis R. S. 2005. Isotopic analysis of presolar graphite from the KFB1 Murchison separate. *Meteoritics and Planetary Science Conference*. Abstract #5261.

Arnould M., and Goriely S. 2003. The p-process of stellar nucleosynthesis: astrophysics and nuclear physics status. *Physics Reports* 384:1–84.

Barnard A. S., Russo S. P., and Snook I. K. 2003. Coexistence of bucky diamond with nanodiamond and fullerene carbon phases. *Physical Review B* 68:073406.

Bernatowicz T. J., Gibbons P. C., and Lewis R. S. 1990. Electron energy loss spectrometry of interstellar diamonds. *The Astrophysical Journal* 359:246–255.

Besmehn A., and Hoppe P. 2003. A NanoSIMS study of Si- and Ca-Ti-isotopic compositions of presolar silicon carbide grains from supernovae. *Geochimica et Cosmochimica Acta* 67:4693–4703.

Boato G. 1954. The isotopic composition of hydrogen and carbon in the carbonaceous chondrites. *Geochimica et Cosmochimica Acta* 6:209–220.

Bradley J. P., Sanford S. A., and Walker R. M. 1988. Interplanetary dust particles. In *Meteorites and the early solar system*. Tucson, AZ: University of Arizona Press. pp. 861–895.

Brownlee D. 2014. The Stardust mission: Analyzing samples from the edge of the solar system. *Annual Review of Earth and Planetary Sciences* 42:179–205.

Burbidge M. E., Burbidge G. R., Fowler W. A., and Hoyle F. 1957. Synthesis of the elements in stars. *Reviews of Modern Physics* 29:547–654.

Clayton R. N. 1963. Carbon isotope abundance in meteoritic carbonates. *Science* 140:192–193.

Clayton R. N., Grossman L., and Mayeda T. K. 1973. A component of primitive nuclear composition in carbonaceous meteorites. *Science* 182:485–488.

Clayton D. D. 1989. Origin of heavy xenon in meteoritic diamonds. *The Astrophysical Journal* 340:613–619.

Clayton D. D., Liu W., and Dalgarno A. 1999. Condensation of carbon in radioactive supernova gas. *Science* 283:1290–1292.

Dai Z. R., Bradley J. P., Joswiak D. J., Brownlee D. E., Hill H. G. M., and Genge M. J. 2002. Possible in situ formation of meteoritic nanodiamonds in the early Solar System. *Nature* 418:157–159.

Daulton T. L., Eisenhour D. D., Bernatowicz T. J., Lewis R. S., and Buseck P. R. 1996. Genesis of presolar diamonds: Comparative high-resolution transmission electron microscopy study of meteoritic and terrestrial nano-diamonds. *Geochimica et Cosmochimica Acta* 60:4853–4872.

Deneault E. A.-N., Clayton D. D., and Meyer B. S. 2006. Growth of carbon grains in supernova ejecta. *The Astrophysical Journal* 638:234–240.

Fedkin A. V., Meyer B. S., and Grossman L. 2010. Condensation and mixing in supernova ejecta. *Geochimica et Cosmochimica Acta* 74:3642–3658.

Floss C., and Haenecour P. 2016. Presolar silicate grains: Abundances, isotopic and elemental compositions, and the effects of secondary processing. *Geochemical Journal* 50:3–25.

Hoppe P., Amari S., Zinner E., Ireland T., and Lewis R. S. 1994. Carbon, nitrogen, magnesium, silicon, and titanium isotopic compositions of single interstellar silicon carbide grains from the Murchison carbonaceous chondrite. *The Astrophysical Journal* 430:870–890.

Hoppe P., Strebel R., Eberhardt P., Amari S., and Lewis R. S. 1996. Type II supernova matter in a silicon carbide grain from the Murchison meteorite. *Science* 272:1314–1316.

Hoppe P., Annen P., Strebel R., Eberhardt P., Gallino R., Lugaro M., Amari S., and Lewis R. S. 1997. Meteoritic silicon carbide grains with unusual Si-isotopic compositions: Evidence for an origin in low-mass, low-metallicity asymptotic giant branch stars. *The Astrophysical Journal Letters* 487:L101–L104.

Hoppe P., Strebel R., Eberhardt P., Amari S., and Lewis R. S. 2000. Isotopic properties of silicon carbide X grains from the Murchison meteorite in the size range 0.5-1.5 μm. *Meteoritics & Planetary Science* 35:1157–1176.

Huss G. R., and Lewis R. S. 1994a. Noble gases in presolar diamonds I: Three distinct components and their implications for diamond origins. *Meteoritics & Planetary Science* 29:791–810.

Huss G. R., and Lewis R. S. 1994b. Noble gases in presolar diamonds II: Component abundances reflect thermal processing. *Meteoritics & Planetary Science* 29:811–829.

Huss G. R., and Lewis R. S. 1995. Presolar diamond, SiC, and graphite in primitive chondrites: Abundances as a function of meteorite class and petrologic type. *Geochimica et Cosmochimica Acta* 59:115–160.

Huss G. R. 2005. Meteoritic nanodiamonds: Messengers from the stars. *Elements* 1:97–100.

Huss G. R., Ott U., and Koscheev A. P. 2008. Noble gases in presolar diamonds III: Implications of ion implantation experiments with synthetic nanodiamonds. *Meteoritics & planetary science* 43:1811–1826.

Hynes K. M., and Gyngard F. 2009. The presolar grain database: http://presolar.wustl.edu/~pgd. *40th Lunar and Planetary Science Conference*. Abstract #1198.

Hynes K. M., Croat T. K., Amari S., Mertz A. F., and Bernatowicz T. J. 2010. Structural and isotopic microanalysis of presolar SiC from supernovae. *Meteoritics & Planetary Science* 45:596–614.

Jadhav M., Amari S., Zinner E., and Maruoka T. 2006. Isotopic analysis of presolar graphite grains from Orgueil. *New Astronomy Reviews* 50:591–595.

Jadhav M., Zinner E., Amari S., Maruoka T., Marhas K. K., and Gallino R. 2013. Multi-element isotopic analyses of presolar graphite grains from Orgueil. *Geochimica et Cosmochimica Acta* 113:193–224.

Jorgensen U. G. 1988. Formation of Xe-HL-enriched diamond grains in stellar environments. *Nature* 332:702–705.

Lewis R. S., Ming T., Wacker J. F., Anders E., and Steel E. 1987. Interstellar diamonds in meteorites. *Nature* 326:160–162.

Lewis R. S., Anders E., and Draine B. T. 1989. Properties, detectability and origin of interstellar diamonds in meteorites. *Nature* 339:117–121.

Lewis R. S., Huss G. R., and Lugmair G. 1991. Finally, Ba & Sr accompanying Xe-HL in diamonds from Allende. *22nd Lunar and Planetary Science Conference*. pp. 807–808.

Lin Y., Gyngard F., and Zinner E. 2010. Isotopic analysis of supernova SiC and Si3N4 grains from the Qingzhen (EH3) chondrite. *The Astrophysical Journal* 709:1157–1173.

Liu N., Nittler L. R., Alexander C. M. O., Wang J., Pignatari M., José J., and Nguyen A. 2016. Stellar origins of extremely 13C- and 15N-enriched presolar SiC grains: Novae or supernovae? *The Astrophysical Journal* 820:140 (14pp).

Maas R., Loss R. D., Rosman K. J. R., De Laeter J. R., Lewis R. S., Huss G. R., and Lugmair G. W. 2001. Isotope anomalies in tellurium and palladium from Allende nanodiamonds. *Meteoritics & Planetary Science* 36:849–858.

Marks N. A., Lattemann M., and McKenzie D. R. 2012. Nonequilibrium route to nanodiamond with astrophysical implications. *Physical Review Letters* 108:075503.

Marty B., Chaussidon M., Wiens R. C., Jurewicz A. J. G., and Burnett D. S. 2011. A 15N-poor isotopic composition for the solar system as shown by Genesis solar wind samples. *Science* 332:1533–1536.

Meibom A., Petaev M. L., and Krot A. N. 1999. Primitive FeNi metal grains in CH carbonaceous chondrites formed by condensation from a gas of solar composition. *Journal of Geophysical Research* 104:22053.

Nittler L. R., Amari S., Zinner E., Woosley S. E., and Lewis R. S. 1996. Extinct 44Ti in presolar graphite and SiC: Proof of a supernova origin. *The Astrophysical Journal Letters* 462:L31–L34.

Nittler L. R., Alexander C. M. O., Gao X., Walker R. M., and Zinner E. 1997. Stellar sapphires: The properties and origins of presolar Al2O3 in meteorites. *The Astrophysical Journal* 483:475–495.

Nittler L. R., and Alexander C. M. O. 2003. Automated isotopic measurements of micron-sized dust: Application to meteoritic presolar silicon carbide. *Geochimica et Cosmochimica Acta* 67:4961–4980.

Nittler L. R., and Hoppe P. 2005. Are presolar silicon carbide grains from novae actually from supernovae? *The Astrophysical Journal Letters* 631:L89–L92.

Nittler L. R., Alexander C. M. O., Gallino R., Hoppe P., Nguyen A. N., Stadermann F. J., and Zinner E. K. 2008. Aluminum-, calcium- and titanium-rich oxide stardust in ordinary chondrite meteorites. *The Astrophysical Journal* 682:1450–1478.

Nuth J. A., and Allen J. E. 1992. Supernovae as sources of interstellar diamonds. *Astrophysics and Space Science* 196:117–123.

O'D Alexander C. M. 1993. Presolar SiC in chondrites: How variable and how many sources? *Geochimica et Cosmochimica Acta* 57:2869–2888.

Owen T., Mahaffy P. R., Niemann H. B., Atreya S., and Wong M. 2001. Protosolar nitrogen. *The Astrophysical Journal* 553:L77–L79.

Pepin R. O., Becker R. H., and Rider P. E. 1995. Xenon and krypton isotopes in extraterrestrial regolith soils and in the solar wind. *Geochimica et Cosmochimica Acta* 59:4997–5022.

Pirali O., Vervloet M., Dahl J. D., Carlson R. M. K., Tielens A. G. G. M., and Oomens J. 2007. Infrared spectroscopy of diamondoid molecules: New insights into the presence of nanodiamonds in the interstellar medium. *The Astrophysical Journal* 661:919–925.

Richter S., Ott U., and Begemann F. 1998. Tellurium in pre-solar diamonds as an indicator for rapid separation of supernova ejecta. *Nature* 391:261–263.

Russell S. S., Arden J. W., and Pillinger C. T. 1991. Evidence for multiple sources of diamond from primitive chondrites. *Science* 254:1188–1191.

Russell S. S., Arden J. W., and Pillinger C. T. 1996. A carbon and nitrogen isotope study of diamond from primitive chondrites. *Meteoritics & Planetary Science* 31:343–355.

Stroud R. M., Chisholm M. F., Heck P. R., Alexander C. M. O., and Nittler L. R. 2011. Supernova shock-wave-induced co-formation of glassy carbon and nanodiamond. *The Astrophysical Journal Letters* 738:L27 (5pp).

Swart P. K., Grady M. M., Pillinger C. T., Lewis R. S., and Anders E. 1983. Interstellar carbon in meteorites. *Science* 220:406–410.

Van Kerckhoven C., A. G. G. M Tielens, and Waelkens C. 2002. Nanodiamonds around HD 97048 and Elias 1. *Astronomy & Astrophysics* 384:568–584.

Verchovsky A. B., Fisenko A. V., Semjonova L. F., Wright I. P., Lee M. R., and Pillinger C. T. 1998. C, N, and noble gas isotopes in grain size separates of presolar diamonds from Efremovka. *Science* 281:1165–1168.

Verchovsky A. P., Fisenko A. V., Semjonova L. F., Bridges J. C., Lee M. R., and Wright I. P. 2006. Nanodiamonds from AGB stars: A new type of presolar grain in meteorites. *The Astrophysical Journal* 651:481–490.

Woosley S. E., and Weaver T. A. 1995. The evolution and explosion of massive stars. II. Explosive hydrodynamics and nucleosynthesis. *The Astrophysical Journal Supplement Series* 101:181–285.

Yastrebov S., and Smith R. 2009. Nanodiamonds enveloped in glassy carbon shells and the origin of the 2175 Å optical extinction feature. *The Astrophysical Journal* 697:1822–1826.

Zinner E., Amari S., and Jadhav M. 2006. On the stellar sources of presolar graphite. *Proceedings of Science (NIC-IX)* Abstract #019.

Zinner E., Jadhav M., Gyngard F., and Nittler L. R. 2010. Bonanza: Isotopic anatomy of a large presolar SiC grain of type X. *Meteoritics and Planetary Science Supplement* 73:5137.

Zinner E. 2014. Presolar Grains. In *Treatise on Geochemistry*, 2nd ed. Elsevier. pp. 181–213.

Chapter 2: Experimental and Analysis Methods

The scientific questions addressed by this thesis would be straightforward to answer, given the availability of a survey of the precise, accurate $^{12}C/^{13}C$ ratios of individual meteoritic nanodiamond grains and disordered C from meteoritic acid residue. To measure these values would require the ability to achieve order 100% atomic detection efficiency, with sufficient mass resolution to distinguish 12 and 13 amu, and nm-scale spatial resolution. It would also require the removal or correction of all sources of uncertainty. If the resolution were only 10-100 nm, it would still be possible to determine if the $^{12}C/^{13}C$ ratios of a large fraction of the nanodiamonds were significantly anomalous by analyzing distributions of multiple measured ratios for broadening compared to the expected distribution, as established by statistical modeling and comparison to standards with known isotopic ratio distributions.

Moving away from this idyllic situation, counting statistics put a limit on how precisely it is physically possible to measure the isotopic ratio of a reservoir of two isotopes by sampling material from that reservoir. The quantification of this limit is the minimum uncertainty or error for any measurement and calculation. The only way to entirely remove this limit would be direct measurement of every atom in the reservoir. Given that we are discussing a reservoir in the remote past and far distant from us, our ability to measure a significant fraction of the material, or even to know what fraction we have measured, is severely limited. Instrumental biases and artifacts increase the uncertainty. If they are identified, the measurement may be corrected and the uncertainty quantified. Random errors may be assessed by studying the distribution of a number of experiments, but systematic errors can only be assessed by measuring standards with

known values. If a bias or artifact goes unassessed, our reported precision in the measurement will be erroneously high, because the calculated uncertainty will be erroneously small.

In addition to these fundamental experimental concerns, our ability to achieve our experimental ideals is limited by the available instrumentation. Spatial resolution, mass resolving power, and isotope detection efficiency less than the ideals given above reduce the information that even an ideally conducted, corrected, and standardized experiment can give about the isotopic contents of the material. Various methods exist to assess and overcome some of these limitations, including selecting spatial regions of interest, modeling aggregates of material, and quantitatively separating overlapping mass peaks, but each of these comes at the cost of added statistical uncertainty.

The possibility of errors in the theory used to pose the scientific questions and to suggest models introduces uncertainties that are difficult to quantify. Assessing our confidence in our models and quantifying how much other interpretations would change the results is relevant during choice of experimental approach, but is mostly the province of the introduction and discussion chapters and sections.

Given these statistical and instrumental limitations, a great deal of the work necessary to assess the isotopic ratios of meteoritic nanodiamonds has been the proper design and conduct of sample preparation, characterization, and isotopic analysis, modeling of experimental biases, and proper standardization.

The remainder of this chapter is organized as follows: I discuss the methods used to analyze nanodiamond-containing acid residue separated from the meteorite Allende, as well as terrestrial detonation nanodiamonds, carbon paint, and graphite standards (Section 2.1). For bulk

measurements, and to serve as a correction and standard for instrumental bias in the atom-probe, I utilized Nanoscale Secondary Ion Mass Spectrometry (NanoSIMS), which is introduced in Section 2.2 and discussed in detail in Section 3.2. For isotopic measurements of individual grains, I implemented a novel application of atom-probe tomography (APT) (Section 2.3), taking advantage of recent advances in instrumentation and data analysis for that instrument and the focused ion beam (FIB) microscope.

2.1 Materials

Though rare and small, meteoritic nanodiamonds are the most abundant presolar grain type by mass, at ~1400 ppm (Zinner 2014). I have studied grains from the carbonaceous chondrite Allende CV3, which were separated from the meteoritic host matrix by Roy Lewis at the University of Chicago, using acid dissolution and size separation, following the method used for the nanodiamonds studied in Lewis et al. (1987); Lewis, Anders, and Draine (1989); and Daulton et al. (1996). For an outline of similar processing, for which 250 ppm of Allende was separated as nanodiamond-containing acid residue, see Huss and Lewis (1995). The result is nanodiamonds colloidally suspended in a few ounces of deionized water and then deposited onto a gold foil. The same process was followed for terrestrial nanodiamonds, which are produced synthetically by detonation (Greiner et al. 1988).

For NanoSIMS measurements of nanodiamond acid residue aggregates, nanodiamond-containing acid residue deposits on gold foil were introduced to the spectrometer analysis chamber.

For the NanoSIMS measurements I used three standard materials – detonation nanodiamonds prepared similarly to the Allende nanodiamonds, graphite, and carbon paint.

The graphite was in the form of a planchette from Ted Pella, Inc. Category No. 16711 "Standard Specimen Mount, Carbon." This was observed to have significant surface morphology, so I polished it using the procedure wenol→lint free cloth→acetone (5 min ultrasonicating)→methanol (5 min ultrasonicating)→bake, which created large flat regions easy to target in the NanoSIMS.

The carbon paint (DAG) was painted onto the graphite planchette, and exhibited morphological heterogeneity (surface roughness) visible under optical and secondary electron microscopy.

For more information on the sample preparation and experimental procedure for the NanoSIMS experiments, see Section 3.2.

2.2 NanoSIMS

One of the two major sources of data in this thesis is from secondary ion mass spectrometry. I used the Cameca NanoSIMS 50 at Washington University. An 8 kV beam of Cs+ primary ions was focused orthogonally onto a ~50 nm spot on the sample of nanodiamond-containing acid residue deposit or carbonaceous standard. The Cs^+ ions sputter away surface atoms and molecules, slowly milling down into the sample. On the order of 1% of the sputtered material is ionized and then extracted and delivered to a magnet by electron optics. Five detectors were arranged to collect ions with certain masses as selected by the magnet. Several statistical approaches were used to search thousands of measurements of small aggregates of nanodiamonds for isotopic anomalies. This methodology is only used in Chapter 3, so I leave the detailed discussion of the method to Section 3.2.

2.3 Atom-probe Tomography

2.3.1 Multilayer Preparation

To prepare samples for analysis by APT, I first prepared nanodiamonds in a multilayer substrate suitable for FIB liftout. Three multilayers have been prepared to date. The multilayers designated pND (presolar NanoDiamonds) and sND (synthetic NanoDiamonds) were prepared by Dieter Isheim and Frank Stadermann in 2010 at Northwestern University and were used for the meteoritic and terrestrial data sets, respectively, through data set R06 20172. Dieter Isheim and I created the multilayer designated pND3 in October 2013, also at Northwestern University. Similar procedures were followed for each deposition. Here I report the procedure for pND3. Beginning with a Ni stub cleaned for use in a vacuum system, I deposited a 130-170 nm layer of Pt using a Southbay Technologies IBSe Ion Beam Sputtering system. In order to deposit nanodiamonds onto this Pt substrate without significant agglomeration, I ultrasonicated both the destination Pt-Ni substrate and the origin Au-steel disk during the transfer. This was accomplished using ultrasonicating knives with customized heads that accept metal stubs (Figure 2.1a and b).

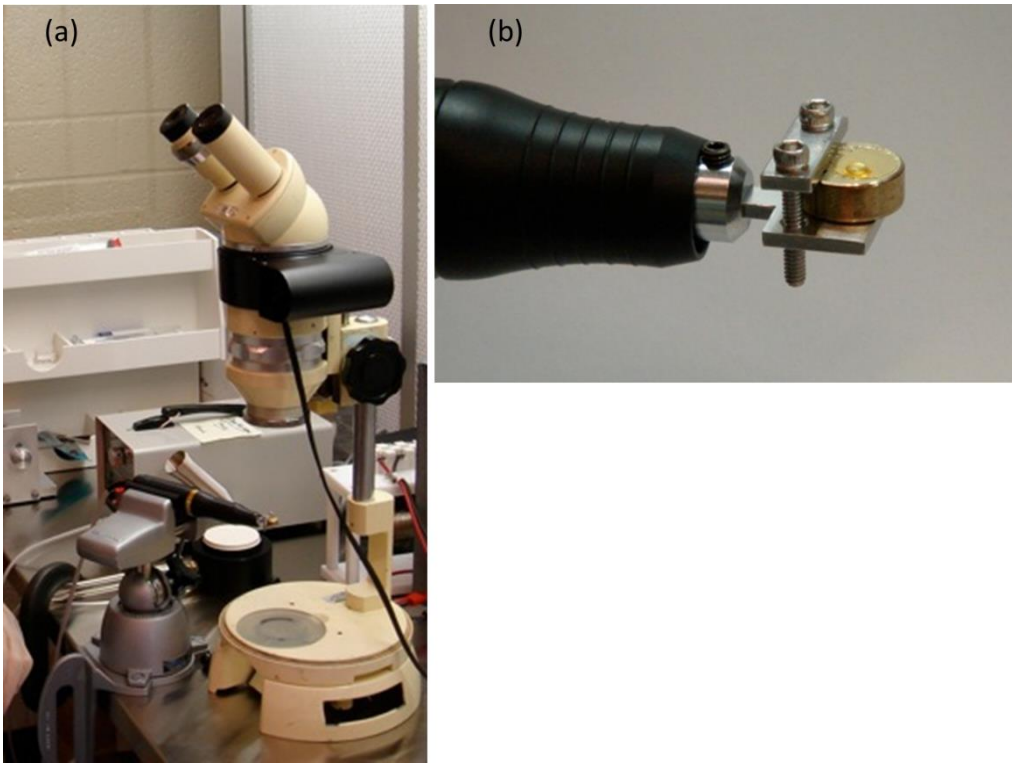

Figure 2.1 (a) Ultrasonicator with articulating clamp (left) and power supply (light gray box behind ultrasonicator). (b) Nanodiamond deposit on Au-foil, in ultrasonicating head.

The steel disk became hot to the touch during ultrasonication. For multilayer pND3, a ~50 microliter droplet of deionized water was pipetted onto the ultransonicating Au foil. For multilayers pND and sND, a smaller droplet was pipetted onto the Au foil. For pND3, it took several minutes for most of the liquid to evaporate, at which time I micropipetted 2 microliters of the remaining suspension to the Pt-substrate. For pND and sND, pipetting onto the Pt-substrate was done without such a long wait period, as it was not necessary to allow as much of the liquid to evaporate to ensure acid residue had become entrained in suspension. The remaining liquid evaporated in a few seconds, leaving behind a circular deposit. A second 150 nm layer of Pt was deposited on top of the deposit, beginning within a few minutes of depositing the acid residue. This was followed by a cap layer of Ni.

The resulting Ni-Pt-nanodiamond-Pt-Ni “sandwich” multilayer was the source of atom-probe samples via FIB liftout. The region where the nanodiamond residue deposit has pushed up the Ni layer is visible in SE imaging, which allowed us to select what density of agglomerates to target for FIB liftout (Figure 2.2).

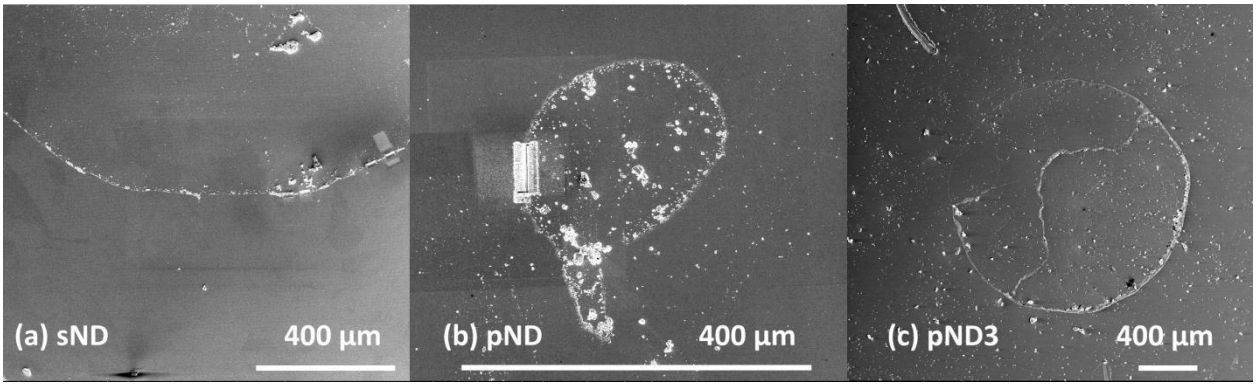

Figure 2.2 SEM images of deposits in each multilayer, showing a Ni cover layer pushed up by nanodiamond-containing acid residue material. Liftouts target the outer edge of these circular deposits for atom-probe analysis. The right-hand side of image (a), sND, shows a liftout region surrounded by a rectangle of lighter-color material altered by the electron and ion beams. The left-hand side of (b), pND, also shows a liftout. The long feature at the upper-left of image (c), pND3, is a fiduciary scratch left by a tweezer for use at lower magnifications.

2.3.2 Focused Ion Beam Liftout of Multilayers

The following procedure is given in a step-by-step “recipe” format where each step is accompanied by the appropriate figure, as this should be the best presentation for the reader and the researcher. Figures are secondary electron images taken by scanning electron microscopy, unless stated otherwise. Tilted images were taken at a 52 degree angle to the surface. An illustration of the target geometry and steps to achieve it is given in Figure 2.3.

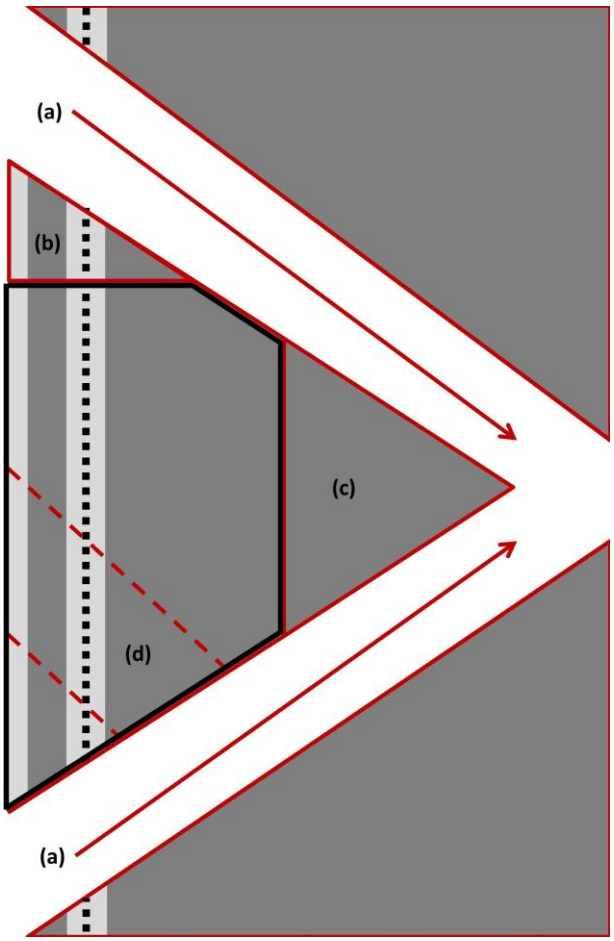

Figure 2.3 Diagram of the liftout geometry. The surface of the multilayer is on the left-hand side. Dark gray is Ni, Light gray is Pt. The black dashed line is the nanodiamond-containing acid residue. The multilayer is oriented on its side so that the liftout is in the orientation it presents when attached to the top of a micropost. (a) The red arrows show the ion beam paths for the two undercuts. (b) This red triangle shows the material milled away by the face trim. (c) This red triangle shows the material milled away by the belly trim after 90 degree rotation. (d) The two dashed red lines mark the bounds of the mortise and tenon which runs through the interior of the slice and initially attach it to the micropost flat top, which will be at the bottom from this perspective. The shape of the slice prior to sharpening is outlined in black.

An FEI Quanta dual beam FIB/SEM was used for liftout of sections of the multilayer. Secondary electron imaging was conducted at 2 kV using a 1 mm aperture and 4 nA beam current from a Schottky thermal emission source in analytical mode. I selected 25×5 μm areas for liftout (Figure 2.4).

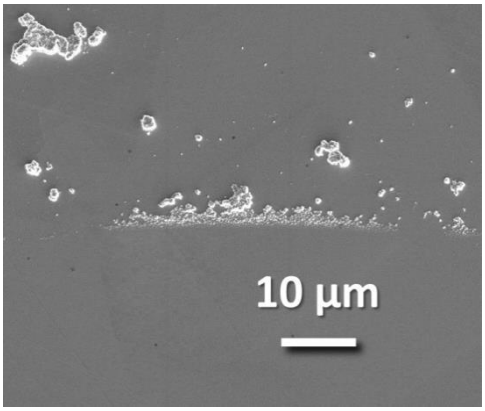

Figure 2.4 The multilayer sND, showing a 25 µm long region with acid residue deposit pushing up the surface.

I selected regions where the points at which cluster sizes becoming vanishingly small form a line centered in the liftout (Figure 2.5).

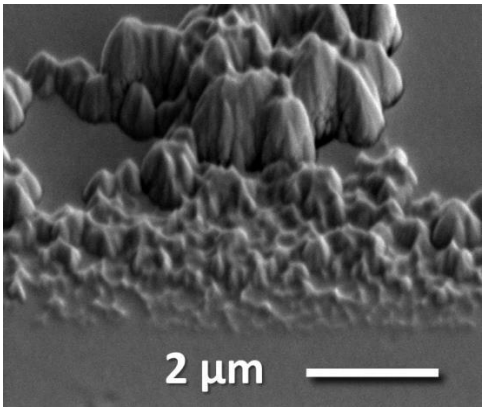

Figure 2.5 The multilayer surface imaged at a tilted (52 degree beam incidence) angle, zoomed in on the deposit surface, showing a line where the deposit height becomes vanishingly small.

I deposited 0.15 µm of Pt from a gas injection system (GIS) over the selected area using a 0.3 nA current of Ga ions to crack the Pt-organo-metallic precursor gas (Figure 2.6). The Ga beam energy was 30 kV (30 kV was used in following ion beam steps, unless stated otherwise). I often deposited over an area slightly larger than the dimensions of the liftout. This Pt cap served as a sacrificial layer against ion beam damage.

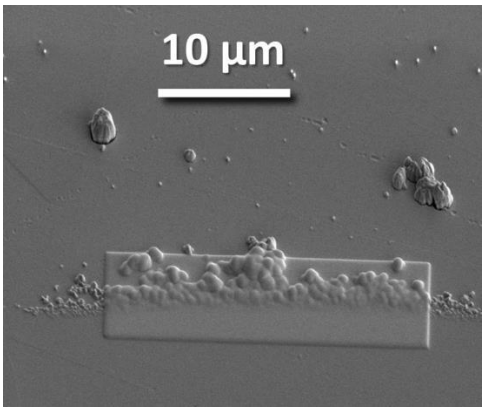

Figure 2.6 The liftout region covered with GIS-deposited Pt sacrificial layer.

I then made a wedge cut underneath each long side of the liftout, using a pattern of dimensions 1.5 µm wide by 30 µm long by 7 µm deep (not corrected for projection) (Figures 2.3a and 2.7), using 7 nA of Ga ions at a 52 degree angle tilt from normal incidence to the multilayer surface.

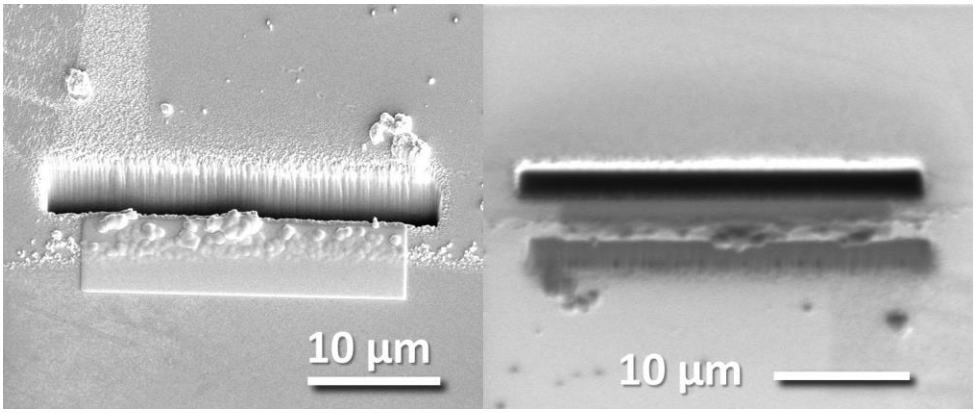

Figure 2.7 (a) The first ion-beam wedge undercut. (b) Tilted ion beam image of the second undercut.

Still at 52 degree tilt incidence, I milled a 1.25×6.25 µm pattern from one end of the liftout (dimensions are not corrected for tilt), until that end of the liftout was free of the multilayer (Figure 2.8).

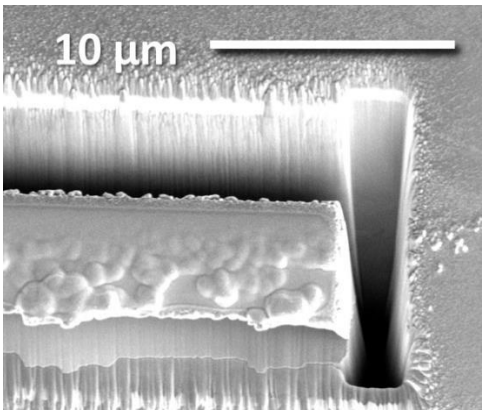

Figure 2.8 The first side cut.

Rotating the stage 180 degrees, I inserted the micromanipulator needle and attached it to the free end of the liftout with a roughly 1×1 µm Pt deposition patch using a 30–50 pA current Ga beam (Figure 2.9).

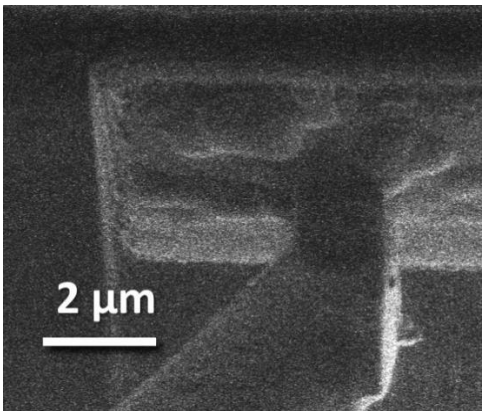

Figure 2.9 Ion beam image of the free end of the liftout with the tip of the micromanipulator needle (bottom and center) attached to the surface by a GIS-deposited Pt patch (dark, center).

At this point only the opposite end of the liftout was still attached to the rest of the multilayer. Maintaining the 52 degree tilt from Ga ion beam normal incidence, I sliced the liftout free using another 1.25×6.25, 1 nA pattern. Redeposition of milling material beneath the liftout often occurred during this step. Tapping the instrument or changing the ion beam current while imaging in SE created vibrations through the micromanipulator and helped assess if the liftout

was free of the multilayer. As soon as the multilayer was free I raised the liftout on the micromanipulator (Figure 2.10).

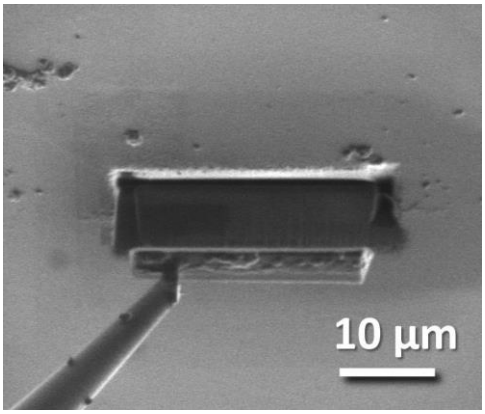

Figure 2.10 A tilted ion beam image of the liftout (bottom) attached to the micromanipulator needle (bottom left corner) just after removal from the multilayer, leaving a hole behind.

I aligned the free end of the liftout with the tip of the tungsten needle on an ARM (Axial Rotational Mechanism), attached them to each other with Pt deposition (Figure 2.11), and cut free the micromanipulator.

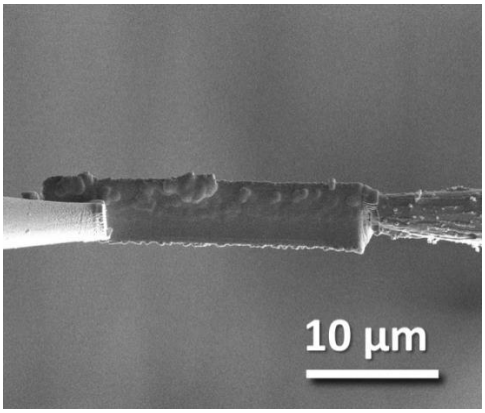

Figure 2.11 The liftout attached to the ARM needle by Pt-patching.

Tilting to 0 degrees ion beam incidence (beam normal to the multilayer top surface), I milled away the acid-residue-free edge of the liftout with a 1 nA Ga beam, leaving approximately 2

microns from the edge to the first visible clusters of acid residue and exposing a cross section of the multilayer (Figures 2.3b and 2.12).

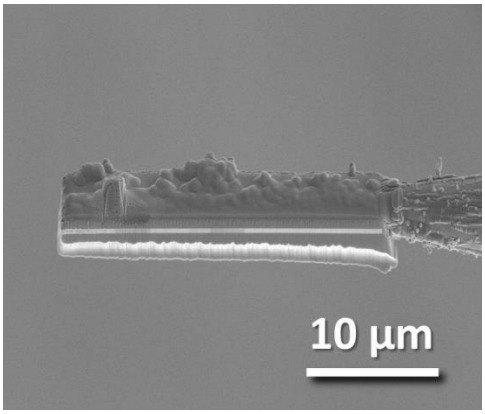

Figure 2.12 The liftout after a face trim reveals a cross section of the multilayer (the narrow strip of lighter-colored material is the Pt-nanodiamond-Pt sandwich.

I then vented the system in order to access and actuate the ARM 90 degrees about the long axis of the liftout. Pumping the system again, this rotation allowed me to tilt the stage to bring the sample surface edge-on to the Ga IB. From this orientation I conducted a “belly” trim, thinning the bottom of the liftout using 1 nA of current (Figures 2.3c and 2.l3).

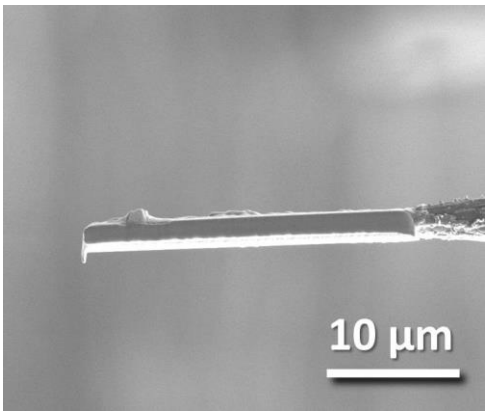

Figure 2.13 The finished liftout after rotation of the ARM and belly trim, which removed material from the bottom.

At this point in the procedure in early samples I deposited protective Pt on the exposed cross section of the multilayer, but in later liftouts I bypassed this step.

2.3.3 Micropost Preparation on Prefabricated Arrays

Atom-probe tomography using the LEAP series of instruments requires that samples be raised above surrounding material to prevent electrical discharge from nearby sharp surfaces. For samples on which correlated TEM (transmission electron microscopy) was not conducted, I used prefabricated Si micropost arrays to accomplish this geometry. These arrays hold 36 or 22 etched Si microposts with 2 μm flat tops. I sliced each liftout into a number of ~2 μm sections, attached to the microposts. A typical 25 μm liftout yielded 8 such sections. These slices were mounted onto all of the posts on the 22-post arrays and onto the outer two rows on each side of 36 post array (24 posts). The middle two rows of the 36 post arrays were left empty to avoid obstructing the line of sight of the thermal-pulsing laser in the atom-probe tomograph.

After the trimming described in Section 2.2.2, the cross section of the liftout through the long axis is a trapezoid with one side truncated. The parallel sides are oriented vertically and the top side is truncated to reveal the multilayer (Figure 2.3, solid black outline).

If the plane of the deposition layer is not entirely vertical, a slight stage tilt throughout the following steps can be used to align the microposts with it.

To attach and slice free a section from a liftout I drove the free end of the liftout to just above a micropost and lowered it until the long bottom edge of the liftout made contact. I used a “mortise and tenon” method, in which a 30–50 pA, 1×1 μm Ga ion beam raster pattern mills through the top of the multilayer (Figure 2.3d). Redeposition typically attached the micropost to the liftout at this point, but regardless it was held stationary by the micromanipulator. Ion-beam activated GIS deposition with the same raster pattern as the mortise created a tenon joint by backfilling the mortised holes with Pt. Sometimes a raster pattern with a slightly reduced area was used for the tenon to discourage Pt from growing over the top of the mortised hole before it could backfill.

At this point the liftout was attached to the micropost and to the micromanipulator needle. It was important to quickly cut the micromanipulator free, or else drift would cause the whole system to rotate and bend about the Pt patches, eventually rupturing one of the patches, allowing the liftout to spring back to its original, unstrained orientation, which could cause it to break free entirely and be lost.

To quickly cut free an attached section I used a 3 nA, 0.75×6 μm raster pattern and drove the micromanipulator directly away from the newly separated section (in our configuration this is to the left).

After I completed slicing and attaching each piece of the liftout, and the micromanipulator needle was retracted, I rotated the stage 180 degrees and conducted "back-welding," depositing Pt into the gap between the micropost and the bottom of each slice.

At this point the microtips were secure on the array and the samples could be removed from vacuum and stored at atmosphere as necessary.

2.3.4 Micropost Preparation on Electropolished Cu Half-grids

Microtips for correlated TEM/APT studies were prepared atop Cu TEM half-grids, allowing them to be safely introduced both into the TEM and the atom-probe. I used Ted Pella #460-205 Omniprobe® Lift-Out Grids, Cu with 5 posts. The cross sections of these posts are too large and rough for use in the atom-probe as-is. I used an electropolishing cell to reduce the posts to a more slender profile and smooth the rough edges. Half-grids HG01–HG04 were electropolished using an electropolishing cell maintained at Northwestern University in the center for atom-probe tomography (NUCAPT). Half-grids HG05 and HG06 were electropolished at Washington University at a cell built by me and technician Tim Smolar in the Laboratory for Space Sciences.

The electropolishing cell at Washington University uses a <10 mA current from a power supply that is conducted through a room temperature electrolyte solution of approximately 2.5% phosphoric acid in distilled water. The posts were immersed into the cell for less than 30 seconds, as sufficient for a polish, assessed by an optical microscope. Half-grids were dipped in acetone immediately following polish to remove residual phosphoric acid. Half-grids that might otherwise be sources of errant signal under APT analysis were further cleaned by ultrasonication in methanol and baking, and were stored in membrane holders until liftout slice attachment. Prior to introduction into the FIB and the atom-probe, I mounted the half-grids in Electron Microscopy Sciences 5956-01 FIB Sample Holders, also known as fortress holders. I machined off the protective rims of these holders prior to use to allow line-of-sight for the atom-probe laser.

To further sharpen the posts prior to attaching slices of a multilayer liftout I used rectangular Ga ion beam pattern mills at 52 degrees to thin the width of the posts to roughly 6 µm (Figure 2.14a–c). An additional mill smoothed the apex of the post (Figure 2.14c). Finally, I used an annular mill pattern at 0 degrees relative to the post in order to narrow the apex to a 3 µm cross section (Figure 2.14e–f).

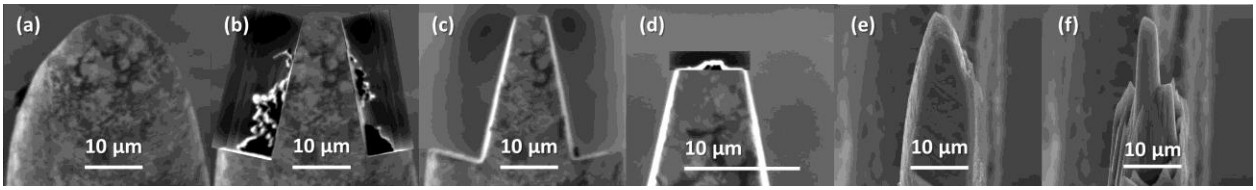

Figure 2.14 Sequence of SEM images showing ion beam milling of electropolished Cu half-grid posts prior to attachment of multilayer samples. (a) Electropolished post, broad side Ga beam perspective, ion beam imaging. (b) Post during narrowing. (c) Post after narrowing. (d) Post during apex smoothing. (e) Narrow-side view, electron gun perspective and imaging, during 3 µm annular mill. (f) After 3 µm annular mill.

2.3.5 Focused Ion Beam Sharpening of Microtips

After attachment to a micropost, initial annular milling to sharpen a slice of a multilayer liftout into a microtip was conducted using 0.1 nA Ga ions with the beam parallel to the long axis of the

micropost, using an annular mill pattern of outer radius 3 μm, inner radius 2 μm. Additional patterns were used around the edges as necessary to remove any material outside the radius of the central pattern.

It is important to limit annular milling to prevent overthinning of the Pt patch interface between the multilayer slice and the micropost below it, as this is a weak point in the microtip. At this point I used "pyramidal sharpening" to narrow the apex of the multilayer without thinning the Pt patch. I used 30 pA Ga ion rectangular mill patterns at 15 degrees off-axis (37 degrees tilt in the FEI Quanta) to mill each of four sides of the sample, leaving a roughly 0.5 μm^2 square cross section at the apex of a tetrahedral microtip with exposed multilayer down two of the faces (Figure 2.15a). Then I conducted a series of mills using annular 16-bit stream file patterns provided by Cameca Instruments Inc., all at 30 pA Ga current. First I used pattern AMP3B-16bit at 50 k× magnification (Figure 2.15b), followed by AMP4B-16bit, a pattern with a smaller inner radius, also at 50 k× magnification (Figure 2.15c). At this point I used electrostatic beam shifting to move a 0.75 μm circular mill pattern across the sample, cleaning up any sharp features less than 2 μm below the apex. I then increased magnification to 60 k× and used AMP4B-16bit (Figure 2.15d). I continued this mill until the radius of a circle fit to the apex of the microtip is smaller than 30 nm.

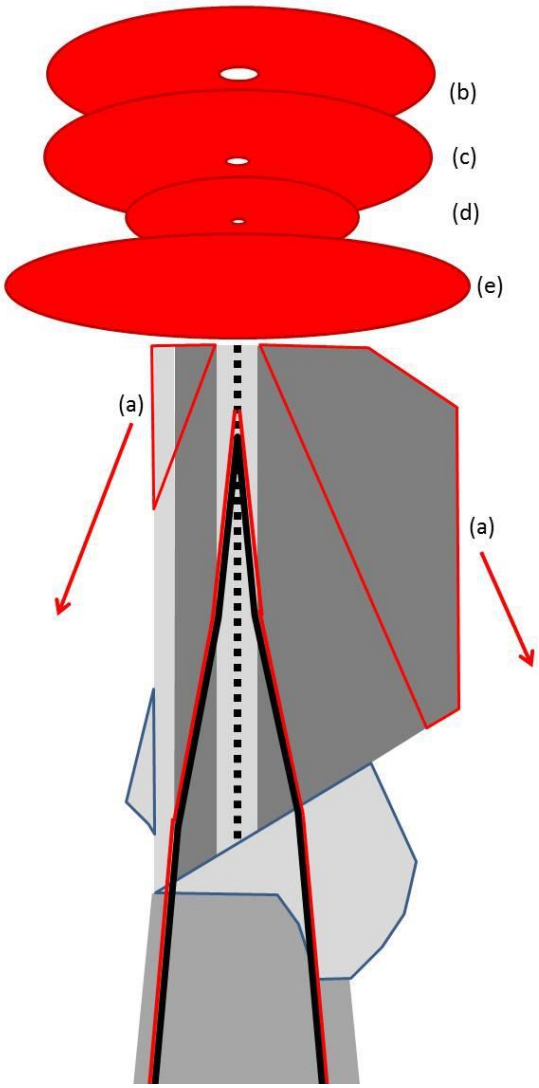

Figure 2.15 Microtip sharpening steps. Dark gray represents Ni, medium gray is the Si or Cu micropost, light gray is Pt, and the dashed black line is the deposition layer. Blue enclosed regions are GIS-deposited Pt used to attach the slice of a multilayer liftout to the micropost, using a mortise and tenon (left), and backfill (right) method. The red outlines in (a) enclose two of the regions milled away by pyramidal sharpening. (b)–(d) represent annular mill patterns that further sharpen the microtip after pyramidal steps. (e) represents the pattern used with 5 kV Ga to clean the microtip surface and target the microtip apex to a region of interest along the deposition layer. The solid black line shows the silhouette of the final microtip, ready for APT or TEM.

The Ga beam amorphizes the surface layer of crystalline material it mills. It has been shown by atom-probe tomography that lowering the beam voltage dramatically lowers the depth of the amorphized region (Thompson et al. 2007). Therefore, before proceeding to sample analysis, I conducted at least 10 seconds of 48 pA Ga milling at 5 kV with a 3 µm circular pattern (Figure

2.15e). This mill can be continued until the apex has been milled down to within 100 nm of a visible cluster of acid residue, distinguished as darker material by SEM contrasted with surrounding lighter layers of Pt.

I coated some of the microtips with Ni after sharpening. This increased overall stability during APT data collection, reduced the overall electric field required for field evaporation, served as a fiduciary marker of the beginning of the Pt multilayer, and made it easier to observe during APT data collection if microfractures were occurring, especially if one of the Pt layers was falling off, based on whether the Pt data being collected was ringed by Ni all the way around or only on one side. I used the Southbay Tech IBSe deposition system at Northwestern University, with a 9 kV, 6–6.8 mA plasma, a vacuum pressure prior to deposition $2–3\times10^{-6}$ Torr, and plasma pressure of $4–6\times10^{-4}$ Torr, while rotating the sample to aid in homogeneous deposition. I found these parameters on this instrument resulted in a consistent 35 million ions (primarily Ni) collected in a LEAP 4000X Si prior to milling into the Pt layer.

2.3.6 Transmission Electron Microscopy

Prior to Ni coating, some of the sharpened microtips are characterized by TEM, including scanning transmission electron microscopy (STEM), high angle annular dark field imaging (HAADF), and electron energy loss spectroscopy (EELS). These techniques revealed high resolution details about the microtip shape, the acid residue deposition layer, individual nm-scale particles, and even allowed me to carry out elemental and crystal matrix identification of carbon, graphite, and diamond in some microtips. Some of these microtips were later analyzed by APT.

TEM measurements are reported and discussed only in Chapter 7, so I leave detailed discussion of these techniques and the analysis of the data to Section 7.2.

2.3.7 Atom-probe Data Collection

Atom-probe tomography is an analysis technique that is undergoing a period of rapid technological and technical development as it approaches maturity (Gault et al. 2012; Kelly and Larson 2012; Larson et al. 2013; Seidman and Stiller 2009). It has, however, been in use by scientists since 1967 (Müller et al. 1968), and its predecessor, field ion microscopy, has been studied and utilized scientifically since 1951 (Müller 1951). For quantitative examples of instrumental capabilities, I will refer to the specifications of the instrument primarily used in this study, the Cameca LEAP 4000X Si.

Samples are introduced to ultra-high vacuum (10^{-10} Torr or lower) through a load-lock and buffer chamber system, and aligned with the microtip apex near a local electrode. The introduction of a local electrode, rather than the remote electrode used in the 1990s, now allows multiple microtips to be prepared on the same sample coupon without concern for interference or collision, broadens the field of view, and lowers the required voltages for field evaporation, which allows broader microtips to be analyzed (Nishikawa and Kimoto 1994).

The best orientation for the half-grids is about 15 degrees away from normal to the laser. This enables the operator to distinguish the microtips in the analysis chamber camera view (Figure 2.16a), an important capability for alignment, while still giving a nearly vertical orientation of the series of microtips from the perspective of the laser (Figure 2.16b). The magnification of the laser perspective camera view is often sufficient to note when a microtip has fractured or melted as a result of electrostatic discharge, as is the case for microtip D in Figure 2.16b.

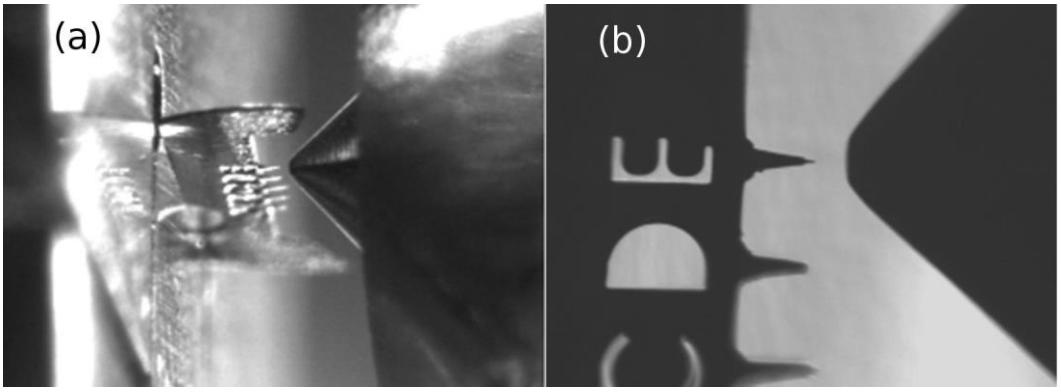

Figure 2.16 (a) Ni-coated Cu half-grid HG06 (center), clamped in Ni-coated stainless steel holder FH1 (left), aligned with a local electrode (right) in the atom-probe tomograph. Analysis chamber camera view. (b) Micropost E is aligned with the local electrode. Laser perspective camera view. For scale, the half-grid is about 3 mm across.

Under electric fields of order ten billion volts per meter, atoms of a variety of solid materials can be removed from a surface as ions. This process is called field evaporation. The electric field on a sphere of radius *r* at an electric potential *V* is given as *V/r*, so for spheres with radii on the order of 100 nm, a field of ten billion volts per meter can be achieved with voltages on the order of 1 kV. The magnitude of the electric field *E* produced at the apex of a sharp conical object by voltage *V* may be estimated to be

$$E = \frac{V}{kr} \tag{2.1}$$

where *k*, the field factor, is a correction factor greater than one, found to be ~3 for many atom-probe applications. The field factor corrects for the effects that the non-sphericity of the microtip has on the electric field for a given voltage and radius of curvature. A complete description of the physics of field evaporation (also called “field desorption”) has not emerged, so the evaporation fields required for various materials, and which factors affect those values, are estimated based on measurements and the predictions of incomplete models. The evaporation field for Pt has been fairly well-characterized as 45 V/nm (Tsong 1978). The field for carbon is estimated to be

103 V/nm but is much more poorly known, and is likely to vary between the different phases of carbon.

The electric field on the surfaces of the microtip away from the apex is significantly lower, meaning that for a homogeneous sample, an electric field just high enough to field evaporate ions at the apex will not evaporate ions from elsewhere on the sample, unless there is a sharp secondary microtip close to the apex.

The geometry and thus the electric field are complicated by the roughness of the sample at the atomic level. The electric field is strongest at the sharp edges of atomic planes in crystalline solids, removing atoms from these edges first.

At the microtip apex, field lines will be close to radial, with a small correction due to the field factor. Thus field evaporated ions will accelerate radially away from the microtip, projecting onto the far field where the image may be considered to lie on a hemispherical section. 2D planar detectors are used due to their simple geometry. A detector placed some distance away will detect a magnified image; this geometry allows a field evaporation instrument to function as a point-projection microscope, where the sample itself is a dynamically-shaped lens. The magnification is calculated as

$$M = \frac{L}{\xi R} \tag{2.2}$$

where L is the flightpath length, 90 mm, R is the radius of the apex of the microtip, and ξ is image compression factor, typically about 1.5, which takes into account that the field lines are neither perfectly radial due to the non-spherical microtip, nor are they perfectly straight, due to the presence of the local electrode, which bends them towards the detector. This gives magnification on the order of $10^6\times$, resulting in lateral spatial resolution that is less than a

nanometer. The spatial resolution along the cylindrical shaft of the sample can be as small as the spacing between atomic planes. Indeed, my experiments sometimes reproduced Pt crystal planes. For a known material, planar spacing can be used to precisely calibrate the scale along the shaft.

Historically, voltage pulsing was used to demarcate time of flight windows. Pulsing the voltage up to the evaporation field of the sample material for a brief window of time causes a large increase in the probability of field evaporation. Ions are assumed to field evaporate during this narrow time interval, so the difference between the detection time and the voltage pulse peak is equal to the time of flight of a detected ion with a small uncertainty. Alternatively, as pioneered in laser atom-probe instruments (Tsong et al. 1982), a thermal pulse delivered to the specimen microtip via a laser greatly increases the probability of thermal activation of the field evaporation process. Advances in laser technology and commercial development made laser-pulsed atom-probes viable tools for university researchers in the 2000s (Kelly and Larson 2012; Seidman and Stiller 2009).

Heat affects the field evaporation process by exciting vibrational modes of atoms and molecules, increasing the likelihood that for a given static deformation of charge distributions and nuclear position (i.e., polarizing a surface atom), one or more electrons will quantum tunnel away from the ion. Most atom-probe experiments are run in conditions below 100 K through cryocooling, although for thermal pulsing the specimen microtip temperature at the time of field evaporation will briefly be significantly higher than the standing temperature. Ions may be ionized multiple times by field evaporation, arriving in charge state 2^+ or higher. Higher charge state ions are more likely to form at lower temperatures, in which case more of the energy of ionization is delivered via electric potential. The effects of the interaction between electric potential and thermal energy, while actually complex, may be treated as additive, in which picture the laser

pulse replaces some fraction of the voltage necessary for field evaporation. The fraction of the energy for field evaporation provided by the laser pulse is called the pulse fraction. This is a useful analogy, not a physical principle – for example, a 100% pulse fraction does not lead to thermal ionization; field evaporation is accomplished by electric field; thermal effects are limited to activating the electric field affect.

The majority of the potential gradient is within a few nanometers of the microtip apex; therefore, most of the acceleration of an ion takes place in the first few nanometers of a 10 mm flight – that is, almost instantaneously. Velocities range from order 10^3–10^5 m/s for elements of interest, with flight times ranging from 10^3–10^1 ns. Estimating a constant ion velocity, one can conduct time of flight mass spectrometry based on the pulse time and detection time for each ion. Atom-probe tomography may therefore be described as a combination of point projection microscopy and time-of-flight mass spectrometry.

Field evaporated ions are accelerated by the electric field through the local electrode and projected onto the 2D detector positioned approximately 10 mm away from the sample (Figure 2.17).

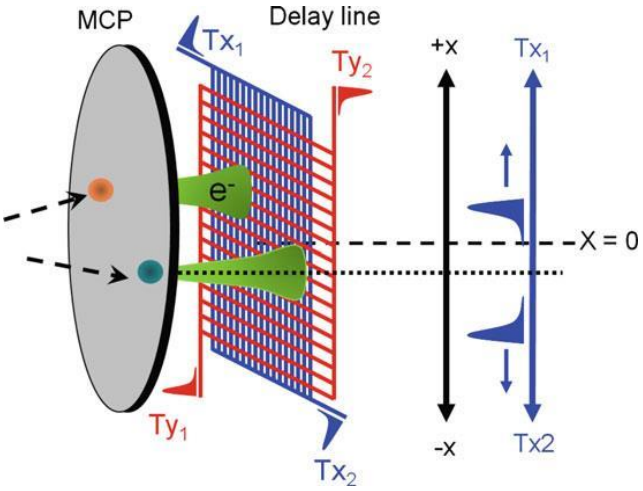

Figure 2.17 Illustration of the basic features of the LEAP 4000X detector system. Ions are accelerated by the electric field and projected onto the microchannel plate (MCP). T_2-T_1, the delay between the processing of a pair of timing signals in one of several delay lines, gives a position estimate for where along the axis of orientation of a delay line the pulse passed through. Taken with permission from Gault et al. (2012, 46).

The current generation of detectors uses delay lines, capable of 2 ns timing and distinguishing many multi-hit events. A microchannel plate with 57% open space (Larson et al. 2013; Sakurai and Hashizume 1986) is placed in front of the delay lines at a slight angle to the flightpath so an ion can enter a microchannel but then impacts on a side, producing an electron cascade to be detected. Thus the ideal atomic detection efficiency is 57% for the LEAP 4000X SI, as this is the fraction of the atoms that can be expected to enter the microchannels and produce an electron cascade rather than impacting on the face of the microchannel plate. This effect is not element dependent.

Data collection is also limited by the field of view, which depends on the distance of the sample microtip from the local electrode and the detector, distances that vary sample to sample. The LEAP 4000X Si has a field of view as high as 200–250 nm (Kelly and Larson 2012; Larson et al. 2013, 2). It is designed in a wide field of view configuration and has a shorter flight path than

reflectron instruments, so the field of view in samples collected with this instrument is close to optimal for current technology.

The voltage is controlled by automated algorithms to maintain a low average ion detection rate, reported as the percent of detection windows in which an ion is detected. I used rates of 0.1–5%, that is, 1 ion detected per 1000–20 detection windows. Low detection rates greatly suppress the occurrence of multiple hits during a detection window. The electronics can record up to 16 hits during a single detection window, which is thus the maximum number of ions that can be detected from a single pulse-event on the microtip sample. Any higher number of ions creating electron cascades will not be recorded. This is the detector pileup effect.

There are other sources of signal loss at the detector in addition to detector pileup. Multiple ions arriving close together in space and time are subject to several effects. Even if the individual pulses created on the delay lines are all distinct they may be detected close enough together to leave multiple solutions for where the two or more electron cascades passed through the delay lines. With three delay lines at different angles the capacity for this effect is several ions in a very short period of time, but the capacity varies based on where on the detector surface the ions arrive, and there is no published map of the detector sensitivity for the LEAP detectors.

It is also possible for ions of similar mass to arrive so close together in space and time that they create overlapping pulses that cannot be resolved as two events by the electronics and are recorded as only one ion at that mass. This multihit effect depends not only on the counts per detection window but also on how energetically favorable it is for pairs of ions with the same mass-to-charge-state ratio to co-evaporate from adjacent atomic or molecular positions on the surface of the microtip sample, an effect called correlated evaporation. Carbon is particularly

prone to correlated evaporation (Rolander and Andrén 1988; Thuvander et al. 2011, 2013; Yao et al. 2010). Lower detection efficiency has been shown to lessen this effect by screening out some of the correlated ions (Thuvander et al. 2013), but the low number of ^{13}C atoms in an individual nanodiamond would lead to prohibitively large uncertainties if I lowered the detection efficiency.

The most common way for an atom-probe data collection session to end is in sample failure and loss. The high field stresses the microtip and can strain it to the point of fracture, most often at a weak interface such as the Pt patch that attaches the sample liftout slice onto the micropost, or at the deposition layer running along the long axis of the microtip. Often a fracture will facilitate electrostatic discharge between the micropost and the local electrode, delivering an electric arc through the micropost. These electrostatic discharges typically melt the Si or Cu micropost, leaving a deformed microtip with no clear evidence of where the fracture occurred. Sometimes a piece of the sample falls off in what is called a microfracture, but there is no electrostatic discharge and the run may continue, although with a discontinuity in the region of the sample analyzed and possible roughness on the sample. If a fracture or fracture-and-discharge occur, post-APT review by SEM and TEM are less informative than if the data collection is stopped by the user prior to microtip fracture.

2.3.8 Atom-probe Data Reduction

Improvements such as the implementation of automation, laser pulsing, faster laser pulse rates, smaller laser spot size, local electrodes, faster detector electronics, and improved hit detection algorithms have greatly increased the range of materials that can be analyzed by atom-probe tomography as well as the throughput, efficiency, and quality of the data collection (Gault et al. 2012; Kelly and Larson 2012; Larson et al. 2013; Seidman and Stiller 2009). Such advantages have made the isotopic study of nanoscale, insulating particles possible for the first time. But

data reduction and interpretation are not straightforward, especially since the focus of our analysis, the measurement of isotopic ratios, is an uncommon application of the technique and has not been previously thoroughly developed. It has therefore been important to consider the various sample preparation problems and potential instrumental artifacts that may affect our data.

Data reduction and analysis was largely carried out using IVAS, the Imago Visualization and Analysis System, a computer software package (Cameca Instruments Inc., (Kunicki et al. 2006)).

I have introduced the field factor k, the image compression factor ξ, and the detection efficiency (call it η), three parameters that must be estimated to correct for biases in the atom-probe. These parameters are not easy to determine precisely, but incorrect values will result in deformation of the reconstructed volume (Figure 2.18), allowing the user to test for better values, especially if there is good documentation and characterization of the microtip shape and any subgrains at high magnification by SEM or TEM.

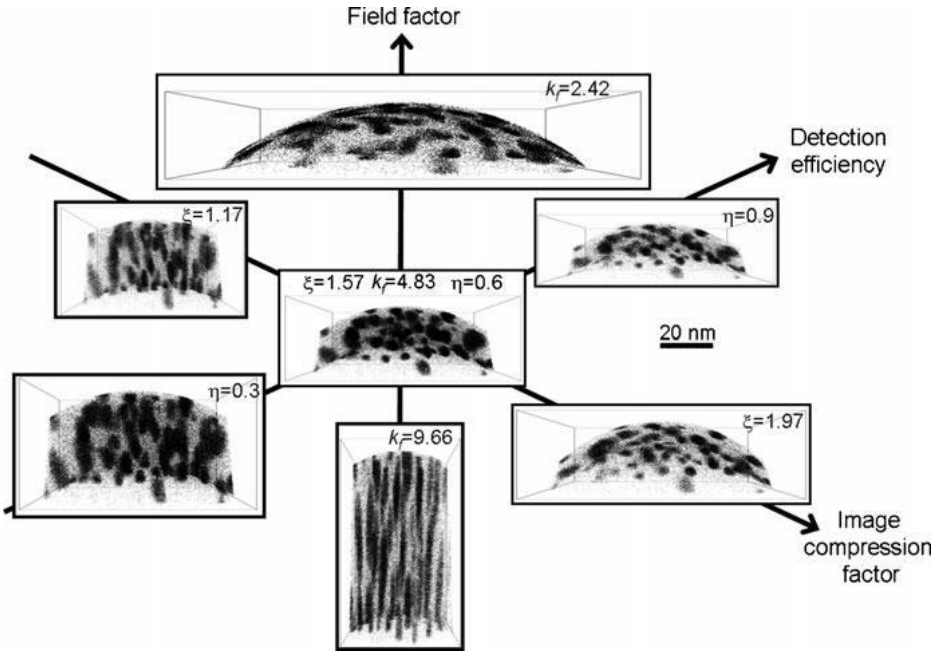

Figure 2.18 Illustration of the effects that choice of estimations for the field factor *k*, detection efficiency η, and image compression factor ξ has on a reconstruction. The center image has the known correct proportions, based on the volume and shape of the dark inclusions. The surrounding images are all poor reconstructions due to improper estimation of one of these three reconstruction parameters. Taken with permission from Gault et al. (2012, 181).

Projecting ions from a hemispherical microtip onto a planar detector introduces variations in the time of flight for ions of the same mass-to-charge-state ratio depending on the location on the microtip from which they were ionized. Furthermore, the recorded times of flight for different ions of the same element or molecule vary due to ions being field evaporated at different voltages. The microtip is a rough hemisphere at the end of a post, not a sphere. I use algorithms in the IVAS software to iteratively fit models to these effects by varying the model parameters to minimize the width of the largest peak in the mass spectrum. These fits are called the bowl and voltage corrections. For my samples, the largest peak is almost always from the most abundant isotope of Pt, ^{195}Pt, sometimes at charge state 1^+ (195 amu), sometimes at 2^+ (97.5 amu), depending on the experimental conditions. The bowl correction F_B fits a function for a

hemispherical projection onto a plane. The voltage correction fits the equation $F_V = a_0/\sqrt{a_1 + V_{DC} + a_2 V_{DC}^2}$. The corrected time of flight is given as

$$t_{cor} = F_V F_B (t_{raw} - t_0) \tag{2.3}$$

(Larson et al. 2013, 113–114).

At this point in the reconstruction process I had the corrected time of flight information for each ion detected, but wished to calculate the mass-to-charge-state ratio. Based on the transfer of the electric potential energy into kinetic energy of the accelerated ion, this ratio is approximated as $m/n = 2eVt_{corr}^2/L^2$ where *m* is the mass of the ion, *n* is the charge state, *e* is the charge of the electron, *V* is the applied voltage, t_{cor} is the time of flight, and *L* is the length of the ion flight path from sample to detector. This is only an approximation because not all the energy imparted to the ion is transformed into kinetic energy, and because the ion's velocity is not precisely constant, since it does take a nonzero (if miniscule) fraction of its time of flight to accelerate to its maximum velocity. Instead of requiring precise estimates of these factors, the data reconstruction software takes user identifications of several peaks in the mass spectrum and uses them to fit the parameters *c* and t_0 in the equation

$$\frac{m}{n} = \mathrm{c}(\mathrm{t_{corr}} - \mathrm{t_0})^2 \tag{2.3}$$

(Larson et al. 2013, 116).

Al and Pt peaks are always present from the sputter deposited Pt, with several charge states and/or isotopes in distinct patterns, so it is easy to avoid misidentifying peaks during this process, even in the rare cases where this correction is more than a few 10ths of an amu for some peaks.

Among atom-probe tomograph users there are multiple accepted methods for selecting a peak "range," that is, what upper and lower limits of the mass-to-charge-state spectrum should be used for a particular peak. For example, as recently as 2013 Larson et al. (2013, 118) write "There is currently no standard, universally accepted, method for determining peak ranges, so it is very important to indicate the procedures used and to be consistent in their application throughout multiple analyses." Chapters 6 and 7 use atom-probe data from multiple experimental runs, which was presented in earlier chapters using different procedures for determining peak ranges. In each case the old data sets were re-analyzed with updated procedures, so that the older and newer data sets are comparable.

Using the average FWHM peak width for the APT data sets in this work, the average mass resolution is calculated to be roughly 400 for $^{12}C^{++}$ and $^{13}C^{++}$, and roughly 600 for $^{12}C^{+}$ and $^{13}C^{+}$. This is comparable to the typical, approximate APT mass resolution of 500 ($M/\Delta M$ for FWHM) (Gault et al. 2012, 128). While this is sufficient to easily distinguish the main ^{12}C and ^{13}C peaks from each other, higher temperatures on the microtip can lead to large tails toward higher mass in the spectrum, such that ^{13}C peaks at 6.5 amu (charge state 2^{+}) and 13 amu (charge state 1^{+}) must be checked for interference from the tails of the ^{12}C peaks at 6 and 12 amu. The common isobar for $^{13}C^{+}$, the $^{12}CH^{+}$ hydride, cannot be separated with the MRP of current atom-probe tomograph designs. However, our ability to measure the ratio of $^{12}C/^{13}C$ from the peak counts at charge state 2^{+} as well as 1^{+} allows us to assess the level of hydride interference by comparing the two ratio measurements. The nearest commonly observed peaks from contaminant elements in the Pt matrix are Al (13.5 and 9 amu) and N (14 and 7 amu), neither of which pose any risk of peak interference. $(^{12}C^{13}C)^{++}$ peaks are observed at 12.5 amu in a number of data sets, suggesting

the presence of some interference from $^{12}C_2^{++}$ at 12 amu, which theoretically should contribute $(^{12}C/^{13}C)^2$ more counts to the peak at ^{12}C than to $^{13}C_2^{++}$ at 13 amu.

Regions of interest in the reconstructed volume, as well as selection of peaks and widths, were completed using a variety of criteria to find a method that best assesses the signal from the acid residue in a reproducible, easy-to-implement fashion. Various methods are described in the methods sections of Chapters 4, 6, and 7 (Heck et al. 2014; Lewis et al. 2015). One concern in choosing a region of interest is that ions from the Pt matrix and acid residue often overlap in the reconstructed volume. This is partly due to preferential magnification of the nanodiamonds through trajectory aberration. Figure 2.19 illustrates this process. Diamond has a higher evaporation field than Pt (Tsong 1978), so it resists ion loss when it is exposed at the evaporating microtip apex. The field at a given point is inversely proportional to the radius formed by the rounded microtip (Equation 2.1). As a result, once a nub of higher-field material is exposed, forming a smaller, secondary radius, the local field increases dramatically until ions begin to field-evaporate with more divergent trajectories than the Pt ions field evaporating from the matrix. This causes the signal from the nanodiamond to be preferentially magnified. Furthermore, at such high fields, it is possible, even likely, that multi-atomic pieces of exposed carbonaceous material will field evaporate in chunks. This is most likely to proceed as entire nanodiamonds being removed from beds of disordered C. Contaminants and disordered C between the diamond surfaces and the Pt will not be as strongly bonded as the C atoms inside a nanodiamond are to each other. Analysis of both the hole left in the Pt matrix and the cluster of C ions detected can give a good estimation of the original particle size, which allows the estimation of the density. If one knows the density of the carbonaceous particle – be it diamond, graphite, or a disordered phase of C – one can estimate the detection efficiency for that particle.

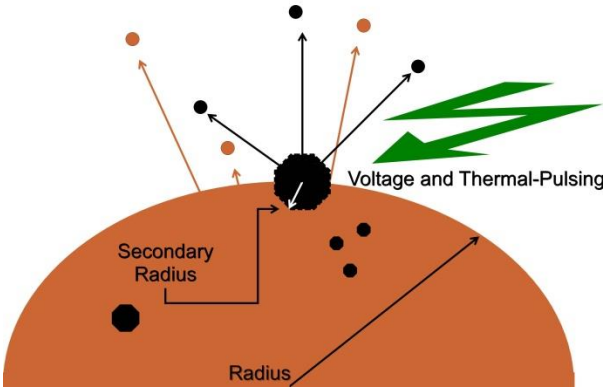

Figure 2.19 Preferential magnification and cluster loss. A material with a higher evaporation field (black) such as diamond embedded inside of a material with a lower evaporation field (orange) such as platinum will be preferentially magnified through trajectory aberrations.

After peak selection and background assessment I corrected for instrumental artifacts related to multiple hits on the detector during the same time of flight window. Two methods for deadtime correction are described in detail in Chapters 5 and 6 (Lewis et al. 2015; Stephan et al. 2015). The deadtime correction algorithm that is described in Chapter 6 and used for deadtime corrected data reported in Chapters 6 and 7 is given in Appendix 1.

Details of the analysis and correction processes varied for the results discussed in Chapters 4–7, and are reported in the methods sections of those chapters. Section 7.2 details the state of the art for our atom-probe methodology.

2.4 References

Daulton T. L., Eisenhour D. D., Bernatowicz T. J., Lewis R. S., and Buseck P. R. 1996. Genesis of presolar diamonds: Comparative high-resolution transmission electron microscopy study of meteoritic and terrestrial nano-diamonds. *Geochimica et Cosmochimica Acta* 60:4853–4872.

Gault B., Moody M. P., Cairney J. M., and Ringer S. P. 2012. *Atom Probe Microscopy*, New York: Springer.

Greiner N. R., Phillips D. S., Johnson J. D., and Volk F. 1988. Diamonds in detonation soot. *Nature* 333:440–442.

Heck P. R. et al. 2014. Atom-probe analyses of nanodiamonds from Allende. *Meteoritics & Planetary Science* 49:453–467.

Huss G. R., and Lewis R. S. 1995. Presolar diamond, SiC, and graphite in primitive chondrites: Abundances as a function of meteorite class and petrologic type. *Geochimica et Cosmochimica Acta* 59:115–160.

Kelly T. F., and Larson D. J. 2012. The second revolution in atom probe tomography. *MRS Bulletin* 37:150–158.

Kunicki T. C., Beerman D., Geiser B. G., Oltman E., O'Neill R. W., and Larson D. J. 2006. Atom probe data reconstruction, visualization and analysis with the Imago Visualization and Analysis System (IVAS). *19th International Vacuum Nanoelectronics Conference & 50th International Field Emission Symposium*. pp. 535–536.

Larson D. J., Prosa T. J., Ulfig R. M., Geiser B. P., and Kelly T. F. 2013. *Local electrode atom probe tomography - A user's guide*, 1st ed. New York: Springer-Verlag.

Lewis R. S., Ming T., Wacker J. F., Anders E., and Steel E. 1987. Interstellar diamonds in meteorites. *Nature* 326:160–162.

Lewis R. S., Anders E., and Draine B. T. 1989. Properties, detectability and origin of interstellar diamonds in meteorites. *Nature* 339:117–121.

Lewis J. B., Isheim D., Floss C., and Seidman D. N. 2015. 12C/13C-ratio determination in nanodiamonds by atom-probe tomography. *Ultramicroscopy* 159:248–254.

Müller E. W. 1951. Das feldionenmikroskop. *Zeitschrift für Physik* 131:136–142.

Müller E. W., Panitz J. A., and McLane S. B. 1968. The atom-probe field ion microscope. *Review of Scientific Instruments* 39:83–86.

Nishikawa O., and Kimoto M. 1994. Toward a scanning atom probe — computer simulation of electric field. *Applied Surface Science* 76:424–430.

Rolander U., and Andrén H.-O. 1988. On atom-probe analysis of cubic MX-type carbides and carbonitrides. *Le Journal de Physique Colloques* 49:C6-299–C6-304.

Sakurai T., and Hashizume T. 1986. Determination of the detection efficiency of a channelplate electron multiplier. *Review of Scientific Instruments* 57:236–239.

Seidman D. N., and Stiller K. 2009. An atom-probe tomography primer. *MRS Bulletin* 34:717–724.

Stephan T., Heck P. R., Isheim D., and Lewis J. B. 2015. Correction of dead time effects in laser-induced desorption time-of-flight mass spectrometry: Applications in atom probe tomography. *International Journal of Mass Spectrometry* 379:46–51.

Thompson K., Lawrence D., Larson D. J., Olson J. D., Kelly T. F., and Gorman B. 2007. In situ site-specific specimen preparation for atom probe tomography. *Ultramicroscopy* 107:131–139.

Thuvander M., Weidow J., Angseryd J., Falk L. K. L., Liu F., Sonestedt M., Stiller K., and Andrén H.-O. 2011. Quantitative atom probe analysis of carbides. *Ultramicroscopy* 111:604–608.

Thuvander M., Kvist A., Johnson L. J. S., Weidow J., and Andrén H.-O. 2013. Reduction of multiple hits in atom probe tomography. *Ultramicroscopy* 132:81–85.

Tsong T. T. 1978. Field ion image formation. *Surface Science* 70:211–233.

Tsong T. T., McLane S. B., and Kinkus T. J. 1982. Pulsed-laser time-of-flight atom-probe field ion microscope. *Review of Scientific Instruments* 53:1442–1448.

Yao L., Gault B., Cairney J. M., and Ringer S. P. 2010. On the multiplicity of field evaporation events in atom probe: A new dimension to the analysis of mass spectra. *Philosophical Magazine Letters* 90:121–129.

Zinner E. 2014. Presolar Grains. In *Treatise on Geochemistry*, 2nd ed. Elsevier. pp. 181–213.

Chapter 3: Origin of Nanodiamonds from Allende Constrained by Statistical Analysis of C Isotopes from Small Clusters of Acid Residue by NanoSIMS

This chapter has been submitted for publication to Geochimica et Cosmochimica Acta and is under review. It was submitted in collaboration with Christine Floss and Frank Gyngard (Lewis et al. 2017). This author's personal contribution was to conduct experimental analyses, develop statistical methods and scripts for data reduction, all data analysis, the writing of the manuscript, and management of drafts and revisions in collaboration with the coauthors. In Section 3.3 I report the use of a script to read, process, and conduct statistical analyses on NanoSIMS .IM binary data files. That script is given in Appendix 2.

3.1 Introduction

Potentially presolar nanodiamonds were first observed in nature in 1987 (Lewis et al. 1987), identified by transmission electron microscopy (TEM) examination of the residual material after acid dissolution, and size and density separations of material from the primitive carbonaceous chondrite Allende. They are ubiquitous in carbonaceous chondrites, at levels up to 1400 ppm by mass (Zinner et al. 2014). They have a log-normal size distribution that varies from 2.6–3.0 nm in median diameter depending on meteorite and separation method (Lewis et al. 1989; Daulton et al. 1996).

The isolation of these nanodiamonds and their designation as the first type of presolar grain was the result of tracing the anomalous Xe isotopic component, Xe-HL, through a series of chemical

and physical separation processes. The resulting acid residues contain a number of isotopic anomalies in gases that can be observed by stepped heating. Xe-H has an overabundance of the heavy, *r*-process isotopes ^{134}Xe and ^{136}Xe; Xe-L is enriched in the lighter, *p*-process isotopes ^{124}Xe and ^{126}Xe, relative to solar abundances. As these two nucleosynthetic processes are only known to occur together during supernova explosions, the isotopically anomalous Xe-HL is strong evidence of supernova material present in the acid residues. And, as expected if the nanodiamonds formed from supernova remnant material, there are other isotopically anomalous components present, including excess ^{128}Te and ^{130}Te (Richter et al. 1998), and ^{110}Pa (Maas et al. 2001). No competing mechanism has been proposed to produce Xe-HL other than supernovae. For the nanodiamonds themselves, carbon stars and their environs are obvious source candidates, because they have the required high C/O ratio necessary for C-rich minerals to condense. Lewis et al. (1987, 1989) first suggested that nanodiamonds formed in red giants or planetary nebulae by a mechanism akin to laboratory chemical vapor deposition (CVD), and were later implanted with Xe-HL traveling at 10^3 km/s, presumably provided by the explosion of the host star as a Type II (core-collapse) supernova. Alternatively, it is possible that the nanodiamonds formed in expanding Type II supernova remnants, where chemical and isotopic heterogeneity is expected (Clayton 1989; Nuth and Allen 1992; Clayton et al. 1995), or in the envelopes of Carbon stars in binary systems, where the companion star later exploded as a Type I supernova, implanting the nanodiamonds with Xe-HL. Notable anomalies in the ^{12}C/^{13}C isotopic ratio of presolar nanodiamonds are expected in either of these scenarios. Finally, it has been suggested that nanodiamonds are formed by supernova shock in the interstellar medium (ISM) (Tielens 1990; Stroud et al. 2011). Nanodiamonds also carry He, Ne, Ar, and Kr whose isotopic ratios are distinct from solar and appear to be associated with the Xe-HL; as few as 1 in 10^6 grains are

required to carry Xe-HL, but to account for these additional trace elements would require roughly 1 in 10 nanodiamonds (Huss and Lewis 1994a; Huss and Lewis 1994b; Huss and Lewis 1995; Huss et al. 2008; see Huss (2005) for an overview).

The isotopic ratio of $^{12}C/^{13}C$ (and, to a lesser degree, that of $^{14}N/^{15}N$), is the only attribute of these grains that can conclusively establish where the presolar carriers of the Xe-HL formed, since the noble gases may not have co-originated with the grains. Swart et al. (1983) and Russell et al. (1991, 1996) conducted stepped heating measurements on aggregates of billions of nanodiamonds, but found carbon and nitrogen isotopic ratios consistent with solar composition. Small isotopic anomalies, or small fractions of nanodiamonds with larger anomalies, could easily be hidden in these bulk measurements. Thus, there remains debate as to where meteoritic nanodiamonds formed, and whether all the nanodiamonds, or even a majority of them, are presolar (Dai et al. 2002).

The surfaces of the nanodiamonds appear to be damaged by the hydrofluoric and hydrochloric acid treatment, as the infrared spectrum of the acid residue shows absorption from -CH, -COOH, and C-O bonds (Lewis et al. 1989). It is possible, based on infrared spectral observations of the ISM, that the nanodiamonds were originally encased in sp^2-bonded fullerene shells, which were damaged and transformed into the disordered C, possibly by the acid dissolution process (Yastrebov and Smith 2009).

While the acid residue is generally identified as nanodiamond, a significant fraction of it is composed of sp^2-bonded disordered C. Swart et al. (1983), Russell et al. (1991), and Verchovsky et al. (1998) each note a fraction of material in the residue that releases carbon at lower temperatures and with a ~10 per mil smaller $\delta^{13}C$ than that observed for the sample as a whole.

Russell et al. (1991, 1996) conducted stepped heating analyses on nanodiamond residues from a suite of meteorites. The maximum anomalies detected in a single temperature fraction ranged from $\delta^{13}C$ = -38.8±<0.1‰ in ALH 83100 (CM2) to $\delta^{13}C$ = -32.5±0.1‰ in Inman (L3.4), relative to Pee Dee Belemnite (PDB, $^{12}C/^{13}C$ = 88.99). Our study used Allende (CV3), for which Russell et al. (1991 and 1996) obtained a maximum carbon isotopic anomaly of $\delta^{13}C$ = -35.5±<0.1‰. In earlier work Swart et al. (1983) measured a maximum anomaly of $\delta^{13}C$ = -38 for the as-yet unidentified nanodiamond separate in Allende. Including carbon released at lower temperatures, probably from non-diamond material in the residues, the Allende nanodiamond-containing acid residue has a $\delta^{13}C$ value of -30.4‰ (Swart et al. 1983) or -32.7±0.1‰ compared to a range of -28.0±4.4‰ to -36.1±0.1‰ for a variety of other meteorites (Russell et al. 1996). Different separation and analysis techniques are used by different researchers, potentially influencing the results. To summarize these studies, the most anomalous $^{12}C/^{13}C$ ratio measured in the acid residues is isotopically light, but the magnitude of the anomaly is small compared to the variations found in the solar system.

Implantation is not a viable explanation for the presence of N, as it is for the trace noble gases, so it must have co-originated in the nanodiamonds (Russell et al. 1996). Nitrogen is present in the acid residues at levels ranging from 1800 to 13,000 ppm. The nitrogen is isotopically light compared to nitrogen in terrestrial air, with $\delta^{15}N$ = -348±7‰ (Russell et al. 1996, and references therein), but it is close to the solar value of -383±8‰ determined from Genesis solar wind data (Marty et al. 2011).

Modeling based on Electron Energy Loss Spectroscopy (EELS) data by Bernatowicz et al. (1990) indicates that roughly half the carbonaceous material is disordered. Scanning transmission electron microscopy (STEM) confirmed the presence of disordered carbon and minor elements

(Stroud et al. 2011, 2016). It is not clear whether the disordered carbon was a precursor for the nanodiamonds, co-originated with nanodiamonds in the ISM (Stroud et al. 2011), was created by acid dissolution damage of nanodiamonds, or has a different origin from the nanodiamonds and is aggregated from the meteoritic material during the dissolution process. With our methodology (Section 2.2), we cannot easily distinguish between disordered C and nanodiamonds.

In addition to the nanodiamonds and disordered C, the acid residue has been reported to contain ~600 ppm SiC (Lewis et al. 1989), as well as TiC and metal nuggets (Stroud et al. 2016), residual Na and NaOH from laboratory contamination, and F and Cl from the acid treatment (Lewis et al. 2016).

Other studies have revealed evidence of subpopulations within the nanodiamond acid residues. The carbon and nitrogen isotopic ratios are not identical within uncertainties when measured in nanodiamond residues from different meteorites. This is surprising, considering that the concentration of Xe-HL in the residues does not vary greatly between these meteorites, and the ratio of Xe-H to Xe-L is identical (Schelhaas et al. 1990). Russell et al. (1996) observed a carbonaceous component with carbon isotopes slightly depleted in ^{13}C, $\delta^{13}C$ = -25‰, that released at lower temperatures during stepped heating. They estimated that this component comprises ~20% of the carbonaceous material. Verchovsky et al. (2006) investigated subpopulations of nanodiamonds by differential centrifugation of acid residues, further isolating material that is coarser and less prone to forming colloids. They found isotopically heavy C, isotopically light N, and different noble gas isotopic signatures compared to the original separates. Although SiC could be responsible for these signatures, Verchovsky et al. (2006) argue that the signatures are from asymptotic giant branch (AGB) star-produced nanodiamonds. $\delta^{15}N$ values range from 0 to <-350‰ in stepped heating from Allende (Russell et al. 1991),

although the initial, relatively ^{15}N-rich signal could be fractionation caused by preferential loss of ^{14}N-rich molecular N_2 in the laboratory. In an ongoing study, nanodiamonds have been separated into subpopulations based on size, degree of chemical surface damage, and fraction of disordered C, using electrophoresis (Shatoff et al. 2015; Stroud et al. 2016; Pravdivtseva et al. 2016).

With the exception of ongoing investigations using atom-probe tomography (Heck et al. 2014; Isheim et al. 2013; Lewis et al. 2015), no viable methods exist for measuring the ^{12}C/^{13}C ratio in individual nanodiamonds, due to limitations in size and atomic count. Thirty-four ng of nanodiamond acid residue, the smallest sample we have found reported (Swart et al. 1983, in a single stepped heating step), should contain roughly 10^{15} atoms, enough for 10^{12} nanodiamonds (given a diamond density of 3.51 g/cm^3).

To investigate these potential subpopulations, we measured thousands of clusters of as few nanodiamonds as possible, using nanoscale secondary ion mass spectrometry (NanoSIMS) with a minimized beam spot, collecting data from thousands of small regions across a deposit of nanodiamonds (Sections 3.2.1 and 3.2.2). The resulting data are sensitive to a variety of isotopic signatures that, if present, would indicate presolar origins, which may not be evident in larger bulk studies because of dilution and averaging of anomalies (Section 3.2.3). The data were analyzed to determine the overall ^{12}C/^{13}C ratio (Section 3.3.1), and to search for outlier ratios (Section 3.3.2) and significant broadening of the distribution of measured ratios (Section 3.3.3), which would indicate multiple isotopic sources. After discussing silicon observed in the acid residues (Section 3.3.4), we present detection limits and assess what isotopically anomalous populations are ruled out by our data (Section 3.3.5). In Section 3.4, we discuss the implications of the data for existing research and for the probable stellar origins of nanodiamonds, and summarize our conclusions in Section 3.5.2.

3.2 Methods

3.2.1 Samples

A droplet of nanodiamond-bearing Allende acid residue, designated DM (Lewis et al. 1989), suspended in deionized water was deposited onto gold foil by Roy Lewis (Figure 3.1a).

For standards, we used 4–7 nm diameter nanodiamonds created by detonation (Greiner et al. 1988) that were separated and prepared similarly to the Allende deposit (Figure 3.1b). Additional standards included DAG carbon paint, $\delta^{13}C$ = (-29.3 to -24.6)±1.7‰ relative to PDB (Amari et al. 2014), and a polished graphite planchette (Figure 1c). We observed much lower count rates for the detonation nanodiamond standards than the Allende nanodiamonds. A possible explanation is that the detonation nanodiamond deposits onto gold foil are much sparser than the meteoritic nanodiamond deposits.

The abbreviations for the samples are ADM (Allende DM nanodiamond-containing acid residue), DND (detonation nanodiamond acid residue standard), GRP (polished graphite planchette), and CPT (DAG carbon paint).

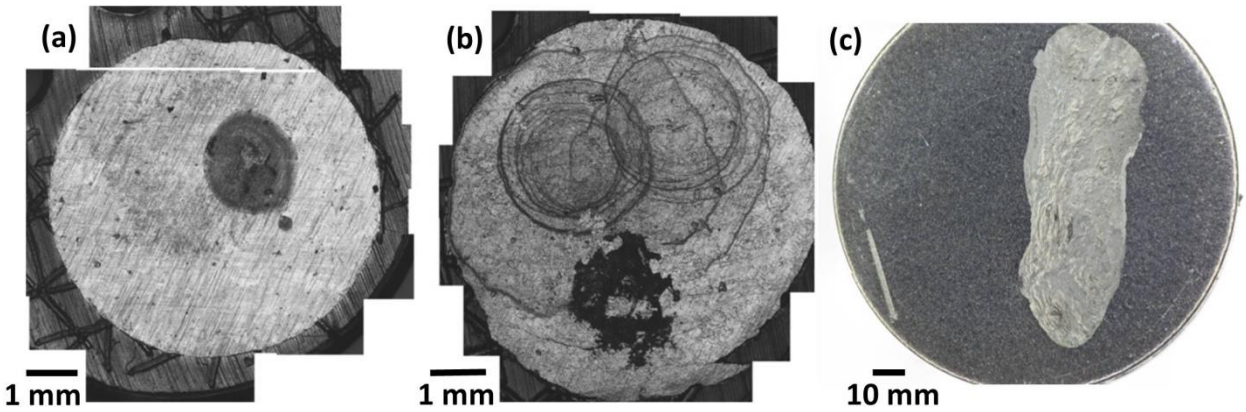

Figure 3.1 Grayscale mosaics of reflected light optical microscopy images of samples. (a) Stub with Allende DM nanodiamond residue on gold foil. (b) Stub with terrestrial detonation nanodiamonds on gold foil. (c) Stub made of polished graphite (darker). "DAG" carbon paint (lighter) was applied to the right-hand side.

3.2.2 Data Collection

Our experimental goal was to conduct thousands of measurements of ^{12}C and ^{13}C, each of as few nanodiamonds as possible. We used the Cameca NanoSIMS 50 at Washington University in St. Louis. We chose this instrument for its high spatial resolution (down to 50 nm), mass resolving power sufficient to distinguish ^{13}C from $^{12}C^{1}H$, and multicollection that allowed us to simultaneously collect ^{12}C and ^{13}C for the major isotope ratio and ^{28}Si to detect SiC or any other Si-bearing phase in the acid residue. Using the NanoSIMS, we bombarded the sample with a Cs^{+} primary beam, implanting Cs ions and sputtering away material. The NanoSIMS achieves high spatial resolution through the use of co-axial primary and secondary ion beams, allowing the ion extraction optics to be placed much closer to the sample than in other SIMS instruments, and by using a primary beam that is perpendicular to the sample, minimizing the cross section of the sample struck by the beam. In order to measure as few nanodiamonds as possible in aggregate, we tuned the NanoSIMS to a small beam. While the beam size has numerous dependencies, the key changes we made were using a source demagnification lens to decrease the primary beam size and using the smallest field aperture diaphragm in the immersion lens. The secondary ion current is low, not only because of the smaller primary beam diameter, but also due to a drop in current density inherent to this configuration.

To measure the primary beam diameter, we scanned the beam perpendicularly across a sharp boundary between carbon paint and a void (Figure 3.2a). For our small beam, the signal should fall off rapidly, based on the width of the material transition (close to a step function) convoluted with the size of the beam. We measured the signal on either side of the boundary and calculated how far the beam traverses as the signal intensity falls from 84% to 16%, resulting in an upper limit for the beam size. Over a number of measurements, the smallest this value fell to was 70

nm (Figure 3.2b). We emphasize that this is an upper limit; we expect our beam was closer to 50 nm in size, but so as not to dramatically overestimate our sensitivity to isotopic anomalies, we take 70 nm as our beam diameter. Spot sizes as small as 30 nm in diameter have been reported for the NanoSIMS (e.g., Hoppe et al. 2015). Such measurements would reduce the number of nanodiamonds analyzed per beam spot by 80% (such a change would be an improvement but not an unqualified one, the accompanying drop in counts as a result of measuring less material would slow data collection).

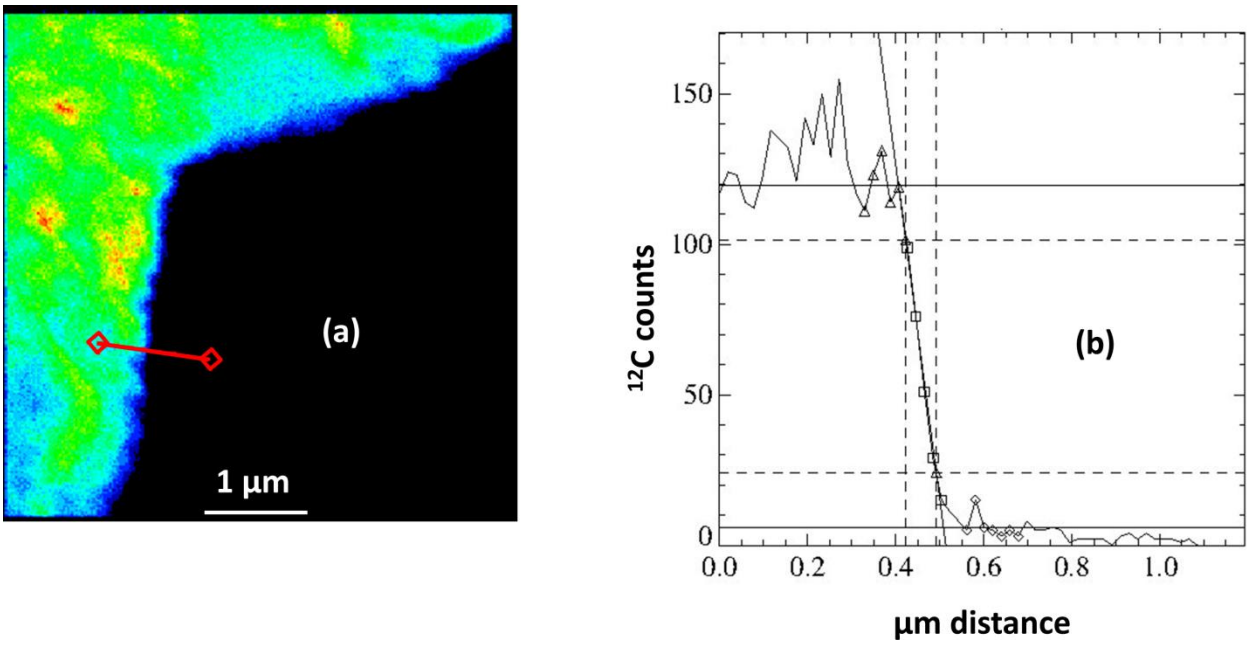

Figure 3.2 Beam diameter minimization. We conducted a linescan across a near-step function in signal intensity (a), represented by the red line and diamond endpoints. The beam full width half max is given by fitting the linescan data (b), where boxes denote points used to fit the signal drop-off, and triangles and diamonds denote points used to fit the high and low signals, respectively. The width of the beam is taken to be the distance over which the beam falls from 84% to 16% intensity, and in this case is less than 70 nm.

To serialize acquisition of spot measurements, we used imaging mode with an image size of 1.2×1.2 µm^2 and 16×16 pixels, where the distance between two pixels (75 nm) is larger than the beam full width half max, minimizing overlap in the material measured. We used multiple cycles with the maximum dwell time of 1 second. The time between each 1 second dwell on a spot is

256 seconds. It took several hours to acquire 256 pixel data sets with 26–150 cycles. Table 1 gives the number of cycles, carbon count rates, and collection time for each data set. If the primary beam experienced extreme drift, on the order of 50 nm during the time between the first and last 1 second dwell on a pixel, it would as much as double the number of nanodiamonds sampled for that pixel, decreasing our sensitivity to anomalies in small areas. Unfortunately, the analysis software did not allow us to use longer dwell times in imaging mode, and to conduct thousands of measurements in spot mode would have been prohibitively time intensive. It would be ideal if the control software allowed for the automated collection of large numbers of depth profile measurements, as this would minimize drift time per pixel. However, drift correction algorithms in the L'Image image processing software suggest the drift is already smaller than one 75 nm diameter pixel.

Table 3.1 Measurement conditions for each NanoSIMS data set.

Data Set[a]	Cycles	Mean C counts per pixel per cycle	Analysis Time (minutes)
ADM 26-1	60	1130	256
ADM 26-3	130	279	555
ADM 27-3	122	180	521
DND 25-4	105	28	448
DND 28-1	60	64	256
DND 28-3	35	91	149
GRP 29-2	26	3020	111
GRP 29-4	150	3123	640
CPT 28-1	91	2279	388

[a] ADM: Allende DM nanodiamond-containing acid residue.

DND: Terrestrial detonation nanodiamond-containing acid residue.

CPT: Carbon paint.

GRP: Graphite planchette.

In order to assess our sensitivity to isotopic anomalies, it is important that we know how much material we have analyzed. Making such an estimate is non-trivial. One method for approximating the number of nanodiamonds sampled from (N_C) is based on the number of carbon counts detected, n_D:

$$N_C = \frac{n_D}{\frac{4}{3}\pi r^3 \rho_D U} \tag{3.1}$$

where r is the radius of a spherical unit of Allende nanodiamond-containing acid residue, ρ_D is the number of carbon atoms per volume of diamond, 176 carbon atoms per nm^3, and U is the useful yield. This method does not require knowledge of the size of the crater excavated, but also

does not take into account nanodiamonds that were only partially milled. Another method for approximating the number of nanodiamonds from which we sampled is based on the volume of material sputtered through:

$$N_V = \frac{R^2 d}{\frac{4}{3} r^3} \tag{3.2}$$

where R is the radius of the Cs^+ primary beam, and d is the depth to which the sample was milled.

For both estimates, it is important to define the radial unit size of the carbonaceous material analyzed, r. The unit size for the disordered carbon is unknown, while that of the nanodiamonds is a log-normal distribution (Lewis et al. 1987, Daulton et al. 1996) covering several orders of magnitude in volume, with a median value of 2.7 nm in diameter for Allende DM. The sp^2-bonded disordered carbon has undergone the same separation procedures, so we expect a single unit of this material to be similar to the nanodiamonds. Equation 3.1 includes the approximation that a unit of nanodiamond or disordered carbon will contain the same number of carbon atoms. Equation 3.2 uses the different approximation that a unit of nanodiamond or disordered carbon will take up the same volume. The difference between these approximations is the difference between the densities of C atoms in the two phases. The density of disordered carbon is ~1.5 g/cm^3, or ~75 carbon atoms/nm^3; Shigemitsu et al. 1979) and that of diamond is 3.51 g/cm^3, or 176 carbon atoms per nm^3. We take an intermediate value as the density of nanodiamond-containing acid residue, ρ_A = ~2.5 g/cm^3, that is, ~125 carbon atoms per nm^3. The residue is composed of disordered sp^2-bonded carbon and sp^3-bonded diamond, possibly with layered shells of sp^2-bonded C. It is unclear if there is any void space in between units of disordered

carbon and nanodiamonds. It is likely that there is variability in how compact the disordered material is packed and what fraction of the material is diamond.

We define *U*, the useful yield, as the fraction of carbon atoms sputtered from the sample that are also detected by the NanoSIMS. Only a fraction of sputtered material is ionized, and only a fraction of that ionized material arrives at the detectors. The higher our estimate of *U*, the higher our estimate of sensitivity to isotopic anomalies. We routinely achieve ~1% useful yield on a Si wafer. Our materials may behave significantly differently from Si, so we use $U = 0.5\%$ in order to not overestimate our sensitivity.

Given these values, the typical nanodiamond contains an average of ~2000 atoms, $N_c = \sim 0.110 \times n_D$, and we detect approximately 10 atoms per nanodiamond or unit of disordered carbon. We will use "cycle" to refer to the raw data from a 1 second NanoSIMS beam shot, and "data point" to refer to the counts summed over multiple consecutive cycles from the same pixel to add up as close as possible the target count of 2917 $^{12}C + {}^{13}C$ atoms. 2917 is the average number of $^{12}C + {}^{13}C$ for a data point summed over all cycles for a pixel in the data set with the lowest count rates, DND 25-4. Data points for other data sets were similarly constructed by summing over a number of cycles until they contain as close as possible to an average 2917 $^{12}C + {}^{13}C$ counts. If each nanodiamond in the beam is average-sized and milled completely through, there are ~300 nanodiamonds and units of acid residue in each data point. However, if we milled through less than 3 nm of material, it would be incorrect to assume we sampled from only N_c nanodiamonds. Instead, we would have sputtered partway through N_V nanodiamonds, where *d* is 3 nm.

Given the values of *r*, and the primary beam *R*, that we have estimated, the number of nanodiamond-sized units of volume sputtered through in a data point is $N_V = 373 \times d$. However,

this does not take into account packing or the different densities of the disordered carbon and the nanodiamonds, and it only makes sense geometrically for d=3 nm or greater. For every 3 nm layer, there is enough volume for roughly 1000 nanodiamonds.

The counts and cross section approximations vary by more than a factor of two, estimating that there are 300 and 1000 nanodiamonds, respectively, per 3 nm layer in a 70 nm diameter spot size. In addition, positively charged 8kV Cs ions should penetrate significantly farther into a carbonaceous sample than the ~3 nm diameter of a typical nanodiamond (stopping and range of ions in matter simulations give 14 nm; Ziegler et al. 2010), creating some amount of amorphization and mixing. So even if we correctly estimate how much material is sputtered away, we cannot be positive none of the sputtered material was gardened up to the surface from a greater depth. For these reasons, there is uncertainty as to the depth milled, but both counts-based and volume-based methods agree that the 2917 average C count data points sample only from the top layer of nanodiamond-containing acid residue.

To measure *d*, the depth sputtered through, we excavated a series of cross sections out of one of the 1.2×1.2 μm^2 analysis areas using a Ga focused ion beam (FIB) microscope and performed secondary electron imaging. Figure 3.3 shows one of these cross sections. At the edge of the sputtered region what appears to be a presputter crater edge is visible, with a depth of 30–60 nm, but no further excavation is visible. A series of 10–20 nm deep craters should be resolvable, but craters less than 3 nm in depth would not be. We also estimated the mill depth using the equation

$$d = \frac{n_D}{\pi R^2 \rho_A U} \tag{3.3}$$

which gives the mill depth based on the carbon counts collected, and the estimations of the density and beam spot size, reducing to $d = (4\times10^{-4}) \times n_D$. Summed over all cycles for the

Allende data sets, counts per pixel range from 2–7×10^4 counts, giving *d* on the order of 10 nm. This is large enough to be resolved by our cross sections. n_D = 2917 carbon counts per data point gives an approximate mill depth of 1 nm.

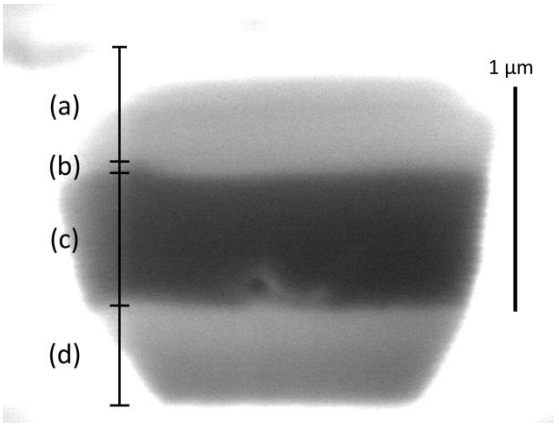

Figure 3.3 Cross section of deposit after NanoSIMS analysis. Secondary electron image obtained with a FIB/SEM dual-beam microscope. (a) FIB-deposited Pt layer applied prior to sectioning. (b) Depth of NanoSIMS presputter (30–60 nm). (c) ADM deposit (~600 nm). (d) Gold foil beneath deposit.

For measurements that sum counts across all cycles in a pixel, we use the counts-based approach to estimate the number of nanodiamonds we have milled through.

3.3 Data Reduction

We used custom scripts to read Cameca .im binary data files, and to reduce and analyze the data (Appendix 2). Images are not drift corrected, because drift corrections use pixel-size steps, while our beam spot is sub-pixel in size. Drift correction algorithms in the L'Image software suggested at most one-pixel shifts. Our instrument has a 36 nanosecond deadtime, which we do not correct, because corrections will be insignificant (less than 1 count for any pixel with fewer than 5270 counts detected), which includes all the pixels in our data. See Table 3.1 for the average ^{12}C + ^{13}C counts per pixel per cycle for each data set. We did not correct for the quasi-simultaneous arrival (QSA) effect, because it will not be significant for our analyses.

All our analyses detect isotopic anomalies either by comparing or normalizing isotopic ratios. Ratio measurements made under the same experimental conditions on the same or a similar matrix will be equally affected by QSA. All our analyses are either on ratio measurements on the same matrix, or are Allende nanodiamond materials normalized to detonation nanodiamond material, which is a comparable matrix. Thus our results are not affected by the QSA effect. The uncertainty in a ratio calculation is based on counting statistics for the numbers of each isotope collected. Calculations with 0 counts for an isotope of carbon were discarded. To exclude calculations made with counts far lower than the target number, we discarded pixels with 2.5 times less than the maximum $^{12}C + {}^{13}C$ counts for a pixel of a data set. Pixels were checked for potential SiC or silica using the ^{28}Si counts as well as the ratio of ^{28}Si counts to summed C counts.

3.3.1 Bulk Ratio Analysis

We report the ratio as per mil deviation, using the bulk ratio from the 3 DND data sets as our standard:

$$\delta^{13}C_{bulk} = \left(\frac{\left(\frac{^{13}C}{^{12}C}\right)_{ADM}}{\left(\frac{^{13}C}{^{12}C}\right)_{DND}} - 1 \right) * 1000‰ \quad (3.4)$$

The uncertainty in the bulk C isotopic anomaly, $Err(\delta^{13}C_{bulk})$ is the sum in quadrature of (1) the fractional standard deviation of the $^{13}C/^{12}C$ ratios for the data from each of the three grids, and (2) the fractional standard deviation calculated from three grids of terrestrial detonation nanodiamonds. In per mil this is given by:

$$Err\left(\delta^{13}C_{bulk}\right) = 1000\frac{\left(\frac{^{13}C}{^{12}C}\right)_{ADM}}{\left(\frac{^{13}C}{^{12}C}\right)_{DND}}\sqrt{\left(\frac{\sigma_{ADM}}{\left(\frac{^{13}C}{^{12}C}\right)_{ADM}}\right)^2 + \left(\frac{\sigma_{DND}}{\left(\frac{^{13}C}{^{12}C}\right)_{DND}}\right)^2}\ ‰ \quad (3.5)$$

The bulk $^{13}C/^{12}C$ ratio was calculated from 3×10^7 carbon counts from 768 pixel spots located in three 1.2×1.2 μm^2 grid areas, designated as data sets ADM 26-1, ADM 26-3, and ADM 27-3. We estimate these data represent approximately 8×10^9 carbon atoms sputtered from the sample, taken from 4×10^6 nanodiamonds (or 2×10^6 nanodiamonds and accompanying disordered carbon). While results are reported and discussed in terms of $^{12}C/^{13}C$, analyses were conducted using $^{13}C/^{12}C$, to prevent low counts in the denominator from skewing the calculation of the standard deviation and . Bulk $^{13}C/^{12}C$ ratios, prior to standardization, are calculated as the sum of ^{13}C counts from all pixel spots from the three Allende data sets *i*, divided by the sum of ^{12}C counts:

$$\frac{\overline{^{13}C}}{^{12}C} = \frac{\sum_i {}^{13}C_i}{\sum_i {}^{12}C_i} \quad (3.6)$$

where for this calculation, $\frac{\overline{^{13}C}}{^{12}C} = \frac{^{13}C}{^{12}C}_{ADM}$ or $\frac{^{13}C}{^{12}C}_{DND}$. We sum all counts from an isotope prior to dividing, since averaging over a number of calculated ratios, even with proper weighting, introduces a positive bias in the ratio (Ogliore et al. 2011).

For this calculation and others in the manuscript, the weighted standard deviation σ of an isotopic ratio or a number *i* of data points or data sets is defined as

$$\sigma_{\frac{\overline{13C}}{12C}} = \sqrt{\frac{\Sigma_i w_i}{(\Sigma_i w_i)^2 - \Sigma_i w_i^2}\sum_i w_i \left(\frac{^{13}C_i}{^{12}C_i} - \frac{\overline{^{13}C}}{^{12}C}\right)^2}. \quad (3.7)$$

$\overline{\frac{^{13}C}{^{12}C}}$ is the bulk mean ratio for which the standard deviation is being calculated. For σ_{ADM} and σ_{DND}, i is the index for the data from one data set of Allende, or detonation nanodiamonds, respectively, but elsewhere in the manuscript i represents data from pixels rather than data sets. The weights are defined as

$$w_i = \left(\frac{1}{Err(^{13}C_i/^{12}C_i)}\right)^2 \tag{3.8}$$

These are the weights for each data point or data set i, based on the uncertainty in the $^{13}C/^{12}C$ ratio of the summed isotope counts for each data set. This takes into account the width of the error bars on each data point in terms of $^{13}C/^{12}C$ ratio. For the same $^{12}C+^{13}C$ counts in a given data point, ^{13}C-enriched data points have larger ratios and thus larger absolute uncertainties, in spite of having lower fractional uncertainties.

Using the methods described above, the terrestrial standard nanodiamonds have a raw, that is, un-normalized $^{12}C/^{13}C$ ratio of 98^{+3}_{-4} over three data sets, designated DND 25-4, DND 28-1, and DND 28-3. While per mil precision isotopic studies of the detonation nanodiamond separates we used are not available, the real value for these nanodiamonds should be close to the known terrestrial value (~89, Coplen et al. 2002); the difference indicates that matrix effects, topography, and potential systematic errors do significantly affect our small-beam measurements on acid residue deposits, and that proper standardization is essential.

3.3.2 Broadening Analysis

We searched for indications of isotopic anomalies by examining the shape of distributions of $^{13}C/^{12}C$ ratios for Gaussian broadening compared to the shape expected from statistics and standards. Given sufficiently low variance in the denominator, the quotient of two Gaussian

distributions may be modeled as a Gaussian (Hayya et al. 1975). If there is isotopically anomalous material in the acid residues, distributions of ratio measurements will be the combination of multiple distributions. All the data points with counts from isotopically anomalous nanodiamonds may be well within uncertainty of the mean, and the distribution need not be double-peaked, but the distribution will be broader overall if the material is drawn from more than one isotopic reservoir. Systematics can produce Gaussian and non-Gaussian broadening, so we corrected our data using standards.

(1) To calculate the amount of systematic broadening (that is, non-Gaussian broadening), we used the term

$$B_S = \frac{\sigma_{observed} - \overline{\sigma}_{expected}}{\overline{\sigma}_{expected}} \tag{3.9}$$

$\overline{\sigma}_{expected}$ is the standard deviation (Equation 3.7) of the carbon isotopic ratio derived from the assumption that the data fit a Gaussian distribution.

We fit $\sigma_{observed}$ in our standards using a reduced chi-squared model. The reduced chi-squared for a distribution of $^{13}C/^{12}C$ ratio data points is given by:

$$\chi^2_{red} = \sum_i \left(\frac{^{13}C_i/^{12}C_i - \overline{^{13}C/^{12}C}}{\sigma} \right)^2 / dof \tag{3.10}$$

where the mean ratio is the ratio of the summed counts over all data points *i*, *dof* is the number of degrees of freedom, that is, the number of data points, *N*, minus 1, and σ is the fitted parameter. We used $\overline{\sigma}_{expected}$ (Equation 3.7) as the initial value of σ. If the residual $\chi^2_{red} - 1 \neq 0$, indicating a non-optimal fit, we adjusted σ by a fraction of the residual and recalculated χ^2_{red}. This process was repeated until χ^2_{red} converged to a value of one. The final value of σ is $\overline{\sigma}_{observed}$.

Given these definitions for $\overline{\sigma}_{\text{observed}}$ and $\overline{\sigma}_{\text{expected}}$ we calculated Bs. We used all the data points from a given data set in a single distribution, which minimizes the uncertainty. On the order of 10^6 nanodiamonds are present in each of the three Allende distributions.

(2) To calculate Gaussian broadening we compared directly to the standards. We subtracted the mean fractional deviation of our standard data sets from the fractional standard deviation, σ, for the data set for which we are calculating the Gaussian broadening,

$$B_G = \sigma - \overline{\sigma}_{Standards} \tag{3.11}$$

where $\overline{\sigma}_{Standards}$ is the average fractional σ for the DND, GRP, and CPT data sets. $Err(B_G)$, the uncertainty in B_G, is the sum in quadrature of $Err(\sigma)$ and $Err(\overline{\sigma}_{standards})$. The uncertainty in the standard deviation is given by,

$$Err(\sigma) = \frac{\sigma}{\sqrt{2(N-1)}} \tag{3.12}$$

(Taylor 1997, 294–298), where, for $\sigma_{Allende,}$ N is the number of data points in the data set being evaluated for Gaussian broadening, and for $\sigma_{standards,}$ N is the number of data sets averaged over (in which case N=6).

Given that we corrected for B_S, the systematic broadening, if B_G exceeds the uncertainty, there are two explanations: Either a statistical difference in the data set is simulating the presence of multiple distributions, or the Allende data set contains isotopically anomalous material.

If the counts per data point vary in a distribution of data points, the effect on the standard deviation will be similar to drawing from different distributions. We calculated the standard deviation of the ^{12}C counts for all the data points in a data set and tested if the Gaussian

broadening depends on this value. Data points that do not fall along a linear correlation fit cannot be attributed to this effect.

3.3.3 Outlier Analysis

We continued our search for isotopic anomalies by creating distributions of $^{13}C/^{12}C$ isotope ratio data points to search for outliers. We divided the Allende data into a total of 72,103 data points, each from a single spot summed over cycles to include as close as possible to 2917 carbon counts, which is the mean number of carbon counts-per-pixel (summed over all cycles) for DND 25-4, the data set with the lowest count rates. It is serendipitous that 2917 counts corresponds to roughly 1 nm mill depth, sampling from one, but only one, layer of approximately 1000 nanodiamonds, as this allows us to measure the isotopic ratio from a minimum number of nanodiamonds and still have data points that sample from a similar number of nanodiamonds for each data set and material, in spite of the low counts from the detonation nanodiamond standards.

We used a rolling sum, so each cycle of raw data from a pixel is included in *n* data points, where *n* is the number of cycles summed over to achieve the target counts (this is a simplification as *n* is not always the same for every data point in a sample). For example, given consecutive cycles 1, 2, 3, 4, and 5, and *n*=3, the first data point will sum cycles 1, 2, and 3 before reaching the target counts; the second data point will start at cycle 2 and sum cycles 2, 3, and 4. Data point three will sum cycles 3, 4, and 5. Data point four starts at cycle four. So cycle 3 is included in *n* (three) data points. If instead of a rolling sum, we skipped over previously summed cycles we would have up to an (*n*-1)/*n* chance to overlook any outlier. In the worst-case scenario, an isotopic anomaly persists over exactly *n* cycles. For example, suppose the counts from cycles 2–4 in our example are anomalous enough to constitute an outlier. A rolling sum with *n*=3 will

detect an outlier in the second data point, which sums cycles 2–4. But an exclusive sum starting at cycle 1 or cycle 3 will dilute the signal with non-anomalous cycles 1 or 5 and not detect the outlier. Thus, 2/3 of the time, or (*n*-1)/*n* of starting points, this outlier would be missed.

Each data point represents approximately 8×10^5 carbon atoms sputtered from the sample, or as many as 1000 nanodiamonds (or fewer nanodiamonds and accompanying disordered carbon). By using data points that have close to the same counts on average, we created statistically similar distributions from data sets taken from different sample areas and materials. For the calculation of the standard deviation, each data point was weighted based on the uncertainty due to counting statistics for each of the isotopes. The typical weights, which in this case we will call w' were normalized as w, such that $\Sigma_i w_i = N$, the number of measured ratios, using

$$w_i = N \frac{w_i'}{\Sigma_i w_i'} \tag{3.13}$$

where

$$w_i' = \left(\frac{1}{Err\left({}^{13}C_i/{}^{12}C_i\right)}\right)^2. \tag{3.14}$$

Using normalized weights allowed us to use the simple, unweighted expression for the fractional uncertainty in the standard deviation (Equation 3.12).

The mean ratio is calculated as the sum of ^{13}C counts divided by the sum of the ^{12}C counts, to avoid the bias that would be introduced by averaging over a number of ratios (Ogliore et al. 2011). The uncertainty in the mean ratio is given by the standard error of the mean, SEOM,

$$SEOM = \frac{\sigma}{\sqrt{N}}. \tag{3.15}$$

For readability, ratios are plotted in terms of $^{12}C/^{13}C$, but the distributions are displayed linearly with respect to $^{13}C/^{12}C$, to avoid the appearance of tails at high $^{12}C/^{13}C$ ratios, due to low counts in the denominator of $^{12}C/^{13}C$ ratio data points.

We further investigated outliers greater than 4σ from normal with more than half the data set average relative significance in Allende and our standards by analysis of depth profiles for each signal (^{12}C, ^{13}C, ^{16}O, ^{28}Si, and secondary electrons), as well as for $^{13}C/^{12}C$. These profiles allow us to see if isotopic outliers persist over several cycles and if signals from the other ions and secondary electrons remain stable during the same cycles, both of which are indicative of isotopic anomalies, but not experimental artifacts. Because of lower count rates in ADM compared to CPT and GRP standards, each data point in the ADM data is summed over more cycles to create roughly comparable counting statistics; therefore, an outlier in Allende represents a more significant result than an outlier in the CPT and GRP standards. After the first rolling sum in a pixel sums to the last cycle of the data set, we do not consider data points starting at subsequent cycles, as these will all sum to the end of the data set without reaching the target 2917 C counts, and therefore do not represent any new data.

3.3.4 Detection Limit Calculation

In order to assess which anomalous components our experiment rules out by non-detection, we posited a model of the isotopic composition of the nanodiamonds. We take a simple, two-component model, a normal component with isotopic ratio R_n equal to the solar system value, and an anomalous component, with a ratio, R_a, comprising a fraction, f_a, of a sample. We derived an expression for the detection limit as a function of R_a that includes R_O, the ratio we would observe, and R_n, the terrestrial ratio:

$$f_a(R_a) = \frac{(R_a+1)(R_o-R_n)}{(R_a-R_n)(R_o+1)} \quad (3.16)$$

This expression is for ratios in terms of $^{12}C/^{13}C$. For the sensitivity of the bulk ratio technique described in Section 3.3.1, we used the measured bulk C isotopic ratio that would constitute a 2σ outlier as R_O. To assess the sensitivity of the outlier ratio technique described in Section 3.2.2 to individual aggregates that are isotopically anomalous, we calculated the ratio that would constitute a 5σ outlier for a data point in our Allende data, and use that ratio as R_O.

3.4 Results

3.4.1 Bulk $^{12}C/^{13}C$ Ratio

The "bulk" isotopic composition of the Allende nanodiamonds we measured is $\delta^{13}C = 8 \pm 35‰$, normalized to the detonation nanodiamonds (Figure 3.4). The uncertainty includes counting uncertainty, matrix effects, topography, and differences between sample and standard as well as tuning on different data collection runs. We estimate this measurement sputtered through 8×10^9 atoms of Allende acid residue, and represents approximately 4×10^6 nanodiamonds. Our results are consistent with solar system values. There is a small enrichment in ^{13}C in our samples compared to previous studies, at the 1σ level.

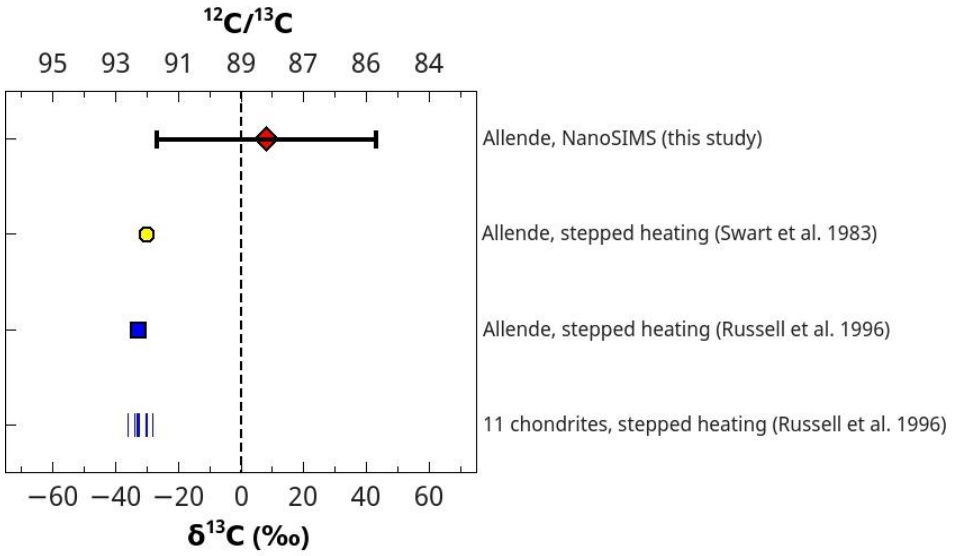

Figure 3.4 Bulk measurement of $\delta^{13}C$ compared to previous studies. Data points from previous studies are the average $\delta^{13}C$ detected over the course of stepped heating of less than 100 μg of nanodiamond-containing acid residue per sample (Russell et al. 1996), and 34–68 ng per step (Swart et al. 1983). The minimum $\delta^{13}C$ (most extreme anomaly) is a few per mil farther from terrestrial in each case. The error bars for the data point from Allende, this study, are ±1σ. Swart et al. (1983) do not report errors. Errors for Allende by Russell et al. (1996) are smaller than the size of the symbol. Errors are 0.1 to a few per mil for the range of 10 chondrites by Russell et al. (1996).

3.4.2 Outlier Ratios

Distributions of $^{12}C/^{13}C$ isotopic ratio measurements for each data set are plotted in Figure 3.5. Since the measurements on Allende were from three different 1.2×1.2 μm^2 areas on the sample, we plotted three different distributions. Figure 3.5 also includes the distributions from the terrestrial detonation nanodiamonds, graphite, and carbon paint standards. ADM 27-3 is distinct from the other two Allende data sets in that it does not have tails of the same length, nor is the peak as smooth of a curve. It also has the highest mean $^{12}C/^{13}C$ ratio and standard deviation. Table 3.2 describes the mean, standard deviation, and uncertainties for these isotopic ratio distributions, using $^{13}C/^{12}C$ since the standard deviation, uncertainty in the standard deviation, and uncertainty in the mean are all asymmetric in $^{12}C/^{13}C$. The standard deviation should be similar for each data set, because the counts per data point are similar values as a result of summing over multiple cycles to a target count. Even though different data sets contain

dramatically different numbers of data points, each data point has similar uncertainty, and, therefore, contributes to a similar distribution, so long as systematic errors are minimal, and each distribution is drawn from only one mean ratio.

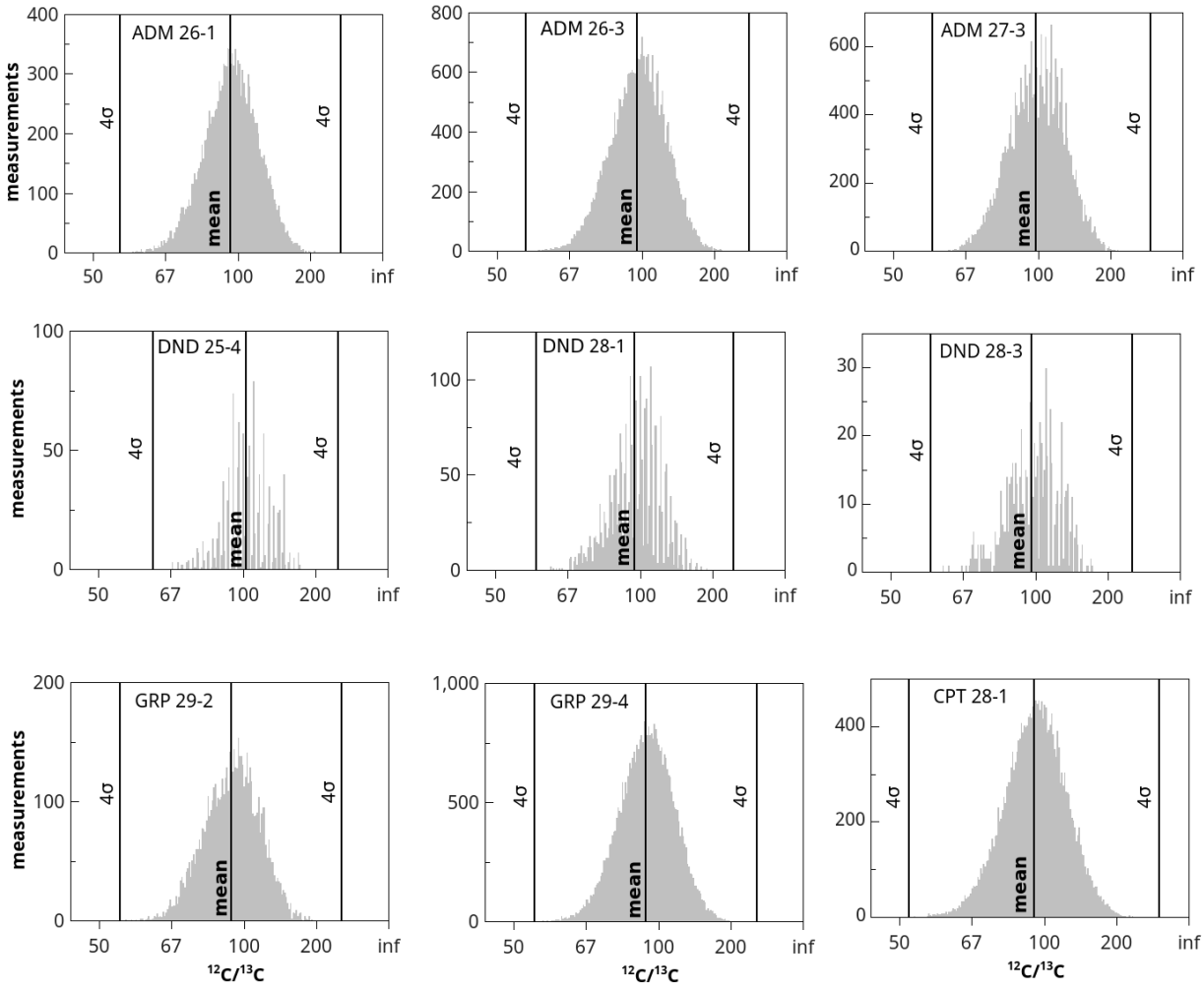

Figure 3.5 Histogram of measurements for data sets. The mean and 4σ deviations in each direction are marked. The abscissa is not linearly scaled, rather it is in terms of $^{13}C/^{12}C$. Histograms and deviations are calculated using $^{13}C/^{12}C$, because small errors in ^{13}C create large tails at high $^{12}C/^{13}C$ that do not represent statistically significant outliers. Labels are in $^{12}C/^{13}C$ for ease of reading. The data sets have roughly the same average C counts per data point. The center of the distribution for each data set is at a slightly higher $^{12}C/^{13}C$ ratio than the mean because ratios with higher $^{12}C/^{13}C$ ratios have slightly lower counts on average, a statistical feature inherent to distributions of ratios (Ogliore et al. 2011).

Table 3.2 Statistical data for distributions of isotopic ratio measurements.

Data Set	N[a]	CPM[b]	$^{13}C/^{12}C \pm$ SEOM[c]	$\sigma \pm$ Err(σ)	Gaussian broadening (%)[d]	^{12}C counts variation[e]
ADM 26-1	14852	3009	0.01053±0.00002	0.00191±0.00001	0.6	342
ADM 26-3	30879	3447	0.01032±0.00001	0.00193±0.00001	1.2	84
ADM 27-3	26372	2918	0.01015±0.00001	0.00193±0.00001	1.5	49
DND 25-4	1062	2917	0.00983±0.00005	0.00160±0.00003	-1.21	12
DND 28-1	2572	2918	0.01039±0.00003	0.00170±0.00002	-1.11	20
DND 28-3	706	2919	0.01029±0.00007	0.00175±0.00005	-0.54	24
GRP 29-2	6448	3118	0.01090±0.00002	0.00191±0.00002	0.04	233
GRP 29-4	38400	3123	0.01089±0.00001	0.00192±0.00001	0.16	277
CPT 28-1	23159	2430	0.01070±0.00001	0.00216±0.00001	2.67	418

[a] *N* is the number of measurements (data points) for the data set.

[b] Similar mean C counts per measurement (CPM) are achieved by summing multiple cycles for the same pixel into a single measurement.

[c] Ratios are not normalized. SEOM stands for the standard error of the mean, which is the uncertainty in the mean ratio.

[d] Gaussian broadening, B_G, is the difference between σ for that data set as a fraction of the mean, and the mean value of the fractional standard deviation for all the standard data sets.

[e] The standard deviation of CPM, the counts per measurement, for this data set.

The Allende data contain 5 data points that are over 4σ away from the mean ratio for their respective data sets (Table 3.3, Figure 3.6), 3 from ADM 26-1 and 2 from ADM 26-3. The two outlier data points in ADM 26-3 are from consecutive sets of summed cycles in the same pixel (located at row 13, column 4), and therefore share most of the same raw data cycles. The three

outlier data points in ADM 26-1 are not from physically adjacent pixels in the analysis. None of the Allende outliers included the first cycle. All are ^{13}C-rich; after normalizing to the detonation nanodiamond standards, they have δ^{13}C on the order of 800‰, near ^{12}C/^{13}C = 50. Across these three data sets, we predict we would see 4 or 5 outliers > 4σ given a Gaussian distribution and the same significance for every data point (Table 3.4). The detonation nanodiamond standards are not instructive in comparison since the expected and observed frequency of 4σ outliers are both less than one. In the graphite data we expect 3 or 2 > 4σ outliers and observed 3, the most extreme of which was 4.7σ away from normal. In the carbon paint we expect 1 or 2 outliers > 4σ and observed 4, although one was in the first cycle, which is prone to artifacts. The outliers in our standards demonstrate that systematics in our analytical approach can produce outliers larger than those observed in our measurements of Allende, and at similar frequency per data point, possibly due to background spikes or electronics artifacts. However, a key difference between the standard and Allende data is that depth profiles show that the anomalous data points in Allende are consistent over several cycles, whereas all 7 outliers from the standards are the result of increased counts in only a single cycle (Figure 3.7). In each case, the outlier is a peak in a curve composed of 2–5 ^{13}C-rich data points, each of which is summed over multiple raw data cycles, collected minutes or hours apart, and thus not attributable to background or artifacts. 3 data points represent ~3 nm in depth milled based on our approximations – that is, the diameter of the average Allende nanodiamond. For the standards GRP and CPT, outliers are only one data point deep, and in each case the data point is only composed of data from one cycle. Therefore,

the Allende outliers are much more significant than those in the standard materials.

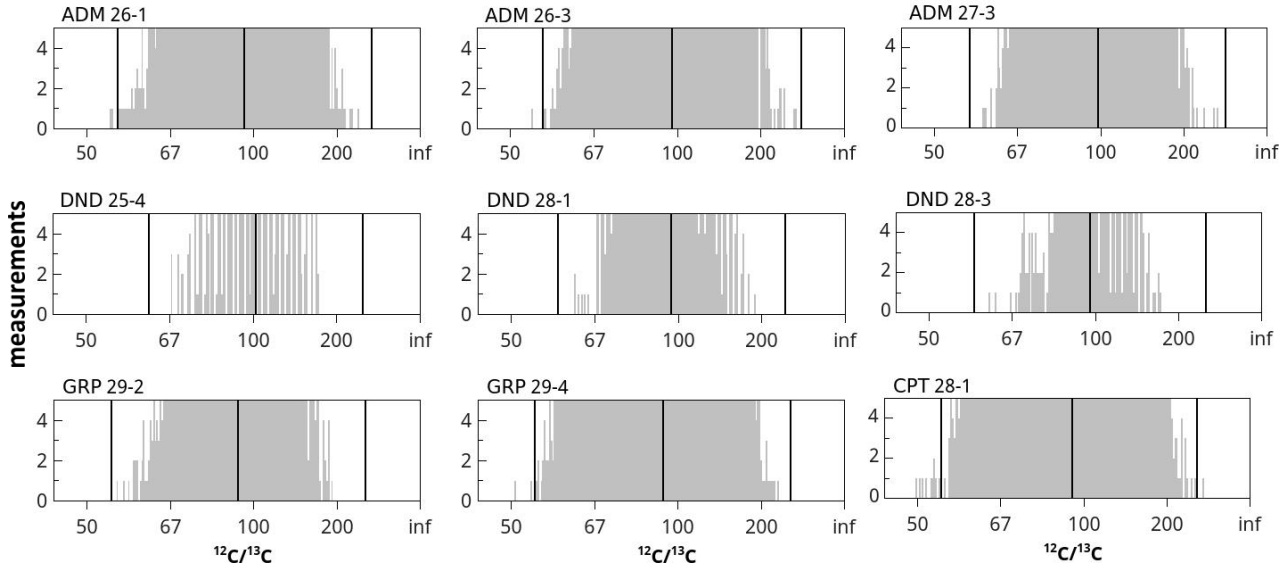

Figure 3.6 Vertically stretched view of $^{12}C/^{13}C$ isotopic ratio distributions, highlighting the > 4σ outliers in ADM 26-1, ADM 26-3, GRP 29-4, and CPT 28-1. Left to right, the three vertical lines in each image are -4σ, mean, and +4σ in $^{12}C/^{13}C$. All outliers are to the ^{13}C-enriched side.

Table 3.3 Outlier data points[a]

Sample	Depth-row-column			Outlier magnitude (×σ)	$^{12}C/^{13}C$ (normalized)	^{12}C	^{13}C	^{28}Si	^{16}O
ADM 26-1	10	8	3	4.065	50^{+9}_{-7}	2406	44	3	207
	27	11	10	4.265	49^{+9}_{-6}	2464	46	6	199
	30	12	11	4.183	49^{+8}_{-6}	2971	55	4	171
ADM 26-3	62	13	4	4.020	50^{+9}_{-6}	2764	50	2	233
	63	13	4	4.349	49^{+8}_{-6}	2777	52	3	243
CPT 28-1	0	2	4	4.095	47^{+9}_{-6}	2303	45	0	122
	31	11	5	4.388	45^{+9}_{-6}	2082	42	0	102
	34	7	13	4.282	46^{+9}_{-6}	2106	42	0	115
	51	0	3	4.182	46^{+9}_{-6}	2129	42	0	82
GRP 29-4	131	14	9	4.006	49^{+8}_{-6}	2903	54	1	77
	142	14	8	4.675	46^{+7}_{-6}	2866	57	0	75
	144	0	13	4.115	48^{+8}_{-6}	2605	49	0	65

[a] Each outlier samples from approximately 1000 nanodiamonds.

Table 3.4 Observed vs. predicted numbers of outliers

Sample	Measurements	>4σ outliers observed	>4σ outliers expected
ADM	67312	5	4.3
DND	4340	0	0.3
GRP	44848	3	2.8
CPT	23159	4	1.5

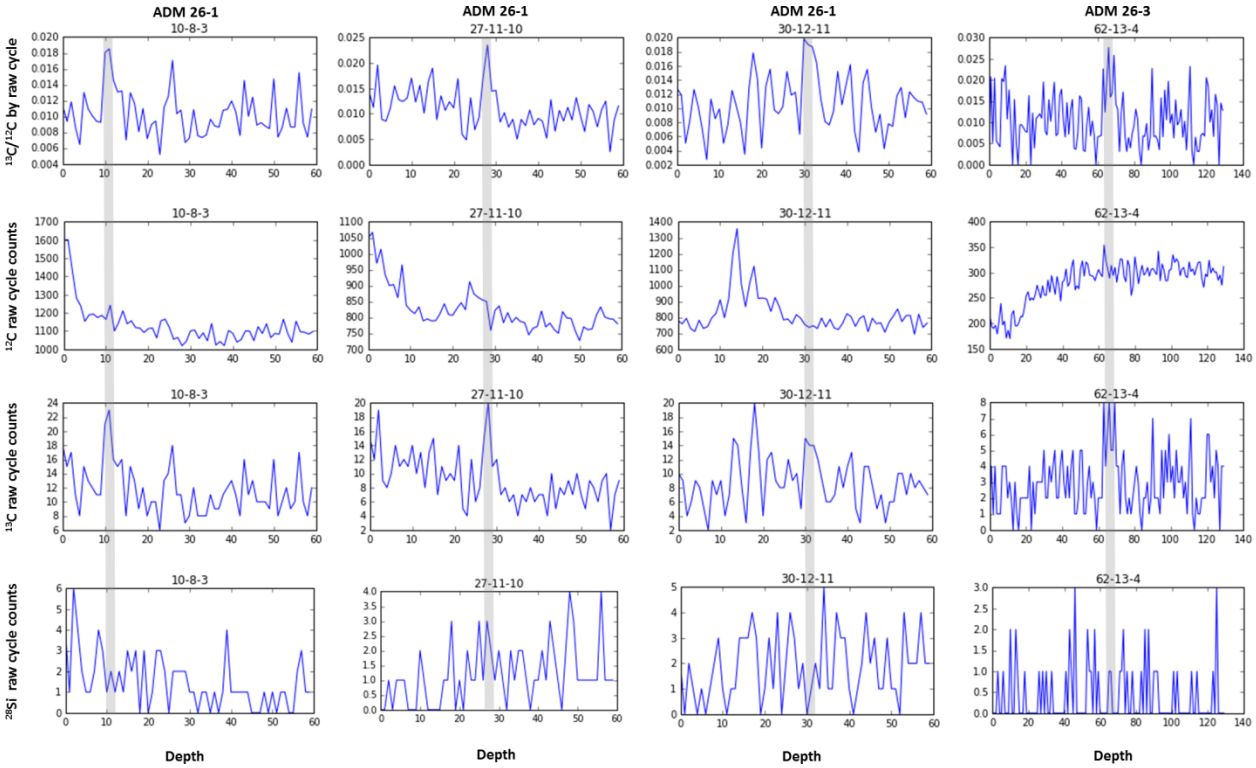
ADM 26-1
10-8-3
27-11-10
30-12-11
ADM 26-3
62-13-4
$^{13}C/^{12}C$ by raw cycle
^{12}C raw cycle counts
^{13}C raw cycle counts
^{28}Si raw cycle counts
Depth

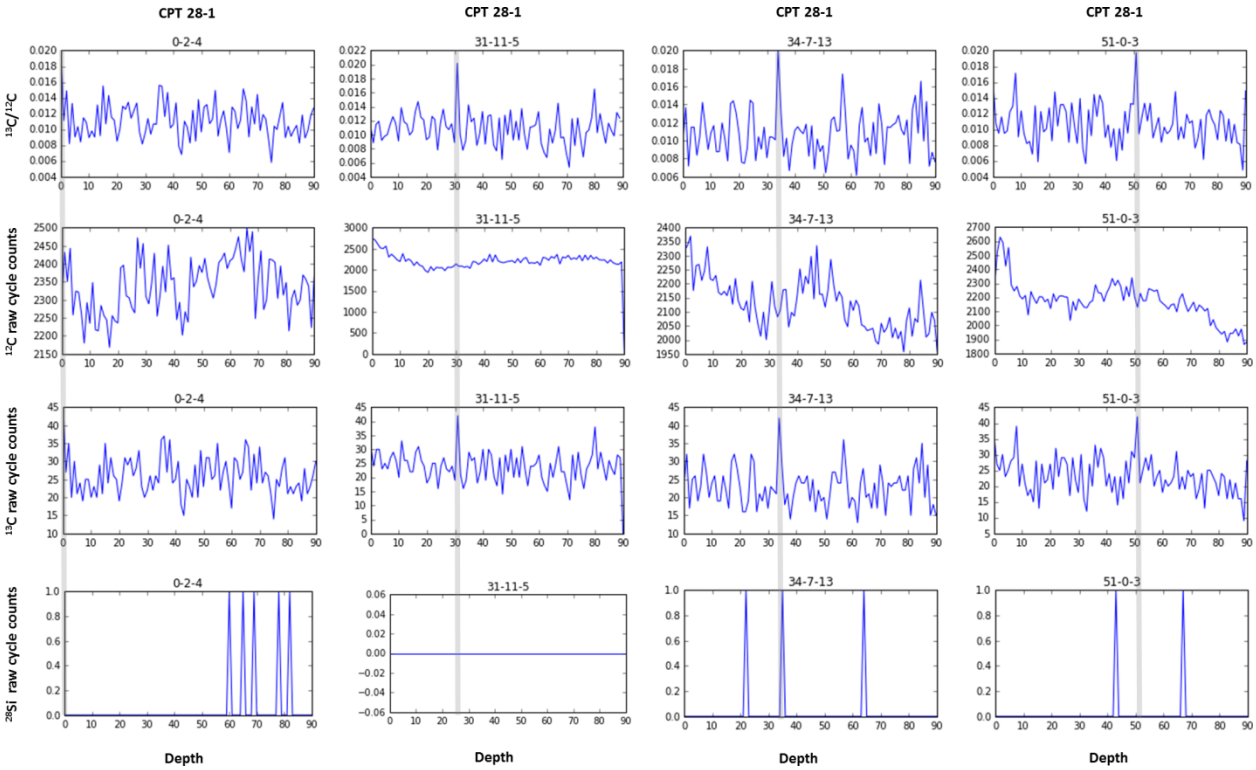
CPT 28-1
0-2-4
31-11-5
34-7-13
51-0-3
$^{13}C/^{12}C$
^{12}C raw cycle counts
^{13}C raw cycle counts
^{28}Si raw cycle counts
Depth

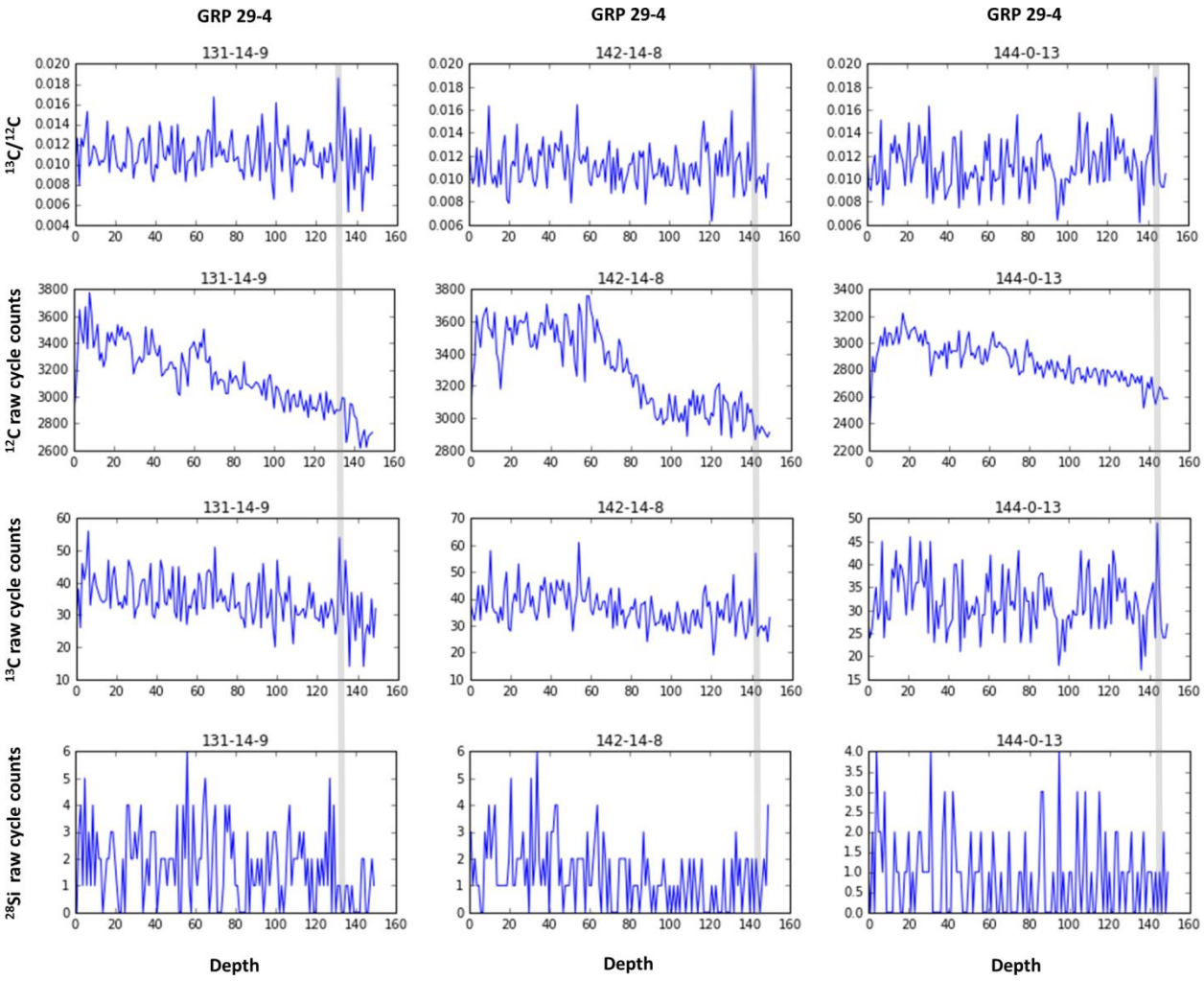

Figure 3.7 Depth profiles for 4σ and greater outliers in each Allende and standard material data set. Each profile is labeled *depth-row-column*. Row and column indicate the pixel position in a 16×16 image. For Allende data, $^{13}C/^{12}C$ by raw cycle, ^{12}C counts, ^{13}C counts, and ^{28}Si counts are presented. Data points used in the outlier searches and histograms (Figures. 5 and 6) are constructed from the counts of several of the consecutive cycles plotted here as depth. But for each of the depth profiles for standards, each data point was only over 1 cycle, so the counts for a single step in depth here represent the same counts that were used in outlier searches and histograms (Figures 5 and 6). Ratios are given in $^{13}C/^{12}C$ to avoid low counts in the denominator that would skew the appearance of the profiles. ADM 26-3 row 13 pixel 4 is unique in that data points 62-13-4 and 63-13-4 are consecutive > 4σ outliers. Each plot is scaled to fit all the cycle data for that plot.

3.4.3 Broadening of Ratio Distributions

If a number of isotopically anomalous grains are scattered throughout our measurements, this will lead to some measurements that are shifted towards the anomalous value, relative to a Gaussian distribution. Any individual measurement may be well within uncertainty of the mean, and the distribution need not be double-peaked. However, the distribution will be broader

overall. We quantified how far each of the observed $^{12}C/^{13}C$ mean isotope ratios for a distribution varies from a Gaussian curve due to systematics, B_S, and then calculated how much Gaussian broadening the Allende mean ratios exhibit compared to the standards, B_G.

We used all the data points from a given data set in a single distribution, which minimizes *Err(σ)*. On the order of 10^6 nanodiamonds are in each of the three Allende distributions. B_S varies from 0.2 to -1.4% of the experimental standard deviation across our different standards, and from -0.1 to -1.9% across the three meteoritic data sets. That is to say, each of our data sets is a good fit to a Gaussian curve, and the Allende material has the same or less systematic error than our standard materials.

However, the standard deviations of the Allende data sets are greater than those of the standards as a fraction of the mean ratio, in every case except for the carbon paint (Table 3.2, Figure 3.8).

The variation of total C counts per data point is different for each data set, as a result of summing over cycles with different count rates per pixel (Table 3.2, ^{12}C counts variation). For data sets with lower count rates (e.g., DND), cycles with small numbers of counts may be summed very close to the target of 2917 counts per data point, but for data sets with very high counts per pixel (e.g., CPT), where each pixel adds several thousand counts to the sum, the variation is much greater.

The standard data sets show a linear correlation between the variation in the ^{12}C counts and the Gaussian broadening, albeit a poor one ($R^2 = 0.85$ from a regressive linear fit) (Figure 3.8). Counts variation is therefore a good explanation for why the DND data sets have the lowest broadening, the GRP intermediate, and CPT the highest. However, the ADM data sets do not follow this trend. Adding them to the linear fit gives $R^2 = 0.37$. ADM 26-1 plots close to the line

suggested by the standard data sets, albeit not on it – the trend of Gaussian broadening with variation in counts predicts a higher Gaussian broadening for ADM 26-1. ADM 26-3 and 27-3 are much broader than predicted by their counts variations. Taken by themselves, the 3 ADM data sets suggest the opposite of the expected trend: as variation in counts increases sharply, Gaussian broadening decreases. Therefore, the broadening of the ADM data sets, especially ADM 26-3 and ADM 27-3, is not solely attributable to statistical causes; the best explanation is that multiple isotopic reservoirs contribute to these distributions.

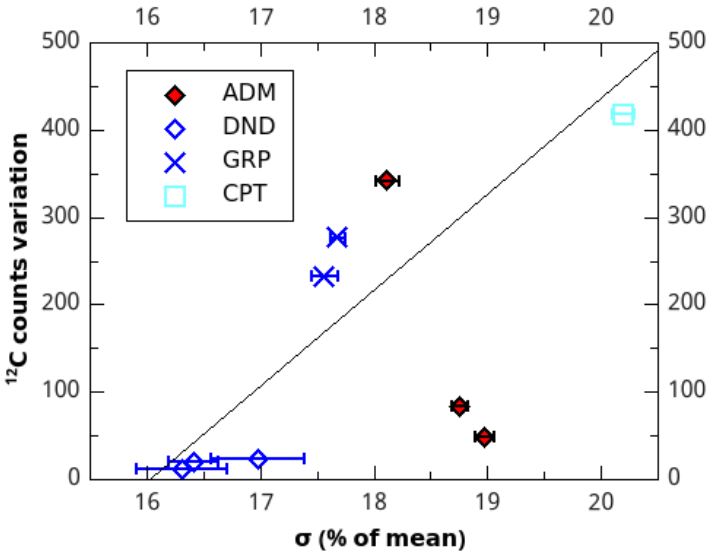

Figure 3.8 Variation in ^{12}C counts per data point for each data set plotted versus ^{12}C/^{13}C standard deviations as a percentage of the respective mean values. The various standards show a trend towards broader distributions of ^{12}C/^{13}C ratios for higher variation in ^{12}C counts per data point. The diagonal line is a linear fit to all the data sets except the three from ADM. One meteoritic data set has a ratio distribution slightly narrower than predicted by the linear fit to the standards. The other two meteoritic data sets have ^{12}C/^{13}C ratio distributions several percent broader than can be explained by statistics. The best explanation for the breadth of these data sets is that they are composed of material drawn from multiple isotopic reservoirs.

3.4.4 Silicon-containing Materials in the Allende Residue

The maximum ratio of ^{28}Si counts to ^{12}C + ^{13}C counts in any data point was 6%. In most cases the silicon signal was less than 1%. Lewis et al. (1989) noted 600 ppm SiC (0.06%) so we do not expect to be sensitive to individual SiC grains with close-to-solar isotopic ratios.

3.4.5 Detection Limits

While direct measurement of isotopically anomalous material is most compelling, it is also informative to consider the isotopic anomalies that were *not* detected, but would have been, if present. It is possible that many different isotopically anomalous populations make up the nanodiamonds. Even limiting our discussion to one solar component and one presolar, isotopically anomalous, component, there remain two variables: the fraction of the measured material that is anomalous, and the magnitude of the anomaly.

For the analyses presented in Section 3.4.1, the observed bulk ratio would be anomalous if it differed from the solar system ratio by more than 2σ, that is, is less than $^{12}C/^{13}C = 82.1$ or more than 97.2. Figure 3.9 illustrates the anomalous fractions that would result in such an observation. Each point on the plot describes a hypothetical aggregate of nanodiamonds made of two components: one "normal" with a solar isotopic ratio, the other anomalous, with a $^{12}C/^{13}C$ ratio R_a, which is plotted on the x-axis, from $^{12}C/^{13}C = 0$ to 150. The anomalous component comprises a fraction f_a of the aggregate, which is plotted on the y-axis from 0 to 100%.

For our bulk ratio measurement presented in Section 3.1, we use Equation 3.16 with R_o set to 82.1 (Figure 3.9, the solid green line at the left, lower ratio) and 97.2 (the solid green line on the right, higher ratio. The technique in Section 3.1 is sensitive to any anomalous components lying on or above the curves, in the regions marked I and II(a and b). All anomalous components lying in these regions are counterindicated by our results in Section 3.3.1 for aggregates of 4×10^6 nanodiamonds.

For analyses presented in Section 3.3.2, a 5σ outlier for data set ADM 26-1, similar to the other ADM data sets, would have a ratio of $^{12}C/^{13}C = 45.5$, if isotopically heavy, or $^{12}C/^{13}C = 2044.1$, if isotopically light. If the composition of the material in the measurement were two-part, one

having a solar system C-isotope ratio, the other composition would have to make up a minimum 1% of the estimated 8×10^5 carbon atoms sputtered by the beam in order to produce a detectable outlier. Therefore, we can rule out the presence of pure ^{13}C clusters larger than 10^4 atoms, and rule out clusters larger than 8×10^5 carbon atoms with a ratio of 45. Figure 3.9 presents the detection limit for this method, with the curve described using Equation 3.16 and, setting the observed ratio R_o to 45.5, our limit for a 5σ detection. Similar to the bulk ratio, any combination of anomalous ratio and fraction lying above the dashed line in region I is ruled out by non-detection, in this case for an aggregate of 1000 nanodiamonds partially sampled, 8×10^5 atoms of carbonaceous material sputtered through, or 2917 detected carbon atoms. We do not plot the curve for $^{12}C/^{13}C = 2044.1$ as it is at very high $^{12}C/^{13}C$ ratio.

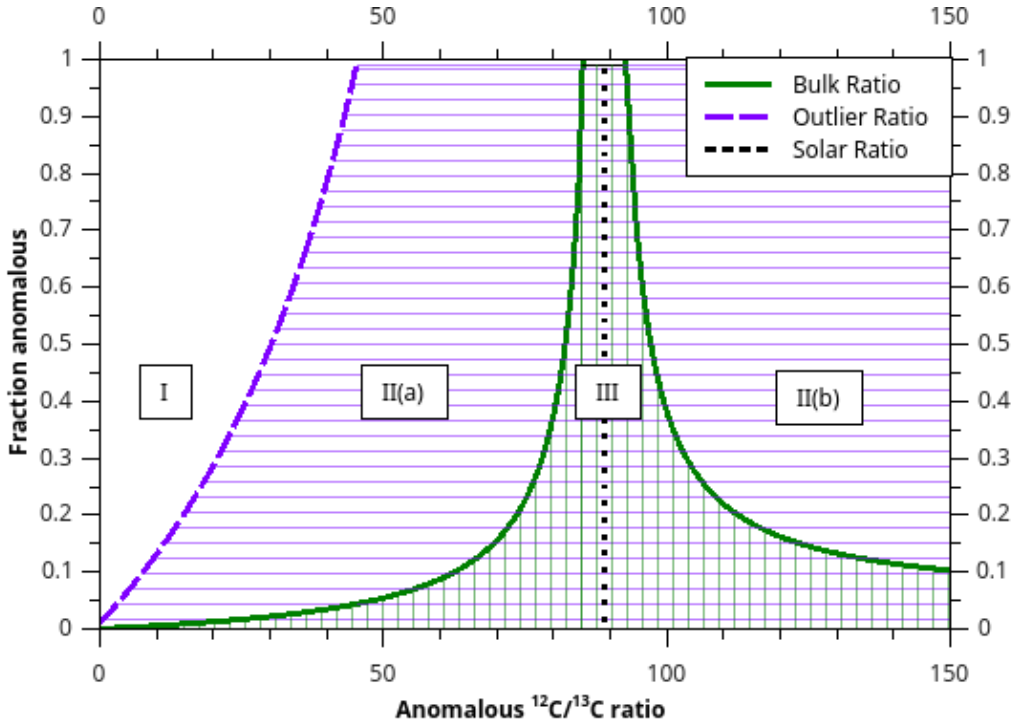

Figure 3.9 Detection limits for isotopic anomalies in C for small beam (~70 nm) NanoSIMS measurements of meteoritic nanodiamonds for two sample sizes. Presolar inclusions with anomalous ratios ranging from 0 to 150 are considered, comprising 0 to 100% of the sample size. Inclusions outside of the vertically lined region (III) are ruled out by our measurements, for aggregates of 4×10^6 nanodiamonds or 8×10^9 atoms of carbonaceous material sputtered through. Presolar inclusions falling in Regions I and II(a and b) would be detected as an anomalous bulk $^{12}C/^{13}C$ ratio with a greater anomaly than the experimental uncertainty reported in Section 3.3.1. Inclusions in the horizontally-lined regions (IIa and IIb) are ruled out by our measurements for aggregates of approximately 1000 nanodiamonds, or 8×10^5 atoms of carbonaceous material sputtered through. Presolar inclusions falling in region I would be observed as 5σ or greater outliers using our experimental methodology. A curve for outlier sensitivity to ^{13}C-light material, which would lie above $^{12}C/^{13}C = 150$, is not shown.

3.5 Discussion

3.5.1 $^{12}C/^{13}C$ Ratio of the Nanodiamond Residues

Our bulk measurement in Section 3.3.1 confirms that the nanodiamond carbon is terrestrial in composition down to 8×10^9 carbon atoms of material, compared to a minimum of 10^{15} carbon atoms in stepped heating measurements. The isotopic composition of the roughly 4×10^6 nanodiamonds represented by this number of carbon atoms is $\delta^{13}C = 8\pm35$‰. Our measurement of the Allende DM ratio is about 40‰ heavier in ^{13}C (but with an uncertainty of more than 30‰)

than previous measurements by stepped heating (Figure 3.4), where bulk Allende acid residue has a $\delta^{13}C$ of -32.7±0.1‰ (Russell et al. 1991) and -30.4‰ (Swart et al. 1983).

As represented by the high uncertainty, the precision of our measurement is necessarily low compared to stepped heating experiments, since we are integrating less material and are affected by sample topography and uncertainty in the per mil isotopic ratio of our standard. There may also be sensitivity differences between the terrestrial nanodiamond standard material and the meteoritic acid residue, which could account for the disparity between our measurements and previous studies. On the other hand, the isotopically heavier value we measured could be due to intrinsic isotopic anomalies, as our small sample size allows us much greater sensitivity to isotopic inhomogeneity in small fractions of the sample than earlier measurements.

3.5.2 Implications of Gaussian Broadening

We see significant Gaussian broadening of the Allende distributions compared to that predicted by statistics and comparison to our standards. All our data sets are a good fit to a Gaussian distribution, so this broadening in the Allende data sets is attributable to the distribution being drawn from multiple isotopic ratios. This result does not conflict with bulk studies, in that the mean ratios are still close to solar composition, but it does suggest that a fraction of the nanodiamonds have a non-solar carbon isotopic composition. On the other hand, our detection limits plotted in Figure 3.9 for the bulk ratio measurement confirm that the nanodiamonds are not composed primarily of material with a mean carbon isotopic anomaly. In an aggregate of only 4×10^6 nanodiamonds, <20% of the nanodiamonds can have $^{12}C/^{13}C$ below 70 or above 100, <10% can have $^{12}C/^{13}C$ below 50 or greater than 110, and <5% can have $^{12}C/^{13}C$ below 40 or above 140.

Given a variety of solar masses, supernova models predict a broad range of carbon isotopic ratios, including both ^{13}C-enriched and -depleted material (e.g., Rauscher et al. 2002). Supernova nanodiamonds are therefore good candidates to produce a small Gaussian broadening, because even the presence of a large number of such grains would not require a detectable shift to the mean ratio. The possible fraction and magnitude of the anomaly is further constrained by our bulk ratio and outlier detection limits (see Section 3.3.5 and Figure 3.9). However, we note that it is unlikely that we would have detected any ^{13}C-depleted material, which is expected to be present if supernovae created a number of the nanodiamonds, since our sensitivity to depletions in ^{13}C is limited in low-count scenarios.

3.5.3 Source of ^{12}C/^{13}C Outliers

For the data from Section 3.3.2, each data point samples on average approximately 2900 carbon atoms from aggregates of 4×10^6 atoms of carbonaceous material sputtered from the Allende residue, sampling material from approximately 1000 nanodiamonds in a single layer. The lowest ratio measured was ^{12}C/^{13}C = 49±~7 (detected three times), about 800‰ isotopically heavier than the mean ratio. The largest anomaly reported in the residues to date is roughly 10‰ isotopically heavier than the bulk acid residue, detected in stepped heating (Swart et al. 1983; Russell et al. 1991; Verchovsky et al. 1998), and has been attributed to a small fraction of non-diamond material, presumed to be disordered C. As noted earlier, the Allende outlier data points are distinct from those in the standards in that each is surrounded by additional data points enriched in ^{13}C compared to the average (Figure 3.7). If the Allende outliers are not statistical anomalies, there are several possible explanations.

(1) Presolar silicon carbide grains are expected to be present in the nanodiamonds (Lewis et al. 1989) and could be the source of the ^{13}C-rich outliers we observe. Since they undergo the same

size separation procedures as the nanodiamonds, these SiC grains should be on the order of a few nanometers to 10 nm in size. However, we see no evidence for silicon carbide grains in the outliers. Si counts rise for some cycles in some of the outlier depth profiles, but there is no consistent increase in Si counts correlating with the increase in ^{13}C signal. Moreover, the Si concentration is very low, 2–6 counts in each of the outliers. For the purposes of a simple approximation, we assume the useful yield of Si is roughly the same as that for C, 0.5%. Thus 6 silicon atoms, the maximum detected for an outlier, would imply the presence of at most 1200 silicon atoms in the volume sputtered, implying 1200 carbon atoms from the same SiC grain. This is not an unreasonable grain size. If all 1200 hypothesized carbon atoms were ^{13}C – an extreme case – we estimate only 6 would be detected, shifting a solar $^{12}C/^{13}C$ ratio data point to a ratio of about 75, which would not register as an outlier in our Allende data sets. Therefore SiC cannot explain the outliers. In addition, the reported SiC concentration in the Allende residue is estimated at 600 ppm (Lewis et al. 1989). If the outliers are due to SiC contamination, their isotopic compositions would have to be highly ^{13}C-enriched, similar to SiC AB grains. These grains comprise up to 5% of the presolar SiC population (Hynes and Gyngard 2009; Zinner 2014). Therefore, the detection of 5 SiC AB grains would suggest that there are 100 total presolar SiC grains scattered throughout our meteoritic data sets, a concentration of approximately 25 ppm, given our estimation of 4×10^6 nanodiamonds. If the outliers are caused by SiC AB grains, it is difficult to explain why we do not see an order of magnitude more of them, enough to create a notable peak in the tail of each of our distributions. The fact that we do not see such a secondary peak calls into doubt whether our samples contain 600 ppm SiC, and further confirms that the outliers are not the result of SiC AB grains.

(2) An isotopically anomalous subpopulation of nanodiamonds and/or clumps of disordered sp^2-bonded carbon could be present in the acid residues. For a single anomalous grain to produce an outlier of the magnitude observed, it would be required to be highly enriched in ^{13}C and fill a significant percentage of the analysis area. Nanodiamonds as large as 10 nm in diameter have been reported (Daulton et al. 1996), and their maximum cross sections would fill about 2% of a 70 nm diameter beam spot. If our spot is actually only 50 nm in diameter, the effect doubles to 4%. Assuming the rest of the material has a $^{12}C/^{13}C$ ratio of 89, a 10 nm presolar grain would be required to have a $^{12}C/^{13}C$ ratio of about 1 for the 2% case, or 4 for the 4% case, in order to produce the isotopic outliers detected with a $^{12}C/^{13}C$ ratio of about 50. This scenario would favor grains from stars with cool bottom processing, including J-stars or novae (Zinner 2014), but does not rule out other sources, such as born-again AGB stars (Zinner 2014) and supernovae (Liu et al. 2016; Nittler and Hoppe 2005). Xe-HL could be implanted into J-star or nova nanodiamond grains in the interstellar medium by a passing supernova shock. However, the presence of a few large presolar nanodiamonds does not explain all of the Xe-HL in the residues, which, in the meteorite Efremovka, is detected in all size fractions (Gilmour et al. 2005).

(3) If more than one presolar grain is present in an outlier data point, smaller anomalies in these grains could produce the outliers observed. In this case we hypothesize presolar nanodiamond material with an average $^{12}C/^{13}C$ ratio of 45. However, the higher the number of presolar grains that are needed to account for an outlier, the more data points must, according to binomial statistics, contain a significant number of these grains. While many data points would contain too few presolar nanodiamonds to register as outliers, the cumulative effect would broaden the distribution and shift the mean ratio. The mean ratio could be balanced by isotopically light material, but broadening of the distribution could not. For a mean presolar nanodiamond $^{12}C/^{13}C$

ratio of 45, as much as 80% of the material in each outlier would need to be composed of presolar nanodiamonds to produce an observed outlier of $^{12}C/^{13}C = 50$.Then, in order for 3 out of the 14,852 (0.02%) of the data points to be outliers for ADM 26-1, and 2 out of 30,879 (0.0065%) for ADM 26-3, the mean percentage of presolar nanodiamonds per data point must be over 15% for ADM 26-1, and over 10% for ADM 26-3. This could be balanced if the remaining material had a mean ratio of 109, for ADM 26-1, and 101, for ADM 26-3. The resulting standard deviation would then be derived from that of the two isotopic sources, which would produce the Gaussian broadening in ratio distributions that we detected. These proportions are similar to the proportions of isotopically light and heavy grains observed in SiC X grains of supernova origin (Zinner 2014). However, the likelihood of such an ad hoc distribution is not very high.

3.6 Summary

(1) We have demonstrated that the nanodiamonds and disordered carbon in the Allende DM residues have $^{12}C/^{13}C$ ratios consistent with solar system values and previous measurements, down to aggregates as small as 10^6 carbon atoms, or 10^3 nanodiamonds.

(2) While our sensitivity rules out large populations of highly anomalous material, a smaller but still significant fraction of the nanodiamonds could carry major isotopic anomalies.

(3) The distributions of the Allende ratios have larger standard deviations than comparable standard data sets, but are still Gaussian in shape. This suggests that multiple isotopic ratios may be represented in the residue, averaging to solar abundances. Presolar nanodiamonds from supernova material, with a range of ^{13}C-enriched and -depleted material, are a good candidate for such a non-solar component, although a fraction of AGB material could also be present together with isotopically light supernovae material.

(4) In addition to broadening over the whole data set, ^{13}C-rich material is observed in several individual aggregates of 10^6 carbon atoms in size, suggesting the presence of a small fraction of ^{13}C-rich nanodiamonds. For SiC, past studies have indicated J-type carbon stars or born-again AGB stars as sources for such grains (Zinner 2014), but more recent work suggests that they could also come from supernovae (Nittler and Hoppe 2005, Liu et al. 2016).

(5) The results, taken together, support the conclusion suggested by the presence of Xe-HL, that some of the nanodiamonds are presolar. The broadening of the distributions of ratios in the Allende data compared to standards, as well as data points with ^{13}C-rich ratios, suggest the presence of supernova nanodiamonds. Nanodiamonds from AGB stars or other sources could also be present and could account for both the outliers and the distribution broadening, but only in conjunction with supernova material to balance out the close-to-solar average ^{12}C/^{13}C ratio and to serve as carriers of the Xe-HL.

(6) Additional experimental and statistical work on smaller aggregates is necessary to confirm and expand on these results. Ideally, this would be carried out with a stable, <50 nm-diameter NanoSIMS beam and control software modified to allow for serialized long measurements, or with atom-probe tomography, which can analyze nanodiamonds individually.

3.7 Acknowledgements

The authors express particular gratitude to inspiration and guidance from Tom Bernatowicz, and acknowledge his contribution of the idea of using a minimized NanoSIMS beam and a statistical approach to detecting isotopic anomalies in presolar nanodiamonds. The authors gratefully acknowledge Frank Podosek for his helpful assistance and contribution to an abstract on an earlier iteration of this work. The authors gratefully acknowledge Larry Nittler and his

L'Image software, and Ryan Ogliore for helpful discussions. The authors gratefully acknowledge associate editor Peter Hoppe, reviewer Thomas Stephan, and an anonymous reviewer, each for insightful suggestions that improved the manuscript. Funding: This work was supported by the National Aeronautics and Space Administration [grant numbers NNX14AP15H, NNX16AD26G].

3.8 References

Amari S., Zinner E., and Gallino R. 2014. Presolar graphite from the Murchison meteorite: An isotopic study. *Geochimica et Cosmochimica Acta* 133, 479–522.

Bernatowicz T. J., Gibbons P. C., and Lewis R. S. 1990. Electron energy loss spectrometry of interstellar diamonds. *The Astrophysical Journal* 359, 246–255.

Clayton D. D. 1989. Origin of heavy xenon in meteoritic diamonds. *The Astrophysical Journal* 340, 613–619.

Clayton D. D., Meyer B. S., Sanderson C. I., Russell S. S. and Pillinger C. T. 1995. Carbon and nitrogen isotopes in Type II supernova diamonds. *The Astrophysical Journal* 447, 894–905.

Coplen T. B., Böhlke J. K., De Bièvre P., Ding T., Holden N. E., Hopple J. A., Krouse H. R., Lamberty A., Peiser H. S., Révész K. others. 2002. Isotope-abundance variations of selected elements (IUPAC Technical Report). *Pure and Applied Chemistry.* 74, 1987–2017.

Dai Z. R., Bradley J. P., Joswiak D. J., Brownlee D. E., Hill H. G. M., and Genge M. J. 2002. Possible *in situ* formation of meteoritic nanodiamonds in the early Solar System. *Nature* 418, 157–159.

Daulton T. L., Eisenhour D. D., Bernatowicz T. J., Lewis R. S., and Buseck P. R. 1996. Genesis of presolar diamonds: Comparative high-resolution transmission electron microscopy study of meteoritic and terrestrial nano-diamonds. *Geochimica et Cosmochimica Acta* 60, 4853–4872.

Gilmour J. D., Verchovsky A. B., Fisenko A. V., Holland G., and Turner G. 2005. Xenon isotopes in size separated nanodiamonds from Efremovka: ^{129}Xe*, Xe-P3, and Xe-P6. *Geochimica et Cosmochimica Acta* 69, 4133–4148.

Greiner N. R., Phillips D. S., Johnson J. D., and Volk F. 1988. Diamonds in detonation soot. *Nature* 333, 440–442.

Hayya J., Armstrong D., Gressis N. 1975. A Note on the Ratio of Two Normally Distributed Variables. *Management Science* 21, 1338–1341.

Heck P. R., Stadermann F. J., Isheim D., Auciello O., Daulton T. L., Davis A. M., Elam J. W., Floss C., Hiller J., Larson D. J., Lewis J. B., Mane A., Pellin M. J., Savina M. R., Seidman D. N., and Stephan T. 2014. Atom-probe analyses of nanodiamonds from Allende. *Meteoritics and Planetary Science* 49, 453–467.

Hoppe P., Leitner, J. and Kodolányi, J. 2015. New constraints on the abundances of silicate and oxide stardust from supernovae in the Acfer 094 meteorite. *The Astrophysical Journal Letters* 808, L9 (6pp).

Huss G. R. 2005. Meteoritic nanodiamonds: Messengers from the stars. *Elements* 1, 97–100.

Huss G. R. and Lewis R. S. 1994a. Noble gases in presolar diamonds I: Three distinct components and their implications for diamond origins. *Meteoritics and Planetary Science* 29, 791–810.

Huss G. R. and Lewis R. S. 1994b. Noble gases in presolar diamonds II: Component abundances reflect thermal processing. *Meteoritics and Planetary Science* 29, 811–829.

Huss G. R. and Lewis R. S. 1995. Presolar diamond, SiC, and graphite in primitive chondrites: Abundances as a function of meteorite class and petrologic type. *Geochimica et Cosmochimica Acta* 59, 115–160.

Huss G. R., Ott U. and Koscheev A. P. 2008. Noble gases in presolar diamonds III: Implications of ion implantation experiments with synthetic nanodiamonds. *Meteoritics and Planetary Science* 43, 1811–1826.

Hynes K. M. and Gyngard F. 2009. The presolar grains database: http://presolar.wustl.edu/~pgd. *40th Lunar and Planetary Science Conference* Abstract #1198.

Isheim D., Stadermann F. J., Lewis J. B., Floss C., Daulton T. L., Davis A. M., Heck P. R., Pellin M. J., Savina M. R., Seidman D. N., and Stephan T. 2013. Combining atom-probe tomography and focused-ion beam microscopy to study individual presolar meteoritic nanodiamond particles. *Microscopy and Microanalysis* 19(Suppl 2), 974–975.

Lewis J. B. Isheim D., Floss C., and Seidman D. N. 2015. $^{12}C/^{13}C$-ratio determination in nanodiamonds by atom-probe tomography. *Ultramicroscopy* 159, 248–254.

Lewis J. B., Isheim D., Floss C., Daulton T. L., and Seidman D. N. 2016. Analysis of Allende nanodiamond residue by correlated transmission electron microscopy and atom-probe tomography. 42nd *Lunar and Planetary Science Conference* Abstract #2248.

Lewis R. S., Ming T., Wacker J. F., Anders E., and Steel E. 1987. Interstellar diamonds in meteorites. *Nature* 326, 160–162.

Lewis R. S., Anders E., and Draine B. T. 1989. Properties, detectability and origin of interstellar diamonds in meteorites. *Nature* 339, 117–121.

Liu N., Nittler L. R., Alexander C. M. O'D., Wang J., Pignatari M., José J. and Nguyen A. 2016. Stellar origins of extremely ^{13}C- and ^{15}N-enriched presolar SiC grains: Novae or supernovae? *The Astrophysical Journal* 820, 140 (14pp).

Maas R., Loss R. D., Rosman K. J. R., De Laeter J. R., Lewis R. S., Huss G. R., and Lugmair G. W. 2001. Isotope anomalies in tellurium and palladium from Allende nanodiamonds. *Meteoritics and Planetary Science* 36, 849–858.

Marty B., Chaussidon M., Wiens R. C., Jurewicz A. J. G., and Burnett D. S. 2011. A ^{15}N-poor isotopic composition for the solar system as shown by Genesis solar wind samples. *Science* 332, 1533–1536.

Nittler L. R. and Hoppe P. 2005. Are presolar silicon carbide grains from novae actually from supernovae? *The Astrophysical Journal Letters* 631, L89–L92.

Nuth J. A. and Allen J. E. 1992. Supernovae as sources of interstellar diamonds. *Astrophysics and Space Sciences* 196, 117–123.

Ogliore R. C., Huss G. R., and Nagashima K. 2011. Ratio estimation in SIMS analysis. *Nuclear Instruments and Methods in Physics Research Section B,* 269, 1910–1918.

Pravdivtseva O., Shatoff E. A., Meshik A., and Stroud R. M. 2016. Separation of Allende nanodiamonds by electrophoresis. *47th Lunar Planetary Science Conference* Abstract #2996.

Rauscher T., Heger A., Hoffman R. D., and Woosley S. E. 2002. Nucleosynthesis in massive stars with improved nuclear and stellar physics. *The Astrophysical Journal* 576, 323–348.

Richter S., Ott U., and Begemann F. 1998. Tellurium in pre-solar diamonds as an indicator for rapid separation of supernova ejecta. *Nature* 391, 261–263.

Russell S. S., Arden, J. W., and Pillinger C. T. 1991. Evidence for multiple sources of diamond from primitive chondrites. *Science* 254, 1188–1191.

Russell S. S., Arden J. W., and Pillinger C. T. 1996. A carbon and nitrogen isotope study of diamond from primitive chondrites. *Meteoritics and Planetary Science* 31, 343–355.

Schelhaas N., Ott U., Begemann F. 1990. Trapped noble gases in unequilibrated ordinary chondrites. *Geochimica et Cosmochimica Acta* 54, 2869–2882.

Shatoff E. A., Meshik A. P., and Pravdivtseva O. V. 2015. Electrophoresis of Allende nanodiamonds in colloidal solution. *46th Lunar and Planetary Science Conference* Abstract #2688.

Shigemitsu T., Matsumoto G., and Tsukahara S. 1979. Electrical properties of glassy-carbon electrodes. *Medical and Biological Engineering and Computing* 17:465–470.

Stroud R. M., Chisholm M. F., Heck P. R., Alexander C. M. O'D., and Nittler L. R. 2011. Supernova shock-wave-induced co-formation of glassy carbon and nanodiamond. *The Astrophysical Journal Letters* 738, L27 (5pp).

Stroud R. M., Pravdivtseva O. V., Meshik A. P., and Shatoff E. A. 2016. Aberration-corrected STEM analysis of electrophoresis separates of Allende nanodiamond. *47th Lunar and Planetary Science Conference* Abstract #2311.

Swart P. K., Grady M. M., Pillinger C. T., Lewis R. S., and Anders E. 1983. Interstellar carbon in meteorites. *Science* 220, 406–410.

Taylor J. R. 1997. *An introduction to error analysis* 2nd ed. University Science Books, California, U.S.A. (first ed. 1982).

Tielens A. G. G. M. 1990. Carbon stardust: From soot to diamonds. In *Carbon in the Galaxy: Studies from Earth and Space* pp. 59–111.

Verchovsky A. B., Fisenko A. V., Semjonova L. F., Wright I. P., Lee M. R., Pillinger C. T. 1998. C, N, and noble gas isotopes in grain size separates of presolar diamonds from Efremovka. *Science*. 281, 1165–1168.

Verchovsky A. B., Fisenko A. V., Semjonova L. F., Bridges J., Lee M. R., and Wright I. P. 2006. Nanodiamonds from AGB stars: A new type of presolar grain in meteorites. *The Astrophysical Journal* 651, 481–490.

Yastrebov S. and Smith R. 2009. Nanodiamonds enveloped in glassy carbon shells and the origin of the 2175 Å optical extinction feature. *The Astrophysical Journal* 697, 1822–1826.

Ziegler J. F., Ziegler M. D., and Biersack J. P. 2010. SRIM – The stopping and range of ions in matter 2010. *Nuclear Instruments and Methods in Physics Research Section B*, 268, 1818–1823.

Zinner E. 2014. Presolar Grains. In *Treatise on Geochemistry* (eds. H. D. Holland and K. K. Turekian; vol. ed. A. M. Davis). Elsevier Ltd., Oxford, 2nd Edition. Vol. 1.4, 181–213.

Chapter 4: Atom-Probe Analyses of Nanodiamonds from Allende

This chapter has been published in the journal, *Meteoritics and Planetary Science* in collaboration with Philipp R. Heck, Frank J. Stadermann, Dieter Isheim, Orlando Auciello, Tyrone L. Daulton, Andrew M. Davis, Jeffrey W. Elam, Christine Floss, Jon Hiller, David J. Larson, Anil Mane, Michael J. Pellin, Michael R. Savina, David N. Seidman, and Thomas Stephan (Heck et al. 2014). The author's personal contributions include the majority of sample preparation, experimental analysis, and all of the data reduction for the St. Louis group, one of the two groups involved in the research, as well as writing the St. Louis methods (Section 4.4.2), and collaborating on paper design, drafting, and revision.

4.1 Introduction

The origin of meteoritic nanodiamonds is still a mystery 26 yr after their discovery. Systematic bulk analyses of different separates from carbonaceous chondrites have shown that nanodiamond-bearing acid residues contain the carrier of the highly anomalous xenon isotope component Xe-HL (Lewis et al. 1987). Xe-HL is enriched in the two lightest xenon isotopes, ^{124}Xe and ^{126}Xe, both produced in the *p*-process, and also in the two heaviest isotopes, ^{134}Xe and ^{136}Xe, produced in the *r*-process. Additionally, the same nanodiamond-rich separates contain small anomalies in the *r*-process nuclides ^{110}Pd, ^{128}Te, and ^{130}Te (Maas et al. 2001; Richter et al. 1998) and in the *r*,*s*-process nuclide ^{137}Ba (Lewis et al. 1991). These *p*- and *r*- process anomalies can only be explained by nucleosynthetic processes that are thought to occur in supernovae. The abundance of these trapped nuclides is relatively low, and only a small fraction of the nanodiamond population can carry these anomalies. For instance, on average, only one of a

million meteoritic diamonds contains a single trapped xenon atom (for a review, see Daulton (2006)); however, more diamonds contain anomalous neon and helium (Huss and Lewis 1994). As a solar system origin of these anomalies can be clearly excluded, meteoritic nanodiamonds have been classified as presolar.

A recent scanning transmission electron microscopy study showed that meteoritic nanodiamond-bearing acid residues also contain an sp^2 carbon phase resembling glassy carbon (Stroud et al. 2011). This two-phase mixture has been explained by the transformation of organic carbon to nanodiamonds and glassy carbon by supernova shockwaves in the interstellar medium (ISM). It is, moreover, consistent with the astronomically observed 2175 Å extinction feature in the ISM (Stroud et al. 2011). The presolar isotopic anomalies could be carried by the nanodiamonds, by the glassy carbon, or by both. Earlier high-resolution (HR)-TEM studies have, however, demonstrated that the growth and defect atomic microstructures of the majority of meteoritic nanodiamonds from Allende and Murchison are inconsistent with shock-transformation processes and instead are consistent with vapor condensation occurring in the gaseous outflows of supernova and asymptotic giant branch stars (Daulton et al. 1996); vapor condensation in the evolving solar nebula is also a possibility. These apparently conflicting results reflect one aspect of the uncertainty of the origin of the meteoritic nanodiamonds.

Furthermore, in contrast to the data for trace elements, the isotopic ratios of the major element carbon and the minor element nitrogen in bulk analyses are similar to solar system ratios (Figure 4). Swart et al. (1983) and Russell et al. (1996) determined $\delta^{13}C$ ranges from -32 to -38‰, while $\delta^{15}N$ values were -330‰ for bulk Allende nanodiamonds (Lewis et al. 1983) and -348±7‰ for bulk nanodiamonds extracted from 11 different primitive chondrites (Russell et al. 1996). δ-values are deviations from standard reference materials in parts per thousand deviations:

$\delta^{13}C = [(^{13}C/^{12}C)_{sample}/(^{13}C/^{12}C)_{PDB} - 1] \times 10^3$ and $\delta^{15}N = [(^{15}N/^{14}N)_{sample}/(^{15}N/^{14}N)_{air} - 1] \times 10^3$ where Vienna-Pee Dee Belemnite and N_2 in air are references for carbon and nitrogen, respectively. Within analytical uncertainty, these $\delta^{15}N$ values are similar to those of the atmosphere of Jupiter ($\delta^{15}N$ = -374±82‰; (Owen et al. 2001) and are close to the values determined for the bulk sun or protosolar nebula and the solar wind ($\delta^{15}N$ = -383±8‰ and -407±7‰, respectively; (Marty et al. 2011)). The nanodiamonds' bulk solar system carbon and nitrogen isotopic compositions, and their absence in certain primitive interplanetary dust particles (Dai et al. 2002) have led to the hypothesis that a fraction of the nanodiamonds could have formed in the early solar system. However, it is important to recognize that the bulk measured $\delta^{13}C$ and $\delta^{15}N$ values from these residues may not be representative of the nanodiamond phase. As noted above, the nanodiamond residues contain a significant component of carbonaceous nondiamond material (Stroud et al. 2011). Furthermore, there may be different populations of meteoritic nanodiamonds with protosolar nebula and/or presolar origins. Thus, the bulk measured isotopic compositions could be an average over many sources.

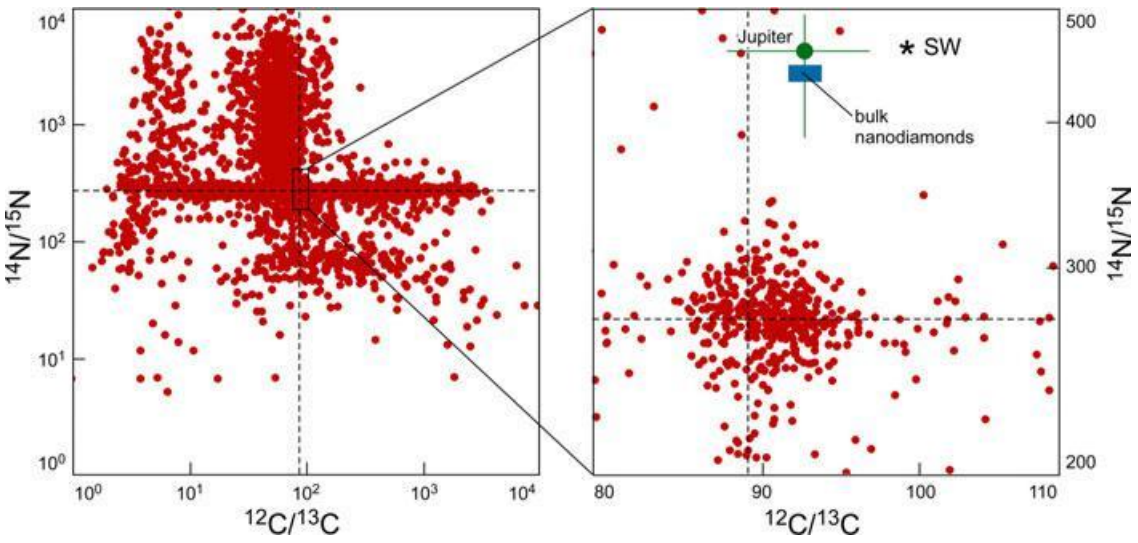

Figure 4.1 Range of carbon and nitrogen isotopic compositions in bulk analyses of nanodiamond-containing acid residues (blue rectangle; data from Russell et al. 1996) compared with solar wind—SW; (Marty et al. 2011), Jupiter (Atreya et al. 2003; Owen et al. 2001), and individual presolar silicon carbide and graphite grains (red dots; data from Presolar Grain Database; (Hynes and Gyngard 2009)). Dashed lines are the terrestrial carbon standard (Vienna-PDB) and terrestrial air nitrogen isotope ratios (Coplen et al. 2002). Error bars are shown if larger than the symbol size.

Isotopic data from individual presolar grains such as presolar silicon carbide, graphite, silicates, and oxides show large variations, which most likely reflect origins in different stellar sources and via different types of processes (see reviews by Clayton and Nittler (2004); Davis (2011); Zinner (2007)). For example, the $^{12}C/^{13}C$ ratios of different presolar silicon carbide (SiC) grains span four orders of magnitude (Figure 4.1), and the average ratios of the different types of SiC are different from both the terrestrial and solar ratios. Because of the small sizes (average diameter approximately 3 nm; (Daulton et al. 1996)) of individual diamond grains, isotopic analyses have not been possible due to limitations in spatial resolution and sensitivity, and all isotopic data so far have been obtained from bulk measurements. To shed light on the origin of nanodiamonds, single-grain isotopic analyses are desirable. The distribution of $^{12}C/^{13}C$ ratios among meteoritic nanodiamonds can help evaluate whether multiple nanodiamond populations are present in the

residues and determine their origin (e.g., solar or presolar). Determining $^{12}C/^{13}C$ ratios of individual nanodiamonds also has the potential to distinguish among different presolar stellar sources.

Atom-probe tomography (APT) is currently the only technique with the spatial resolution and detection sensitivity to analyze isotope ratios of individual particles in the size range of meteoritic nanodiamonds (Seidman and Stiller 2009). The objectives of this study are to develop sample preparation techniques that will allow for atom-probe tomographic analyses of individual meteoritic nanodiamonds, to address the questions of their origins as noted above. The idea of using APT to analyze individual meteoritic nanodiamonds was developed independently and contemporaneously in both Chicago and St. Louis. Rather than competing, the two groups decided to collaborate, exchange information, and report their first achievements in a joint publication. In this article, we summarize development of the different sample preparation techniques and analytical protocols, and present our first results of nanodiamond analyses with the atom-probe tomograph at sub-nm spatial resolution. Preliminary results have been presented in conference abstracts (Heck et al. 2010, 2011a, 2011b, 2011c, 2012; Lewis et al. 2012; Stadermann et al. 2010, 2011).

4.2 Analytical method: Atom-probe Tomography

Atom-probe tomography is based on the coupling of a field-ion microscope, a lensless point-projection instrument that resolves individual atoms on the surface of a sharply pointed (<50 nm) tip at magnifications of greater than 10^6 with sub-nm resolution, with a time-of-flight mass spectrometer (Müller et al. 1968). Atoms on the surface of a specimen at a positive potential with respect to ground are ionized in the presence of a strong electric field (the so-called “field evaporation” effect) and are then repelled from it toward a multichannel plate detector. The

pulsed electric field removes surface atoms from a sample on an atom-by-atom and atomic layer-by-layer basis. These field-evaporated ions are detected by a position-sensitive time-of-flight detector on the basis of their mass-to-charge-state ratio (m/q). The detector consists of a microchannel plate with single-ion sensitivity, plus a delay line detector, which sits directly behind it. Because a specimen's surface is being field-evaporated atomic layer by layer, it is possible to visualize the three-dimensional structure of the sample at an atomic level. In a local-electrode atom-probe (LEAP) tomograph, a cone-shaped local-electrode is placed between a specimen's microtip and the position-sensitive detector (Figure 4.2), effectively confining the electric field to the space between the microtip and the local electrode, which has an orifice diameter of about 30 μm. Samples are introduced into the ultrahigh vacuum analysis chamber and cooled to 20–120 K, before applying a DC voltage to the microtip. The steady DC voltage is maintained just below the threshold of the evaporation field. The threshold for field evaporation is highly dependent on the sample material (i.e., the constituent elements and their bonding) and depends, in particular, on the sublimation and ionization energies and the local work function. To obtain highly controlled pulsed field evaporation and to provide a precise start time for the time-of-flight detector, the microtip is then illuminated with picosecond pulses from a highly focused ultraviolet laser (λ = 355 nm), resulting in heating of the apex of the microtip, and field ionization and evaporation of the surface atoms. When using a picosecond ultraviolet laser to dissect a microtip, the pulse repetition rate can be up to 1000 kHz. More in-depth descriptions of this technique and its physics can be found in (Kelly and Larson 2012; Kelly and Miller 2007; Seidman 2007; Seidman and Stiller 2009).

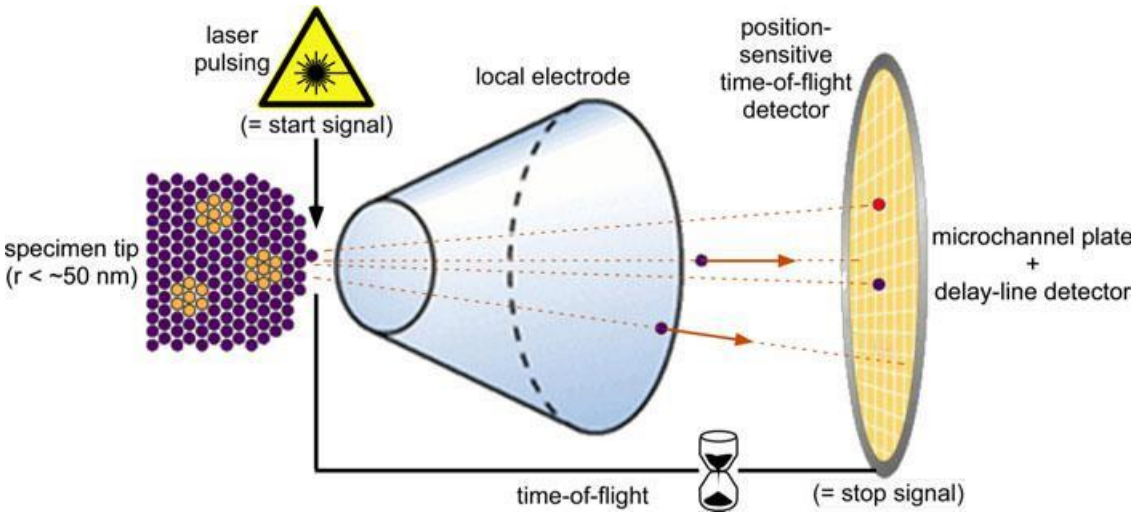

Figure 4.2 Schematic of a local-electrode atom-probe tomograph (not to scale). The specimen is maintained at a high positive potential with respect to earth potential, and picosecond laser pulses, impinging on the specimen's microtip approximately perpendicular to the long axis of the microtip, trigger field evaporation of surface atoms. The field-evaporated ions are accelerated along the diverging electric field lines to project a highly magnified image of the microtip's surface onto the position-sensitive time-of-flight detector. The time-of-flight of the ions is used to identify their mass-to-charge-state ratio and hence their chemical identities.

For our study, we used two LEAP tomographs developed and manufactured by Cameca Instruments Inc. Most of the analyses were performed with a Cameca LEAP 4000X Si APT with a straight time-of-flight path of 90 mm at the Northwestern University Center for APT (NUCAPT). In one session, we used a Cameca LEAP 4000X HR APT in the Applications Laboratory of Cameca Instruments Inc. This latest-generation instrument (denoted as a LEAP HR tomograph) is equipped with a reflectron-type time-of-flight mass spectrometer resulting in a flight path of 382 mm and a higher mass resolving power compared with the LEAP 4000X Si (Scheinfein and Seidman 1993).

The LEAP 4000X Si (hereafter simply denoted as a LEAP tomograph) at NUCAPT has received several upgrades over the course of this study and since its original installation in December 2004. The beam conditioning unit and focusing optics received a major upgrade, with the following performance enhancements:

(1) the diameter of the laser focus on the microtip was reduced, increasing the energy density of the beam by a factor of four, which permits a shortened heat pulse; (2) a continuous laser pulse energy range spanning 30 fJ– 1.5 nJ, equivalent to a 5×10^5 dynamic range, was added, allowing optimum evaporation conditions for a wide variety of materials; (3) the plane of laser polarization can now be rotated in 15° steps from 0 to 90° to vary the precise energy absorption geometry of the laser pulse by the tip; (4) a "ringing" effect that produced spurious peaks in the mass spectrum of some materials was largely eliminated; (5) new motorized in-vacuum optics were added, providing much smoother and better stability with the laser beam alignment; and (6) an active piezoelectric damping system was installed, which efficiently damps all vibrations of the LEAP tomograph. In addition, an upgrade for the LEAP tomograph hardware control PC tripled the maximum data acquisition speed to about 35,000 atoms per second, increasing significantly the throughput of the LEAP tomograph. These enhancements led to significant improvements in data quality over the course of this study.

The laser pulse repetition rate in LEAP tomography has a maximum of 1000 kHz, which makes it possible to measure relatively large volumes of material atom by atom employing reasonable analysis times. The detection efficiency of the microchannel plate detector of the straight-flight path LEAP tomograph ranges from 50 to 60% and is the same for all elements of the periodic table. The efficiency for the LEAP HR tomograph is reduced to 37% due to the field-defining mesh necessary for operation of the reflectron. Its higher signal-to-noise ratio counteracts, however, the sensitivity reduction caused by the lower transmission. Using specialized software (Imago Visualization and Analysis System— IVAS, Cameca Instruments Inc., Kunicki et al. 2006), the data collected can be visualized as three-dimensional distributions of all detected

atoms in the analysis volume, at any angle of observation. Time-of-flight mass spectra can be obtained for the entire reconstruction and from selected subvolumes of interest.

4.3 Samples

For our study, we selected nanodiamonds from the acid dissolution residue Allende DM, a well-studied nanodiamond isolate (Lewis et al. 1989). The Allende DM isolate consists of a mixture of nanodiamonds and glassy carbon as well as trace minerals (including SiC, graphitic carbon, and metal grains). We used both synthetic detonation nanodiamonds (DNDs) and ultrananocrystalline diamonds (UNCDs) as standards. DNDs are produced in a contained explosion by shock-transformation of organic matter (Greiner et al. 1988) and were obtained from Lawrence Livermore National Laboratory. UNCD films are grown by microwave-plasma deposition at Argonne National Laboratory (Auciello and Sumant 2010) directly onto silicon microtips.

4.4 Sample Preparation Methods

To be suitable for APT analyses, samples must be shaped into a sharp microtip with an apex radius of about 50 nm and must be able to withstand the high mechanical stresses present during the analyses. We used several procedures to prepare samples that satisfy these requirements. Material imperfections and weakly bonded interfaces can lead to catastrophic microtip failure and arcing. In the following, we describe briefly the methods developed independently by the Chicago and St. Louis groups.

4.4.1 Chicago Methods

For preparation of the atom-probe tomographic samples of meteoritic or synthetic DNDs, the grains were suspended in an ultrasonicated mixture of isopropanol (Fisher Optima) and water (Millipore Milli-Q). A 2–4 µL drop of the suspension was deposited onto a clean silicon

substrate and evaporated with a heat lamp. To fill open pore space and stabilize the samples, atomic layer deposition (ALD; Elam et al. 2006) was performed at Argonne National Laboratory to deposit Al_2O_3 (approximately 3.6 nm thickness) and tungsten (approximately 1.3 nm thickness) onto the tips. We also prepared control samples that consisted only of deposited Al_2O_3.

Method 1:

In our first approach, the nanodiamond suspension was deposited on a flat silicon wafer. After ALD, the wafer was coated with 60–500 nm of sputter-deposited cobalt to protect the nanodiamonds from the Ga^+ focused ion-beam (FIB) during subsequent milling in the FIB microscope. A wedge-shaped prism was milled with dual-beam FIB microscopes at Argonne National Laboratory (Zeiss 1540XB and Zeiss NVision) or at Northwestern University (FEI Helios), lifted out, and welded onto a flat-top silicon micropost (Thompson et al. 2005) with carbon and platinum (Figure 4.3). To enhance stability, carbon- and platinum-cold-welds were applied on at least two sides. Subsequently, the welded wedge was FIB-milled (Ga^+ ions) with an annular mask into a sharp microtip (Larson et al. 1999). The cobalt cap-layer served as a marker and Ga^+ ion-beam milling was stopped before the last bit of cobalt disappeared.

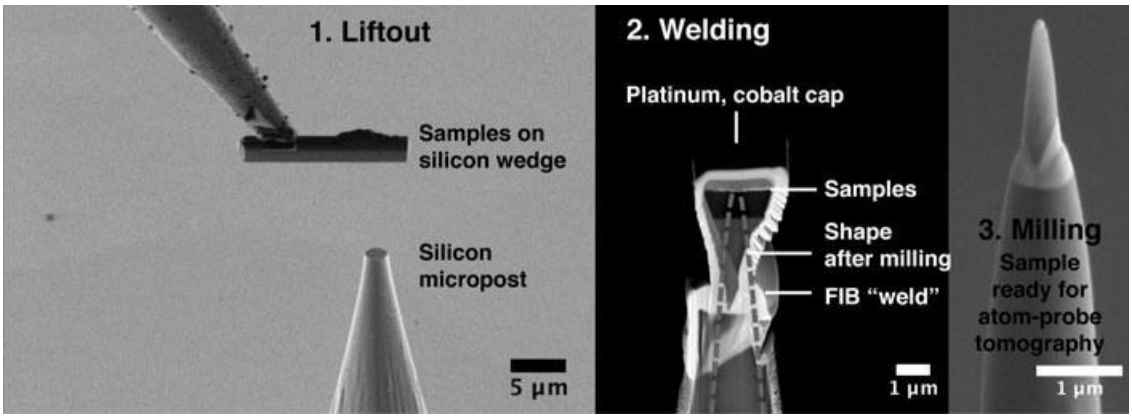

Figure 4.3 Focused ion-beam/scanning electron microscopy–based (1) lift-out, (2) "welding," and (3) milling of a nanodiamond sample deposited on a silicon wafer. After milling, the sample is ready for atom-probe tomography.

Method 2:

In this approach, a drop of the same suspension was placed onto an array of presharpened silicon microtips (Cameca) to cover the whole microtip array, which was then suspended upside down and exposed to a heat lamp for evaporation. Following that, ALD was performed; no additional sample preparation was required for this method. This method has the advantage that there is no possible Ga^+ ion-beam damage to the diamonds from the dual-beam FIB microscope.

As the final step before analysis, microtips prepared by both methods were imaged by scanning electron microscopy to verify that they were sufficiently sharp for field evaporation in the atom probe. To minimize oxidation, the samples were loaded into the ultrahigh vacuum chamber of the APT within a few hours to a day after sample preparation.

4.4.2 St. Louis Method

Meteoritic (or synthetic) nanodiamonds were suspended in a mixture of alcohol and water for deposition onto a high-purity nickel substrate. A thin (170 nm) layer of platinum was deposited onto the nickel substrate by ion-beam sputter deposition, followed by deposition of the nanodiamonds from the suspension onto the platinum-covered nickel substrate (Isheim et al. 2013). To prevent the nanodiamonds from clustering, the suspension was ultrasonicated until

immediately before deposition. The sample was also ultrasonicated during evaporation of the suspension drop to prevent nanodiamonds from agglomerating along the rim of the drop during drying and to obtain more uniform deposition layers on the substrate. To protect the nanodiamonds from surface contamination and to provide a solid-host material for the grains, the sample was then coated with an additional layer of platinum, followed by a final 500 nm layer of nickel to serve as a cover during subsequent FIB milling, thereby creating a Ni-Pt-diamond-Pt-Ni sandwich structure. Sections of this deposition layer were lifted out utilizing the FEI Helios dual-beam FIB microscope at Northwestern University or the FEI Quanta dual-beam FIB at Washington University in St. Louis. Approximately 3 μm long sections of these lift-outs were attached to prefabricated silicon microposts and milled into sharp microtips with a Ga^{+} ion-beam. This method resulted in microtips that contained nanodiamonds in a horizontal layer in close proximity to the pointed end of the column. These early microtips often suffered from mechanical failures along the horizontal nanodiamond layer and led us to modify the sample preparation procedure by rotating the FIB-microscope–extracted section, so that the nanodiamond layer is parallel (cross section mode; Lawrence et al. 2008), rather than perpendicular, to the long axis of the microtip (Figure 4.4). This improves the mechanical stability of the microtip and allows sequential field evaporation of individual or small clusters of nanodiamonds over a larger deposition layer.

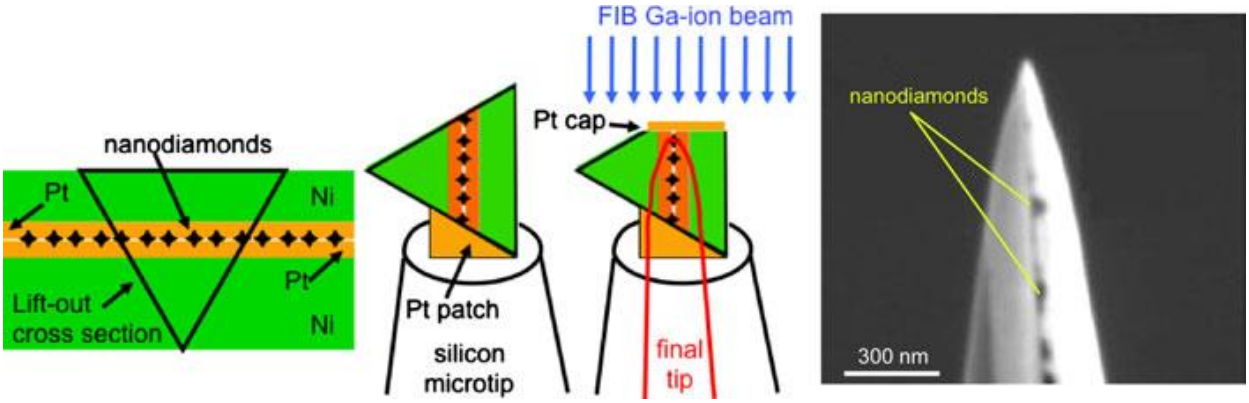

Figure 4.4 Left: schematic illustrating the focused ion-beam (FIB)-microscope extraction and rotation of a nanodiamond sandwich for ion milling and atom-probe tomography analysis. Right: secondary electron image of a nanodiamond sandwich microtip showing Allende nanodiamonds embedded in a platinum matrix.

4.5 Data Processing

Cameca's data processing software, IVAS, was used to create tomographic reconstructions. IVAS can produce and export mass spectra from the integrated data set of an entire microtip or of selected regions of interest (ROIs) within a tip. In IVAS, ROIs can be defined in several different ways: (1) by using a gridded isoconcentration surface calculation that applies a threshold function to envelop volumes of defined density ranges or elemental concentration ranges; (2) by using a cluster algorithm (Marquis and Hyde 2010); and (3) by manually defining a geometric shape (e.g., spheroid) and centering it on a concentration hotspot. We used both the manual method and the threshold isoconcentration surface function to define ROIs for most of the samples.

4.5.1 Uncertainties on Carbon Isotope Peak Ratios

Spectral data of integrated microtips and ROIs were exported from IVAS to integrate the area under peaks, calculate peak ratios, and to create mass spectra. Uncertainties in the peak ratios of isotopes can result from the background correction, hydride interferences, and potential instrumental biases.

A background correction is not necessary if the signal-to-noise ratio is high, but can constitute a major uncertainty if the peak intensities are only slightly above background. Background corrections were made in two ways: (1) automatic background correction by IVAS consists of the subtraction of a fitted function that describes the time-independent background throughout the time-of-flight mass spectrum; and (2) a manual background correction can be made by subtraction of the integrated linear interpolation of the background baseline from the integrated peak. The data from the Chicago group were background-corrected using the first method, whereas data from the St. Louis group were corrected using the second method. Comparison on several spectra indicates that both methods produce similar results.

Another uncertainty is the potential contribution of the $^{12}CH^{+}$ hydride interference to the $^{13}C^{+}$ peak (separated by approximately 0.0045 U). Neither of the LEAP tomograph systems used has a mass resolving power sufficient to resolve this interference. Previous ion-probe microanalyses have detected a high concentration of hydrogen in nanodiamond isolates (Virag et al. 1989), and Fourier-transform infrared spectroscopy has shown the presence of carboxyl (-COOH) surface groups (Lewis et al. 1989) in Allende DM isolates. As half of the carbon atoms in an average-sized meteoritic nanodiamond are within one unit cell of the surface, surface-absorbed species are an important source of hydrogen. In addition, hydride formation can result from the presence of residual hydrogen in the LEAP tomograph. The partial pressure of hydrogen in the analysis chamber is measured with a residual gas analyzer and can be highly variable. Therefore, a constant correction factor cannot be used, and, in fact, to the best of our knowledge, no correction method for hydride formation during field evaporation based on hydrogen partial pressure is known. The probability of forming doubly charged hydrides is expected to be much lower than for singly charged hydrides, so we do not anticipate significant hydride interferences

for $^{13}C^{++}$. We therefore optimized the analytical conditions to decrease the C^{+}/ C^{++} charge-state-ratio and increase the signal at $^{13}C^{++}$. This is done by decreasing the temperature at which field evaporation occurs (decreasing the laser pulse energy), which results in the requirement of a higher voltage for field evaporation (Kingham 1982). The charge-state-ratio cannot, however, be decreased indefinitely; higher voltages and lower laser pulse energy decrease sample stability due to the higher mechanical Maxwell stresses induced at higher electric fields, which result in more frequent tip fractures. In this study, we were able to achieve minimum C^{+}/C^{++} ratios of approximately 2–3 (Tables 4.1 and 4.2). For better readability throughout the manuscript, we label peaks with only the major ion species thought to be responsible for the peak in the mass spectrum, although there can be contributions from isobarically interfering hydrides or other species.

Table 4.1 Carbon isotope peak ratios for integrated microtips from the Chicago group.

Sample	$^{12}C^{+}/^{12}C^{++}$	$^{12}C^{+}/^{13}C^{+}$	$^{12}C^{++}/^{13}C^{++}$	*T* (K)	*E* (pJ)	Comments
Synthetic nanodiamonds						
DND 15874 L11 PSM04	2.3±0.6	41±26	45±45	80	300	--
UNCD 113207 PSM03	6.1±0.9	77±12	*(198±120)*	80	200	Low $^{13}C^{++}$ counts make $^{12}C^{++}/^{13}C^{++}$ peak ratio doubtful. Upgraded laser optics: smaller spot size.
UNCD 113215 PSM04	1.6±0.1	10±1	63±19	80	50	Upgraded laser optics: smaller spot size.
UNCD 113225 PSM08	2.8±0.2	40±4	67±16	80	100	--
UNCD 113233 PSM10	2.7±0.3	89±14	68±24	80	150	--
Mean	**2.3±0.2**	**36±3**	**65±11**	**--**	**--**	**--**
Allende Nanodiamonds						
ADM 14973 L08 M14	4.6±0.4	49±4	39±7	110	300	Sandwich method
ADM 15122 L08 M01	4.2±0.3	32±3	87±47	110	300	--
ADM 15961 L09 M29	12±1	71±7	28±6			Low $^{13}C^{++}$ counts make $^{12}C^{++}/^{13}C^{++}$ peak ratio doubtful.
ADM 15963 L09 M17	9.5±0.6	36±2	51±15	110	300	--
ADM 15964 L09 M16	12±1	31±3	*(6±1)*	110	300	Low $^{13}C^{++}$ counts make $^{12}C^{++}/^{13}C^{++}$ peak ratio doubtful.

Sample	$^{12}C^{+}/^{12}C^{++}$	$^{12}C^{+}/^{13}C^{+}$	$^{12}C^{++}/^{13}C^{++}$	*T* (K)	*E* (pJ)	Comments
ADM 15971 L09 M30	--	78±9	--	110	300	No significant C^{++} counts.
ADM 17134 L17 PSM25	*(5.0±0.4)*	*(3.9±0.3)*	41±97	80	20	Upgraded laser optics: smaller spot size. Large peak at mass-to-charge-state ratio of 13, possible large hydride interference makes $^{12}C^{+}/^{13}C^{+}$ ratio doubtful.
ADM 17137 L17 PSM15	3.2±0.6	20±3	17±10	80	20	Upgraded laser optics: smaller spot size.
Mean	**7.9±0.2**	**43±1**	**47±10**	**--**	**--**	**--**

Errors are 2σ and are based on counting statistics. Means are ratios of integrated counts for each ion species and do not include unreliable data, which are given in parentheses and italics. The nominal set temperatures (*T*) of the microtips and the nominal laser pulse energies (*E*) are also given. A LEAP 4000X HR was used for UNCDs; a LEAP 4000X Si was used for all other samples.

Table 4.2 Carbon isotope peak ratios for integrated microtips from the St. Louis group.

Sample	$^{12}C^{+}/^{12}C^{++}$	$^{12}C^{+}/^{13}C^{+}$	$^{12}C^{++}/^{13}C^{++}$	*T* (K)	*E* (pJ)	Comments
Synthetic nanodiamonds						
DND R06 17619 A61 M35	2.2±1.1	38±16	--	80	40	No significant C^{++} counts. Upgraded laser optics: smaller spot size.
DND R06 17620 A61 M35	1.9±0.5	60±10	61±16	80	40	Upgraded laser optics: smaller spot size.
DND R06 17621 A61 M34	15.2±2.5	31±10	--	80	40	No significant C^{++} counts. Upgraded laser optics: smaller spot size.
DND R06 17626 A62 M4	3.1±0.4	76±12	64±20	55	80–100	Upgraded laser optics: smaller spot size.
DND R06 17629 A61 M31	10.7±1.2	10±2	--	55	70–90	No significant C^{++} counts. Upgraded laser optics: smaller spot size.
DND R06 16013 A46 M1	3.8±0.5	57±22	--	103	150	No significant C^{++} counts.
DND R06 17967 A62 M35	1.5±0.2	30±14	(122±306)	54	40	Low $^{13}C^{++}$ counts make $^{12}C^{++}/^{13}C^{++}$ doubtful. Upgraded laser optics: smaller spot size.
DND R06 17969 A62 M28	1.8±0.1	53±10	57±16	54	40	Upgraded laser optics: smaller spot size.
DND R06 17978 A62 M34	4.2±1.3	30±12	--	95	40	No significant C^{++} counts. Upgraded laser optics: smaller spot

Sample	$^{12}C^{+}/^{12}C^{++}$	$^{12}C^{+}/^{13}C^{+}$	$^{12}C^{++}/^{13}C^{++}$	*T* (K)	*E* (pJ)	Comments
						size.
DND R06 18428 A64aM34	2.2±0.4	72±24	71±44	95	40–80	Upgraded laser optics: smaller spot size.
Mean	**3.0±0.1**	**46±2**	**64±7**	**--**	**--**	**--**
Allende Nanodiamonds						
ADM R06 15004 A36 M1	1.6±0.4	61±18	54±20	95	150	--
ADM R06 15005 A36 M1	1.1±0.2	45±16	83±48	95	150	--
ADM R06 16096 A47 M10	1.7±0.4	96±30	72±26	103	150	--
ADM R06 16097 A47 M11	1.7±0.6	87±42	87±58	102	150	--
ADM R06 16098 A47 M12	1.9±0.5	74±28	73±44	103	150	--
ADM R06 16119 A47 M12	2.2±0.6	69±28	(189±350)	103	150	Low $^{13}C^{++}$ counts make $^{12}C^{++}/^{13}C^{++}$ doubtful.
ADM R06 16120 A47 M13	1.8±0.4	77±16	87±30	102	250	--
ADM R06 18430v01 A65a M06	2.0±0.3	36±6	105±70	95	40–100	Upgraded laser optics: smaller spot size.
ADM R06 18436v01 A65a M05	1.8±0.6	92±44	72±40	95	40	Upgraded laser optics: smaller spot size.
ADM R06 18437 A65a M04	1.8±0.4	57±8	47±10	95	40–80	Upgraded laser optics: smaller spot size.
Mean	**2.0±0.1**	**69±4**	**65±5**	**--**	**--**	**--**

Errors are 2σ and are based on counting statistics. Means are ratios of integrated counts for each ion species and do not include unreliable data, which are given in parentheses and italics. The nominal set temperatures (*T*) of the microtips and the nominal laser pulse energies (*E*) are also given.

4.6 Results and Discussion

4.6.1 Mass Spectra and Tomographic Reconstructions

We define a successful APT measurement as one that results in the detection of major peaks of ^{12}C and ^{13}C with a high signal-to-noise ratio in the mass spectrum and the visualization of carbon-rich regions in the 3D tomographic reconstructions of a microtip. While some of our microtips failed, all sample preparation methods produced specimens that were successfully analyzed. Representative mass spectra of meteoritic and synthetic nanodiamonds and of a blank are displayed in Figure 4.5. As a result of progressive instrument upgrades and improved sample preparation techniques, data quality increased over the 3 years of this study and resulted, in general, in narrower peaks, lower background noise (i.e., improved signal-to-noise ratios), and longer runs due to improved sample stability.

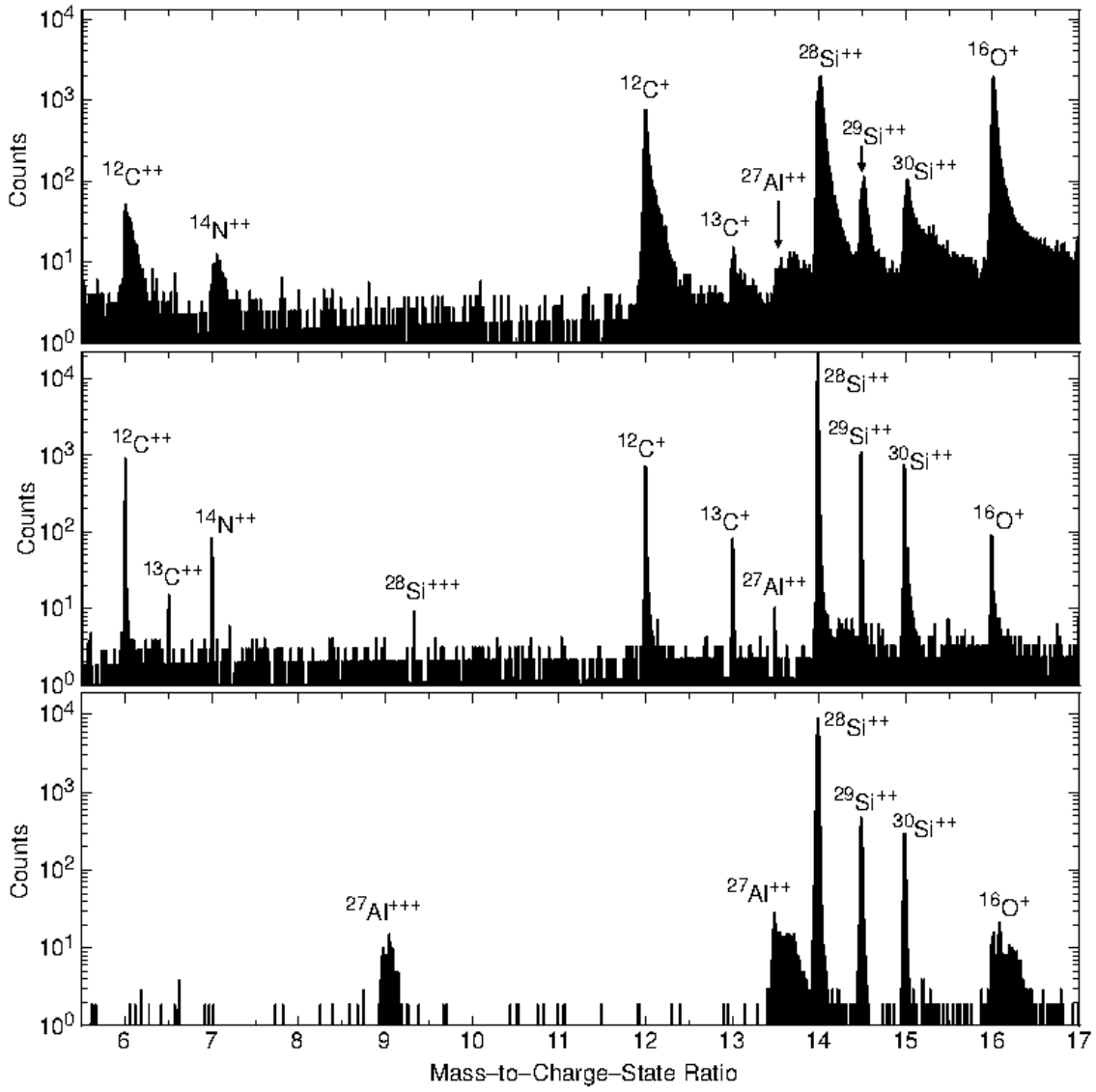

Figure 4.5 Representative mass spectra; the mass-to-charge-state ratio range was selected to display carbon isotope peaks. Top: Meteoritic nanodiamonds (direct deposition method) analyzed with the local-electrode atom-probe (LEAP) 4000X Si before the ultraviolet laser optics upgrade. Middle: Synthetic nanodiamonds (UNCD) analyzed with the upgraded LEAP 4000X HR using a 355 nm wavelength laser. Bottom: No significant carbon peaks are visible in the "blank" measurement of a silicon microtip atomic layer deposition-coated with alumina analyzed with the upgraded LEAP 4000X Si. Note the narrower peaks in the middle and bottom spectra that are the result of heating a smaller volume due to the smaller spot size obtained using a 355 nm laser.

The tomographic 3D reconstructions show different sample geometries resulting from the different preparation techniques utilized (Figures 4.6 and 4.7132). Figure 4.6 shows 3D reconstructions from the ALD and direct deposition methods used by the Chicago group. A densely packed nanodiamond layer is useful to obtain integrated data for a large number of

nanodiamonds, comparable to a bulk analysis (Figure 4.6, left), whereas the direct deposition method results in nanodiamonds that coat the surface of the silicon microtip with a much higher dispersion (Figure 4.6, right). The degree of dispersion depends on the colloidal diamond concentration at the time of deposition. Direct deposition is, therefore, the preferred method to obtain data from individual nanodiamonds. 132Figure 4.7 shows the reconstruction of a meteoritic nanodiamond analysis using the Ni-Pt-diamond-Pt-Ni sandwich method of the St. Louis group. Rotation of the FIB microscope lift-out, such that the nanodiamond layer is parallel to the long axis of the microtip, results in dispersion of the nanodiamonds and, like the Chicago direct deposition method, permits the analysis of individual or small clusters of nanodiamonds.

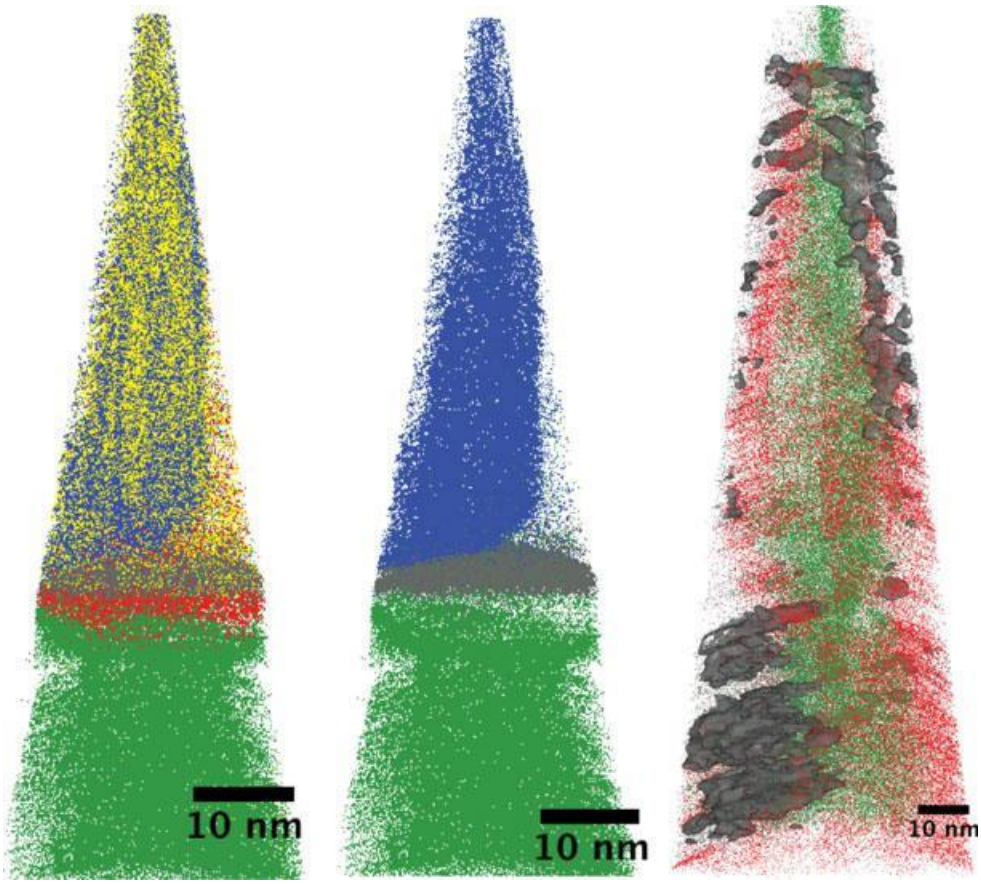

Figure 4.6 3D-tomographic atom-probe tomography reconstructions of nanodiamonds: Each dot represents a single detected atom. Atoms are color coded (carbon gray, oxygen red, cobalt blue, silicon green, gallium yellow). (a) Allende DM sample sandwiched between a flat-top silicon microtip and a cobalt cap. (b) Same as left but without gallium and oxygen atoms to better display carbon. (c) Allende DM sample coating a presharpened silicon microtip. Carbon isoconcentration surfaces are shaded gray and exhibit carbon-rich regions representing nanodiamonds, clusters of nanodiamonds, and associated disordered carbon on the surface of the microtip. The aspect ratio and scale are approximate in all reconstructions.

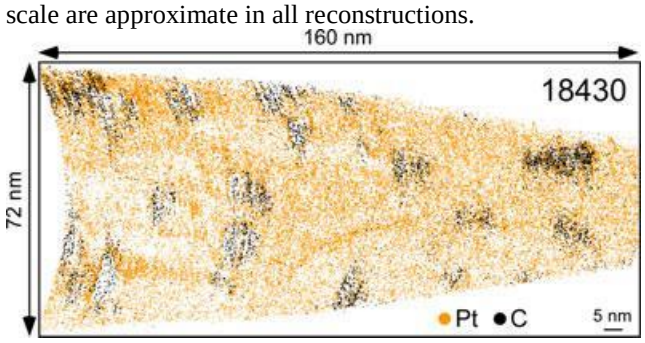

Figure 4.7 3D-tomographic reconstruction of meteoritic nanodiamonds from the Allende DM residue embedded in a platinum matrix. Each dot represents a single atom of platinum (orange) or carbon (black). Note that for clarity, only a fraction of the total platinum atoms are displayed (other atoms present within the analysis are also not shown).

4.6.2 Carbon Isotope Peak Ratios

Carbon isotope peak ratios, based on the background-corrected counts of ^{12}C and ^{13}C integrated over entire microtips, of meteoritic and synthetic nanodiamonds are displayed in Figure 4.8 and are listed in Tables 4.1 and 4.2 for the Chicago and St. Louis groups, respectively. It is important to note that it is not possible to distinguish between nanodiamonds and disordered carbon phases in our 3D tomographic reconstructions, and therefore, our results represent averages of those two phases. In both data sets, $^{12}C^{++}/^{13}C^{++}$ ratios could not be determined for some microtips, due to the small number of $^{13}C^{++}$ counts, and only $^{12}C^{+}/^{13}C^{+}$ ratios are reported. In most cases where statistically significant ratios could be reported for both doubly and singly charged carbon, the two ratios are in fairly good agreement. In six data sets, where the two ratios do not agree, however, the singly charged ion ratio is lower than the doubly charged ion ratio. This difference can be understood in terms of the $^{12}CH^{+}$ hydride contribution to $^{13}C^{+}$ noted above, which will lead to lower ratios. This is shown more clearly in a plot of $^{12}C^{+}/^{13}C^{+}$ versus $^{12}C^{++}/^{13}C^{++}$ peak ratios (Figure 4.9), where most of the data lie on a 45° line showing agreement between ratios of singly and doubly charged ions. The data points that plot below the correlation line have lower $^{12}C^{+}/^{13}C^{+}$ ratios than $^{12}C^{++}/^{13}C^{++}$ ratios, an indication that the $^{13}C^{+}$ peaks contain a contribution from hydride $^{12}CH^{+}$. The lack of data points significantly to the left of the line indicates that hydride (or other) contributions to the $^{13}C^{++}$ peaks are insignificant compared with those at $^{13}C^{+}$.

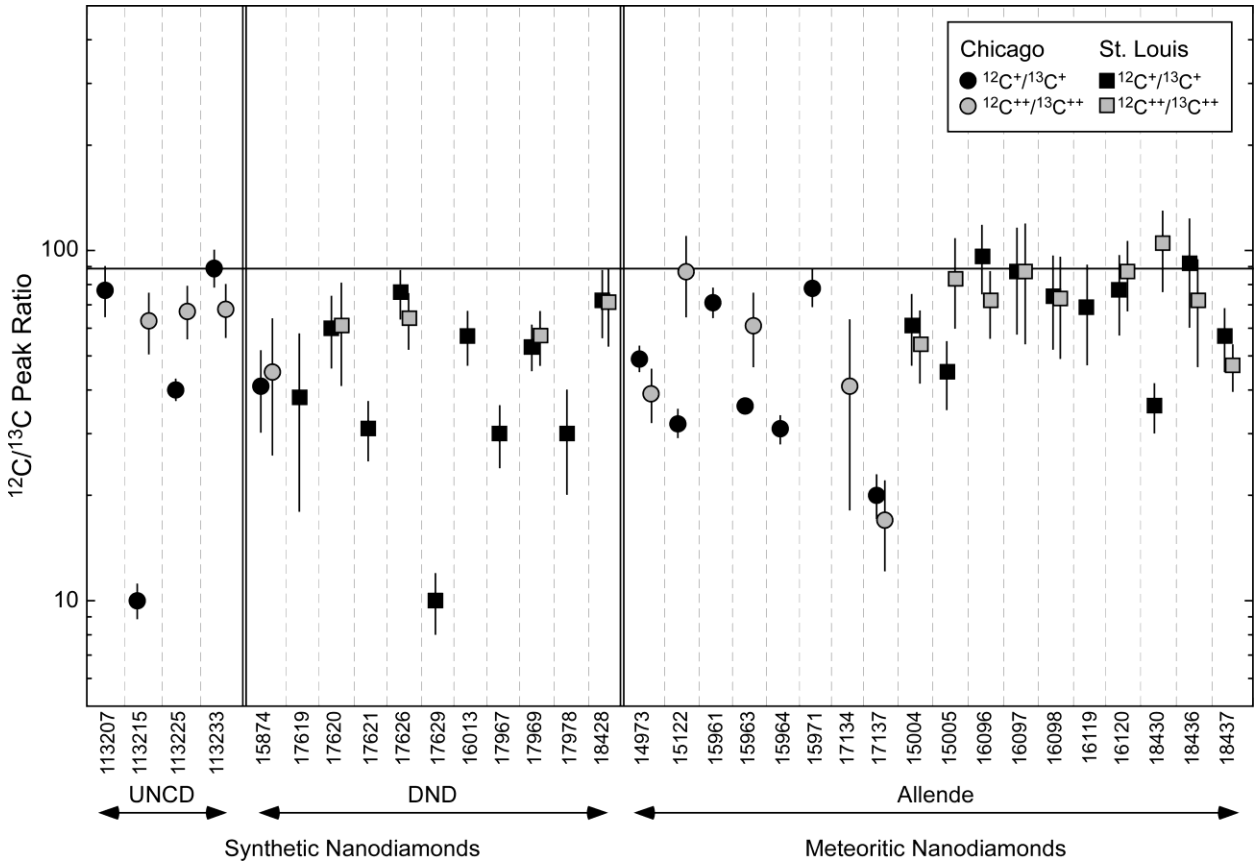

Figure 4.8 Carbon isotope peak ratios of synthetic (DND and UNCD) and meteoritic Allende nanodiamonds measured by atom-probe tomography. Data are the integrated carbon ions detected in entire microtips. Run numbers correspond to those listed in Tables 4.1 and 4.2. The horizontal line corresponds to the terrestrial $^{12}C/\ ^{13}C$ ratio of 89 (Coplen et al. 2002). Error bars are 2σ and are based on counting statistics. Large error bars reflect low total ion counts for $^{13}C^{+}$ and especially $^{13}C^{++}$.

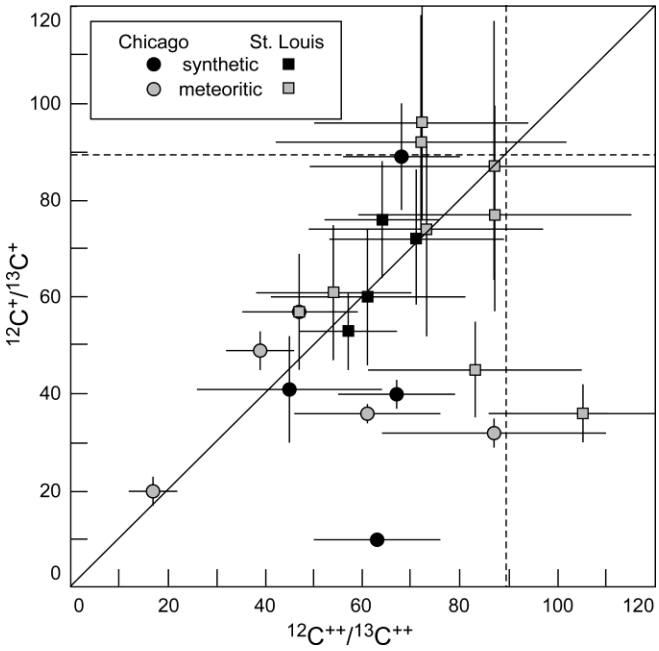

Figure 4.9 Plot of $^{12}C^{++}/^{13}C^{++}$ versus $^{12}C^{+}/^{13}C^{+}$ peak ratios for meteoritic and synthetic tips from the Chicago and St. Louis data sets. The dashed lines correspond to the terrestrial $^{12}C/^{13}C$ ratio of 89 (Coplen et al. 2002). The diagonal line indicates agreement between ratios for singly and doubly charged ions.

Comparing the data for all synthetic and meteoritic nanodiamonds (Tables 4.1 and 4. 2) shows that almost all ratios are lower than the terrestrial $^{12}C/^{13}C$ ratio of 89 (Figure 4.8 and Figure 4.9). While the meteoritic nanodiamonds could, in principle, exhibit large natural deviations from the terrestrial value, the same is not true of the synthetic nanodiamonds. This indicates that, in addition to the statistical uncertainties, there is a currently unidentified uncertainty present, an instrumental bias, which is responsible for the deviation of the measured isotope peak ratios from the expected value. One possible source for this uncertainty may be variations in sample type and, particularly, in analytical conditions. As noted earlier, the LEAP instrument underwent significant upgrades throughout the 3 yr period of study, potentially affecting the reproducibility of results. More important may be that both the Chicago and the St. Louis groups experimented with varying analytical parameters during the measurements, particularly in the early stages of this study, to determine the optimum conditions for field evaporation of these complex samples.

Future work on nanodiamond samples, prepared in the same way and analyzed under similar conditions, should minimize such variations.

Instrumental bias can also occur in the case of a multiple event, when multiple ions impact the detector during the same pulse cycle. If these ions impact close enough together in time or location, deadtime or deadspace events can occur due to the (3 ns) signal resolution time. The pile-up effect occurs if enough ions trigger pulses on the delay-lines before the signals from the first ion are processed (Gault et al. 2012). At higher evaporation rates, these effects increase as the probability of multiple events increases and will result in an underestimation of the affected ion species. During our analyses, we usually experienced low evaporation rates. When encountering interfaces between materials with different field evaporation thresholds, however, bursts of ions can be generated simultaneously from a small volume and result in uncounted impacts (De Geuser et al. 2007). Moreover, it is well known that carbon is an element that is prone to evaporation as multiple events (Andrén et al. 1980). This effect would result in preferential undercounting of the dominant isotope (^{12}C in this case), leading to $^{12}C/^{13}C$ ratios that are systematically too low, as observed in most of our data sets (Figure 4.8 and Figure 4.9).

For selected meteoritic and synthetic nanodiamond tips, we were able to determine carbon isotope peak ratios for carbon-rich ROIs with sizes similar to those of individual nanodiamonds (Figure 4.10). Determination of the appropriate size for the region of interest is not entirely straightforward. In APT, the evaporation field for carbon is significantly higher than that of any viable substrate material (Southworth and Ralph 1969; Tsong 1978). Because of this difference, the nanodiamond inclusions will resist field evaporation until the surrounding matrix has been removed, exposing a smaller radius nub on the larger tip, leading to a local magnification effect (e.g., Miller and Hetherington 1991) of the carbon inclusions in the x- and y-directions. We

therefore selected ROIs centered on the carbon-rich areas that were larger in the x- and y-directions to account for this effect. An individual nanodiamond contains approximately 2000 atoms; with a 50% detection efficiency, we expect to be able to count approximately 1000 of these. The ROIs defined here contain approximately 800–1000 atoms, substantiating this approach to taking the local magnification effect into account. The carbon isotope peak ratios determined from these ROIs have values consistent with those of the larger microtips from which they originate. Within the admittedly rather large uncertainties, we do not see any significant differences between the ratios from the meteoritic and synthetic nanodiamonds (Figure 4.10).

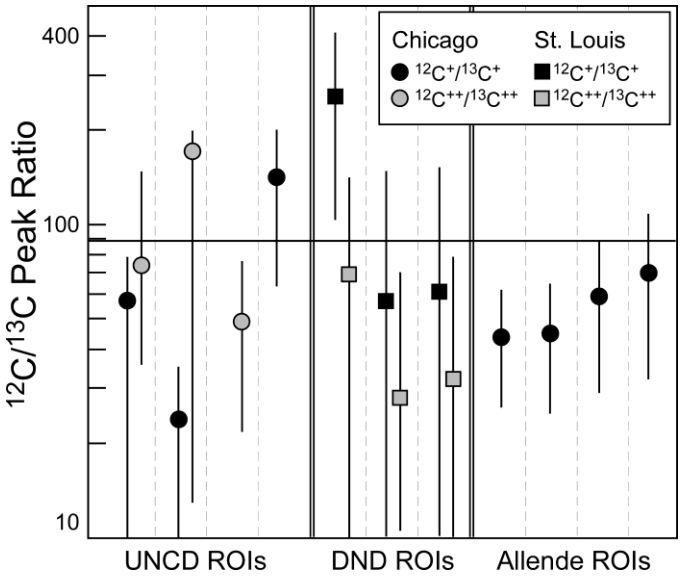

Figure 4.10 Carbon isotope peak ratios of regions of interest defined from selected synthetic (DND and UNCD) and meteoritic Allende nanodiamond tips. The horizontal line corresponds to the terrestrial $^{12}C/^{13}C$ ratio of 89 (Coplen et al. 2002). Error bars are 2σ and are based on counting statistics.

4.6.3 Silicon Isotope Peak Ratios

Finally, we also obtained silicon isotope peak ratios from the silicon microtips used in the Chicago group experiments, as the silicon surface is exposed after the nanodiamond-bearing cover has evaporated. As for carbon in the synthetic nanodiamond samples, we expect the Si isotope ratios for both singly and doubly charged ions to be consistent with the terrestrial values.

Figure 4.11 shows, however, that both $^{29}Si/^{28}Si$ and $^{30}Si/^{28}Si$ ratios show deviations from normal. The shift toward higher $^{29}Si^{+}/^{28}Si^{+}$ ratios compared with $^{29}Si^{++}/^{28}Si^{++}$ (Figure 4.11, left panel) can be best explained by an isobaric interference of $(^{28}Si^{1}H)^{+}$ on $^{29}Si^{+}$. The considerable variability in the $^{29}Si^{+}/^{28}Si^{+}$ ratios probably reflects variability in hydride formation. Isobaric interferences due to hydrides should affect ^{29}Si more than ^{30}Si, because ^{29}Si has a much lower abundance than ^{28}Si. The higher $^{30}Si^{++}/^{28}Si^{++}$ ratios compared with $^{30}Si^{+}/^{28}Si^{+}$ ratios (Figure 4.11, right panel) are more difficult to understand, but may be due to a variable isobaric interference of CH_3^{+} with $^{30}Si^{++}$, inflating the $^{30}Si^{++}$ peak.

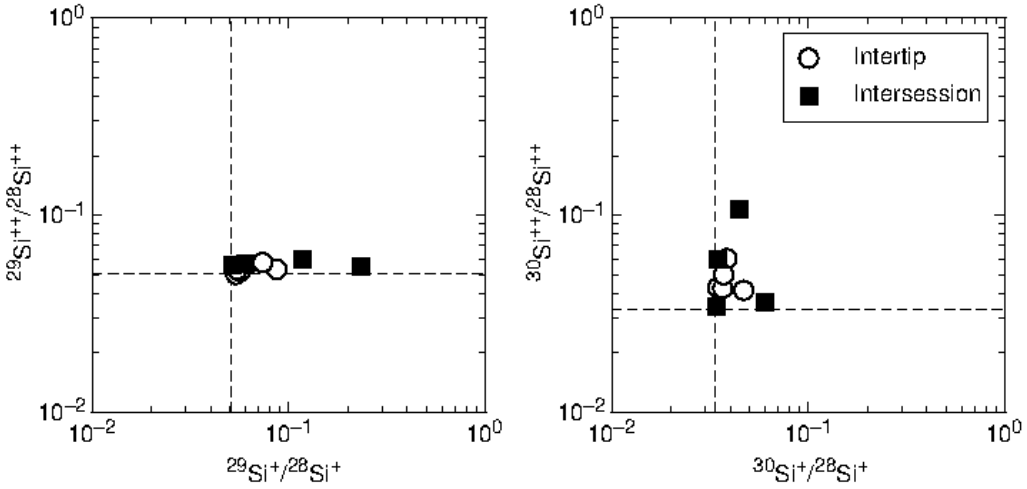

Figure 4.11 Background-corrected silicon isotope peak ratios from silicon microtips analyzed with the LEAP tomography within the same session (intertip) and in different sessions (intersession). 2σ error bars are based on counting statistics and are smaller than the symbol sizes. The dashed lines represent terrestrial (normal) isotope ratios from (Coplen et al. 2002).

4.7 Conclusions and Outlook

We have developed sample preparation methods and optimized analytical conditions for stable APT analyses of nanodiamonds, such that carbon isotopic peak ratios can be determined on a routine basis. Additional work is, however, required to understand completely the analytical biases affecting these measurements. We are currently preparing nanodiamond standards with

different isotopic compositions, which will allow us to compare the ion-peak ratios with the expected isotope ratios for different compositions. In addition to allowing us to confirm (or not) a linear relationship between the measured and true ratios, analyzing standards with different isotopic compositions can provide information on the relative importance of various artifacts or biases present in our data. For example, the analysis of a nanodiamond standard consisting only of ^{12}C can provide constraints on the importance of the hydride contribution at mass 13. Understanding the variations that we observe in our data sets for synthetic nanodiamond samples is an important prerequisite to understanding and interpreting data for meteoritic nanodiamonds.

Two additional intrinsic problems with analyzing individual nanodiamonds are as follows: (1) the limited number of atoms available, leading to relatively large uncertainties; and (2) the presence of a second carbon allotrope (disordered carbon) in the diamond-bearing residues. Despite these challenges, we anticipate that APT will prove to be a powerful technique for analyzing the elemental and isotopic compositions of extraterrestrial nanoparticles, and that useful cosmochemical data for meteoritic nanodiamonds can be obtained.

Acknowledgments—We thank R. S. Lewis for providing the Allende nanodiamond sample, K. Knight for the detonation diamonds, J. Pearson for sputter coating, and D. Schreiber for helpful discussions. We are grateful to I. Lyon, L. Nittler, and J. Matsuda for careful and constructive reviews, which significantly improved this article. This study is supported by NASA grants NNX09AC28G and NNX13AF53G (C.F.), NNX09AG39G (A.M.D. and T.S.), NNX11AG77G (P.R.H.), and by the Tawani Foundation. Atomic layer deposition, UNCD film growth, and some of the FIB microscope work were performed at Argonne National Laboratory. Assistance with UNCD film growth and APT analysis was supported by the US Department of Energy, Office of Science Materials Sciences and Engineering Division, under Contract No. DE-AC02-

06CH11357 (M.R.S., M.J.P, O.A.). The NUCAPT LEAP was purchased and upgraded with funding from NSF-MRI (DMR-0420532) and ONR-DURIP (N00014-0400798, N00014-0610539, N00014-0910781) grants. This study was also supported by the National Science Foundation's MRSEC program (DMR-1121262) and made use of its Shared Facilities at the Materials Research Center of Northwestern University. We also gratefully acknowledge the Initiative for Sustainability and Energy at Northwestern (ISEN) for grants to upgrade the capabilities of NUCAPT.

Editorial Handling—Dr. Ian Lyon

4.8 References

Andrén H. O., Henjered A., and Nordén H. 1980. Composition of MC precipitates in a titanium stabilized austenitic stainless steel. *Journal of Materials Science* 15:2365–2368.

Atreya S. K., Mahaffy P. R., Niemann H. B., Wong M. H., and Owen T. C. 2003. Composition and origin of the atmosphere of Jupiter—an update, and implications for the extrasolar giant planets. *Recent Advances on the Atmosphere of Outer Planets and Titan* 51:105–112.

Auciello O., and Sumant A. V. 2010. Status review of the science and technology of ultrananocrystalline diamond (UNCD^{TM}) films and application to multifunctional devices. *Diamond and Related Materials* 19:699–718.

Clayton D. D., and Nittler L. R. 2004. Astrophysics with Presolar Stardust. *Annual Review of Astronomy and Astrophysics* 42:39–78.

Coplen T. B. et al. 2002. Isotope-abundance variations of selected elements (IUPAC Technical Report). *Pure and Applied Chemistry* 74:1987–2017.

Dai Z. R., Bradley J. P., Joswiak D. J., Brownlee D. E., Hill H. G. M., and Genge M. J. 2002. Possible in situ formation of meteoritic nanodiamonds in the early Solar System. *Nature* 418:157–159.

Daulton T. L., Eisenhour D. D., Bernatowicz T. J., Lewis R. S., and Buseck P. R. 1996. Genesis of presolar diamonds: Comparative high-resolution transmission electron microscopy study of meteoritic and terrestrial nano-diamonds. *Geochimica et Cosmochimica Acta* 60:4853–4872.

Daulton T. L. 2006. 2 - Extraterrestrial Nanodiamonds in the Cosmos. In *Ultrananocrystalline Diamond*, edited by Shenderova O. A., and Gruen D. M. Norwich, New York: William Andrew Publishing. pp. 23–78.

Davis A. M. 2011. Stardust in meteorites. *Proceedings of the National Academy of Sciences* 108:19142–19146.

De Geuser F., Gault B., Bostel A., and Vurpillot F. 2007. Correlated field evaporation as seen by atom probe tomography. *Surface Science* 601:536–543.

Elam J. W., Libera J. A., Pellin M. J., Zinovev A. V., Greene J. P., and Nolen J. A. 2006. Atomic layer deposition of W on nanoporous carbon aerogels. *Applied Physics Letters* 89:053124 3 pp.

Gault B., Moody M. P., Cairney J. M., and Ringer S. P. 2012. *Atom probe microscopy*, New York: Springer. pp. 45–47.

Greiner N. R., Phillips D. S., Johnson J. D., and Volk F. 1988. Diamonds in detonation soot. *Nature* 333:440–442.

Heck P. R. et al. 2010. Atom-probe tomographic analyses of presolar silicon carbide grains and meteoritic nanodiamonds—First results on silicon carbide. *41st Lunar and Planetary Science Conference*. Abstract #2112.

Heck P. R. et al. 2011a. Atom-probe tomographic analyses of meteoritic nanodiamond residue from Allende. *42nd Lunar and Planetary Science Conference*. Abstract #2070.

Heck P. R. et al. 2011b. Atom-probe tomographic analyses of Allende and synthetic nanodiamonds. Lunar and Planetary Institute. Contribution 9096.

Heck P. R. et al. 2011c. Atom-probe tomography of meteoritic and synthetic nanodiamonds (abstract). *Meteoritics and Planetary Science* 46:A90.

Heck P. R. et al. 2012. Atom-probe tomographic analysis: Towards carbon isotope ratios in individual nanodiamonds. *43rd Lunar and Planetary Science Conference*. Abstract #1790.

Hynes K. M., and Gyngard F. 2009. The presolar grain database: http://presolar.wustl.edu/~pgd. *40th Lunar and Planetary Science Conference*. Abstract #1198.

Isheim D. et al. 2013. Combining Atom-Probe Tomography and Focused-Ion Beam Microscopy to Study Individual Presolar Meteoritic Nanodiamond Particles. *Microscopy and Microanalysis* 19(Suppl 2):974–975.

Kelly T. F., and Miller M. K. 2007. Invited Review Article: Atom probe tomography. *Review of Scientific Instruments* 78:31101 (20 pp).

Kelly T. F., and Larson D. J. 2012. Atom Probe Tomography 2012. *Annual Review of Materials Research* 42:1–31.

Kingham D. R. 1982. The post-ionization of field evaporated ions: A theoretical explanation of multiple charge states. *Surface Science* 116:273–301.

Kunicki T. C., Beerman D., Geiser B. G., Oltman E., O'Neill R. W., and Larson D. J. 2006. Atom probe data reconstruction, visualization and analysis with the Imago Visualization and Analysis System (IVAS). pp. 535–536.

Larson D. J., Foord D. T., Petford-Long A. K., Liew H., Blamire M. G., Cerezo A., and Smith G. D. W. 1999. Field-ion specimen preparation using focused ion-beam milling. *Ultramicroscopy* 79:287–293.

Lawrence D., Alvis R., and Olson D. 2008. Specimen Preparation for Cross-Section Atom Probe Analysis. *Microscopy and Microanalysis* 14:1004–1005.

Lewis R. S., Anders E., Wright I. P., Norris S. J., and Pillinger C. T. 1983. Isotopically anomalous nitrogen in primitive meteorites. *Nature* 305:767–771.

Lewis R. S., Ming T., Wacker J. F., Anders E., and Steel E. 1987. Interstellar diamonds in meteorites. *Nature* 326:160–162.

Lewis R. S., Anders E., and Draine B. T. 1989. Properties, detectability and origin of interstellar diamonds in meteorites. *Nature* 339:117–121.

Lewis R. S., Huss G. R., and Lugmair G. 1991. Finally, Ba & Sr accompanying Xe-HL in diamonds from Allende. *22nd Lunar and Planetary Science Conference*. pp. 807–808

Lewis J. B. et al. 2012. Meteoritic nanodiamond analysis by atom-probe tomography. *43rd Lunar and Planetary Institute*. Abstract #2192.

Maas R., Loss R. D., Rosman K. J. R., De Laeter J. R., Lewis R. S., Huss G. R., and Lugmair G. W. 2001. Isotope anomalies in tellurium and palladium from Allende nanodiamonds. *Meteoritics & Planetary Science* 36:849–858.

Marquis E. A., and Hyde J. M. 2010. Applications of atom-probe tomography to the characterisation of solute behaviours. *Materials Science and Engineering R* 69:37–62.

Marty B., Chaussidon M., Wiens R. C., Jurewicz A. J. G., and Burnett D. S. 2011. A ^{15}N-poor isotopic composition for the solar system as shown by Genesis solar wind samples. *Science* 332:1533–1536.

Miller M. K., and Hetherington M. G. 1991. Local magnification effects in the atom probe. *Surface Science* 246:442–449.

Müller E. W., Panitz J. A., and McLane S. B. 1968. The Atom-Probe Field Ion Microscope. *Review of Scientific Instruments* 39:83–86.

Owen T., Mahaffy P. R., Niemann H. B., Atreya S., and Wong M. 2001. Protosolar nitrogen. *The Astrophysical Journal* 553:L77–L79.

Richter S., Ott U., and Begemann F. 1998. Tellurium in pre-solar diamonds as an indicator for rapid separation of supernova ejecta. *Nature* 391:261–263.

Russell S. S., Arden J. W., and Pillinger C. T. 1996. A carbon and nitrogen isotope study of diamond from primitive chondrites. *Meteoritics & Planetary Science* 31:343–355.

Scheinfein M. R., and Seidman D. N. 1993. Time aberrations of uniform fields: An improved reflectron mass spectrometer for an atom-probe field-ion microscope. *Review of Scientific Instruments* 64:3126–3131.

Seidman D. N. 2007. Three-dimensional atom-probe tomography: Advances and applications. *Annual Review of Materials Research* 37:127–158.

Seidman D. N., and Stiller K. 2009. An atom-probe tomography primer. *MRS Bulletin* 34:717–724.

Southworth H. N., and Ralph B. 1969. Image formation from alloys in the field-ion microscope. *Journal of Microscopy* 90:167–197.

Stadermann F. J. et al. 2010. Atom-probe tomographic study of the three-dimensional structure of presolar silicon carbide and nanodiamonds at atomic resolution. *41st Lunar and Planetary Science Conference*. Abstract #2134.

Stadermann F. J. et al. 2011. Atom-probe tomographic characterization of meteoritic nanodiamonds and presolar SiC. *42nd Lunar and Planetary Science Conference*. Abstract #1595.

Stroud R. M., Chisholm M. F., Heck P. R., Alexander C. M. O'D., and Nittler L. R. 2011. Supernova shock-wave-induced co-formation of glassy carbon and nanodiamond. *The Astrophysical Journal* 738:L27.

Swart P. K., Grady M. M., Pillinger C. T., Lewis R. S., and Anders E. 1983. Interstellar carbon in meteorites. *Science* 220:406–410.

Thompson K., Larson D. J., and Ulfig R. M. 2005. Pre-sharpened and flat-top microtip coupons: A quantitative comparison for atom-probe analysis studies. *Microscopy and Microanalysis* 11:882–883.

Tsong T. T. 1978. Measurement of the field evaporation rate of several transition metals. *Journal of Physics F: Metal Physics* 8:1349–1352.

Virag A., Zinner E., Lewis R. S., and Tang M. 1989. Isotopic compositions of H, C, and N in Cδ diamonds from the Allende and Murray carbonaceous chondrites. *20th Lunar and Planetary Science Conference*. Abstract #1158.

Zinner E. 2007. Presolar Grains. In *Meteorites, comets, and planets,* edited by Holland H. D. and Turekian K. K. Treatise on Geochemistry, 2nd ed., vol. 1. Oxford: Elsevier. pp. 1–33.

Chapter 5: Correction of Dead Time Effects in Laser-induced Desorption Time-of-flight Mass Spectrometry: Applications in Atom-probe Tomography

This chapter was published in the *International Journal of Mass Spectrometry* in collaboration with Thomas Stephan, Philipp R. Heck, and Dieter Isheim (Stephan et al. 2015). The author's personal contribution to this work was sample preparation, experimental analyses, and initial data reduction of three of five nanodiamond-containing data sets used in the paper: DND 17620, DND 17626, and DND 17969, as well as collaborating on the editing of the drafts and revisions of the paper.

5.1 Introduction

Any detector is able to reliably distinguish between different events only if they are separated from each other sufficiently either in time or in space. The duration a detector needs to recover after a counting event in order to be able to detect a second event following shortly afterwards is described as the dead time of the detector. It should be clarified that detector in this context describes the entire detection system typically consisting of several components such as the actual detector, typically a photomultiplier or microchannel plate, a discriminator that accepts signals as counting events or rejects them as electronic noise, and a time digitizer, which converts time intervals into digital representations.

In favorable cases, statistical approaches can be used to correct for dead time effects in order to calculate the signal intensities that an ideal detector with no dead time would have delivered.

Dead time correction in time-of-flight mass spectrometry (TOF-MS) is complicated by the fact that signal intensities vary on very short time scales. However, such highly fluctuating signals can often be corrected for dead time effects as described in the literature (Stephan et al. 1994). Correction is possible since each measurement usually averages over a large number of ionization events that, except for statistical fluctuations, are uniform in ionization yield. This is typically fulfilled, e.g., in time-of-flight secondary ion mass spectrometry (TOF-SIMS) as long as the measurement is restricted to a homogeneous sample or sample region and neither sample properties nor primary ion beam intensity vary significantly during the analysis. Here, dead time correction works well and is now standard protocol during quantitative data evaluation (Holzlechner et al. 2013; Keenan et al. 2008; Stephan 2001). An interlaboratory study involving 21 TOF-SIMS instruments has shown that this dead time correction is generally applicable and robust (Lee et al. 2012).

However, for some TOF-MS techniques, ionization yield is not constant and the dead time correction described by Stephan et al. (1994) could not be applied. This is especially the case in techniques where laser-induced desorption is used, e.g., in laser desorption resonance ionization mass spectrometry (RIMS). As described by Savina et al. (2003), the desorption process is nonlinear in laser pulse energy, and moderate fluctuations lead to large variations in the desorbed particle flux. Desorption lasers are therefore often operated in a very low power regime, where particles are desorbed only occasionally, in order to avoid relatively powerful laser pulses that would release many particles in a single shot (Savina et al. 2003). Very low count rates are the consequence, and measurement times have to be increased drastically to achieve sufficient counting statistics, if high precision is required.

This is also the case in atom-probe tomography (APT), which combines field evaporation triggered by pulsing from a focused ultraviolet laser in a constant electric field with TOF-MS (Heck et al. 2014; Kelly and Larson 2012). Using APT in order to measure isotope ratios in nanoparticles would be highly desirable in particular for cosmochemical applications, e.g., to study the origin of meteoritic nanodiamonds (Heck et al. 2014). However, such data so far suffer from instrumental biases (Heck et al. 2014) among which dead time effects seem to play a major role. Therefore, most APT applications until now focused on the elemental composition of samples, where high accuracy is less crucial, as it was previously impossible to get useful isotope ratios.

However, the importance of multi-hit events causing dead time effects, also referred to as pile-up or detector saturation, for interpretation of mass spectra in APT has been recognized in the field. It has been identified already in 1978 that atom-probe data do not directly give the true composition of a sample and that Poisson statistics could be applied for correction (Tsong et al. 1978). In 1984, Cerezo et al. (1984) developed a statistical correction without making any prior assumptions as to the distribution of ions per pulse. In 1988, Menand et al. (1988) made a similar approach but made use of double counting events. More recently, methods such as a contingency table approach have been employed to study correlations in field evaporation and to improve quantification of measured compositions (Saxey 2011).

Here, we present a dead time correction of APT isotope data using Poisson statistics but avoiding some of the deficiencies from previous studies and apply this correction to carbon and silicon data (Heck et al. 2014). By using correlated counting events from isotopes of the same element, the method presented here allows correction of APT data from ion species that vary significantly

in their evaporation behavior with some elements being more prone to evaporation in multiples than others.

5.2 Counting Statistics

In the following, we will focus on the simple case, where for one laser pulse, only one ion per species can be detected, and different species are separated by a sufficient time gap so that they do not interfere with each other. From Equation (8) in Stephan et al. (1994),

$$ {}^{a}E = -N \cdot \ln\left(1 - \frac{a}{N}\right) \text{ and } {}^{b}E = -N \cdot \ln\left(1 - \frac{b}{N}\right). \tag{5.1} $$

Here, ${}^{a}E$ and ${}^{b}E$ describe the corrected peak integrals or *true intensities* for two isotopes of an element *E*, whereas *a* and *b* represent the *measured intensities* for these isotopes, and *N* is the number of ionization events. It should be clarified here that, in general, the number of ionization events is smaller than the number of pulses from the desorption laser, if we assume that many laser pulses do not have the potential to cause ionization of the element of interest. This is different from TOF-SIMS, where each primary ion pulse is considered an ionization event, and *N* is a known quantity. For laser-induced desorption, *N* is unknown and may depend on the ion species. *N* is not the number of pulses in which ionization occurs; rather, it can be best described as the number of laser pulses where the conditions for formation of a given ion species are met. However, we can assume that *N* is identical for different isotopes of the same element and that isotope effects on desorption yields can be neglected.

5.2.1 The Number of Ionization Events

If we now assume that detection of both isotope species is independent, the probability of detecting a correlated event, where both isotopes are detected in a single ionization event, is

$$ \frac{c}{N} = \frac{a}{N} \cdot \frac{b}{N}. \tag{5.2} $$

Here, *c* is the number of laser pulses for which both isotopes are detected. *N* can therefore be calculated as

$$N = \frac{a \cdot b}{c}. \tag{5.3}$$

For the statistical error Δ*N*, one has to take into account that *a* and *b* are not independent from *c*. We therefore introduce

$$a' = a - c \text{ and } b' = b - c \tag{5.4}$$

as independent variables, since they are the number of counting events for both isotopes not including the number of correlated events given by *c*. Equation 5.3 now becomes

$$N = \frac{(a'+c)(b'+c)}{c}. \tag{5.5}$$

The statistical error ΔN now follows from the error propagation theorem as

$$\Delta N = \sqrt{\left(\frac{b'+c}{c}\Delta a'\right)^2 + \left(\frac{a'+c}{c}\Delta b'\right)^2 + \left(\left(1 - \frac{a' \cdot b'}{c^2}\right)\Delta c\right)^2}. \tag{5.6}$$

Using the original variables *a* and *b*, this can also be written as

$$\Delta N = \sqrt{\left(\frac{b}{c}\Delta a'\right)^2 + \left(\frac{a}{c}\Delta b'\right)^2 + \left(\frac{a+b-N}{c}\Delta c\right)^2}. \tag{5.7}$$

5.2.2 Peak Integrals

Using Equation 5.3, the peak integral ${}^{a}E$ from Equation 5.1 can be calculated as

$${}^{a}E = -\frac{a \cdot b}{c} \cdot \ln\left(1 - \frac{c}{b}\right). \tag{5.8}$$

For calculation of the statistical errors, independent variables are needed

$${}^{a}E = -\frac{(a'+c)(b'+c)}{c} \cdot \ln\left(\frac{b\prime}{b\prime+c}\right). \tag{5.9}$$

Then, the statistical error becomes

$$\Delta\,{}^{a}E =$$

$$\sqrt{\left[\left(\frac{b\prime+c}{c}\cdot\ln\left(\frac{b\prime}{b\prime+c}\right)\right)\Delta a'\right]^2+\left[\left(\frac{a\prime+c}{b\prime}+\frac{a\prime+c}{c}\ln\left(\frac{b\prime}{b\prime+c}\right)\right)\Delta b'\right]^2+\left[\left(\frac{a\prime+c}{b}+\left(\frac{a\prime\cdot b\prime}{c^2}-1\right)\ln\left(\frac{b\prime}{b\prime+c}\right)\right)\Delta c\right]^2}. \tag{5.10}$$

Using the original variables *a* and *b*, this can also be written as

$$\Delta\,{}^{a}E =$$

$$\sqrt{\left[\left(\frac{b}{c}\cdot\ln\left(1-\frac{c}{b}\right)\right)\Delta a'\right]^2+\left[\left(\frac{a}{b-c}+\frac{a}{c}\ln\left(1-\frac{c}{b}\right)\right)\Delta b'\right]^2+\left[\left(\frac{a}{c}+\left(\frac{a\cdot b}{c^2}-\frac{a+b}{c}\right)\ln\left(1-\frac{c}{b}\right)\right)\Delta c\right]^2} \tag{5.11}$$

which can be further simplified to

$$\Delta\,{}^{a}E=\sqrt{\left[\frac{{}^{a}E}{a}\Delta a'\right]^2+\left[\left(\frac{a}{b-c}-\frac{{}^{a}E}{b}\right)\Delta b'\right]^2+\left[\left(\frac{a}{c}+\frac{{}^{a}E}{a}+\frac{{}^{a}E}{b}-\frac{{}^{a}E}{c}\right)\Delta c\right]^2}. \tag{5.12}$$

5.2.3 Isotope Ratios

In practical cases, we want to calculate isotope ratios from the measured peak integrals

$$\frac{{}^{a}E}{{}^{b}E}=\frac{\ln\left(1-\frac{c}{b}\right)}{\ln\left(1-\frac{c}{a}\right)}=\frac{\ln\left(\frac{b\prime}{b\prime+c}\right)}{\ln\left(\frac{a\prime}{a\prime+c}\right)}. \tag{5.13}$$

The statistical error can be expressed as

$$\Delta\left(\frac{{}^{a}E}{{}^{b}E}\right)=\sqrt{\left[\frac{c\cdot\ln\left(\frac{b\prime}{b\prime+c}\right)}{a\prime(a\prime+c)\left(\ln\left(\frac{a\prime}{a\prime+c}\right)\right)^2}\Delta a'\right]^2+\left[\frac{c}{b\prime(b\prime+c)\left(\ln\left(\frac{a\prime}{a\prime+c}\right)\right)}\Delta b'\right]^2+\left[\frac{\frac{\ln\left(\frac{b\prime}{b\prime+c}\right)}{a\prime+c}-\frac{\ln\left(\frac{a\prime}{a\prime+c}\right)}{b\prime+c}}{\left(\ln\left(\frac{a\prime}{a\prime+c}\right)\right)^2}\Delta c\right]^2}. \tag{5.14}$$

Using the original variables *a* and *b*, this can also be written as

$$\Delta\left(\frac{{}^{a}E}{{}^{b}E}\right)=\sqrt{\left[\frac{c\cdot\ln\left(1-\frac{c}{b}\right)}{a(a-c)\left(\ln\left(1-\frac{c}{a}\right)\right)^2}\Delta a'\right]^2+\left[\frac{c}{b(b-c)\cdot\ln\left(1-\frac{c}{a}\right)}\Delta b'\right]^2+\left[\frac{\frac{\ln\left(1-\frac{c}{b}\right)}{a}-\frac{\ln\left(1-\frac{c}{a}\right)}{b}}{\left(\ln\left(1-\frac{c}{a}\right)\right)^2}\Delta c\right]^2}, \tag{5.15}$$

which can be further simplified to

$$\Delta\left(\frac{{}^{a}E}{{}^{b}E}\right) = \sqrt{\left[\frac{{}^{a}E\cdot b}{{}^{b}E^{2}}\cdot\frac{\Delta a\prime}{a\prime}\right]^{2} + \left[\frac{a}{{}^{b}E}\cdot\frac{\Delta b\prime}{b\prime}\right]^{2} + \left[\frac{{}^{a}E\cdot b - a\cdot {}^{b}E}{{}^{b}E^{2}}\cdot\frac{\Delta c}{c}\right]^{2}}. \quad (5.16)$$

5.3 Experimental Results and Discussion

In order to evaluate the feasibility of the dead time correction according to Equations 5.13 and 5.16 for APT data, we applied the correction to carbon data obtained from synthetic nanodiamonds and to silicon data from silicon microtips (Heck et al. 2014). In that study, $^{12}C/^{13}C$ ratios as well as $^{28}Si/^{29}Si$ and $^{28}Si/^{30}Si$ ratios that are apparently lower than expected were measured (Heck et al. 2014). This was in part attributed to dead time effects, which leads to an undercount of the major isotopes ^{12}C and ^{28}Si compared to the less abundant isotopes ^{13}C, ^{29}Si, and ^{30}Si (Heck et al. 2014). In addition to undercounting major isotopes, unresolved interference from hydride ions $^{12}CH^{+}$, $^{28}SiH^{+}$, and $^{29}SiH^{+}$ could lead to overestimated $^{13}C^{+}$, $^{29}Si^{+}$, and $^{30}Si^{+}$ signals. However, besides singly charged ions, carbon and silicon both also form doubly charged ions in APT. Since hydrides are not expected to form doubly charged ions and no major interferences are expected at the respective mass-to-charge-state ratios, using doubly charged ions can be advantageous for measuring carbon and silicon isotope ratios.

As mentioned above, we assumed for our dead time correction the simple case, where for one laser pulse, only one ion per species can be detected, and different species are separated by a sufficient time gap so that they do not interfere with each other. Modern APT instruments, however, allow for the detection of more than one ion with a given mass-to-charge-state ratio generated in a single laser pulse, though with a decreased detection efficiency for consecutive ions of the same species. In other words, the detector is not dead after being hit by an ion but has a decreased sensitivity for a certain amount of time. Since this reduced sensitivity is difficult to

account for quantitatively, we counted multiple detections of one ion species only as single events. This required evaluation of single shot data and not just of spectra accumulated from a large number of laser pulses. Although disregarding ion detections might look like throwing away useful data, for the calculation of isotope ratios, we currently cannot make use of any additional information they might carry. Their detection can, however, still deliver valuable information about the three-dimensional distribution of the isotopes, since APT not only provides mass-to-charge ratios but also spatial information (Kelly and Larson 2012).

In some cases, data evaluation suffers from long tails of the respective mass peaks that even affects peaks at the following nominal mass. Sample preparation, material properties such as thermal conductivity, analytical conditions (laser energy and focus, pulse rate, and specimen temperature) can be optimized to minimize the formation of peak tails. For proper dead time correction, it is important to have a mass resolution sufficient to completely separate neighboring mass-to-charge-state ratios. While it is often sufficient to separate mass peaks by fitting them to some idealized shape, such peak deconvolution cannot be executed here since it could not be applied to single shot data. In cases where hydride interference cannot be excluded, the formation of doubly charged ions becomes very important for isotope measurements. Instrument parameters such as laser pulse energy and electric fields can be optimized in order to facilitate the formation of doubly charged ions (Heck et al. 2014; Kingham 1982).

5.3.1 Carbon

Synthetic detonation nanodiamonds (DNDs) and ultrananocrystalline diamonds (UNCDs) have been used as standards in an APT study of nanodiamonds from the Allende meteorite (Heck et al. 2014). These synthetic standards are expected to have a $^{12}C/^{13}C$ ratio close to the terrestrial value of 89 and should be suited to evaluate the dead time correction described above.

From the previous study (Heck et al. 2014), five measurements showed sufficient mass resolution, short peak tails, as well as sufficient counts of doubly charged ions to allow for dead time correction of both singly and doubly charged carbon ion counts. Dead time corrected and uncorrected carbon isotope ratios for these measurements are shown in Figure 5.1. In addition, Table 5.1 shows the number of laser pulses as well as the number of ionization events calculated from the data. As expected, the number of ionization events is smaller than the number of laser pulses: fewer than 0.35% of the laser pulses were above the ionization threshold for singly charged carbon ions, and fewer than 0.015% of the pulses were above the ionization threshold for doubly charged carbon ions. This is certainly in part due to the fact that the nanodiamonds were dispersed heterogeneously in the samples, but also reflects the high evaporation field requirements for carbon and instabilities of the field evaporation process that is thermally activated with the laser heating the sample surface to near the evaporation threshold (Bunton et al. 2007; Vurpillot et al. 2009).

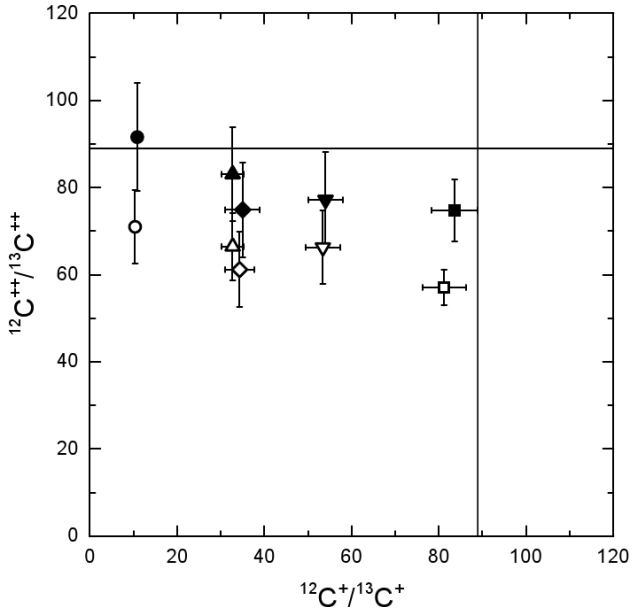

Figure 5.1 Carbon isotope ratios calculated from measurements of singly and doubly charged carbon ions from synthetic nanodiamonds. Open symbols represent data from accumulated spectra not corrected for dead time effects. Data shown as solid symbols are dead time corrected. Error bars are 1σ statistical errors. Solid lines represent the expected $^{12}C/^{13}C$ ratio of 89.

Table 5.1 Carbon isotopes measured by APT in synthetic nanodiamonds as singly and doubly charged ions.[a]

Sample	UNCD 113215	DND 17620	DND 17626	DND 17969	UNCD 20026
Number of laser pulses	2.44×10^{8}	4.93×10^{8}	3.65×10^{9}	8.71×10^{8}	1.25×10^{9}
$N(^{12}C^{+}/^{13}C^{+})$	$(9.0\pm0.8)\times10^{4}$	$(1.7\pm3.8)\times10^{6}$	$(8.8\pm4.1)\times10^{5}$	$(1.1\pm0.5)\times10^{5}$	$(1.9\pm0.4)\times10^{6}$
$^{12}C^{+}/^{13}C^{+}$ (raw data)	10.3±0.4	33±3	53±4	34±3	81±5
$^{12}C^{+}/^{13}C^{+}$ (corrected)	10.8±0.4	33±3	54±4	35±4	84±5
$N(^{12}C^{++}/^{13}C^{++})$	$(1.4\pm0.2)\times10^{4}$	$(1.7\pm0.2)\times10^{4}$	$(2.8\pm0.5)\times10^{4}$	$(1.4\pm0.2)\times10^{4}$	$(1.8\pm0.1)\times10^{5}$
$^{12}C^{++}/^{13}C^{++}$ (raw data)	71±8	67±8	66±8	61±9	57±4
$^{12}C^{++}/^{13}C^{++}$ (corrected)	92±12	83±11	77±11	75±11	75±7

[a] The number of ionization events *N* calculated according to Equations 5.3 and 5.7 is given for singly and doubly charged ions. The number of laser pulses is included for comparison. Ion ratios are calculated from raw data with no deadtime correction and after deadtime correction. Errors are 1σ statistical errors.

Uncorrected peak ratios given in Table 5.1 in some cases differ significantly from values given by Heck et al. (2014). This is due to reevaluation of the data using tighter peak interval definitions than in the previous study, trying to exclude some of the long peak tails that would make dead time correction impossible. However, variations in such interval definitions could not bring uncorrected peak ratios into agreement with expected isotope ratios.

After dead time correction, however, isotope ratios calculated from doubly charged ions are all within 2σ of the expected terrestrial ratio, whereas singly charged carbon ions yield $^{12}C/^{13}C$ ratios that are too low. This is probably due to interference from $^{12}C^{1}H^{+}$, which cannot be resolved from $^{13}C^{+}$. Hydride abundances seem to show huge variations between measurements leading to highly variable ratios of peaks measured at 12 and 13 u.

5.3.2 Silicon

Since some of the experiments described above were performed on nanodiamonds applied on silicon microtips (SMTs), we used data from these experiments to calculate silicon isotope ratios (Heck et al. 2014). As for carbon, we expected isotope ratios for both singly and doubly charged silicon ions to be consistent with terrestrial values ($^{28}Si/^{29}Si = 19.7$, $^{28}Si/^{30}Si = 29.9$, and $^{29}Si/^{30}Si = 1.52$).

As for carbon, the measurements of silicon isotopes could suffer from unresolvable mass interferences. For $^{29}Si^{+}$ and $^{30}Si^{+}$, we expect interferences from $^{28}Si^{1}H^{+}$ and $^{29}Si^{1}H^{+}$, respectively. Since doubly charged ions appear at half nominal mass, one has to consider interferences for silicon isotopes with even mass numbers. Possible interferences for $^{28}Si^{++}$ at mass 14 u are $^{12}C^{1}H_{2}^{+}$ and $^{14}N^{+}$, while $^{12}C^{1}H_{3}^{+}$ and $^{14}N^{1}H^{+}$ could interfere with $^{30}Si^{++}$ at mass 15 u. However, since measurements were performed on silicon microtips, trace abundances of hydrocarbons and

nitrogen should be less crucial, and we only expect major interferences from hydrides that should only affect singly charged silicon ions.

Figure 5.2 shows the deviation of the uncorrected and dead time corrected doubly charged silicon ion ratios $^{29}Si^{++}/^{28}Si^{++}$ and $^{30}Si^{++}/^{28}Si^{++}$ from reference isotope ratios in per mill using the δ notation:

$$\delta\left(\frac{a_E}{b_E}\right) = \left(\frac{\left(\frac{a_E}{b_E}\right)_{measured}}{\left(\frac{a_E}{b_E}\right)_{reference}} - 1\right) \cdot 1000‰. \tag{5.17}$$

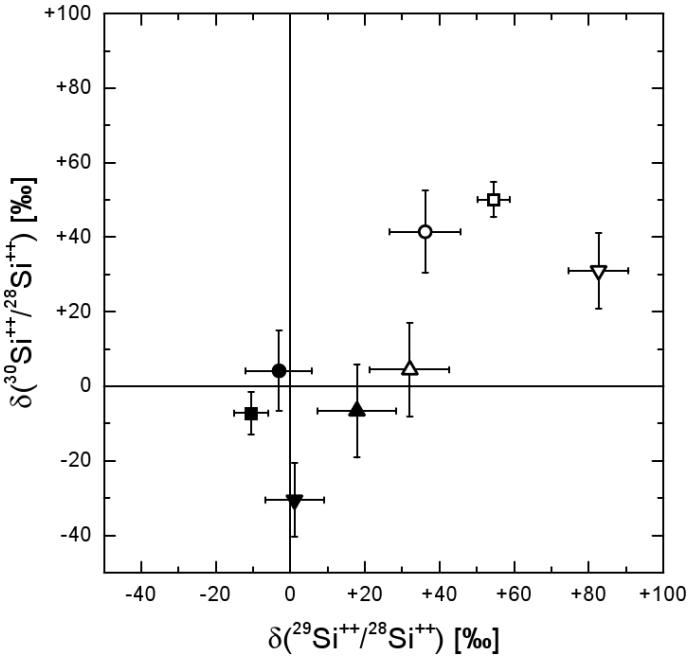

Figure 5.2 Silicon isotope ratios calculated from measurements of doubly charged silicon ions from silicon microtips given in δ notation relative to expected terrestrial isotope ratios (solid lines). Open symbols represent data from accumulated spectra not corrected for dead time effects. Data shown as solid symbols are dead time corrected. Error bars are 1σ statistical errors.

Table 5.2 shows the number of laser pulses as well as the number of ionization events calculated from the data. As expected and similar to carbon, the number of ionization events is smaller than the number of laser pulses, demonstrating that in this case, fewer than 40% of the laser pulses could generate singly charged silicon ions, and fewer than 3% of the pulses were above the

ionization threshold for doubly charged silicon ions. However, these numbers vary a lot among different runs as they depend on the sample properties and analytical conditions. In some cases, formation of doubly charged ions is even favored compared to formation of singly charged ions.

Table 5.2 Silicon isotopes measured by APT in microtips as singly and doubly charged ions.[a]

Sample	SMT 113215	SMT 17134	SMT 17149	SMT 17153
Number of laser pulses	2.44×10^{8}	7.13×10^{8}	3.34×10^{8}	1.74×10^{8}
$N(^{28}Si^{+}/^{29}Si^{+})$	$(1.2\pm0.2)\times10^{7}$	$(1.4\pm0.2)\times10^{7}$	$(1.3\pm0.2)\times10^{8}$	$(1.9\pm1.1)\times10^{6}$
$^{28}Si^{+}/^{29}Si^{+}$ (raw data)	16.3±0.3	4.78±0.06	19.0±0.1	4.6±0.2
$^{28}Si^{+}/^{29}Si^{+}$ (corrected)	16.3±0.3	4.79±0.06	19.0±0.1	4.6±0.2
$N(^{28}Si^{+}/^{30}Si^{+})$	$(1.0\pm0.2)\times10^{7}$	$(1.6\pm1.2)\times10^{7}$	$(1.03\pm0.09)\times10^{8}$	$(1.0\pm1.1)\times10^{6}$
$^{28}Si^{+}/^{30}Si^{+}$ (raw data)	27.8±0.5	22.9±0.5	30.1±0.2	19.2±1.3
$^{28}Si^{+}/^{30}Si^{+}$ (corrected)	27.9±0.6	23.0±0.5	30.2±0.2	19.3±1.3
$N(^{29}Si^{+}/^{30}Si^{+})$	$(7\pm6)\times10^{6}$	--	$(1.2\pm0.5)\times10^{8}$	--
$^{29}Si^{+}/^{30}Si^{+}$ (raw data)	1.71±0.04	4.8±0.1	1.59±0.01	4.2±0.3
$^{29}Si^{+}/^{30}Si^{+}$ (corrected)	1.71±0.04	--	1.59±0.01	--
$N(^{28}Si^{++}/^{29}Si^{++})$	$(3.3\pm0.1)\times10^{6}$	$(1.40\pm0.03)\times10^{7}$	$(6.8\pm0.4)\times10^{6}$	$(2.40\pm0.05)\times10^{6}$
$^{28}Si^{++}/^{29}Si^{++}$ (raw data)	19.0±0.2	18.68±0.08	19.1±0.2	18.2±0.1
$^{28}Si^{++}/^{29}Si^{++}$ (corrected)	19.8±0.2	19.91 ± 0.09	19.4±0.2	19.7±0.2
$N(^{28}Si^{++}/^{30}Si^{++})$	$(3.5\pm0.1)\times10^{6}$	$(1.60\pm0.06)\times10^{7}$	$(8.6\pm0.7)\times10^{6}$	$(3.06\pm0.09)\times10^{6}$
$^{28}Si^{++}/^{30}Si^{++}$ (raw data)	28.7±0.3	28.5±0.1	29.8±0.4	29.0±0.3
$^{28}Si^{++}/^{30}Si^{++}$ (corrected)	29.8±0.3	30.1±0.2	30.1±0.4	30.8±0.3
$N(^{29}Si^{++}/^{30}Si^{++})$	$(3.6\pm0.6)\times10^{6}$	$(1.16\pm0.09)\times10^{7}$	$(5\pm1)\times10^{6}$	$(1.7\pm0.1)\times10^{6}$
$^{29}Si^{++}/^{30}Si^{++}$ (raw data)	1.51±0.02	1.523±0.009	1.56±0.03	1.59±0.02
$^{29}Si^{++}/^{30}Si^{++}$ (corrected)	1.51±0.02	1.53±0.01	1.56±0.03	1.60±0.02

[a] The number of ionization events N calculated according to Equations 5.3 and 5.7 is given for singly and doubly charged ion pairs ($^{28}Si/^{29}Si$, $^{28}Si/^{30}Si$, and $^{29}Si/^{30}Si$). The number of laser pulses is included for comparison. Ion ratios are calculated from raw data with no dead time correction and after dead time correction. Errors are 1σ statistical errors. Expected values for corrected isotope ratios are terrestrial values ($^{28}Si/^{29}Si$ = 19.7, $^{28}Si/^{30}Si$ = 29.9, and $^{29}Si/^{30}Si$ = 1.52).

With three stable isotopes, silicon, in principle, enables evaluating three different isotope pairs. However, isotopic abundances of ^{29}Si and ^{30}Si are both below 5%, and correlated counting events for these isotopes are quite rare. In two cases (SMT 17134 and SMT 17153), there were no correlated counting events measured for $^{29}Si^{+}$ and $^{30}Si^{+}$ at all. In such cases, dead time correction cannot be applied. However, numbers of ionization events *N* for singly charged ion pairs $N(^{28}Si^{+}/^{29}Si^{+})$, $N(^{28}Si^{+}/^{30}Si^{+})$, and also for $N(^{29}Si^{+}/^{30}Si^{+})$, when it could be determined, agree reasonably well within statistical errors. The same is true for doubly charged ion pairs $N(^{28}Si^{++}/^{29}Si^{++})$, $N(^{28}Si^{++}/^{30}Si^{++})$, and $N(^{29}Si^{++}/^{30}Si^{++})$. However, some discrepancies were observed, which might be due to some mass interferences that could have different evaporation thresholds in APT. In general, these discrepancies seem to be larger for singly charged ion pairs than for doubly charged ion pairs.

Corrected isotope ratios for the singly charged silicon ions (Table 5.2) clearly indicate that dead time effects are not the major reason for deviations of the isotope ratios from expected values. As in the case of carbon, we attribute this mainly to interferences from hydrides, which again show high variability. Doubly charged silicon ions after dead time correction, however, yield isotope ratios that are all within 2σ of the expected terrestrial ratios, except for one outlier, which is still within 3σ.

5.4 Conclusions

Correction of dead time effects in laser-induced desorption TOF-MS like, e.g., in APT is complicated by the nonlinearity of the desorption process, which leads to large variations of ionization yields during a typical measurement. Dead time correction following the general concept according to (Stephan et al. 1994), but using single shot data and taking into account correlated counting events from isotopes of the same element, can be used to mitigate these

effects. However, this dead time correction only works if the respective mass peaks do not suffer from unresolved interferences. Due to the limited mass resolving power of current APT instruments and the possibility of unresolved interfering hydride peaks, using doubly charged ion signals can be advantageous to obtain accurate isotope ratios. Performing such measurements at laser pulse energies and field evaporation voltages that facilitate the formation of doubly charged ions can therefore be desirable. The correction presented here unlocks the full potential of APT regarding isotope analysis in small volumes or nanoparticles. This work has tremendous potential for isotope studies at a previously unreachable spatial dimension—the atomic scale.

Future investigations will show if the dead time correction laid out in this study could also be applied to other laser-induced desorption TOF-MS techniques like, e.g., laser desorption RIMS.

5.5 Acknowledgements

We thank M.J. Pellin and C. Floss for helpful discussions. We appreciate thoughtful comments by two anonymous reviewers. This work was supported by NASA through grants NNX09AG39G (T.S.), NNX11AG77G (P.R.H.), NNX13AF53G (J.B.L.), and NNX14AP15H (J.B.L.), and by a grant from the Tawani Foundation (P.R.H.). The LEAP tomograph at NUCAPT was purchased and upgraded with funding from NSF-MRI and ONR-DURIP programs. Instrumentation at NUCAPT was supported by the Initiative for Sustainability and Energy at Northwestern. This research made use of the EPIC facility and Shared Facilities at Northwestern University's Materials Research Science and Engineering Center, supported by the MRSEC program (DMR-0520513 and 1121262) of NSF. P.R.H. thanks Cameca Instruments, Inc., for access to their LEAP tomograph.

5.6 References

Bunton J. H., Olson J. D., Lenz D. R., and Kelly T. F. 2007. Advances in pulsed-laser atom probe: Instrument and specimen design for optimum performance. *Microscopy and Microanalysis* 13:418–427.

Cerezo A., Smith G. D. W., and Waugh A. R. 1984. The FIM100 - Performance of a commercial atom probe system. *J. Phys. Colloques* 45:C9-329–C9-335.

Heck P. R. et al. 2014. Atom-probe analyses of nanodiamonds from Allende. *Meteoritics & Planetary Science* 49:453–467.

Holzlechner G., Kubicek M., Hutter H., and Fleig J. 2013. A novel ToF-SIMS operation mode for improved accuracy and lateral resolution of oxygen isotope measurements on oxides. *Journal of Analytical Atomic Spectrometry* 28:1080–1089.

Keenan M. R., Smentkowski V. S., Ohlhausen J. A., and Kotula P. G. 2008. Mitigating dead-time effects during multivariate analysis of ToF-SIMS spectral images. *Surface and Interface Analysis* 40:97–106.

Kelly T. F., and Larson D. J. 2012. Atom probe tomography 2012. *Annual Review of Materials Research* 42:1–31.

Kingham D. R. 1982. The post-ionization of field evaporated ions: A theoretical explanation of multiple charge states. *Surface Science* 116:273–301.

Lee J. L. S., Gilmore I. S., and Seah M. P. 2012. Linearity of the instrumental intensity scale in TOF-SIMS—a VAMAS interlaboratory study. *Surface and Interface Analysis* 44:1–14.

Menand A., Al Kassab T., Chambreland S., and Sarrau J. M. 1988. Atom-probe study of aluminum-lithium alloys. *J. Phys. Colloques* 49:C6-353–C6-358.

Savina M. R., Pellin M. J., Tripa C. E., Veryovkin I. V., Calaway W. F., and Davis A. M. 2003. Analyzing individual presolar grains with CHARISMA. *Geochimica et Cosmochimica Acta* 67:3215–3225.

Saxey D. W. 2011. Correlated ion analysis and the interpretation of atom probe mass spectra. *Ultramicroscopy* 111:473–479.

Stephan T., Zehnpfenning J., and Benninghoven A. 1994. Correction of dead time effects in time-of-flight mass spectrometry. *Journal of Vacuum Science and Technology A* 12:405–410.

Stephan T. 2001. ToF-SIMS in cosmochemistry. *Planetary and Space Science* 49:859–906.

Tsong T. T., Ng Y. S., and Krishnaswamy S. V. 1978. Quantification of atom-probe FIM data and an application to the investigation of surface segregation of alloys. *Applied Physics Letters* 32:778–780.

Vurpillot F., Houard J., Vella A., and Deconihout B. 2009. Thermal response of a field emitter subjected to ultra-fast laser illumination. *Journal of Physics D: Applied Physics* 42:125502 (7 pp).

Chapter 6: $^{12}C/^{13}C$-ratio Determination in Nanodiamonds by Atom-probe Tomography

This chapter was published in *Ultramicroscopy* in collaboration with coauthors Dieter Isheim, Christine Floss, and David N. Seidman (Lewis et al. 2015). The author's personal contribution to this work included all sample preparation, experimental analysis, development of data correction methods and scripts, data reduction, writing the manuscript, and managing revisions in cooperation with the coauthors.

6.1 Introduction

Grains are identified as presolar based on significant deviations from the terrestrial ratios of stable isotopes such as $^{12}C/^{13}C$ (e.g., Figure 6.1). These isotopic anomalies are large enough that they can only be explained by extrasolar nucleosynthetic processes. Therefore it is believed that, unlike the vast majority of solar system material, presolar grains survived isotopic homogenization in the early solar nebula. The sources of presolar grains are identified by comparing these anomalies to those predicted by models and observed by astronomers. These grains are used to probe various stellar processes in stars and the interstellar medium (ISM) (Zinner 2014).

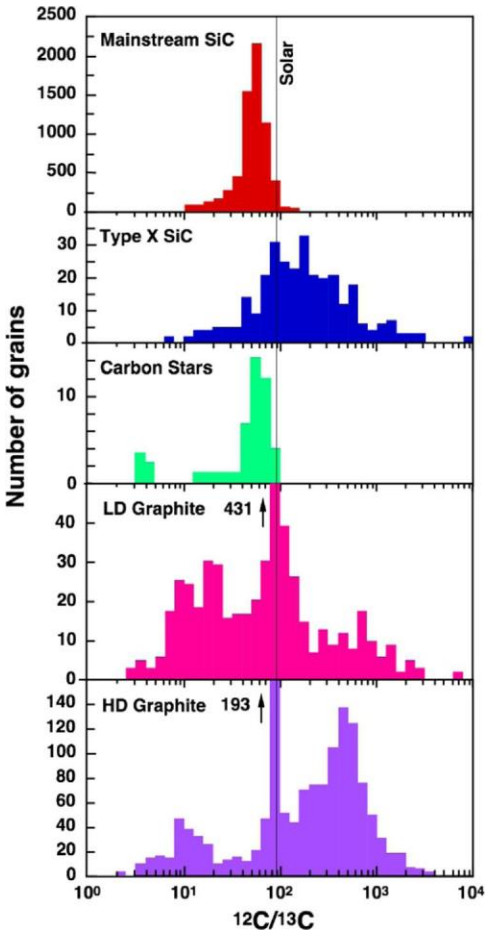

Figure 6.1 From (Zinner 2014), the unique distributions of $^{12}C/^{13}C$ isotopic ratios (logarithmic) for various presolar grain types, measured by SIMS, and for Carbon stars, from astronomical observations. Isotopic ratios can be used to identify and investigate the presolar sources of the grains.

The first presolar grain type was discovered in 1987, when an abundant phase of nanodiamond separated from meteorites (Lewis et al. 1987) was identified as the carrier of trace-element isotopic anomalies associated with nucleosynthetic processes that occur in supernovae. Of all known presolar grain types, nanodiamonds are the most abundant (~1400 ppm (Zinner 2014)) but also the smallest (~3 nm diameter (Daulton et al. 1996)), posing unique analytical challenges. Secondary ion mass spectrometry (SIMS) is used extensively in presolar grain research, as it offers high mass resolving power and high spatial resolution (e.g., down to 50 nm for the Cameca NanoSIMS 50 employed at Washington University in St. Louis) – excellent for analysis

of multiple isotopes in μm-scale grains, but inadequate for analysis of individual nm-scale grains.

In light of this limitation, we have been analyzing meteoritic nanodiamonds and terrestrial nanodiamond standards using atom-probe tomography (APT) (Heck et al. 2014; Lewis et al. 2014a; Stadermann et al. 2011). Our scientific goal is to determine the origins of the nanodiamonds by determining what, if any, anomalies exist in the C isotopes of the nanodiamonds. In bulk (millions of nanodiamonds) the isotopic ratios of the primary element C (Russell et al. 1996) and the secondary element N (Marty et al. 2011) both average to solar system values.

While supernovae were the first source to be suggested for meteoritic nanodiamonds (Lewis et al. 1987) and remain a viable explanation for the origins of a subset of the nanodiamonds, other details have been interpreted to indicate some nanodiamonds formed in the ISM from passing supernova shockwaves (Stroud et al. 2011), in the early Solar System (Dai et al. 2002), and even in asymptotic giant branch stars (Verchovsky et al. 2006).

It is possible that there are subpopulations of nanodiamonds with a variety of anomalies that average to the solar system value or are hidden by a majority of solar system-formed nanodiamonds. Our experimental goal is to measure the $^{12}C/^{13}C$ isotopic ratios of individual or small clusters (<100) of nanodiamonds.

This work provides a step towards the development of standard practices for future isotopic measurements, necessary for meteoritical (Lewis et al. 2014) and geological (Valley et al. 2014) lines of research.

6.2 Methods

6.2.1 Meteoritic Nanodiamonds

Meteoritic nanodiamonds are separated from their host meteorites by acid dissolution and size sorting. The nanodiamonds are damaged by acid treatment, with molecules such as H, COOH, CH, and N bonding to free sites (Lewis et al. 1989); 25–50% of the atoms in an average nanodiamond are within one atomic layer of the surface.

Chemical vapor deposition (CVD) and shock formation have both been proposed for the nanodiamonds based on TEM studies. Twinning is detected in the nanodiamonds (Daulton et al. 1996), and some fraction of the residue is amorphous C sheets rather than nanodiamonds (Stroud et al. 2011).

We study nanodiamonds from the meteorite Allende CV3 provided by R.S. Lewis (separation DM) (Lewis et al. 1989). The hypothetical "average" nanodiamond from Allende is assumed to be spherical, 3 nm in diameter, and contains ~2500 atoms. The low number of atoms will lead to large uncertainties in measured isotopic ratios. However, anomalies in C isotopic ratios in other presolar grain types, such as graphite and SiC, are known to range from ~10 to ~10,000. In addition, many microtips prepared by our method contain several to 10s of nanodiamonds, improving the counting statistics (but potentially diluting anomalies in individual grains).

For standards we use terrestrial nanodiamonds produced by detonation. These nanodiamonds undergo acid treatment similar to the meteoritic nanodiamonds (Greiner et al. 1988).

6.2.2 Sample Preparation

We fabricate Ni–Pt-nanodiamond–Pt–Ni multilayers for APT analysis. We deposit 130–170 nm of Pt onto a cleaned Ni disk using a Southbay Technology IBSe ion beam sputtering system. A

steel disk covered in Au foil containing the nanodiamond residue is placed on one of the two ultrasonicating heads; the Pt-covered Ni disk is placed on the other. While ultrasonicating, we pipet ~50 μL of deionized water onto the nanodiamond-residue on the Au foil. After waiting several minutes, during which a significant portion of the liquid evaporates, we micropipette a 2 μL aliquot of the water onto the Ni disk. We return the Ni–Pt-nanodiamond multilayer to the IBSe and begin another ~130 nm Pt deposition followed by a top layer of Ni.

A roughly circular residue is left behind by the evaporating droplets. Large clusters of nanodiamonds are visible in secondary electron (SE) images. In some regions, cluster size and density falls off gradually to vanishing at the inner and outer edges of the deposit, and it is in these regions where we create focused ion beam (FIB) liftouts (e.g., Figure 6.2) using an FEI Quanta dual-beam FIB. We cover the surface of a 30×6 μm^2 − area liftout region with 150 nm of protective Pt, deposited using the Ga ion beam to crack a precursor gas delivered to the sample by a gas injection system. Ion beam mills are used to undercut the liftout, which is subsequently attached to a micromanipulator and trimmed. The vacuum chamber is then vented to allow us to actuate our custom sample holder 90° to bring the deposition layer from horizontal to vertical relative to the stage. Under high vacuum again, after more trimming, slices of the liftout are mounted onto prefabricated Si micropost arrays using a “mortise and tenon” method. One liftout typically produces 8 slices. We conduct ion beam mills 10–15° off vertical, rotating the sample 90° about its long axis between each mill. This creates a tetrahedral or pyramidal shape at the microtip. The deposition layer runs through this pyramidal microtip. Finally, a series of annular mills are conducted to create a ~15–30 nm radius microtip, ready for introduction into the atom-probe tomograph.

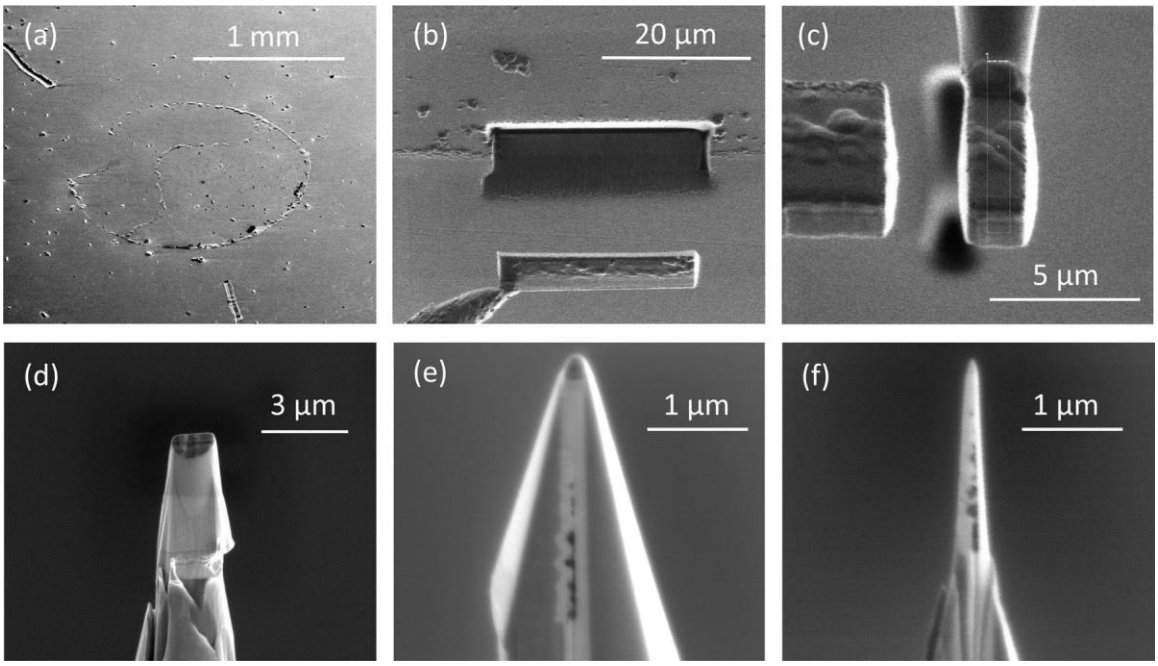

Figure 6.2 Atom-probe tomograph microtip preparation procedure. (a) Nanodiamonds are deposited from a droplet and covered with layers of Pt and Ni. Large clusters of nanodiamonds are visible around the rim of the deposition, pushing up the surface of the multilayer. (b) A ~25 µm region of the deposit rim is lifted out with FIB milling. (c) Slices of the trimmed, rotated liftout are attached to Si microposts with Pt deposition. (d) After Pt welding, initial sharpening creates a conical shape. (e) Pyramidal sharpening reveals the Pt deposition layer (white), which contains large clusters of nanodiamonds (black). (f) After high- and low-kV annular sharpening, nanodiamond clusters large enough to be resolved are located within a few hundred nm of the ~20 nm radius microtip.

6.2.3 Atom-probe Tomography

We use the Cameca LEAP 4000X Si Atom Probe Tomograph at Northwestern University. Atom-probe tomography (Seidman 2007; Seidman and Stiller 2009a; Seidman and Stiller 2009b; Kelly and Miller 2007, and references therein) yields the 3D positions and mass-to-charge-state ratios of ions from a ~100 nm^3 region with sub-nm spatial resolution and atomic ppm concentration sensitivity. For run parameters see Table 6.1. To reconstruct data from our APT runs we use Cameca's IVAS 3.6.6 software (David J. Larson et al. 2013, Chapters 5 and 6). We estimate the evaporation field to be 39 V/nm. For this estimation we use the final radius, calculated using SE images of microtips that survived APT, and the final voltage for those microtips. For each microtip we can then calculate the initial radius using this field estimate and the starting voltage. We reconstruct the microtip profile by fitting to a SE image of the sample prior to APT.

The evaporation field for diamond is not well known, but is certainly much higher than Pt (Tsong 1978). To minimize the uncertainty generated by field inhomogeneity, we used slow evaporation rates (0.1–1%) and control of the mass-to-charge-state ratio of Pt, which is a good indicator of evaporation conditions. Time-constant background can become a significant obstacle to resolving ^{13}C peaks, so the lowest possible evaporation rate is not always optimal.

The difference in the evaporation field between nanodiamond and amorphous C is unknown. To date, we have not been able to distinguish these two phases. For simplicity, we call all high density C regions in our microtips nanodiamonds.

A region of interest (ROI) is selected to exclude the vast majority of the Pt matrix and include the region with the nanodiamonds (e.g., Figure 6.3). We use this as the bulk data.

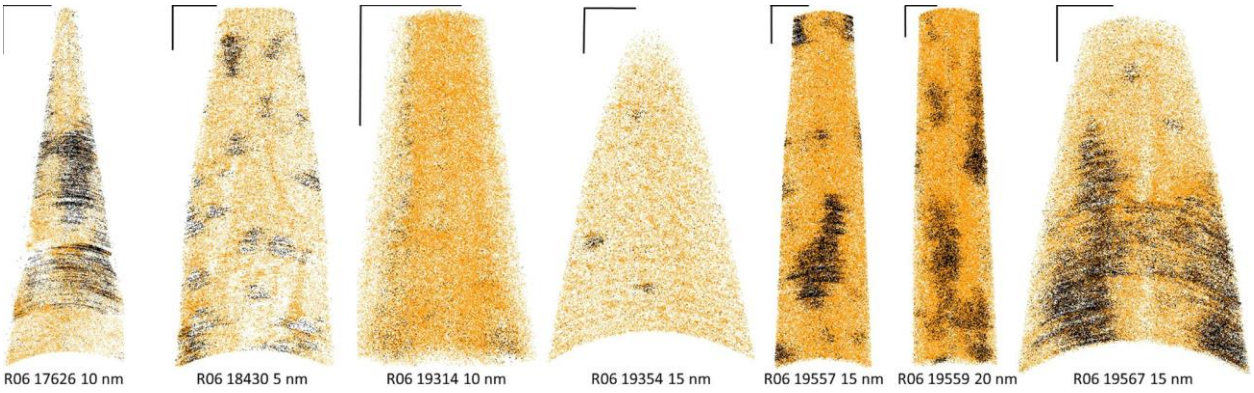

Figure 6.3 Cross sections of 3D reconstructions of six microtips, displaying C (black) and Pt (orange) ions. Scale bars are 20 nm. Only a fraction of the Pt ions are displayed. Run number and cross section depth are noted beneath each reconstruction. See Table 6.1 for the isotopic data corresponding to each run number. (For interpretation of the references to color in this figure caption, the reader is referred to the web version of this paper.)

We use custom-defined range files to select peaks at 6, 6.5, 12, and 13 amu (Figure 6.4). It is clear from both anecdotal and informal statistical evidence that the subjective nature of range selection introduces significant variations into measurements of composition (Hudson et al. 2011). We therefore consistently used the following criteria to define mass-to-charge-state

ranges: Using a bin width of 0.01 amu, we define a peak to range from the bin where the peak is twice the preceding noise to the bin where the peak first drops below twice the preceding noise or where the tail encounters another peak. Statistical error is propagated as we calculate the noise contribution to each peak, subtract it, and then take the ratio of $^{12}C/^{13}C$ for singly charged and doubly charged ions. Lewis et al. (2015) compare this fitting method to one utilizing FWHM, and demonstrates that the two methods preserve similar instrumental artifacts.

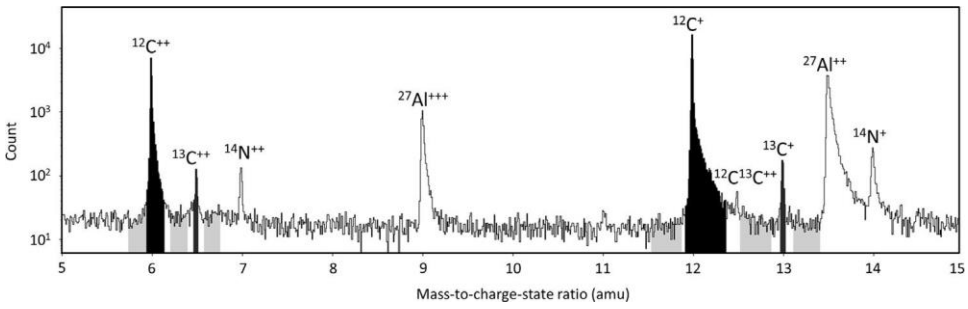

Figure 6.4 Logarithmic mass spectrum from dataset R06 19567 from 5 to 15 amu (bin size 0.01 amu). C peaks are in black. Noise measurement ranges are in light gray. Other visible peaks include N^{+} and N^{++} at 14 and 7 amu, Al^{++} and Al^{+++} at 13.5 and 9 amu, and $^{12}C^{13}C^{++}$ at 12.5 amu.

APT does not have the mass resolving power to distinguish the $^{12}CH^{+}$ hydride from $^{13}C^{+}$. The potential of H present on the surfaces of the nanodiamonds, the tendency of H to migrate to grain boundaries (Nishikawa et al. 1999), and its presence in the high vacuum means that there is the possibility of hydride formation during field evaporation. We assume that the formation of $^{12}CH^{++}$ is much less probable, so the $^{12}C^{++}/^{13}C^{++}$ ratio may be used as a correction. The C charge-state ratio $^{12}C^{+}/^{12}C^{++}$ typically falls between one and three. We use a higher laser pulse fraction to bring this ratio closer to one to improve counting statistics on $^{13}C^{++}$, which is typically the smallest of the four peaks. We are limited, however, by thermal instability in the tip.

$^{12}C_2^{++}$ will interfere with $^{12}C^{+}$ at 12 amu. We do observe small peaks at $^{12}C_2^{+}$ and $^{12}C^{13}C^{++}$ (24 and 12.5 amu) in most of our data sets, so this interference may be significant.

We also observe $^{12}C_3^{++}$ (18 amu), $^{12}C_3^{+}$ (36 amu), and the various PtOC isotopologues. Calculations of isotopic ratios from peaks of molecular ions are difficult since the peaks represent all combinations of the isotopes in the molecule, sub-dividing the signal (e.g., C_2^{+} will populate three peaks, at $^{12}C_2^{+}$, $^{12}C^{13}C^{+}$, and $^{13}C_2^{+}$).

6.2.4 Multi-hit Analysis

The atom-probe tomograph detector is position sensitive and multipart, giving rise to potential deadtime, deadspace, and pileup signal loss in the event that multiple ions field evaporate and are incident on the detector during the same detection window between two laser pulses. Some authors do not explicitly differentiate these effects (e.g., Saxey 2011) while others describe them as independent phenomena (Da Costa et al. 2005). The deadtime effect occurs when electron cascades from two different ions arrive at the delay lines at essentially the same place and close enough together in time that the signals generated on the delay lines cannot be resolved as two separate signals. The deadspace effect occurs when two ions arrive at the microchannel plate at different times and positions, but the electron cascade from the later-arriving ion induces a signal on a delay line that overlaps with one of the signals produced by the electron cascade from the earlier ion, causing the instrumentation to detect only one electrical signal at that end of the delay line, while the other end of the delay line may detect two separate signals. With multiple delay-lines the capacity exists to deconvolve these otherwise “partial” hits, so long as there are not too many ions involved in the multi-hit.

Detector pileup occurs during any multi-hit event where two or more pulse pairs are generated on a delay-line close enough together in time that there is more than one solution for the impact times and positions of the ions. The detector pileup capacity is increased by adding more delay lines oriented along different axes. To make an analogy to solving linear equations, this is the

physical equivalent of adding independent equations in a number of unknown variables to resolve degeneracies due to the high number of unknowns. If the detector pileup capacity is exceeded, none of the ions that form the pileup event can be assigned a conclusive time-of-flight. The detector pileup capacity for our instrument is 15 ions in a 2 μs window. The maximum number of ions detected in a 2 μs window in any of our data sets is 14, therefore it is unnecessary to correct for detector pileup.

We use iterative proportional fitting to correct for the deadtime effect upon pairs of ions of the same mass-to-charge-state ratio. By recording the number of multi-hit ion pairs detected at the intersection of the C mass-to-charge-state ratio ranges at 6, 6.5, 12, and 13 amu, we build a correlation table with populations of detected pairs p_{ij} after Saxey (2011). We use all combinations of ions in the multi-hit as pairs, not just the first two. Originally the entries above the diagonal $x=y$ will be empty, since the order of the pair is based on arrival order. For the correlation table, we shift half the pairs detected in p_{ij} to populate p_{ji}. Thus, the matrix is ensured to be symmetric across the diagonal. Then the probability of a pair of C ions containing an ion of species k as the first/second ion is

$$P(k) = \frac{\sum_j (p_{kj})}{\sum_{ij} (p_{ij})} = \frac{\sum_i (p_{ik})}{\sum_{ij} (p_{ij})} = \frac{n_k}{N}$$

where n_k is the number of pairs that contain an ion of species k as the first/second ion, depending on whether summation is over column/row (for our symmetrized matrix the two values will always be equal). N is the sum of the matrix, which is the number of pairs detected.

The expectation values for the number of pairs of each combination is then

$$e_{ij} = P(i,j)N = P(i)P(j)N = \frac{n_i n_j}{N}$$

where *i/j* are summed over row/column.

We correct the diagonal elements, p_{ii}, iteratively, calculating expectation values based on all the elements, adjusting expectation values of the diagonals, and repeating the process until the expectation values on subsequent iterations change by less than some small value. This is the iterative proportional fitting method introduced by Deming and Stephan (1940) and taken from Everitt (1992), here applied to the correction of APT data for the first time. This method converges quickly for most data sets, given that the sets have enough multi-hit detections.

2D mass-to-charge-state ratio histograms of ion pairs are useful for visualization of instrumental signal loss. They can also indicate where the field evaporation of an ion of a particular species is correlated; that is, where the evaporation of an ion of one species during a detection window significantly changes the probability of an ion of the same or a different species field evaporating during the same detection window (Figure 6.5).

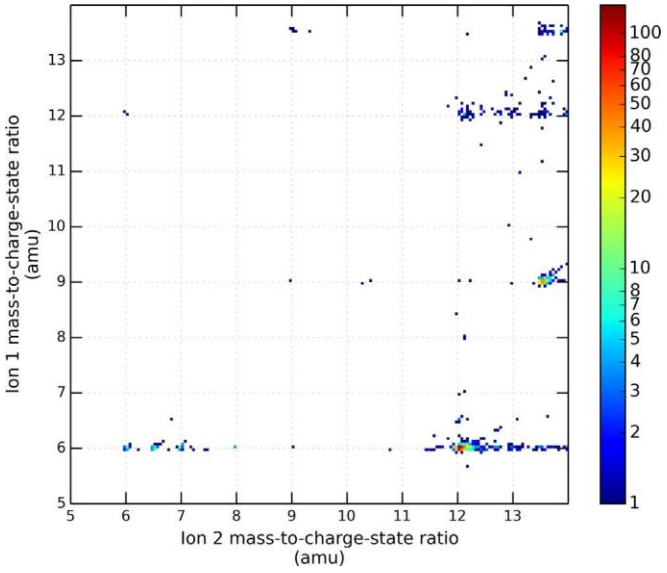

Figure 6.5 2D mass spectrum of multi-hit pairs from R06 19565 from 5 to 14 amu (bin size 0.05×0.05 amu). Hotspots indicate correlated evaporation of two ion species. Detection on the line of equal mass-to-charge-state (diagonal) is suppressed by detector deadtime. Detection above the line of equal mass-to-charge-state is unlikely since the lighter mass in a pair should almost always arrive at the detector first. Horizontal and vertical distributions of multi-hits indicate where one ion in the pair field evaporates at roughly the peak of the thermal pulse and the other ion field evaporates later. Diagonal distributions of multi-hits represent pairs that evaporated together but after the laser pulse.

6.3 Results and Discussion

We calculated $^{12}C/^{13}C$ ratios and uncertainties for 16 detonation nanodiamond (DND) standard and 18 Allende nanodiamond (ADM) data sets. Table 6.1 summarizes these data. Of these, 9 DND and 3 ADM datasets were originally reported in Heck et al. (2014) and are presented here with new ROI selections and deadtime corrections. We exclude data collected prior to the most recent major hardware upgrade to the atom-probe tomograph, which is described in Heck et al. (2014). Figure 6.6 plots the $^{12}C^{+}/^{13}C^{+}$ vs. $^{12}C^{++}/^{13}C^{++}$, where we include only those data sets that have statistically meaningful $^{12}C^{+}/^{13}C^{+}$ and $^{12}C^{++}/^{13}C^{++}$ ratios. We integrated counts to calculate the mean ratios, and also calculated the weighted standard error of the mean and weighted standard deviation for our data (Table 6.2).

Table 6.1 Experimental data. Uncertainties are 2σ. Similar $^{12}C^{+}/^{12}C^{++}$ values indicate similar field evaporation conditions. A## M## indicates the microtip analyzed.

Sample	$^{12}C^{+}/^{12}C^{++}$	$^{12}C^{+}/^{13}C^{+}$	$^{12}C^{++}/^{13}C^{++}$	T (K)	E (pJ)	Comments
Synthetic nanodiamonds						
DND R06 17619 A61 M35	2.2±70.2	38±15	(1772±31,044)	80	40	a,b
DND R06 17620 A61 M35	1.43±0.06	72±19	42±10	80	40	b
DND R06 17621 A61 M34	7.3±1.1	33±13	(83±265)	80	40	a,b,c
DND R06 17626 A62 M04	2.9±0.1	76±17	41±11	55	80–100	b
DND R06 17629 A61 M31	1.9±0.3	20±11	(49±65)	55	70–90	a,b
DND R06 17967 A62 M35	1.3±0.1	54±34	(476±2483)	54	40	a,b,c
DND R06 17969 A53 M28	1.4±0.1	55±11	55±13	54	40	b
DND R06 17978 A62 M34	4.2±0.5	44±21	(96±143)	95	40	a,b,c
DND R06 18428 A64a M34	2.2±0.2	107±54	50±28	95	40–80	b
DND R06 19586 A69 M12	3.9±0.3	45±11	(120±90)	95	80	a
DND R06 19587 A69 M11	1.80±0.07	46±17	70±44	95	80	
DND R06 19589 A69 M12	4.7±0.3	43±9	55±33	95	80	
DND R06 21153 A77 M33	5.2±0.4	65±16	72±43	95	80	
DND R06 21155v02 A77 M35	2.0±0.2	42±22	36±24	95	80	
DND R06 21155v03 A77 M35	3.54±0.06	81±7	54±7	95	80	
DND R06 21157 A77 M30	3.2±0.1	80±15	72±29	95	80	
Allende nanodiamonds						
ADM R06 18430 A65a M06	1.73±0.06	61±12	84±26	95	40–100	b
ADM R06 18436 A65a M05	1.07±0.06	137±66	69±25	95	40	b
ADM R06 18437 A65a M04	1.52±0.04	60±9	55±11	95	40–80	b
ADM R06 19314 A62 M07	1.67±0.1	84±38	93±59	95	60	

Sample	$^{12}C^{+}/^{12}C^{++}$	$^{12}C^{+}/^{13}C^{+}$	$^{12}C^{++}/^{13}C^{++}$	T (K)	E (pJ)	Comments
ADM R06 19315 A62 M08	1.25±0.07	84±34	74±32	95	80	
ADM R06 19354 A62 M10	1.5±0.2	19±9	23±16	95	60	
ADM R06 19557 A70 M25	1.54±0.04	84±14	59±10	95	60	
ADM R06 19559 A70 M25	1.63±0.03	72±8	52±6	95	60–80	
ADM R06 19565 A70 M07	2.12±0.07	66±11	57±14	60	80	
ADM R06 19566 A70 M33	1.17±0.05	69±20	52±14	60	80	
ADM R06 19567 A70 M33	2.19±0.04	88±10	70±11	60	80	
ADM R06 19568 A70 M34	1.63±0.05	99±22	52±11	60	60	
ADM R06 19572 A70 M35	1.83±0.07	80±16	59±15	95	80	
ADM R06 20159 A78 M05	5.0±0.3	71±18	40±17	95	80	
ADM R06 20163 A78 M12	5.6±0.3	44±8	128±105	95	80	
ADM R06 21164 A78 M25	7.4±0.2	59±5	65±16	95	80	
ADM R06 21179 A78 M30	3.7±0.1	69±10	67±23	95	80	
ADM R06 21180 A78 M29	3.4±0.3	78±33	(159±192)	95	80	a,c

[a] No significant $^{13}C^{++}$ counts.

[b] Datasets previously included in Heck et al. (2014), here presented with updated ROIs and deadtime corrections.

[c] Too few multi-hits to deadtime correct.

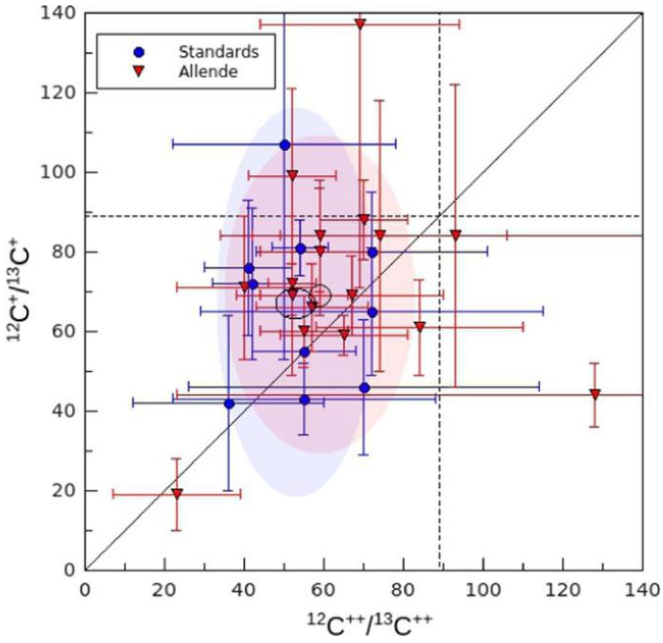

Figure 6.6 Graphical summary of $^{12}C/^{13}C$ isotopic ratios determined by APT. Each data point represents the ratios of counts from an individual microtip. Errors are twice the uncertainty for each data point, based on counting statistics. Dashed lines mark the terrestrial $^{12}C/^{13}C$ ratio of ~89 (Coplen et al. 2002). The solid diagonal line indicates where equal ratios for singly and doubly charged C ions lie. Large open ellipses denote 2σ about the mean, small closed ellipses denote $2\sigma_{\bar{x}}$ about the mean.

Table 6.2 Mean data for detonation nanodiamonds and Allende nanodiamonds, including standard error of the mean $\sigma_{\bar{X}}$, representative of the precision of our measurement of the mean value, and standard deviation σ, which represents the scatter in the data about that mean.

Data Subset	$\left(\frac{^{12}C^{+}}{^{13}C^{+}}\right) \pm (2\sigma_{\bar{X}})$	$(2\sigma) \pm (2\delta\sigma)$	$\left(\frac{^{12}C^{++}}{^{13}C^{++}}\right) \pm (2\sigma_{\bar{X}})$	$(2\sigma) \pm (2\delta\sigma)$
DND	67±4	49±8	53±5	20±6
ADM	69±3	40±3	59±3	24±4

6.3.1 Unidentified Experimental Biases

The standards in Figure 6.6 demonstrate a significant experimental bias with two effects:

(1) the measured $^{12}C/^{13}C$ ratio is lower than the known terrestrial $^{12}C/^{13}C$ ratio of ~89 (Coplen et al. 2002), and

(2) the $^{12}C^{+}/^{13}C^{+}$ ratio is larger than the $^{12}C^{++}/^{13}C^{++}$ ratio.

Effect (1) can only be produced by a bias in at least two peaks – one singly charged-C-ion peak and one doubly charged-C-ion peak. Effect (2) could result from a bias in just one of the four C peaks used for isotope calculations.

While we anticipate bias from hydride interference at $^{13}C^{+}$, this would result in the calculation of a $^{12}C^{+}/^{13}C^{+}$ ratio lower than the calculated $^{12}C^{++}/^{13}C^{++}$ ratio – the opposite of the observed effect. Therefore we assess that hydride interference is minor compared to this unidentified instrumental bias.

Another bias capable of fractionating the measured isotopes is the detector deadtime effect. If our corrections, made with a small number of counts, underestimated the deadtime effect, the result will be the apparent depletion of the most abundant isotope, ^{12}C, compared to the less abundant isotope, ^{13}C, resulting in too low a measurement of both C isotopic ratios – observed effect (1) – but also a $^{12}C^{+}/^{13}C^{+}$ ratio lower than the $^{12}C^{++}/^{13}C^{++}$ ratio – as with hydride interference, the opposite of effect (2). On the other hand, the deadtime effect will be greater for C^{++} ions compared to C^{+} ions because the C^{++} ions have a smaller time of flight, and therefore smaller scatter in time of flight for multiple ions with the same mass-to-charge-state ratio. Therefore it is unclear whether or not effect (2) can be caused by the detector deadtime effect, but effect (1) could be if we are losing a large fraction of the C signal. To restore our standard measurements to the expected terrestrial values require a minimum unanticipated signal loss of 20% for $^{12}C^{+}$ and 40% for $^{12}C^{++}$. Multi-hit analysis reveals that C evaporates in a highly correlated manner. While an average of 10% of all DND ions and 13% of all ADM ions are detected as part of a multi-hit, 38% of C DND ions and 40% of C ADM ions arrive as part of a

multi-hit. Therefore, while we have implemented deadtime corrections, it is possible that we are underestimating the C signal loss.

Indeed, the observed atomic density of nanodiamonds is lower than expected by as much as a factor of 10. For comparison, the measured density of the Pt matrix is typically within a few percent of the known value after correction for the known 57% maximum detection efficiency of the atom-probe tomograph. There are, however, at least three other factors that may contribute to the low measured density of C. One is that we may be measuring amorphous C associated with the nanodiamonds, which is less dense than diamond; however, the difference should only be a few percent. Another factor is that the high evaporation field of diamond can lead to preferential evaporation and trajectory aberrations (Miller and Hetherington 1991), resulting in a local magnification effect, an overestimation of the volume of the nanodiamonds, and thus an underestimation of their density: The evaporation field of carbon is not well known, but may be estimated to be 103 V/nm (Tsong 1978), 2.6 times our estimation of the overall field. Trajectory aberration could therefore cause a 2.6× overestimation of the x and y dimensions of a nanodiamond, yielding a ~7× overestimation of volume and underestimation of density. Finally, it is possible that entire clusters of C atoms field evaporate at once and are lost.

Quantum tunneling at low (<140 K) temperatures has been experimentally shown to produce a lower ratio of $^{10}B^{++}/^{11}B^{++}$ compared to $^{10}B^{+}/^{11}B^{+}$ (Menand and Kingham 1985). While this is similar to effect (2), our experiments employ thermal pulsing, which raises the temperature several hundred K (Vurpillot et al. 2006), well above 140 K. In addition, the magnitude of the bias reported for quantum tunneling is only large enough to account for roughly one-third of the observed bias in our data.

C_2^{++} contribution at 12 amu could, under certain circumstances, result in a higher $^{12}C^+/^{13}C^+$ ratio compared to $^{12}C^{++}/^{13}C^{++}$, explaining effect (2): the ratio of diatomic C ions $^{12}C^{12}C^{++}$ /$^{13}C^{13}C^{++}$ will be much greater than $^{12}C^+/^{13}C^+$ because of combination statistics. If these diatomic C ions contribute to the peaks at 12 amu they will weight the measured $^{12}C^+/^{13}C^+$ ratio towards a higher value. We observe small $^{12}C^{13}C^{++}$ peaks in most of our data sets, but we do not observe $^{12}C^{13}C^{4+}$ at 6.25 amu (or any C_2^{4+} in data sets without C_1^{++} peaks, where the isotopologues would be free of interferences).

The systematic error that lowers our measured standard ratios from the terrestrial value, effect (1), is also present in microtips produced by Heck et al. (2014), but effect (2) is not consistently reproduced. Heck et al. (2014) use two additional sample preparation techniques, one with nanodiamonds in a horizontal layer through the microtip on top of Si, covered in cobalt, the other with nanodiamonds on the exterior of a presharpened Si micropost. We surmise that the instrumental bias producing effect (1) is not a result of the C–Pt interaction or the effect of a vertical deposition layer, but effect (2) could be.

6.3.2 Isotopic Anomalies

What these two biases do not obscure is that the meteoritic mean ratio is similar to but possibly slightly higher than the standard mean ratio. See Table 6.2 and Figure 6.6 for mean data. In all previous SIMS bulk studies the meteoritic nanodiamonds have had the same $^{12}C/^{13}C$ ratio as terrestrial material. However, for the small numbers of nanodiamonds we are studying, it is possible that we will uncover isotopic anomalies whose signals would be diluted in bulk studies. $^{12}C^{++}/^{13}C^{++}$ shows a high probability of small depletions in ^{13}C for Allende nanodiamonds on the mean. The depletion is not statistically significant in $^{12}C^+/^{13}C^+$ however, so further investigation is warranted to increase the precision of the calculated mean values.

For the meteoritic nanodiamonds the mean value could be the mean of sampling multiple populations of nanodiamonds, each with its own isotopic distribution. Therefore the standard deviation, σ, as a measure of the scatter of the datasets, is of great interest. If the scatter of the meteoritic nanodiamonds is significantly greater than that of the standards it would be evidence of nanodiamond sub-populations containing isotopic anomalies.

In the present data set, the calculated standard deviation of the ADMs is close to that of the DNDs. The uncertainty in the standard deviation ($\delta\sigma$) is high enough that, even ignoring systematic errors, there is a significant probability (>5%) that the unequal measurements do not reflect a difference between the real distributions from which we are taking our samples. If large isotopic anomalies are contained in a single microtip, the corresponding data point may be detected as an outlier many standard deviations from the mean. The only data point with greater than 2σ deviation in both $^{12}C^{+}/^{13}C^{+}$ and $^{12}C^{++}/^{13}C^{++}$ is ADM R06 19354, which is highly enriched in ^{13}C. However, the $^{12}C/^{13}C$ ratio of the terrestrial C contaminating the sputter-deposited Pt matrix in this microtip has a similarly low $^{12}C/^{13}C$ ratio. While this prevents us from drawing conclusions about the origins of the nanodiamonds in this microtip, we can conclude that the instrumental biases at work are not exclusively affecting C in nanodiamond form. It also demonstrates the necessity of microtip-by-microtip normalization. Simply averaging a number of standard data sets cannot provide a sufficient normalization for our samples.

6.4 Conclusions

We have measured a statistically significant set of small (<100) clusters of nanodiamonds with the atom-probe tomograph. Data from standards reveal two instrumental artifacts affecting our isotopic measurements of nanodiamonds and C dispersed throughout the Pt matrix. Carbon experiences highly correlated field evaporation, leading to deadtime effects that can bias ratios

and abundances. We implement iterative proportional fitting, but due to a small number of counts we may be underestimating the deadtime effect. Interference from diatomic C ions may also contribute to ratio bias. Data from meteoritic nanodiamonds does not reveal significant isotopic anomalies relative to standards.

6.5 Acknowledgments

This work is supported by NASA Grant NNX13AF53G (C.F.). We are indebted to Dr. Frank Stadermann whose ideas and enthusiasm this research is based upon. The LEAP tomograph at NUCAPT was acquired and upgraded with equipment grants from the NSF-MRI program (DMR- 0420532) and NRL-DURIP (N00014-0400798, N00014-0610539, N00014-0910781). This work made use of the EPIC facility (NUANCE Center- Northwestern University), which has received support from the MRSEC program (NSF DMR-1121262) at the Materials Research Center; the Nanoscale Science and Engineering Center (NSF EEC– 0647560) at the International Institute for Nanotechnology; and the State of Illinois, through the International Institute for Nanotechnology. Instrumentation at NUCAPT was supported by the Initiative for Sustainability and Energy at Northwestern.

6.6 References

Coplen T. B. et al. 2002. Isotope-abundance variations of selected elements (IUPAC technical report). *Pure and Applied Chemistry* 74:1987–2017.

Da Costa G., Vurpillot F., Bostel A., Bouet M., and Deconihout B. 2005. Design of a delay-line position-sensitive detector with improved performance. *Review of Scientific Instruments* 76:013304.

Dai Z. R., Bradley J. P., Joswiak D. J., Brownlee D. E., Hill H. G. M., and Genge M. J. 2002. Possible in situ formation of meteoritic nanodiamonds in the early Solar System. *Nature* 418:157–159.

Daulton T. L., Eisenhour D. D., Bernatowicz T. J., Lewis R. S., and Buseck P. R. 1996. Genesis of presolar diamonds: Comparative high-resolution transmission electron microscopy

study of meteoritic and terrestrial nano-diamonds. *Geochimica et Cosmochimica Acta* 60:4853–4872.

Deming W. E., and Stephan F. F. 1940. On a least squares adjustment of a sampled frequency table when the expected marginal totals are known. *The Annals of Mathematical Statistics* 11:427–444.

Everitt B. S. 1992. *The analysis of contingency tables*, 2nd ed. Boca Raton: Chapman & Hall.

Greiner N. R., Phillips D. S., Johnson J. D., and Volk F. 1988. Diamonds in detonation soot. *Nature* 333:440–442.

Heck P. R. et al. 2014. Atom-probe analyses of nanodiamonds from Allende. *Meteoritics & Planetary Science* 49:453–467.

Hudson D., Smith G. D. W., and Gault B. 2011. Optimisation of mass ranging for atom probe microanalysis and application to the corrosion processes in Zr alloys. *Special Issue: 52nd International Field Emission Symposium* 111:480–486.

Kelly T. F., and Miller M. K. 2007. Invited review article: Atom probe tomography. *Review of Scientific Instruments* 78:031101.

Larson D. J., Prosa T. J., Ulfig R. M., Geiser B. P., and Kelly T. F. 2013. *Local electrode atom probe tomography - A user's guide*, 1st ed. New York: Springer-Verlag.

Lewis R. S., Ming T., Wacker J. F., Anders E., and Steel E. 1987. Interstellar diamonds in meteorites. *Nature* 326:160–162.

Lewis R. S., Anders E., and Draine B. T. 1989. Properties, detectability and origin of interstellar diamonds in meteorites. *Nature* 339:117–121.

Lewis J. B., Isheim D., Floss C., Daulton T. L., and Seidman D. N. 2014a. Deadtime correction and hydride evaluation for atom-probe data, with applications for studies of nanoscale grains and carbon. *Microscopy and Microanalysis* 20:1768–1769.

Lewis J. B., Isheim D., Floss C., Groopman E., Gyngard F., and Seidman D. N. 2014b. Isotopic composition and trace element abundances of a presolar SiC AB grain reconstructed by atom-probe tomography. *77th Annual Meteoritical Society Meeting*. Abstract #5367.

Lewis J. B., Isheim D., Floss C., Daulton T. L., and Seidman D. N. 2015. Nanodiamond analysis methods compared for consistency. *46th Lunar and Planetary Science Conference*. Abstract #1480.

Marty B., Chaussidon M., Wiens R. C., Jurewicz A. J. G., and Burnett D. S. 2011. A ^{15}N-poor isotopic composition for the Solar System as shown by genesis solar wind samples. *Science* 332:1533–1536.

Menand A., and Kingham D. R. 1985. Evidence for the quantum mechanical tunnelling of boron ions. *Journal of Physics C: Solid State Physics* 18:4539.

Miller M. K., and Hetherington M. G. 1991. Local magnification effects in the atom probe. *Surface Science* 246:442–449.

Nishikawa O. et al. 1999. Atomic level analysis of electron emitter surfaces by the scanning atom probe. *Applied Surface Science* 146:398–407.

Russell S. S., Arden J. W., and Pillinger C. T. 1996. A carbon and nitrogen isotope study of diamond from primitive chondrites. *Meteoritics & Planetary Science* 31:343–355.

Saxey D. W. 2011. Correlated ion analysis and the interpretation of atom probe mass spectra. *Ultramicroscopy* 111:473–479.

Seidman D. N. 2007. Three-dimensional atom-probe tomography: Advances and applications. *Annual Review of Materials Research* 37:127–158.

Seidman D. N., and Stiller K. 2009a. An atom-probe tomography primer. *MRS Bulletin* 34:717–724.

Seidman D. N., and Stiller K. 2009b. A renaissance in atom-probe tomography. *Materials Research Society Bulletin* 34:717–749.

Stadermann F. J. et al. 2011. Atom-probe tomographic characterization of meteoritic nanodiamonds and presolar SiC. *42nd Lunar and Planetary Science Conference.* Abstract #1595.

Stroud R. M., Chisholm M. F., Heck P. R., Alexander C. M. O., and Nittler L. R. 2011. Supernova shock-wave-induced co-formation of glassy carbon and nanodiamond. *The Astrophysical Journal Letters* 738:L27.

Tsong T. T. 1978. Field ion image formation. *Surface Science* 70:211–233.

Valley J. W. et al. 2014. Hadean age for a post-magma-ocean zircon confirmed by atom-probe tomography. *Nature Geoscience* 7:219–223.

Verchovsky A. P., Fisenko A. V., Semjonova L. F., Bridges J. C., Lee M. R., and Wright I. P. 2006. Nanodiamonds from AGB stars: A new type of presolar grain in meteorites. *The Astrophysical Journal* 651:481.

Vurpillot F., Gault B., Vella A., Bouet M., and Deconihout B. 2006. Estimation of the cooling times for a metallic tip under laser illumination. *Applied Physics Letters* 88:094105.

Zinner E. 2014. Presolar grains. In *Treatise on geochemistry*, 2nd ed. Elsevier. pp. 181–213.

Chapter 7: Origins of Meteoritic Nanodiamonds through Isotopic and Complementary TEM Studies

7.1 Introduction

Prior chapters have detailed our work to assess the origins of meteoritic nanodiamonds based on their $^{12}C/^{13}C$ isotopic ratios:

The presence of a small fraction of isotopically anomalous material is suggested by the statistical study of thousands of ratio measurements from small aggregates of nanodiamonds (Lewis et al. 2017, Chapter 3). That chapter reported the adaptation of NanoSIMS imaging for use as a serialized cluster analysis technique. The presence of a small fraction of highly ^{13}C-enriched grains are indicated, and these grains are consistent with formation from Type II supernova material, which is also suggested by Xe-HL observed in the nanodiamonds by gas mass spectrometry of trace components released by stepped-heating of aggregates of billions of nanodiamonds. Asymptotic giant branch (AGB) stars can produce ^{13}C-enriched grains, but the degree of enrichment required to explain the observed outliers makes AGB stars a poor candidate. J-stars and novae are also candidates to produce highly ^{13}C-enriched grains, but the concentration of J-star and novae grains amongst other presolar phases such as SiC is very low, so it is difficult to understand why these sources would produce nanodiamonds given that we do not observe evidence to support many more supernovae and AGB-produced nanodiamonds. The bulk $^{12}C/^{13}C$ isotopic ratio in Chapter 3 is within 2σ of solar, but is ^{13}C-enriched at the 1σ level compared to previous bulk measurements, which show consistent ^{13}C depletion on the order of 20–30‰ (Russell et al. 1991, 1996; Swart et al. 1983). A number of ^{13}C-depleted grains,

probably from supernovae, or possibly from AGB stars, could explain this shift. Finally, Chapter 3 reported the detection of broadening in the distribution of isotopic ratios from Allende compared to all of the measured standards, implying that the isotopic ratio is not drawn from a single reservoir.

Measurements of C isotopic ratios from individual nanodiamonds and clusters containing 1–10 nanodiamonds have revealed reproducible results, but also unidentified experimental artifacts. The technique for these studies of individual nanodiamonds, atom-probe tomography (APT), has been adapted from materials physics and industry, and collaborative efforts have refined the sample preparation technique, leading to better sample stability under analysis conditions in the atom-probe (Heck et al. 2014, Chapter 4). But the measured $^{12}C/^{13}C$ isotopic ratio of detonation nanodiamond standards of roughly 60/1 is systematically lower than the known solar system value of 89/1 (Coplen et al. 2002). A few data sets have isotopic ratios with large ^{13}C enrichment compared to the mean ratio, but without careful normalization and statistical analysis the significance of these data sets has been unclear.

Attempts to quantify various sources of error, including multihit signal loss, deadtime and deadspace effects, detector pileup, and ^{12}CH hydride interference with ^{13}C, have explained only a small fraction of this systematic effect. Improved procedures have been introduced for data reduction, differentiation between acid residue and the Pt matrix, and quantification of isotopes from mass spectra. Additional data sets processed using these procedures confirm the presence of an unidentified systematic artifact that leads to an estimate of the $^{12}C/^{13}C$ that is too low (Lewis et al. 2016; Stephan et al. 2015; Chapters 5 and 6).

To continue this work, I have conducted and herein describe and discuss additional APT measurements, correlated with transmission electron microscopy (TEM) and SEM data, which give me a large enough number of atom-probe data sets to carry out statistical analyses analogous to those presented in Lewis et al. (2017) (Chapter 3), in this case with aggregate sizes down to one nanodiamond in a data set. Because atom-probe collects time-of-flight mass spectra I am also able to conduct studies of various molecular forms of C, and other species associated with the nanodiamond-containing acid residue. These studies allow me to qualitatively distinguish atom-probe data sets that are dominated by disordered C from those that are dominated by nanodiamonds, and assess these two phases for differences in C isotopic contents.

7.2 Methods

Additional samples of meteoritic nanodiamonds in acid residues have been analyzed by APT. This brings the number of meteoritic nanodiamond data sets collected by atom probe (36 data sets with good isotopic data from the Allende acid residues) high enough for statistical analyses. This chapter details these analyses. When applicable, the statistical analyses are conducted and presented using similar procedures to those employed collecting the NanoSIMS data used in Lewis et al. (2017) (Chapter 3). An essential step in this process is the normalization of isotopic ratios from the meteoritic nanodiamonds using the ratios collected from terrestrial standards. This effectively corrects for the portion of the still unknown instrumental artifact in the atom-probe that affects all microtips to the same degree. We take this step only after intense study of the problem, and using a procedure analogous to what has become standard for other isotopic measurement techniques. For example, hotspots in isotopic ratio in NanoSIMS isotopic images are normalized to the mean ratio of the remaining pixels in the image, without identification and

quantification of all of the artifacts present that cause that background ratio measurement to initially be incorrect.

In addition to normalization of the meteoritic isotopic ratios, we carry out additional analysis work, including studies of the effects of different sample preparation and reconstruction parameters, assessment of different methods for selecting the portion of the data set that contains information about the acid residue, and better techniques for peak selection and noise, tail, and multihit corrections. Finally, techniques introduced in Lewis et al. (2017) (Chapter 3) are also used to assess the sensitivity of our method to isotopic anomalies in individual nanodiamonds.

Another focus of this chapter is to distinguish between the disordered C and nanodiamonds. Both the NanosSIMS and APT approaches have, to date, not distinguished between different types of carbonaceous material in the acid residue. This is problematic, as a significant fraction of the residue is composed of sp^2-bonded disordered C, probably about half (Bernatowicz et al. 1990; Stroud et al. 2011). It is unknown whether these residues have the same origin as the nanodiamonds, so it is desirable to study the phases separately.

Previous atom-probe studies of nanodiamonds have used only SEM for characterization of nanodiamond-containing microtips prior to their introduction to the atom-probe for analysis. To further assist in distinguishing between the two phases of carbon in the acid residues, we collected TEM data from microtips prepared for APT with embedded acid residue. Some of these microtips were subsequently analyzed by APT, yielding not just complementary, but also correlated data.

The methodology used in this chapter builds on that described in Chapter 2 and the methods sections of Heck et al. (2014) and Lewis et al. (2015 and 2017) (Chapters 3, 4, and 6). Here we

include additional material. This includes sections on the isotopic ratios of the terrestrial detonation nanodiamonds used to normalize the material (7.2.1), focused ion beam microscopy (7.2.2), transmission electron microscopy (7.2.3), atom-probe tomography (7.2.4), and details of atom-probe data reduction (7.2.5) and analysis methods (7.2.6) used in this chapter.

7.2.1 Samples and Sample Preparation

Nanodiamond-containing acid residue is separated from the Allende meteorite by a series of dissolution, disaggregation, and sorting processes, and deposited onto a gold-covered steel disk for transport (see Section 2.1).

Multilayers with acid residue deposited between two layers of IBS-deposited Pt were then prepared for FIB liftout (see Section 2.3.1).

Liftouts from multilayer pND3 contain more Na contamination and fewer isolated ~3 nm spheres of C (presumably nanodiamonds) in the deposition layer, compared to the previous multilayer, pND. The droplet used to suspend acid residue for transfer from Au foil to a Pt substrate for multilayer pND3 was larger than the droplet used for pND. The larger droplet contained a greater total amount of acid residue, such that when the liquid evaporated there was a larger density of acid residue material deposited, which presumably trapped more of the nanodiamonds in large chunks of disordered C. Furthermore this droplet took longer to evaporate, meaning the deposit was exposed to atmosphere longer before a top layer of sputter-deposited Pt could cover it. This could lead to higher N and O contamination from the atmosphere, and may have given more time for Na to aggregate into clusters compared to multilayer pND.

Terrestrial detonation nanodiamond standards were prepared using the same procedure as for the Allende nanodiamonds. Greiner et al. (1988) report that these nanodiamonds are 4 nm in

diameter in one preparation and 7 nm in a different preparation. These nanodiamonds are created from controlled combustion of RDX and TNT explosives. In a study of 100 samples of RDX from 12 factories, $\delta^{13}C$ ranges from -49.5‰ to -16.6‰ relative to VPDB (Howa et al. 2014). For at least one sample of TNT, the $\delta^{13}C$ = -28.2±0.1‰ normalized to PDB (Coffin et al. 2001). Anisichkin (2007) report the natural ratio of one of the two combustion materials, RDX, as $^{13}C/^{12}C$ = 0.011, but it seems likely they reported a low-precision value from the literature, rather than reporting a measurement they conducted. Regardless, they do not report uncertainty, so we must assume the range is at least from $^{13}C/^{12}C$ = 0.0105–0.0114, which corresponds to a range of $^{12}C/^{13}C$ values from 95.2 to 87.7 and $\delta^{13}C$ from -66 to +14‰. Anisichkin (2007) does not report the natural isotopic ratio of the other combustion material, TNT, likely because it was ^{13}C-labelled prior to use, making the natural ratio irrelevant to that study. Furthermore, it is unclear if any fractionation occurs during combustion formation of the nanodiamonds.

26 atom-probe microtips containing detonation nanodiamonds were prepared by the same methodology as the microtips containing Allende nanodiamonds, and used as standards.

7.2.2 Focused Ion Beam Microscopy

An FEI Quanta 3D FIB microscope with SE imaging, an Omniprobe micromanipulator, and a Pt GIS was used to conduct cross-sectional liftouts of the deposition layer, trim and attach slices of the liftouts to polished Si microposts (for APT only) or Cu microposts (for correlated TEM/APT), and sharpen the slices into microtips of ~20 nm in diameter, with acid residue in the deposition layer aligned at the apex (see Sections 2.3.2–2.3.5). These microtips are suitably thin for transmission of 200 kV electrons in TEM and for field-evaporation of ions from the apex in APT. We used 30 kV Ga^+ ions to mill material in the FIB, and 5 kV Ga^+ ions for final passes on microtips to minimize the depth to which Ga is implanted in the final sample.

7.2.3 Transmission Electron Microscopy

We conducted transmission electron microscopy using the 200 kV JEOL 2100F TEM / HAADF STEM at Washington University in the Institute for Materials Science and Engineering. Tyrone Daulton operated the instrument while I observed and identified regions of interest. The vacuum in the TEM column near the specimen was on the order of 0.8×10^{-5} Pa (6×10^{-8} Torr).

For energy dispersive x-ray spectrometry (EDXS) the TEM is equipped with a Bruker Quantax 200 STEM EDXS system, which has a 60 mm^2 active area detector with an energy resolution of 133 eV for the full width half max of Mn Kα.

For electron energy loss spectrometry (EELS) the TEM is equipped with a Gatan Model 863 Tridiem electron energy-imaging filter (GIF). The GIF has a 2048×2048 pixel, 16-bit CCD camera. Spectra were corrected for dark current and channel-to-channel gain variation of the GIF CCD detector array and collected in the diffraction mode of the TEM. To collect an EELS spectrum we first collected a core-loss spectrum (~175 eV–790 eV) at each pixel inside the region of interest. The spatial resolution of the spectral image is defined by the nominal probe diameter of 0.2 nm. Power-law background was calculated and subtracted from each edge by fitting to the region just below the edge. C and O edge signals were integrated over an energy window 45 eV wide, so that effects of thickness variations in the specimen (i.e., plural scattering effects) would be the same for each of the measured elements. Ratios of integrated EELS core-loss signal between C and O were converted into their corresponding atomic ratios using partial cross sections that were calculated from theoretical Hartree-Slater models. Using these relative elemental compositions allows us to avoid artifacts due to variations in specimen thickness and electron diffraction.

One half-grid, HG04, was prepared so that the deposition layer could be imaged edge-on (Figure 7.1a). This orientation makes it easier to identify material in the deposition layer by imaging and elementally-sensitive techniques such as EELS and EDXS, at the expense of losing information about the number and arrangement of nanodiamonds in the deposition layer. Most samples were analyzed with the electron beam perpendicular to the plane of the deposition layer (Figure 7.1b). In this orientation we were best able to map out the contents of the deposition layer for later correlation to atom-probe data.

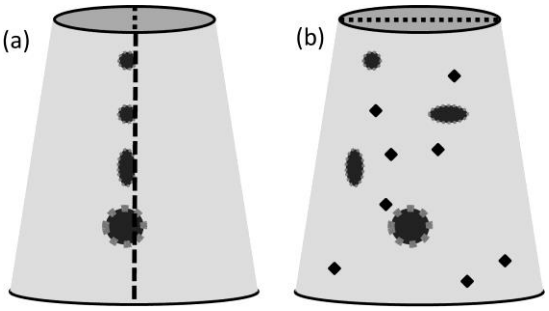

Figure 7.1 Schematic of a section of a microtip in two different imaging orientations: (a) shows the perspective for the TEM with the electron beam parallel to the deposition layer, edge-on. (b) shows the perspective of the TEM with the electron beam perpendicular, face-on to the deposition layer.

Prior to analysis, the half-grids on which the samples were mounted were electron irradiated for one-half to one hour, a "beam shower," designed to crack and immobilize hydrocarbons on the half-grid so that when we focused the electron beam on our microtips, hydrocarbon would not migrate to that area and accumulate.

Electrons were able to penetrate the microtips sufficiently for imaging up to a microtip radius of about 50 nm.

We used three primary types of imaging, traditional TEM, STEM HAADF (scanning transmission electron microscopy high angle annular dark field), and STEM BF (bright field). Each is sensitive to different attributes of the sample, and are variously affected by artifacts and

features which may, taken in isolation, be misinterpreted. The image contrast of STEM HAADF depends primarily on Z-contrast. Since our samples are composed of carbonaceous acid residue (z = 6 for C) embedded inside Pt (z = 78 for Pt), regions of the microtip containing nanodiamonds, disordered C, or voids will be visible as darker regions in STEM HAADF. Such features may also produce brighter contrast in STEM BF, but STEM BF is also dependent on diffraction effects, so interpretation of these images is more nuanced.

We examined the images for void-like features a few nanometers in size. These are tentatively identified as nanodiamonds. In a few samples, imaging at various tilts helped rule out artifacts.

Fast Fourier transforms (FFTs) of conventional TEM images were used to identify potential diamond diffraction signals, which were followed up by collecting diffraction images. Diffraction patterns were analyzed using software written by Tyrone Daulton (Daulton et al. 2010).

7.2.4 Atom-probe Tomography

I used the LEAP 4000X Si local electrode atom-probe tomograph at Northwestern University in Evanston, Illinois, to collect data for isotopic analyses, and, in the case of microtips HG01-B and –C, for correlated APT/TEM. This instrument is rated to 57% ionic detection efficiency, that is, position and time-of-flight data are recorded for 57% of the ions originally located inside the field of view in the microtip. The first several ADM data sets presented were collected prior to a laser upgrade to the instrument (described in detail in Section 4.2). The laser spot size was larger for these data sets, and higher laser energies were used, because the energy density of the laser was roughly ¼ that of later experiments.

The LEAP 5000X Si atom-probe tomograph at Cameca's application lab in Madison, Wisconsin, was used to analyze the correlated TEM/APT microtips from half grids HG05 and HG06, but of these, only two samples (HG05-E and HG06-C) survived long enough to collect Pt from the microtips, and only about 1 million Pt ions were collected from each sample. The LEAP 5000X Si is rated for a detection efficiency of about 80%. Compared to the LEAP 4000X Si it has improved multihit discrimination capabilities, a larger field of view, and improved laser control algorithms.

7.2.5 Atom-probe Data Correction and Normalization

After the initial reconstruction of a data set collected during APT (Section 2.3.8), I identified peaks in the mass-to-charge state spectrum and selected the sequence of bins whose contents will be summed over for the counts at that peak. This sequence of bins is known as a range, peak, or mass window. Lewis et al. (2015) (Chapter 6) define a peak in the mass-to-charge-state spectrum of an APT data set by using a 0.01 amu bin size, selecting the first bin to rise above twice the average value of the local noise as the start of the sequence, and selecting the first bin to drop back below twice the average of the local noise as the end of the sequence (Figure 7.2). In the current chapter I used a different criterion. First, the background was calculated based on a fit to the whole mass spectrum, and subtracted. For a given element and charge state I selected the major isotope and adjusted the bin size until the full width at half max (FWHM) lay inside of exactly five bins. The software utilized offers a limited number of options for bin size. If the selectable bin sizes skipped over the size that would capture the FWHM inside of exactly five bins, I used a bin size that captures the FWHM in 6 or 4 bins, in that order of preference. I used the same width to range all other isotopes of the same element and charge state (e.g., I used the same width for the peak at 13 amu as for that at 12 amu, but for 6.5 amu I used the width for 6

amu). In this way I used the peak with higher counts to give information on the peak width, assuming that neighboring isotopes have similar widths as a result of similar evaporation conditions. As with other methods of range fitting, this is only an approximation to the peak shape, and does not take into account the small difference between mass-to-charge state width expected between the ^{12}C and ^{13}C peaks as a result of converting from time-of-flight to mass-to-charge-state ratio. Still, to first order this method preserves similarity between different isotopes, which is the primary concern.

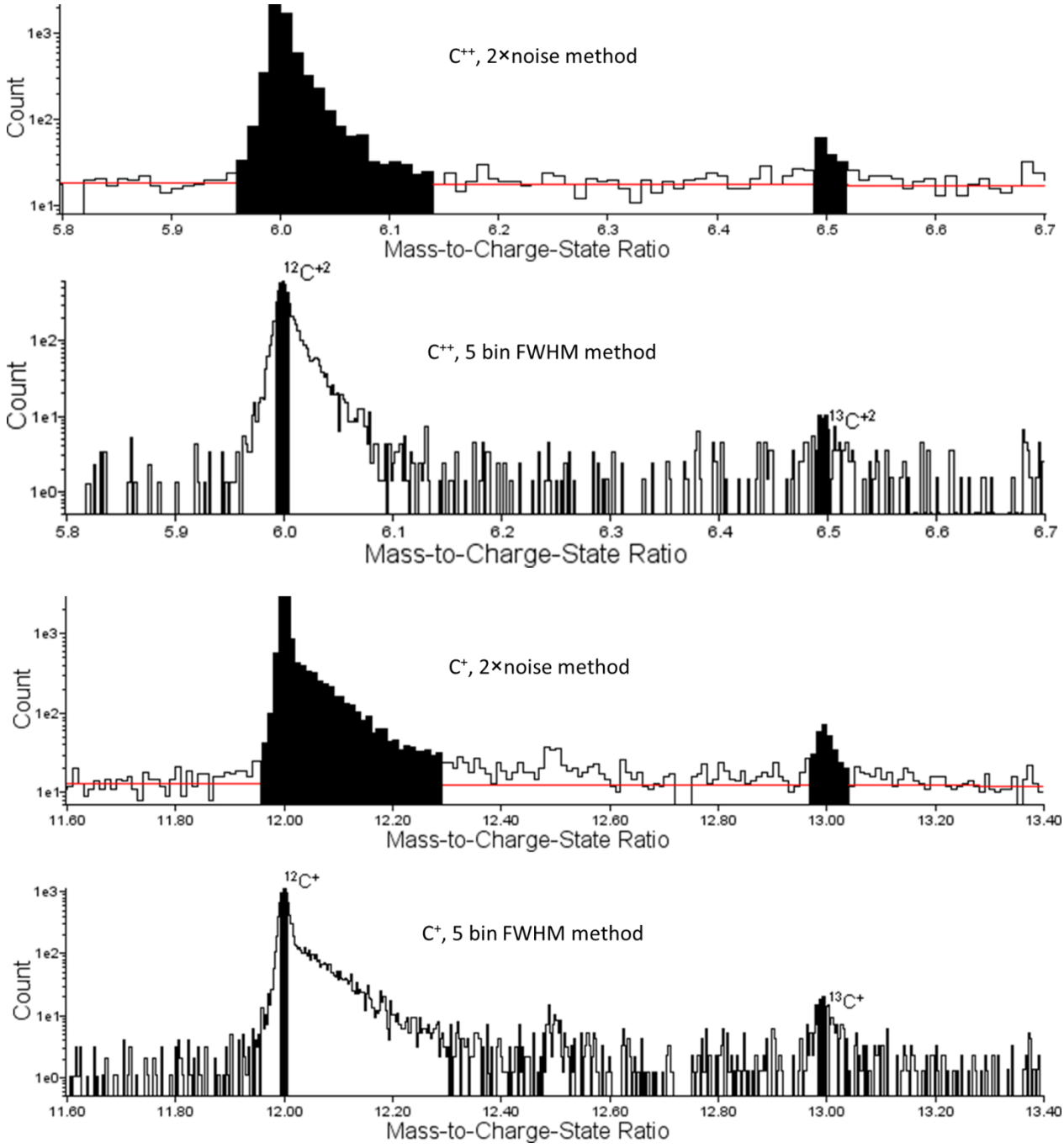

Figure 7.2 Mass spectra from a 20 nm wide rectangular solid region of interest that encapsulates the deposition layer in data set ADM 18430. Two sections of the spectrum are shown, one with $^{12}C^{++}$ and $^{13}C^{++}$ at 6 and 6.5 amu, respectively, the other with $^{12}C^{+}$ and $^{13}C^{+}$ at 12 and 13 amu. For each section two versions are shown: one using the twice-noise peak selection method from Chapters 4 and 6, with 0.01 amu per bin. The calculated fit to the background of the whole spectrum is displayed (red line). The other version uses a bin width that allows for the FWHM of the major isotope (^{12}C) to be ranged with five bins, and uses the same width for the minor isotope (^{13}C). In these images the background has been subtracted.

After ranging peaks I selected a region of interest (ROI) that is a sub-section of the reconstructed volume defined by one of three criteria. Isoconcentration (I.C.) surfaces divide regions with concentration below a certain fraction from regions with concentration above that fraction. Concentration is the counts of a certain species detected in a volume, typically C, C_2, C_3, and PtOC ions, divided by the sum total of all identified ions detected in that volume. Isodensity (I.D.) surfaces divide the volumes with more or less than a certain density of C atoms detected per nm^3 of the reconstructed volume. Finally, the region of interest can also be a rectangular solid fit to the approximate bounds of the deposition layer (D.L.).

For each region of interest I re-ranged the peaks of interest in the mass spectrum, since differences in local field evaporation conditions may lead to different peak shapes.

Up to this step most of the data reduction and analysis was done using IVAS, the Imago Visualization and Analysis System (Cameca Instruments Inc., (Kunicki et al. 2006)). To compile counts and background estimates from multiple reconstructions, I used Python scripting (Appendix 3).

For $^{12}C/^{13}C$, corrected but not yet normalized, ^{12}C and ^{13}C were each calculated as

$$^{i}C = {}^{i}C_{raw} - {}^{i}C_{noise} - {}^{i}C_{tail} + {}^{i}C_{multi} \quad (7.1)$$

C_{raw} is the uncorrected counts that fall inside of the selected peak width. C_{noise} is given by fitting the background of the entire time of flight spectrum by the IVAS software. C_{tail} contributions are additional background that is produced by the overlap of a tail in a peak from slightly lower mass-to-charge state ratio (e.g., the mass window for $^{13}C^{++}$ may contain some counts from the tail of the $^{12}C^{++}$ peak). Corrections were calculated by sampling the height of the tail above the background estimate at a mass-to-charge-state just lower than that of the peak (averaging this

with another window immediately after the peak is also useful, so long as the peak's own tail does not contribute significantly). The IVAS software can save multihit data from reconstructions, but for ROIs it can only save position and mass data, not multihit data. So in order to find C_{multi} corrections for a region of interest we first filtered the multi-hit data for the region of interest out of the data set for the entire experimental run, which usually includes a large volume of Pt matrix. To do this we compared the mass and position data for the region of interest with that recorded for the entire data set, atom-by-atom, and saved the multihit data for the atoms contained in the region of interest. The script for this procedure is recorded in Appendix 4. Multi-hit corrections are based on theory described in Lewis et al. (2015) (Chapter 6), using the script recorded in Appendix 1.

The counts from reconstructed and fitted APT data set ROIs, used for ratio calculations and normalization, are reported in Appendix 5, along with the temperature and laser energy used for the collection of each data set.

The uncertainty in each of the four components of C is given by the square root of the counts in that component, and the uncertainty in the corrected counts is the sum in quadrature of those uncertainties, which simplifies to

$$Err(\ {}^{i}C) = \sqrt{{}^{i}C_{raw} + {}^{i}C_{noise} + {}^{i}C_{tail} + {}^{i}C_{multi}} \tag{7.2}$$

Any ratio of C isotope and charge state may now be calculated as $R = {}^{i}C^{j}/{}^{k}C^{l}$, along with the absolute uncertainty, given by

$$Err(R) = \frac{{}^{i}\mathrm{C}^{j}}{{}^{k}\mathrm{C}^{l}} \times \sqrt{\left(\frac{Err(\ {}^{i}C^{j})}{{}^{i}C^{j}}\right)^{2} + \left(\frac{Err(\ {}^{k}C^{l})}{{}^{k}C^{l}}\right)^{2}} \tag{7.3}$$

I used a direct method to calculate the bulk ratio, not a mean:

$$\overline{R} = \frac{\sum_i {}^{13}C_i}{\sum_i {}^{12}C_i} \tag{7.4}$$

This is to avoid statistical artifacts introduced by even a weighted mean of ratios (Ogliore et al. 2011).

The weighted standard deviation was calculated as

$$\sigma = \sqrt{\frac{\sum_i w_i}{(\sum_i w_i)^2 - \sum_i {w_i}^2} \times \sum_i w_i (R_i - \overline{R})^2} \tag{7.5}$$

where weights are defined as $(1/\mathrm{Err}(R_i))^2$. The standard error of the mean (SEOM) is

$$\sigma_{\overline{R}} = \frac{\sigma}{\sqrt{n}} \tag{7.6}$$

where σ and $\sigma_{\overline{R}}$ are the statistical attributes of the Gaussian distribution that best describes the normalized data points, but use the direct bulk ratio rather than the weighted mean of the data points. σ represents a good prediction of the deviation from the mean one would observe from additional individual measurements, and $\sigma_{\overline{R}}$ is a good predication of how much one's calculation of the mean would vary if the experiment were perfectly reproduced. What they do not represent is the uncertainty derived from the counting statistics on the C counts for each DND and ADM data set using the calculus of partial derivatives; those values are given as *Err(R)* and *Err($\overline{R}$)*.

I normalized the ratios based on the ratios of the standards. The normalized δ^{13}C for a given ^{13}C/^{12}C ratio, *R* is

$$\delta^{13}C = \left(\frac{R}{R_{standard}} - 1\right) \times 1000 \tag{7.7}$$

I used the weighted direct bulk ratio from all 26 of the synthetic detonation nanodiamond data sets as $R_{standard}$. The normalized per mil value can be converted into normalized $^{12}C/^{13}C$ or $^{13}C/^{12}C$ using the known solar system isotopic ratio in place of $R_{standard}$:

$$\delta^{13}C = \left(\frac{R_{normalized}}{R_{solar\ system}} - 1\right) \times 1000 \tag{7.8}$$

Substituting Equation 7.8 into Equation 7.7, the expression reduces into the simple expression to directly calculate the normalized ratio:

$$R_{normalized} = \left(\frac{R_{solar\ system}}{R_{standard}}\right) \times R \tag{7.9}$$

The uncertainty in the normalized ratio is

$$Err(R_{normalized}) = \mathrm{R}_{normalized} \times \sqrt{\left(\frac{Err(R)}{R}\right)^2 + \left(\frac{\sigma_{Rstandard}}{\overline{R}_{standard}}\right)^2} \tag{7.10}$$

This is the expression for normalization of a ratio from a single data set, where $\sigma_{Rstandard}$, the weighted standard deviation of the standard ratio measurements, correctly represents how much a single new measurement is expected to vary from the mean. The bulk normalized ratio uses the counts-based $Err(R_{standard})$ in place of $\sigma_{Rstandard}$. The standard error of the mean $\sigma_{\overline{R}standard}$ is the technically correct value for the uncertainty in the mean of a distribution, but I use a direct bulk method, not a mean, for R. I used $^{13}C/^{12}C = 0.01124$ ($^{12}C/^{13}C = 89$) as the terrestrial ratio $R_{solar\ system}$. It is to be expected that the synthetic detonation nanodiamonds will differ from this value by several per mil, however, in the absence of a thorough study of the topic, and the presence of large uncertainties in our data, this uncorrected systematic error is a second-order concern. Indeed, terrestrial materials have a range of about (-80–0)‰ from $^{12}C/^{13}C = 89$ (Coplen et al. 2002).

The mean normalized ratio, normalized standard deviation of the ratio, and SEOM were calculated using the same processes that were used for the un-normalized values.

The above is the first of two approaches I used to normalize isotopic ratios calculated from APT data sets. To summarize, separate samples were measured with similar material (nanodiamond acid residue) and the same microtip preparation, data collection, and data reduction methods. There are two limitations to this method. It is impossible to perfectly reproduce the sample preparation and data collection procedures. It is also impossible to know for certain that the same procedures produce similar samples and data collection conditions. SEM and TEM pre- and post-analysis imaging, atom-probe parameter settings, and measurements of experimental conditions can give a significant amount of information about sample preparation and data analysis, but the spatial resolution of SEM, limitations in identification of C phases in the TEM, and inability to perfectly measure the nm-scale local field and temperature conditions for atom-probe data collection still limit the completeness of information that can be collated about a data set. Thus one cannot be sure of one-to-one correspondence between a sample and the standard used to normalize an isotopic ratio measurement.

For data sets that had C isotopic ratios at least 4σ from the mean of the distribution, I used an additional step. I used the isotopic ratio of the C in the Pt matrix surrounding the nanodiamond-containing acid residue to self-standardize data set by data set by directly comparing the two ratios. This removed any doubt that a sample and its standard underwent the same preparation steps, since they are in fact the same sample. However, measuring C isotopic ratios from two different materials, even in the same microtip, introduces potentially significant differences in experimental artifacts, count rates, local electric field and temperature, and may be affected by imperfect reconstructions that mis-assign detected C ions to standard or sample (e.g., due to the

higher evaporation field for carbonaceous materials compared to Pt, trajectory aberrations may cause ions originating in the acid residue to be projected onto areas of the detector where the Pt matrix is detected).

7.2.6 Criteria to Assess Disordered C vs. Diamond in APT Reconstructions

I use the ratio of (PtOC+Na+NaO)/(C_1+2×C_2+3×C_3) as a qualitative assessment of the fraction of the acid residue that is composed of disordered C vs. the fraction that is composed of diamond.

The disordered C is composed of loosely packed fragments of curved sheets; it is primarily sp^2-bonded, lacks long range order, and is less dense than diamond (Stroud et al. 2011). These features, along with its survival of harsh chemical treatments, lead Stroud et al. (2011) to identify this particular phase of disordered C as glassy C, not to be confused with amorphous C (Harris 2004). It likely has a very high surface to volume ratio compared to nanodiamond, due to the exposed surfaces of the many loosely packed sheet fragments. This is in spite of the high surface/volume ratio for the nanodiamonds (about half of the C atoms are within one or two unit cells of the surface).

Na and NaO are probably from laboratory contamination, and possibly from minerals that were dissolved during acid processing of the meteorite. In APT reconstructions they are almost always spatially correlated with PtOC rather than C molecules, and they are often present in clusters. Concentrated PtOC indicates regions where exposed surfaces in the acid residue deposit experienced Pt deposition. On the other hand, C is more likely to form C_1, C_2, and C_3 clusters if it is isolated from species other than C, such as embedded inside of a diamond lattice. Thus, higher (PtOC+Na+NaO)/(C_1+2×C_2+3×C_3) ratios suggest the presence of more porous material, and thus infer a higher fraction of disordered C compared to diamond. I used ionic counts rather

than atomic counts in my calculations – (e.g., PtOC counts as one (ion), not three (atoms)), although we do not see differences in the trends regardless of which was used.

The N/O ratios of the microtips were used as another criterion to distinguish nanodiamonds from disordered C. TEM observations by Stroud et al. (2011) show that N in the acid residues is typically fixed in or on the nanodiamonds, while O tends to be more mobile, moving through the disordered C.

Thus two independent sets of measurable quantities are available to give qualitative insights on the disordered C and diamond contents of the acid residue: (PtOC+Na+NaO) vs. (C_1+2×C_2+3×C_3) and O vs N.

7.3 Results

7.3.1 Atom-probe Results

The overall bulk $^{12}C/^{13}C$ ratio from the carbon in the 36 APT data sets is 98±26‰ for the ratio of C^+ isotopes and -192‰±47‰ for C^{++} (Table 7.1). This is after normalization to the bulk ratio of the carbon isotopes in the 26 DND standard data sets. Figure 7.3 gives a graphical representation of the bulk values, compared to the results of other studies. σ and SEOM are calculated based on the statistical distribution of the data set ratios about that mean value, whereas the uncertainty in the ratio, $Err(R_{normalized})$, is calculated purely based on error propagation calculus using the uncertainty on each ^{12}C and ^{13}C count for a data set. These two bulk measurements, both with large anomalies, bracket the terrestrial value. The bulk 1^+ ratio is closer to the recent NanoSIMS measurements of small clusters of millions of nanodiamonds by Lewis et al. (2017) (Chapter 3, see Figure 7.3), while the bulk 2^+ ratio is closer to the results of stepped heating measurements of billions of nanodiamonds (Russell et al. 1991, 1996; Swart et al. 1983). Both measurements of

the isotopic ratio are within 2σ of the terrestrial value using the standard deviation, but the bulk values do not agree with each other within 2×SEOM or the statistically calculated $2\times Err(R_{normalized})$.

Table 7.1 Atom-probe normalized mean data.

C^+	$R_{normalized}$	$Err(R_{normalized})$[a]	σ[b]	SEOM[c]
$\delta^{13}C$	98‰ ± 26‰		305‰	8‰
$^{13}C/^{12}C$	0.0123 ± 0.0003		0.0034	0.0001
$^{12}C/^{13}C$[d]	81	$^{+2}_{-2}$	+31 / -18	+1 / -1
C^{++}	$R_{normalized}$	$Err(R_{normalized})$	σ	SEOM
$\delta^{13}C$	-192‰ ± 47‰		168‰	6‰
$^{13}C/^{12}C$	0.0091 ± 0.0005		0.0019	0.0001
$^{12}C/^{13}C$[d]	110	$^{+7}_{-6}$	+29 / -19	+1 / -1

[a] Calculated based on counting statistics, $Err(R_{normalized})$ is the lower bound for our uncertainty in the bulk ratio, and does not include any systematic errors.

[b] σ is the approximation of the width of the distribution of isotopic ratios that would be constructed from infinite data sets. A good estimation for our uncertainty in the ratio for any additional data set measured, σ takes into account all uncertainties, known and unknown, that affected these measurements, assuming a good fit to a Gaussian.

[c] *SEOM*, the standard error of the mean, is based on σ and the number of data sets measured. It is the uncertainty in what mean value we would measure if we repeated our experiment with the same number of data sets.

[d] The uncertainties are asymmetric in $^{12}C/^{13}C$ because of the asymmetric effects low counts in the denominator has on a distribution of ratios.

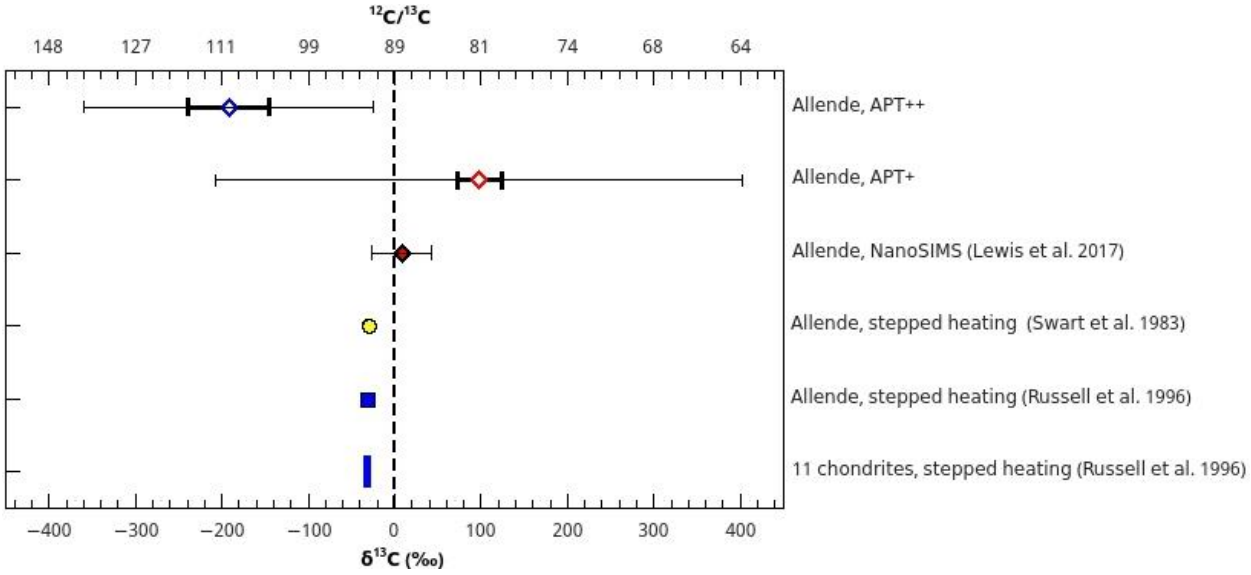

Figure 7.3 The isotopic ratio for all ADM data sets (Table 7.1) reported for ions taken from each charge-state, along with the weighted standard deviation of the distribution of atom-probe measurements (longer, thin bars) and counts-based statistical uncertainty in the bulk ratio (shorter, thick bars) calculated using the ratio and uncertainty from each data set. For comparison, the plot includes the results of studies of the isotopic ratio from Allende nanodiamonds by NanoSIMS with 1σ error bars (Lewis et al. 2017) and by stepped heating studies with uncertainties smaller than the symbol sizes (Russell et al. 1996; Swart et al. 1983) as well as the ratios from 11 different chondrites (Russell et al. 1991). The NanoSIMS error bars are calculated using the uncertainties in the fractional standard deviations of the distribution of the ADM data sets and that of the DND data sets.

Without normalization, the mean ADM $^{12}C^{+}/^{13}C^{+}$ ratio is slightly lower than the mean ADM $^{12}C^{++/13}C^{++}$ ratio, not significantly higher, as it is after normalization. The mean C^{++} ratio for the DND standards is lower than that of the C^{+} DND standards, leading to a different normalization factor.

Surprisingly, the scatter in the C^{++} ratios is significantly less than that for the C^{+} ratios, in spite of generally lower count rates and resultant higher counting statistics uncertainties (Figure 7.3). This suggests that there is an instrumental artifact that affects the C^{+} ratios more than it affects the C^{++} ratios.

7.3.2 Isotopic Outliers

The isotopic ratios and uncertainties of the individual data sets are presented in Table 7.2, along with the charge state ratio ($^{12}C^{+}/^{12}C^{++}$) and the total C counts (summed from all ions detected,

including C_1, C_2, C_3, PtOC, and CO_2). Given 50% detection efficiency, the actual amount of C in the volume is expected to be 2× greater than the reported counts. Assuming no additional sources of signal loss, this value can be used to approximate the amount of carbonaceous material measured, although the counts also include unknown, but probably small, amounts of C, primarily from the IBS-deposited Pt. The normalized ratios are presented graphically in Figure 7.4, which plots the C isotopic ratio at each charge state, as well as the data set name and the mean and terrestrial ratio values. Several data sets have large ^{13}C-enrichments in the C^+ ratio, but also high uncertainty (e.g., data sets ADM R06 15005, 19354, 23612, and 23617). Figure 7.5 plots isotopic ratios at charge states 1^+ and 2^+ against each other, highlighting their degree of agreement or disagreement not just with the terrestrial isotopic ratio but with each other. The ratios are generally within uncertainties of each other. A number of data points plot off the expected line of equal 1^+ and 2^+ ratios, with $^{12}C^{++}/^{13}C^{++}$ ratios higher than the corresponding $^{12}C^{+}/^{13}C^{+}$. This could be the result of over or under-detection of one or more of the peaks in the ADM or DND ratios. Measurement of too low of a DND $^{12}C^{++}/^{13}C^{++}$ ratio would cause this observed shift. There are also a few ADM $^{12}C^{+}/^{13}C^{+}$ ratios that are anomalously low, and these scatter about the solar system value for $^{12}C^{++}/^{13}C^{++}$.

Table 7.2 Experimental data.

Sample[a]	ROI[b]	$^{12}C^{+}/^{13}C^{+c}$	$^{12}C^{++}/^{13}C^{++c}$	$^{12}C^{+}/^{12}C^{++d}$	Counts[e]
ADM R06 15004 A36 M01[f]	I.D. 1 C/nm^3	60 +27 -14	118 + 57 -29	1.76±0.07	4596
ADM R06 15005 A36 M01[f]	I.D. 1 C/nm^3	40 +23 -11	89 + 42 -22	0.68±0.04	2575
ADM R06 16096 A47 M10[f]	I.D. 0.5 C/nm^3	56 +25 -13	127 + 56 -30	1.47±0.05	1438
ADM R06 16097v03 A47 M11[f,g]	I.D. 1 C/nm^3	74 +54 -22	82 + 49 -22	1.43±0.09	5903
ADM R06 16098 A47 M12[f]	I.D. 1 C/nm^3	105 +77 -31	*(179 + 177 -59)*	1.60±0.09	4825
ADM R06 16119 A47 M12[f]	I.D. 0.5 C/nm^3	109 +90 -34	*(152 + 260 -59)*	2.3±0.1	2265
ADM R06 16120 A47 M13[f]	I.D. 0.5 C/nm^3	70 +29 -16	150 + 62 -34	2.03±0.06	11995
ADM R06 18430 A65a M06[f]	D.L. 20 nm	61 +25 -14	112 + 40 -23	1.70±0.04	5721
ADM R06 18436 A65a M05[f]	I.C. 2.5% C C2 PtOC	79 +44 -21	85 + 35 -19	1.27±0.06	7926
ADM R06 18437 A65a M04[f]	D.L. 20 nm	75 +29 -16	117 + 33 -21	1.92±0.04	2318
ADM R06 19314 A62 M07[h]	D.L. 10 nm	85 +53 -24	*(100 + 78 -31)*	2.2±0.1	25417
ADM R06 19315 A62 M08[h]	D.L. 10 nm	75 +47 -21	*(263 + 772 -112)*	1.37±0.06	26342
ADM R06 19354 A62 M10[h]	D.L. 15 nm	17 +14 -5	59 + 617 -28	0.81±0.06	4111
ADM R06 19557 A70 M25[h]	D.L. 15 nm	104 +41 -23	120 + 34 -22	1.77±0.03	19956
ADM R06 19559 A70 M25[h]	D.L. 20 nm	88 +32 -19	138 + 34 -23	1.86±0.02	24774
ADM R06 19565 A70 M32[h]	I.C. C2 PtOC 1%	81 +32 -18	95 + 30 -18	2.40±0.06	7637
ADM R06 19566 A70 M33[h]	I.C. C 5%	84 +41 -21	110 + 42 -24	1.44±0.05	10986
ADM R06 19567 A70 M33[h]	D.L. 15 nm	105 +38 -22	117 + 28 -19	2.70±0.03	48118

Sample[a]	ROI[b]	$^{12}C^{+}/^{13}C^{+c}$	$^{12}C^{++}/^{13}C^{++c}$	$^{12}C^{+}/^{12}C^{++d}$	Counts[e]
ADM R06 19568 A70 M34[h]	I.C. 5% C C2 PtOC	138 + 60 -32	92 + 26 -17	2.01±0.05	3522
ADM R06 19572 A70 M35[h]	I.C. 5% C C2 PtOC	99 + 41 -22	112 + 34 -21	1.97±0.05	5331
ADM R06 20159 A78 M05[h]	I.C. 10% C C2 PtOC	78 + 34 -18	65 + 38 -18	7.6±0.4	19570
ADM R06 20163 A78 M12[h]	I.C. 1% C PtOC	85 + 37 -20	103 + 87 -32	5.8±0.2	2245
ADM R06 21164 A78 M25[h]	I.C. 2.5% C C2 PtOC	78 + 28 -16	134 + 41 -25	6.9±0.1	8191
ADM R06 21179 A78 M30[h]	I.C. 2.5% C C2 PtOC	92 + 36 -20	101 + 35 -21	4.2±0.1	20094
ADM R06 21180 A78 M29[g,h]	I.C. 2.5% C C2 PtOC	109 + 67 -30	*(143 + 202 -53)*	4.1±0.3	23705
ADM R06 21886 A84 M10[i]	I.C. 10% C	84 + 32 -18	87 + 26 -16	3.47±0.08	12054
ADM R06 21903 A84 M04[i]	D.L.15 nm	48 + 18 -10	69 + 21 -13	3.37±0.08	14664
ADM R06 22577 A94 M04[i]	I.D. 0.5 C/nm^3	54 + 30 -14	*(-305 + 758 191)*	12.7±1.7	3876
ADM R06 22582 A94 M18[i]	I.D. 1 C/nm^3	92 + 34 -20	97 + 32 -19	7.2±0.2	2747
ADM R06 22595 A94 M18[i]	I.D. 1 C/nm^3	66 + 32 -16	*(147 + 881 -68)*	7.7±0.6	2164
ADM R06 22596 A94 M18[i]	I.D. 0.5 C/nm^3	87 + 32 -19	172 + 128 -51	12.3±0.4	8490
ADM R06 22597 A94 M13[i]	I.D. 0.5 C/nm^3	60 + 23 -13	*(153 + 112 -45)*	8.5±0.3	2651
ADM R06 22598 A94 M13[i]	I.D. 0.5 C/nm^3	72 + 45 -20	*(68 + 128 -27)*	6.8±0.7	2986
ADM R06 23612 A98 M21[i]	D.L. 10 nm	36 + 32 -11	*(97 - 260 -59)*	3.8±0.4	6457
ADM R06 23617 A94 M19[i]	D.L. edge	25 + 19 -8	*(112 - 2194 -58)*	1.5±0.1	51793
ADM R06 23619 A94 M20[i]	D.L. 0.25 C	99 + 45 -24	88 + 39 -21	3.7±0.1	62314

[a] A## M## indicates the microtip analyzed.

[b] Method used to select the volume of interest within an atom-probe reconstruction: Deposition Layer (D. L.), IsoConcentration (I. C.), or IsoDensity (I. D.) (see Section 7.2.5 for details).

[c] Isotopic ratios, corrected for background, tail interferences, multihit anomalies, and normalized to detonation nanodiamonds. 1σ + and – errors are asymmetric due to the asymmetric effect that + and – uncertainties in low ^{13}C counts have on the $^{12}C/^{13}C$ ratios. Ratios italicized and in parenthesis are from data sets with fewer than 10 $^{13}C^{++}$ counts, for which the 2^+ ratio is not used in the mean, standard deviation, or uncertainties of the bulk data set. In some cases corrections gave 0 ^{13}C counts, and in other cases 1σ passes 0 in the ratio, in each case causing the uncertainties to be undefined.

[d] Ratio of ^{12}C ions detected in the 1^+ charge state over those detected in the 2^+ charge state. These values are corrected for background, tails, and multihits, but are not normalized. A higher ratio indicates thermal effects played a greater role in activating field evaporation.

[e] Sum of C atoms detected in the mass spectrum at all identified peaks, including not only C_1 but also in the form of the molecular ions C_2, C_3, PtOC, and CO_2. These counts were only corrected for background, not tail interferences or deadtime correction.

[f] Data sets was first published in Heck et al. (2014), here presented with updated ROIs and deadtime corrections.

[g] Too few multi-hits to deadtime correct.

[h] Data set was first published in Lewis et al. (2015), here presented with updated ROIs and deadtime corrections.

[i] Sample from multilayer pND3. All other Allende samples are from multilayer pND.

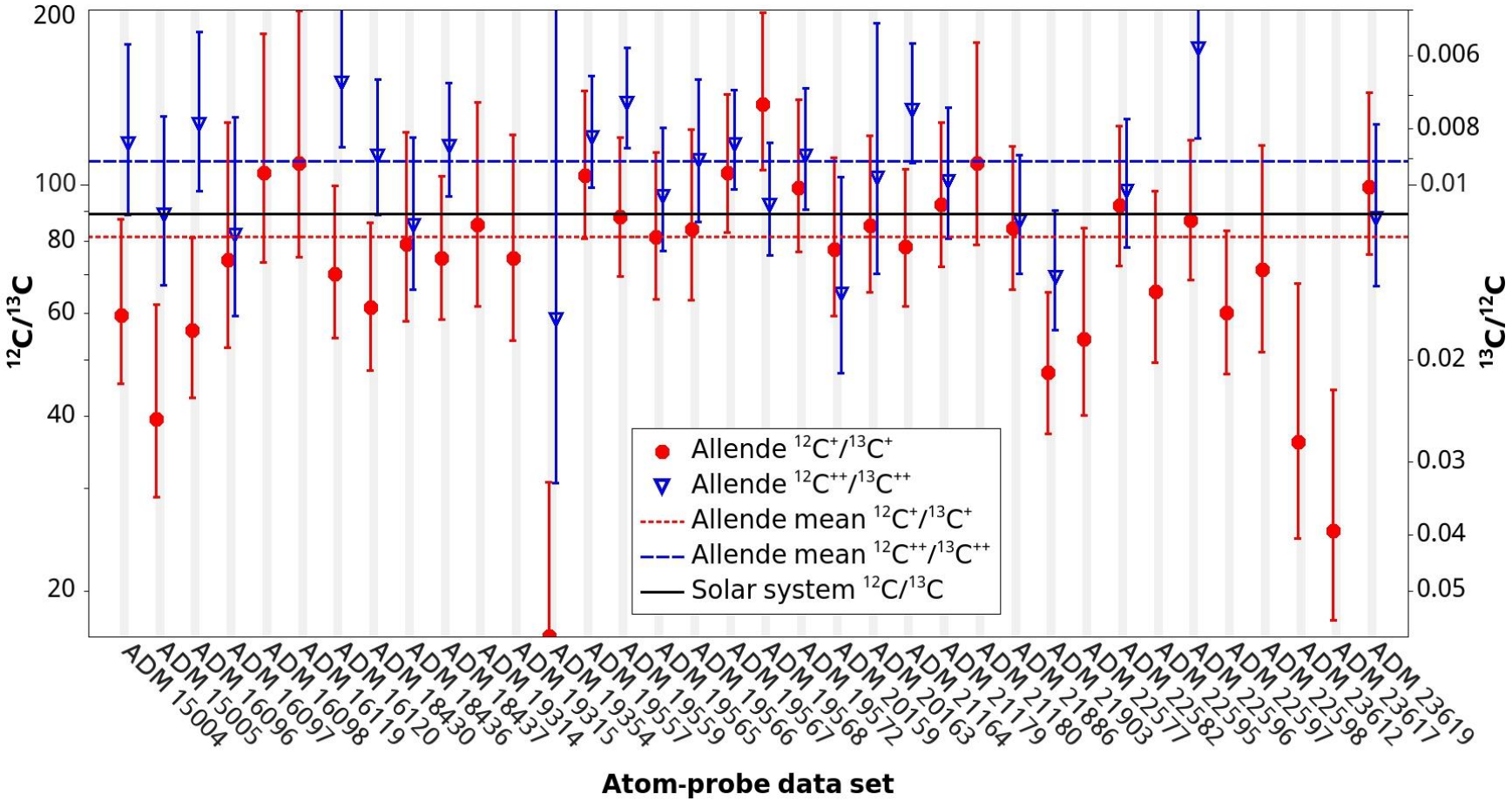

Figure 7.4 C isotopic ratios from atom-probe measurement regions of interest. Two ratios are reported for each data set, one using the ratio of $^{13}C^{+}$ and $^{12}C^{+}$ counts (red), the other using the ratio of $^{13}C^{++}$ and $^{12}C^{++}$ counts (blue). The graph is logarithmic in $^{13}C/^{12}C$ ratio (right axis), and the $^{12}C/^{13}C$ ratio is reported on the left axis. Data sets are ordered chronologically by measurement date. Error bars are 1σ. The mean ratio measured at each charge state is plotted as the dashed lines.

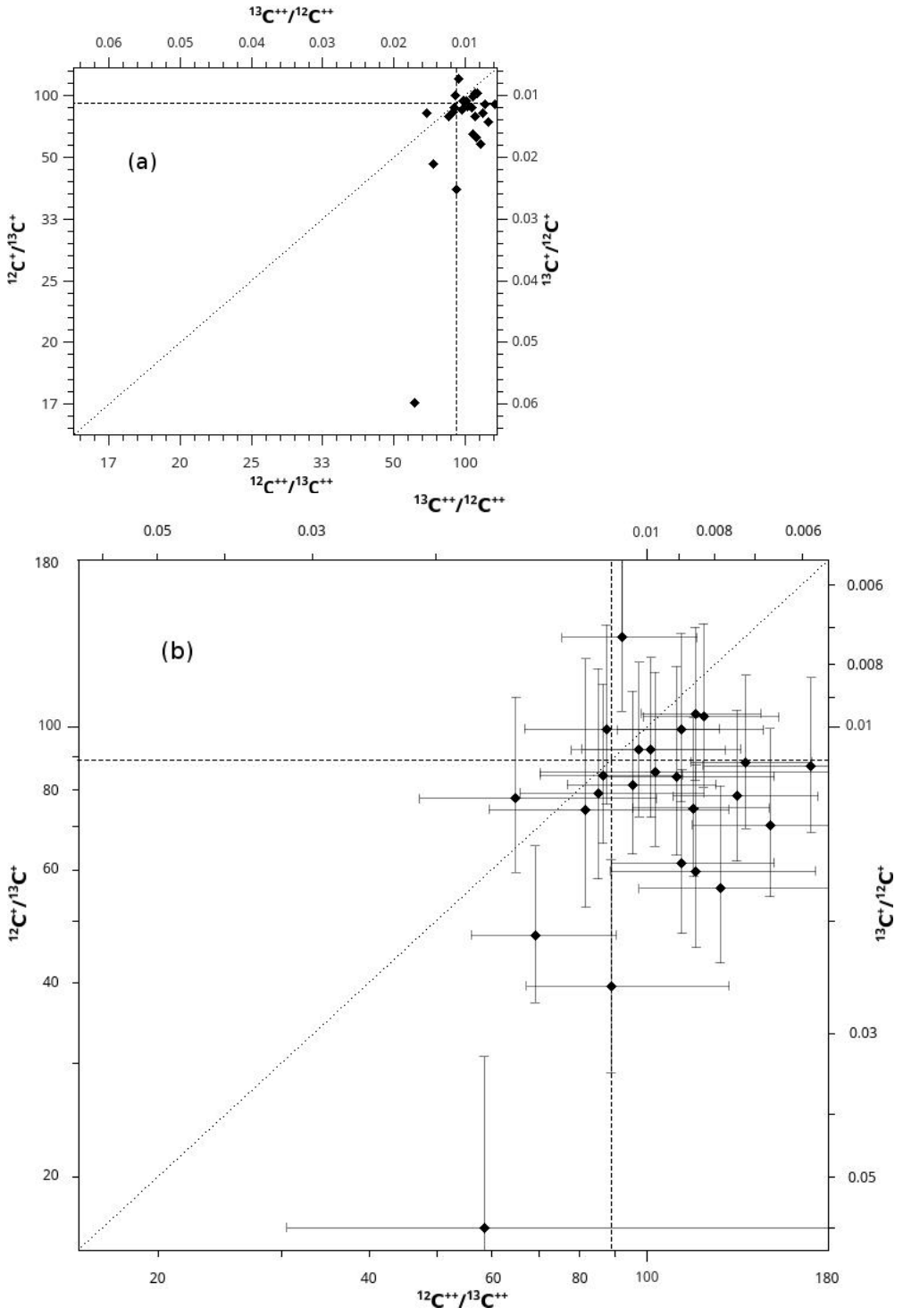

Figure 7.4 Two differently scaled images of the corrected, normalized C isotopic ratios in Allende acid residue-containing atom-probe microtip regions of interest. The y and x axes record the ratios measured at charge state 1^+ and charge state 2^+, respectively. The top image (a) is scaled linearly to ^{13}C /^{12}C. The left and bottom axes record increasing $^{12}C/^{13}C$ ratio; the right and top record decreasing $^{13}C/^{12}C$ ratio. In the bottom plot (b), axes are scaled to the log of the $^{13}C/^{12}C$ ratio with tighter ranges and 1σ error bars.

The charge state ratio is a good qualitative proxy-value that represents a number of conditions in the APT instrument. Most importantly, it can be used to gain an understanding of how great an effect thermal activation is having on field evaporation. The greater the ratio of charge-state 1^+ to 2^+ ions of a species, the more thermal effects are active, at least for the region of the sample from which that species is being evaporated. Since we use the C charge state ratio, we are assessing the field evaporation conditions primarily for the acid residue and nanodiamonds (although there is a low level of C contamination in the Pt from the sputter target and chamber contamination). In Figure 7.6 we plot the isotopic ratio vs the charge state ratio, which is indicative of field evaporation conditions, with a higher value indicating that heat is contributing more to activating field evaporation. The distribution of isotopic ratios is the same for a broad range of charge state ratios, but all five data sets with $^{12}C^+/^{13}C^+$ ratio below 67/1 (ADM R06 15005, 19354, 21903, 23612, and 23617) have a charge state ratio of $^{12}C^+/^{12}C^{++} < 2/1$. They have a range of uncertainties (i.e., counts), and their $^{12}C^{++}/^{13}C^{++}$ ratios are significantly higher than the $^{12}C^+/^{13}C^+$ ratios in each case, except for ADM 21903.

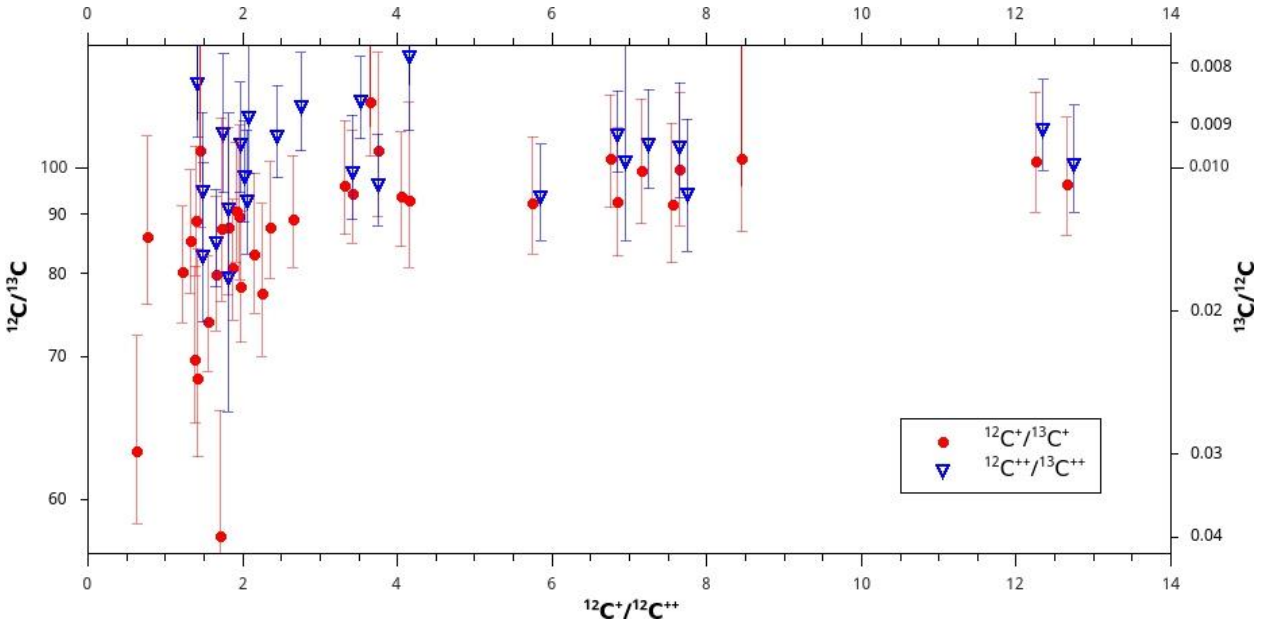

Figure 7.5 C isotopic ratio vs. the charge state ratio $^{12}C^+/^{12}C^{++}$. Ratios are plotted on a logarithmic $^{13}C/^{12}C$ scale (right axis), with logarithmic $^{12}C/^{13}C$ given on the left axis. Error bars for isotopic ratios are 1σ. Symbols for the charge state ratio for $^{12}C^+/^{13}C^+$ data points are shifted 0.05 lower than their actual values, and the charge state symbols for $^{12}C^{++}/^{13}C^{++}$ are shifted 0.05 higher, so that data points for the same data set do not overlap.

Detection of outliers from the ADM data set does not necessarily require normalization. For data sets with similar measurement protocols, the question is not if they are far from the terrestrial isotopic ratio, but if they are outliers from the distribution of ratio values, whatever the mean value measured for that distribution. Therefore, since normalization introduces additional uncertainty which is not meaningful to this question, I plot the un-normalized ratios in comparison to the DND ratio distributions (Figure 7.7). This figure uses a style similar to that used to present the much more numerous NanoSIMS measurements in Lewis et al. (2017) (Chapter 3). Insets in this figure have x-axes with the width as used in the analogous Figure 3.5 to give a comparison of the scatter. The bin size used here is ten times larger (0.001 steps in $^{13}C/^{12}C$ ratio, rather than 0.0001), to account for the much lower number of data points in this study. The 4σ error bars are much narrower for the distributions in this study compared to Chapter 3, because there are higher counts in each data set (on the other hand, the SEOM, the

uncertainty in the mean, is larger because of the lower number of data sets). The APT DND data sets have slightly larger scatter than the APT ADM data sets, presumably because of lower counts. Clearly this methodology is not as sensitive to Gaussian broadening as that used by Lewis et al. (2017) (Chapter 3). The distributions are not well-approximated by a Gaussian curve; all of them have tails of ^{13}C-enriched data points. A single outlier here represents only 1–10 nanodiamonds, compared to order 1000 in previous work, at least two orders of magnitude higher sensitivity to individual isotopically anomalous grains.

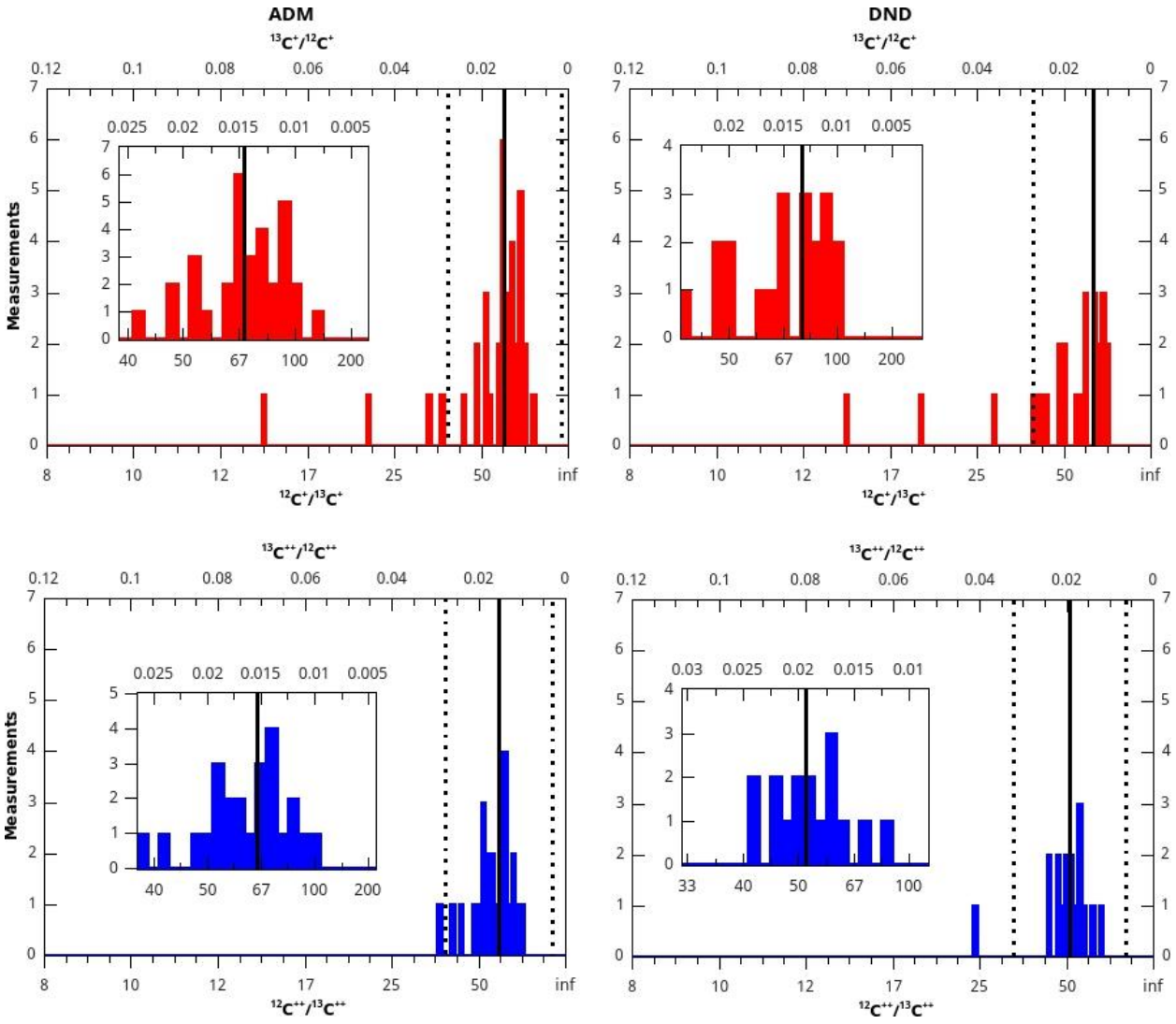

Figure 7.6 Distributions of ratio measurements prior to normalization. Mean (solid lines) and 4σ uncertainty-weighted deviations (dotted lines) are plotted over the distributions for the DND and ADM, charge state 1^+ (red) and 2^+ (blue) data sets. Insets are zoomed in on regions with the same width in $^{13}C/^{12}C$ scale as used in the histograms in Lewis et al. (2017) (Chapter 3). Bin size is 0.001 in $^{13}C/^{12}C$ scale. The 4σ error bar right of the mean for the DND (1^+) data set is negative in $^{13}C/^{12}C$ ratio – outside the logical and graphically represented limits of the plot.

All four distributions have mean values that are significantly ^{13}C-enriched compared to the solar value of $^{12}C/^{13}C = 89$ (Coplen et al. 2002), evidence for an instrumental artifact. The C isotopic ratios measured at charge state 2^+ in the DNDs have the most ^{13}C-enriched ratio of any of the 4 data sets. It is to this mean value that the ADM 2^+ data points are normalized, leading to their being reported as ^{13}C-depleted (Figure 7.3). If the DND 2^+ data points were more affected by the

unidentified instrumental artifact than the others, then this feature of our results is representative only of an instrumental artifact.

There are data sets with >4σ deviation from the mean for both of the DND and both of the ADM distributions, greater in number and isotopic anomaly for the (1^+) ratios than the (2^+) ratios. They are all in the ^{13}C-enriched direction (for the DND (1^+) distribution, 4σ outliers in the ^{13}C-depleted direction are impossible, since they would have to have $^{13}C/^{12}C$ ratios less than 0, a meaningless isotopic ratio). Unless there are features of the ADM outlier data points that distinguish them from the DND outlier data points, we must attribute these outliers to instrumental artifacts or other uncorrected errors.

7.3.3 Distinguishing Phases in the Acid Residue Using APT

Using (C_1+2×C_2+3×C_3) vs. (PtOC+Na+NaO) to distinguish between nanodiamonds and disordered C is based on APT observations of two spatially distinct phases: isolated regions of carbonaceous material a few nm in size are typically dominated by C, while lower density, larger, and less ordered regions of acid residue material are dominated by PtOC and laboratory contaminants such as Na and NaO (Figure 7.8), and also acid dissolution products Cl and F. Based on the higher porosity of the disordered C, we associate it with the latter, while nanodiamonds are associated with the C-dominated regions because of their size and their inability to easily incorporate contaminants. Stroud et al. (2011) showed that in the acid residues O is more often associated with the disordered C, N with the nanodiamonds, so N/O should provide an independent measure of the fraction of the two carbonaceous phases. There are several tests of these two approaches based on the APT data.

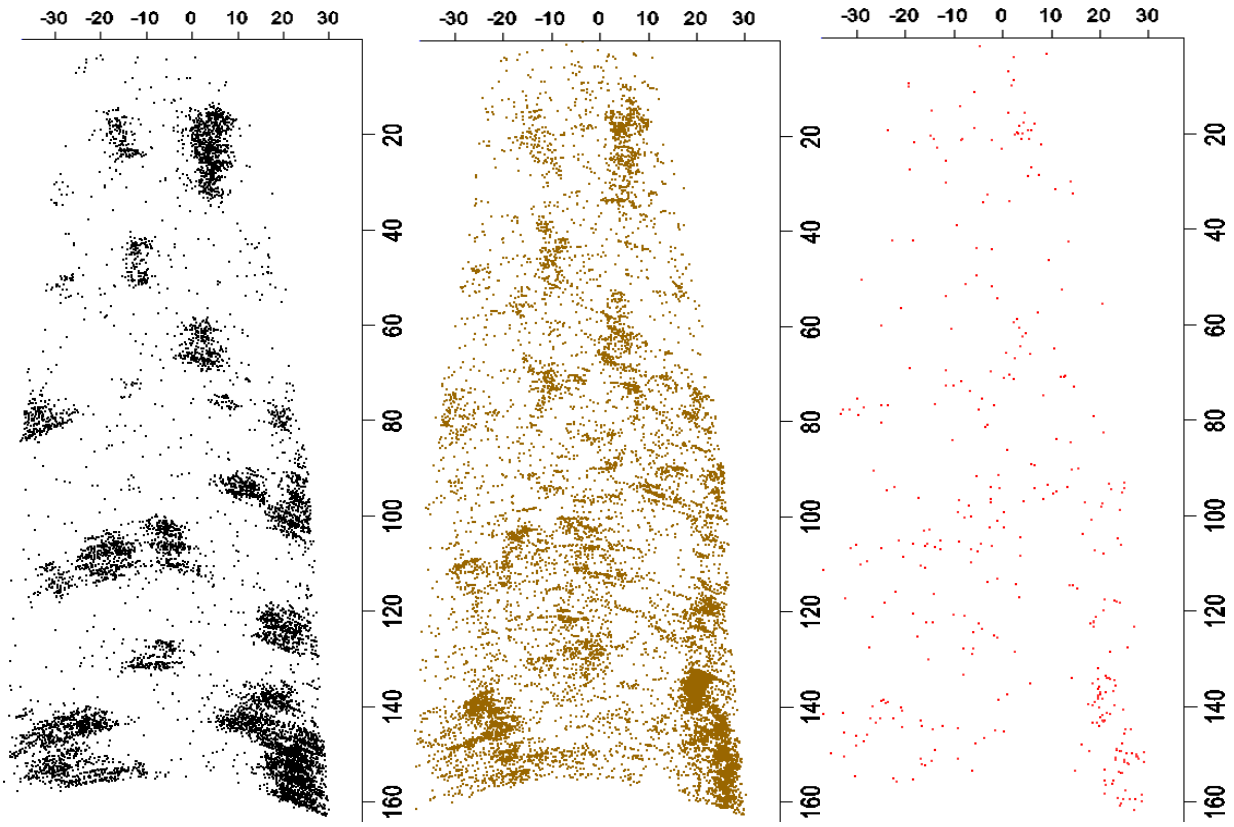

Figure 7.7 20 nm thick cross section of reconstructed APT data set ADM R06 18430, with C atoms in black, PtOC in brown, and Na, NaO in red. Scale bars are in nm.

First we mutual test the two approaches against each other. I plot (C_1+2×C_2+3×C_3) and (PtOC+Na+NaO) vs. N/O in Figure 7.9. This is a qualitative rather than quantitative approach, because there is likely a mixture of disordered C and diamond in each data set, and because there are variable amounts of O and N in both phases. We therefore are looking for trends, rather than a good fit to a line. Figure 7.9 shows a very loose trend: The highest concentrations of (C_1+2×C_2+3×C_3)/residuals (residuals is the summed counts of all the atoms associated with the acid residue (C, Na, Cl, F, N, O)), correspond to the highest N/O ratios, and for (C_1+2×C_2+3×C_3) concentrations over 0.6 the minimum N/O ratio increases steadily from <0.01 to 0.05. 1/7 (~14%) of data sets with (C_1+2×C_2+3×C_3)/residuals < 0.4 have N/O ratio > 0.05, but 9/29 (~31%) with (C_1+2×C_2+3×C_3)/residuals > 0.4 have N/O ratio > 0.05. There is a similarly loose

trend of lower N/O for higher (PtOC+Na+NaO) concentration: 1/8 (~13%) of data sets with (PtOC+Na+NaO)/residuals > 0.45 has N/O > 0.05, and 9/28 (~32%) with (PtOC+Na+NaO)/residuals < 0.45 has N/O > 0.05. These trends suggests that these two ratios record information about a mixture of two phases, such that data sets with extreme values in one of these ratios contain acid residue composed primarily either of disordered C, for O and PtOC+Na+NaO, or of diamond, for N and (C_1+2×C_2+3×C_3). Some of the correlation for PtOC+Na+NO with N/O is no doubt due to the fact that O is present in PtOC and NaO, both of which are also included in the residuals count, but the lack of N and higher O for lower (C_1+(2×C_2)+(3×C_3))/residuals is consistent with our use of this value as a qualitative proxy for the fraction of the acid residue that is nanodiamond. This trend is not easily discernable when instead of N/O other tracers such as N, N/residuals, or O are used, that is to say, N and O are anticorrelated in the acid residues, as expected.

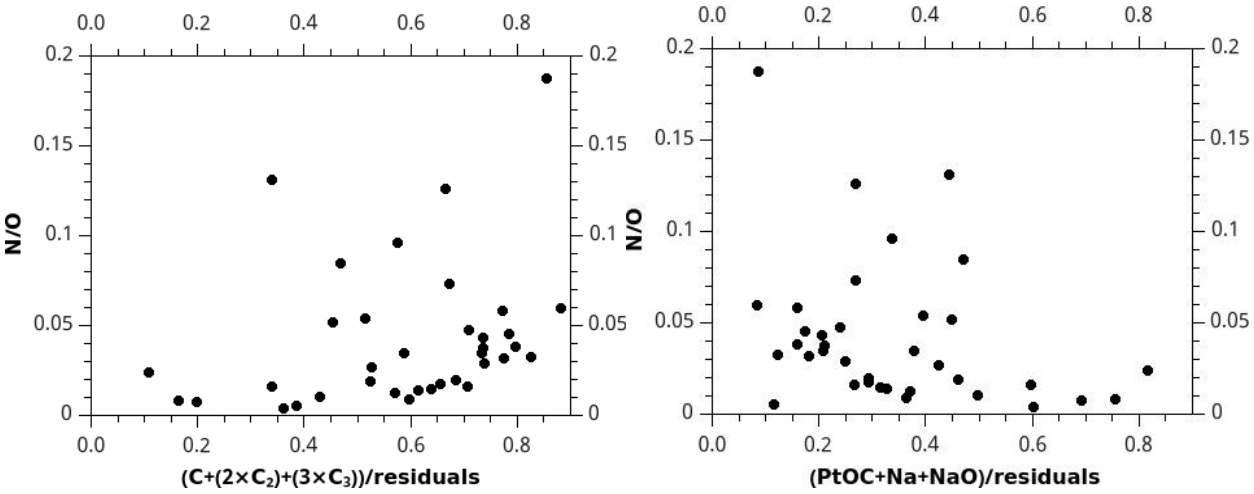

Figure 7.8 Plots of N/O vs. the concentrations of two different sets of molecules in APT reconstructed acid residues. The denominator on the x axis, residuals, is the sum of the C atoms from C_1, C_2, C_3, and PtOC, as well as the Na, NaO, Cl, and F ions.

If the ratios (C_1+(2×C_2)+(3×C_3))/residuals, (PtOC+Na+NaO)/residuals, and N/O do trend with disordered C vs. diamond, we would expect data sets with extreme values of these ratios to field

evaporate with different charge-state ratios, since they are different materials with different evaporation fields. So, as a further test of the validity of this approach, we plot both N/O and $(C_1+(2\times C_2)+(3\times C_3))/(PtOC+Na+NaO)$ vs. $^{12}C^{+}/^{12}C^{++}$ (Figure 7.10). There is a loose anticorrelation for $(C_1+(2\times C_2)+(3\times C_3))/(PtOC+Na+NaO)$ vs. $^{12}C^{+}/^{12}C^{++}$, but not for N/O. Since N/O does not yield a clear trend, this suggests $(C_1+(2\times C_2)+(3\times C_3))/(PtOC+Na+NaO)$ may be a better criterion to distinguish the two phases. If $(C_1+(2\times C_2)+(3\times C_3))$ and (PtOC+Na+NaO) are associated with 2 distinct phases, the C-rich, Pt-and-Na-poor phase tends to field evaporate under lower charge-state ratio conditions, and thus, by proxy, to field evaporate at higher voltages or lower laser energies.

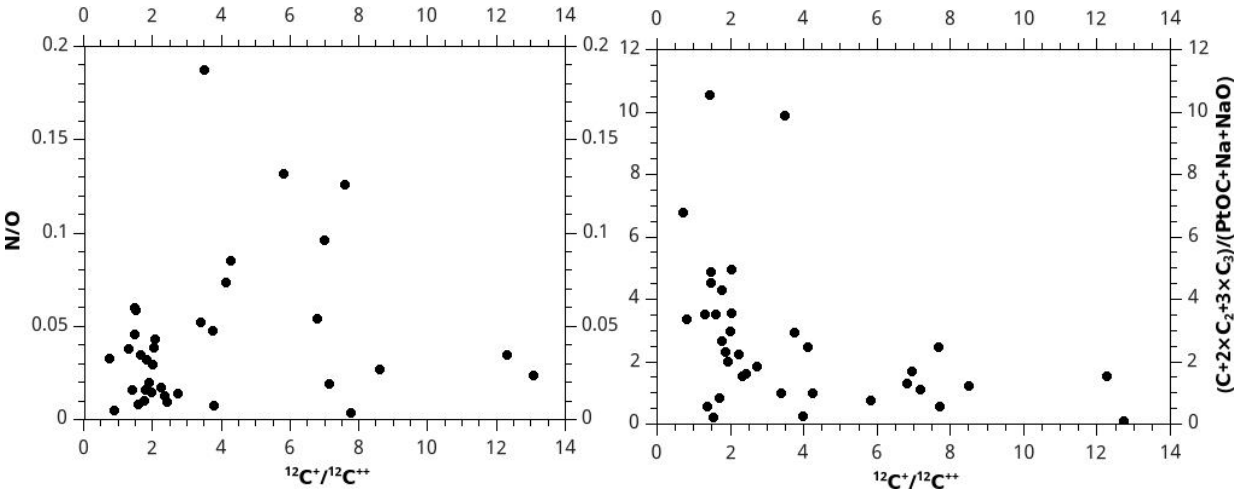

Figure 7.9 Plots of two ratios used to assess what fraction of the acid residue is disordered C and what fraction is diamond, vs the charge state ratio of ^{12}C.

Given the interpretation that spatial correlation, and trends in Figures 7.9 and 7.10 indicate $(C_1+(2\times C_2)+(3\times C_3))/(PtOC+Na+NaO)$ is a qualitative indicator of the fraction of disordered C diamond, anticorrelation of this ratio with $^{12}C^{+}/^{12}C^{++}$ suggests that diamond has a higher evaporation field than disordered C, evaporating at higher voltages for a set laser energy, such that the ratio of laser energy to voltage, and of 1^{+} to 2^{+} ions, are both lower. This is consistent

with the number of C-C bonds for these materials: A C atom on the surface of a nanodiamond has up to 3 C-C bonds, whereas an exposed sp^2-bonded C atom has at most 2 C-C bonds. Therefore, a higher field is required to polarize and ionize a C atom from a diamond surface than at the edge of a graphene sheet. Another interpretation is that one of the phases includes more Pt matrix, and that the difference in evaporation field is due to differences in matrix vs. acid residue, not diamond vs. disordered C.

The most interesting question we can ask using these criteria is whether the C isotopic ratio correlates with the fraction of acid residue that is nanodiamond, since this would suggest that the disordered C and nanodiamonds in the acid residue have different isotopic ratios, and thus different origins. We plot N/O and $(C_1+2\times C_2+3\times C_3)/(PtOC+Na+NaO)$ vs. $^{12}C/^{13}C$ (Figure 7.11). There is no clear correlation between these two parameters and the C isotopic ratios, although at higher $^{12}C/^{13}C$ ratio the minimum N/O rises slightly, and for lower $^{12}C/^{13}C$ ratio, only in 2^+, the minimum $(C_1+2\times C_2+3\times C_3)/(PtOC+Na+NaO)$ rises slightly.

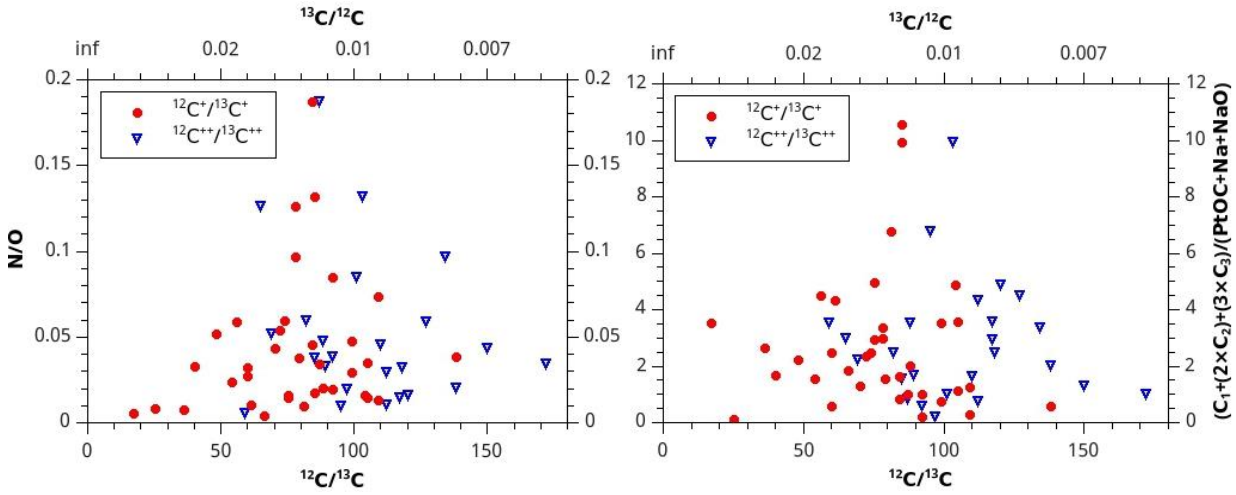

Figure 7.10 N/O ratio and $(C_1+2\times C_2+3\times C_3)/(PtOC+Na+NaO)$ ratios plotted vs. the normalized isotopic ratios.

To further investigate the relationship of the C isotopic ratios to these quantities, we plot the $^{12}C/^{13}C$ ratios at each charge state, in order of increasing ratio, alongside several quantities, including N, O, PtOC+Na+NaO, and $C_1+2\times C_2+3\times C_3$, each of which has been divided by the sum of the ions associated with the acid residue (Figure 7.12). The linear fits are poor for all quantities. For the 2^+ ratios, all of the adjusted R^2 values for the four fits are less than 0.1, and the slopes have greater than 100% error, except for O, which has a negative R^2 value. For the 1^+ ratios, the adjusted R^2 is negative for N and 0.04 for (PtOC+Na+NaO)/residuals. However, C does increase for the 1^+ ratios, with a slope of 0.004±0.001 in units of $((C_1+2\times C_2+3\times C_3)/\text{residuals})/(^{12}C/^{13}C)$, albeit with an adjusted R^2 of only 0.18. O decreases slightly with $^{12}C^+/^{13}C^+$ ratios, with a slope of -0.004±0.001 in units of $(O/\text{residuals})/(^{12}C/^{13}C)$, with an adjusted R^2 of 0.30. This suggests that there may be a higher C isotopic ratio for diamond than sp^2-bonded material. However, this could also be a statistical anomaly, as no such correlations exist for the 2^+ ratios, and the link between O and disordered C is not as well indicated by the APT data as that between $(C_1+2\times C_2+3\times C_3)$ and the nanodiamonds. The lack of similar correlations in the 2^+ ratios suggests that rather than inherent isotopic anomalies, these trends could be due to an instrumental artifact that affects 1^+ ratios more than 2^+, and that predominantly affects either disordered C or nanodiamond. If this effect is hydrocarbon interference at ^{13}C, then it must affect disordered C more than diamond, because the effect always lowers the $^{12}C/^{13}C$ ratio, and Figure 7.11 indicates lower ratios for the disordered C.

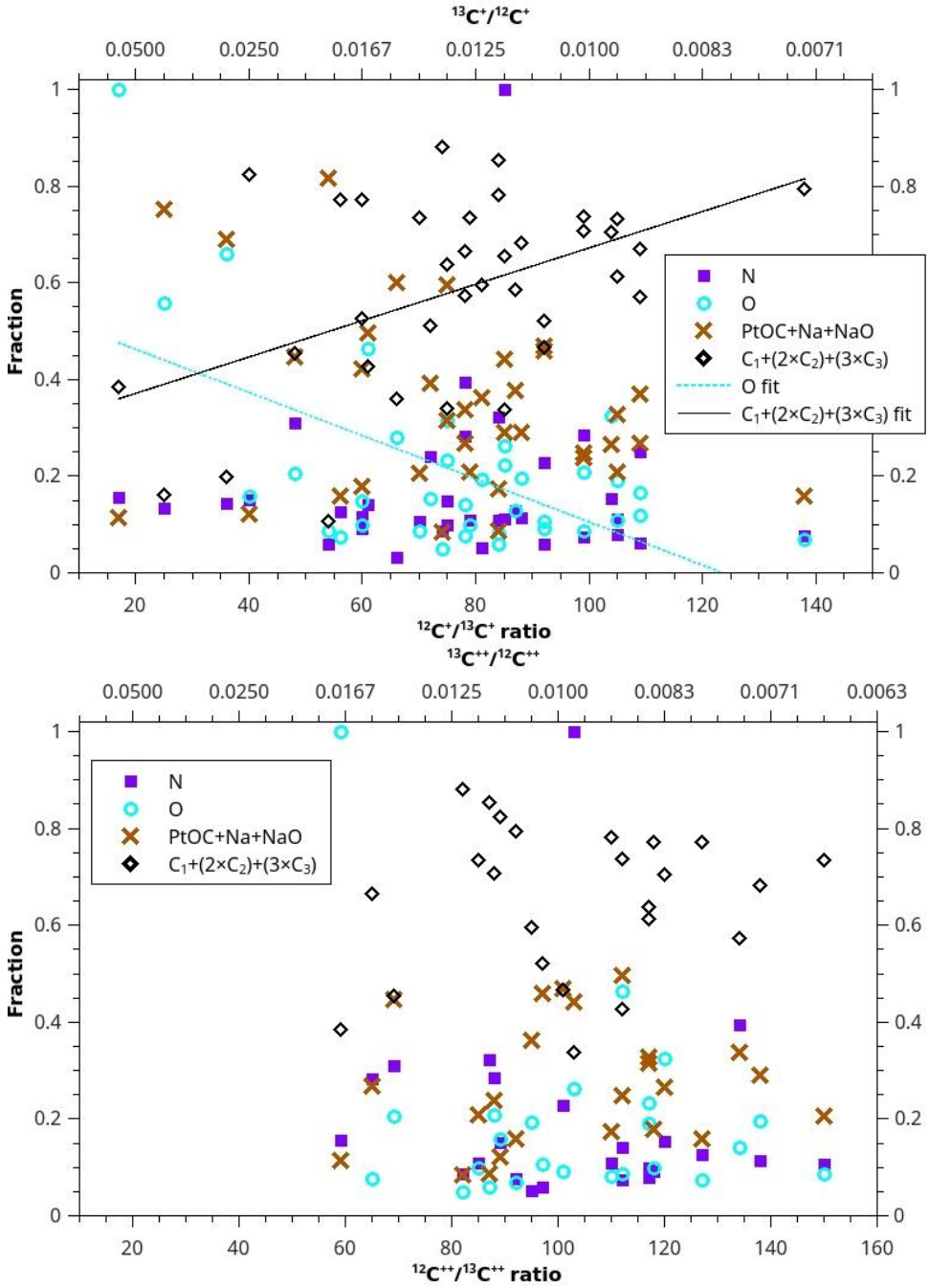

Figure 7.11 Four different quantities used for tracing the fraction of the acid residue that is disordered C and the fraction that is nanodiamond, plotted vs. the corrected, standardized $^{12}C/^{13}C$ 1^+ and 2^+ isotopic ratios of meteoritic nanodiamonds. N, O, PtOC+Na+NaO, and $C_1+(2\times C_2)+(3\times C_3)$ are each divided by the sum of the ions associated with the acid residue and then normalized to lie between 0 and 1 (see legend). Linear fits are shown for those quantities where a loose trend is detected. Note that the fractions displayed in the two plots are the same, even though some 2^+ ratios are not plotted due to low ^{13}C counts.

An alternative interpretation of the trends in Figures 7.10 and 7.12 is that they reflect increasing amounts of O contamination and dilution of the C signal as the amount of contamination from the Pt matrix increases. To test this interpretation, we plot the quantities from Figure 7.12 vs. the number of Pt ions detected in each data set (Figure 7.13). The O fraction trends upward with higher Pt counts, with a slope of $(2.8\pm0.9)\times10^6$ and an adjusted R^2 of 0.19 for a linear fit, whereas the C fraction decreases slightly, but with an adjusted R^2 of less than zero from a linear fit. Therefore, this is a viable interpretation for the trend in O, which is already questionable due to the lack of correlation of N/O with the C charge state ratio in Figure 7.10, but it is not valid for the trend in the C fraction.

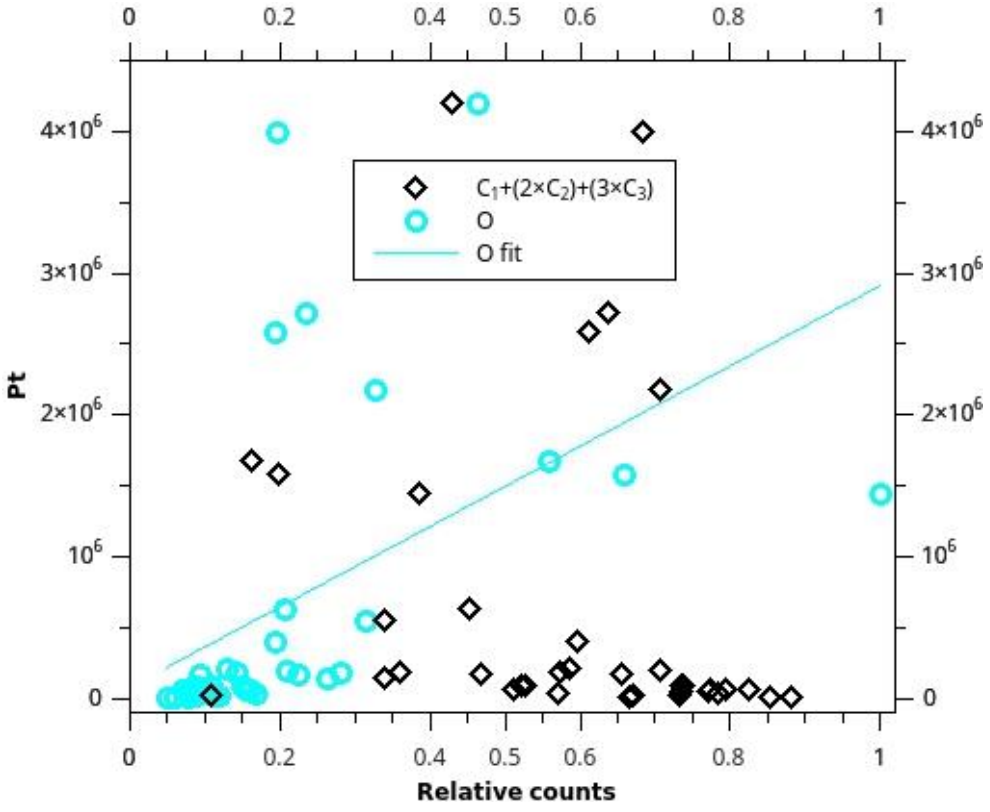

Figure 7.12 Pt atoms detected in a data set vs. values used to distinguish disordered C from diamond. Both O and $C_1+2\times C_2+3\times C_3$ are divided by the sum of the counts of all the ions associated with the deposition layer. A linear fit to the O data is also shown.

7.3.4 Detailed Discussion of Anomalous APT Data Sets

A case by case study of the anomalous data sets is required to understand whether measured isotopic anomalies are artifacts or inherent isotopic differences between samples of the acid residue. In this section, notable data sets from Figures 7.4–7.6 are studied individually (Table 7.3). All the ADM data sets considered in this section except for the ^{13}C-depleted ADM R06 19568 (1^+) have smaller-than-average weights. The weight indicates what fraction of an average data set they represent in terms of statistical significance. If they have a weight less than 1, they have less significance than one outlier of average weight. Similarly, all the DND outliers have weights less than one (DND 21905 (1^+), which has a weight of 10.9, is not an outlier). σ-values in Table 7.3 are the weighted standard deviation for the data set ROIs from the respective material (ADM or DND) and charge state (1^+ or 2^+), after corrections but prior to normalization.

Table 7.3 APT subvolume ratios, corrected but not normalized.

Sample	subvolume[a]	$^{12}C^{+}/^{13}C^{+}$[b]	W (1^{+})[c]	#σ (1^{+})[d]	$^{12}C^{++}/^{13}C^{++}$[b]	W (2^{+})[c]	#σ (2^{+})[d]	$^{12}C^{+}/^{12}C^{++}$	Counts[e]
ADM R06									
19354	D.L. 15 nm	14 +9 -4	0.004	17.3	34 +299 -16	0.003	2.3	0.8	2245
19354	I.D. 0.5 C/nm^3	8 +2 -1	0.005	36.1	21 (-133) -11	0.0007	5.4	2.4	4955
19354	<D.L. 15 nm	8 +2 -1	0.006	35.1	--	--	--	7.1	3191
20159	I.C. 10% (C)	62 +11 -8	0.5	0.2	38 +19 -9	0.03	1.8	7.6	4111
20159	<I.C. 2% (C)	37 +5 -4	0.3	3.8	34 +19 -9	0.02	2.3	3.8	28445
15005	I.D. 1 C/nm^3	51 +11 -7	0.1	1.4	33 +20 -11	0.04	2.4	1.5	2318
15005	<D.L. 15 nm	7 +2 -1	0.002	42.1	--	--	--	1.4	1212
23612	D.L. 10 nm	30 +19 -8	0.02	5.6	55 (-153) -34	0.003	0.4	4.0	3876
23612	<D.L. 15 nm	7 +10 -3	0.0004	38.3	--	--	--	--	1156
23617	D.L. edge	21 +11 -5	0.01	9.8	65 (-1667) -33	0.009	-0.05	1.5	5331
23617	<D.L. edge	9 +5 -2	0.001	31.6	23 (-65) -14	0.001	4.8	1.2	3378
18430	D.L. 20 nm	52 +7 -6	0.5	1.4	65 +16 -11	0.2	-0.05	1.7	24774
18430	<D.L. 20 nm	8 +1 -1	0.01	36.1	19 (-7502) -9	0.0008	6.4	7.8	4222
19568v01	I.C. 5% C	110 +18 -14	2	-1.9	53 +9 -7	0.3	0.5	2.0	11995
19568v01	<I.C. 5% C	69 +35 -17	0.1	-0.05	66 +91 -24	0.03	-0.09	2.2	7915
DND R06									

Sample	subvolume[a]	$^{12}C^{+}/^{13}C^{+}$[b]	W (1^{+})[c]	#σ (1^{+})[d]	$^{12}C^{++}/^{13}C^{++}$[b]	W (2^{+})[c]	#σ (2^{+})[d]	$^{12}C^{+}/^{12}C^{++}$	Counts[e]
21905	I.D. 10 C/nm^3	97 +5 -0.4	10.9	-0.9	38 +2 -2	0.2	1.9	26.3	58574
21905	<I.D. 5 C/nm^3	91 +12 -10	1.6	-0.7	122 (-994) -65	0.1	-3.4	11.5	11008
17621	D.L. 10 nm	19 +3 -2	0.03	11.7	--	--	--	7.1	6282
17621	<D.L. 15 nm	12 +2 -2	0.01	21.2	6 +24 -3	0.0005	44.1	4.9	10676
17629	D.L. edge	14 +4 -2	0.004	16.6	62 (-111) -43	0.007	-1.0	1.3	9740
17629	<D.L. edge	10 +1 -1	0.03	25.4	21 (-26) -18	0.0002	8.1	36.4	17036

[a] Process used to select subvolume. 'I.D.': Isodensity surfaces. 'D.L.': Deposition layer ("edge" indicates that rather than a specific width, the region of interest extends all the way to one bound of the reconstructed volume, because the deposition layer is on the edge of the reconstruction). 'I.C.': Isoconcentration. '<' indicates that the lower gradient side of the isosurface or the outside of the deposition layer were used for this reconstruction (that is, this subvolume contains matrix, not acid residue). Horizontal rules divide subvolumes from different microtip data sets. The first subvolume presented for each data set is the region of interest used for analysis of the acid residue (Table 7.2).

[b] C isotopic ratio with uncertainties in the plus and minus directions.

[c] Weights, $1/\mathrm{Err}(R)^2$.

[d] Deviation from the bulk isotopic ratio for the given data set and charge state, as a multiple of the standard deviation σ for that charge state.

[e] Total C atoms detected in the sample, including the atomic counts of carbon from C_1, C_2, C_3, PtOC, and CO_2, corrected only for background.

ADM R06 18430

This microtip is not anomalous; a detailed analysis is included here for comparison. The reconstruction of this microtip has multiple clusters of C ions, often surrounded by smaller clusters of PtOC (Figure 7.8). The carbonaceous features all lie in a flat plane that bisects the reconstruction (Figure 7.14). The Pt on either side of this plane has different concentrations of Al contamination, for unknown reasons (Figure 7.15). This plane is the intersection of the two IBS-deposited Pt layers, with carbonaceous acid residue captured in the middle. Detection of a flat deposition layer is common in APT reconstructions of these samples, and correlates well with observations by SEM and TEM. In some reconstructions poles from two different orientations of the Pt crystal are observed on the two sides of the deposition layer, and observation of only a single crystallographic region consistently correlates with only one side of the Pt multilayer being present in the microtip, as confirmed by SEM, post-APT. In some data sets the acid residue deposit is thicker or clumpier, with one flatter side, and one more bulbous side, the latter of which was originally the top of the acid residue deposit. Cross-sectioning reveals voids in the Pt where the clusters of C are located (7.16). A significant fraction of the ions in the C clusters were detected outside of the associated voids in the Pt, suggesting trajectory aberrations due to the higher evaporation field of C compared to Pt. The number of C atoms detected in each cluster in ADM 18430, and in general for all our APT data sets, is significantly smaller than the number of atoms required to account for a carbonaceous cluster the size of the associated void in the Pt and the density of diamond or disordered C, even after correction for ~50% ionic detection efficiency. Multi-hit corrections to the counts are small compared to this discrepancy. The predicted density of the material from the clusters is as much as a factor of 10 lower than that of diamond. Experimental systematics may have caused uncorrected signal loss, via uncorrected

correlated evaporation, or loss of whole chunks of carbonaceous material at once. Indeed, observations during data collection support the idea that chunks of material are lost: As the microtip is milled from the apex down, voids in the Pt often appear, are subsequently sparsely filled with iterative bursts of C, and then suddenly are filled in by more Pt, typically after an unusually large burst of C detections followed by a higher-than-usual rate of Pt detection filling in the area (e.g., Figure 7.16) – this has been observed in numerous microtips and indicates the exposure of a particle with an evaporation field much higher than that of Pt, the beginning of unstable bursts of field evaporation of C from the particle due to higher local fields, and finally the removal of the remainder of the particle as one or more large chunks, precluding the detection of much or most of the material from that particle, and finally rapid evaporation of the now exposed sharp edges of the hole in the Pt (see further discussion in Section 2.3.8, Figure 2.19 and Section 7.3.6).

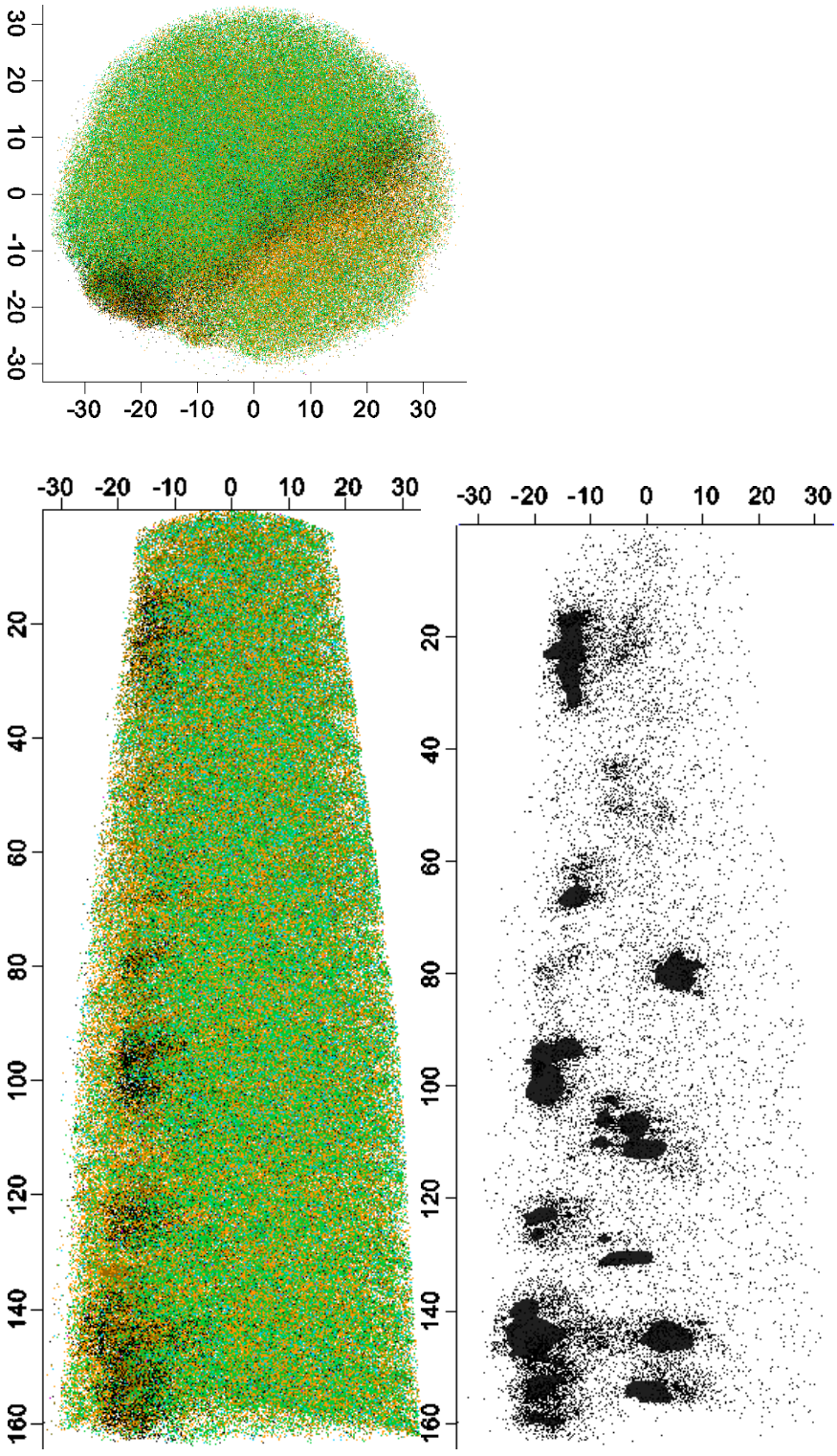

Figure 7.13 Reconstruction of C (black), Pt (orange), Al (green), and O (blue) ions in microtip ADM R06 18430. Well over 90% of detected ions were Pt, but only a fraction of the Pt ions are displayed here, to improve viewing of the minority ions, all of which are displayed The C reconstruction shows 5% C isoconcentration surfaces (black solids) superimposed on top of the ions. Scale bars are in nm.

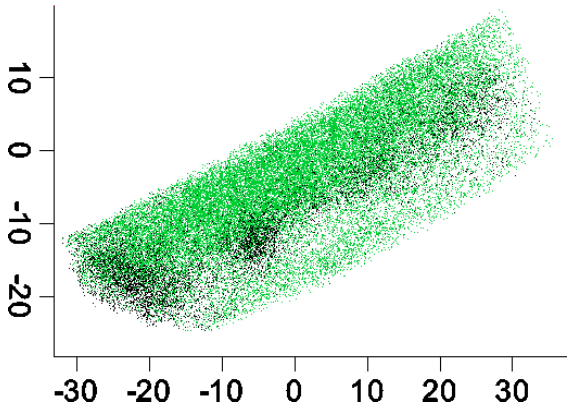

Figure 7.14 The deposition layer of ADM R06 18430, with nanodiamonds (black C atoms) between two layers of sputter-deposited Pt, one of which has higher aluminum content (green) than the other. This is an example of the deposition layer (D.L.) method of selecting a subvolume that contains the acid residue. In this case the deposition layer is 20 nm thick. Scale bars are in nm.

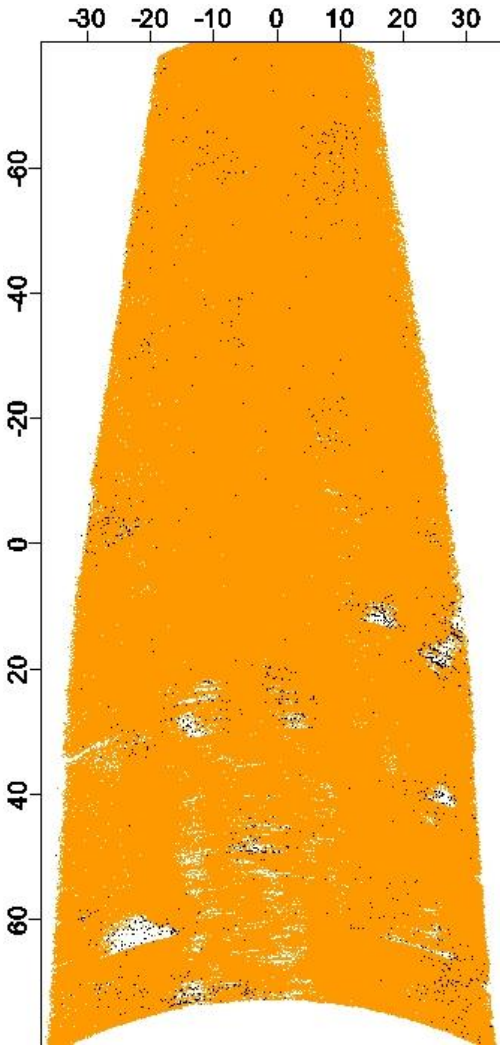

Figure 7.15 5 nm deep cross section of the plane in which the acid residue was deposited in data set ADM R06 18430. All Pt ions (orange) are displayed, along with C ions (black). There are holes in the Pt corresponding with, but not densely filled by, the C. Scale bars are in nm.

ADM R06 19354

Reconstructions of microtip 19354 show three C-rich volumes, each roughly spherical and three nm in diameter (Figure 7.17). They lack accompanying low-density material, and are consistent with nanodiamonds that are free of disordered C and laboratory contamination. The mass spectrum from the acid residue ROI for this microtip (selected using a 15 nm wide deposition layer) is notably double-peaked in C (Figure 7.18).

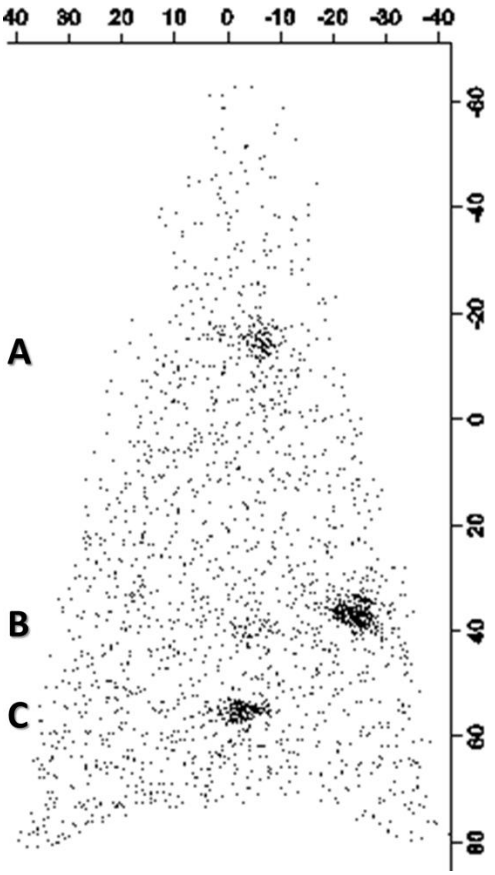

Figure 7.16 15 nm deep cross section of R06 19354, with C_1 ions, showing 3 clusters identified as nanodiamonds A, B, and C. Scale bars are in nm.

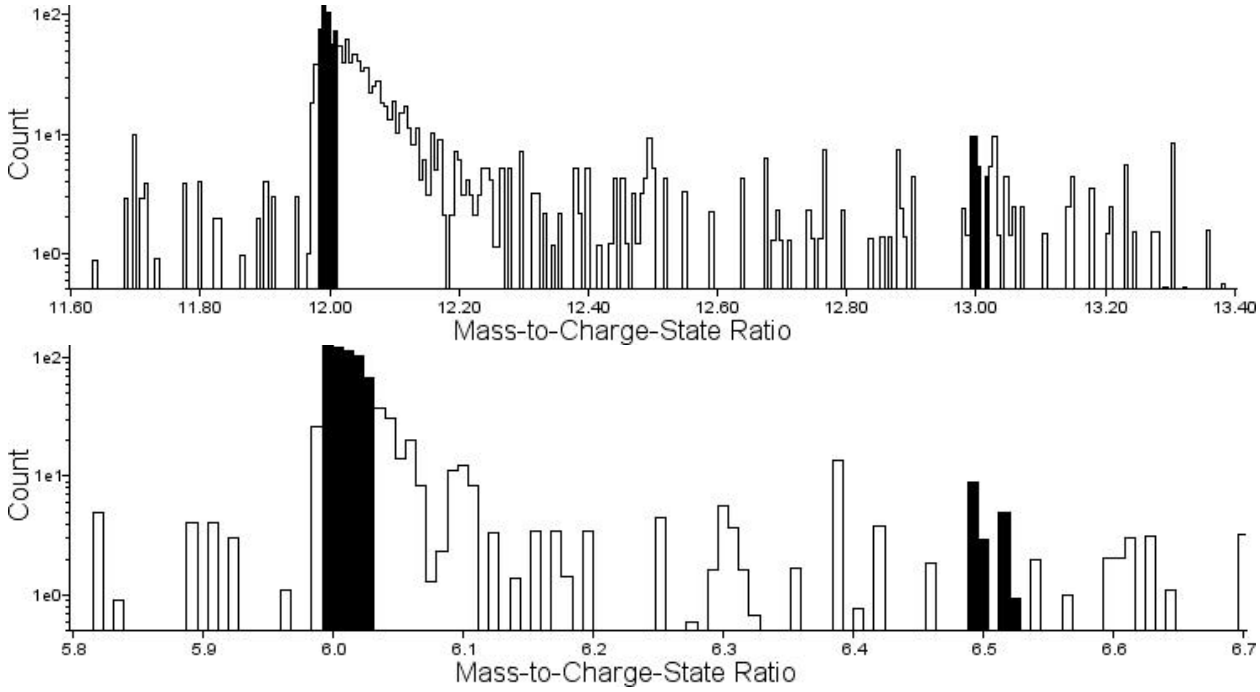

Figure 7.17 Mass spectra in units of amu, for R06 19354, 15 nm deposition layer, for 1^+, and 2^+ C.

After background corrections the three nanodiamonds together contain fewer than 1000 detected C atoms, and fewer than 100 atoms in any $^{12}C^+$ or $^{12}C^{++}$ peak from a single nanodiamond. Based on their size, each of these nanodiamonds should contain roughly 2000 C atoms. This indicates a significant loss of C signal, either from correlated evaporation or diamonds falling out of the microtip during field evaporation.

Nanodiamond 19354-A contains 21 ^{12}C ions (1^+ and 2^+ summed) and 0 ^{13}C atoms after background subtraction. Nanodiamond 19354-B has isotopic ratios of 88/2 = ~50 (2^+) and 89/0.5 = ~190 (1^+), after background correction. Nanodiamond 19354-C has isotopic ratios of 41/2 = ~21 (2^+) and 53/2 = ~27 (1^+) after background correction. The spectrum for nanodiamond 19354-C contains stronger secondary peaks than –A or –B, suggesting it is the source of the double-peaked features in the overall acid residue ROI (Figure 7.18). The laser energy remained constant during data collection, so this indicates the local electric field changed significantly

during field evaporation of the C in this region. While the field for the microtip might be changing for unrelated causes simultaneous to the field evaporation of this nanodiamond, it is more likely that this is evidence that the C ions are from a particle with a significantly different evaporation field from that of Pt (i.e., diamond or disordered C).

If the ^{13}C-enriched regions are the result of artifacts that affected this data set more than most of the others, the isotopic ratio of the C in the Pt matrix may also be anomalous. The isotopic ratios for the deposition layer and matrix, after removal of all atoms from regions with greater than 0.5 C atoms/nm^3 are 8^{+2}_{-1} (1^+) and 21^{UND}_{-11} (2^+) (background and tail corrected), where the positive uncertainty for 2^+ is *UND* (undefined) due to an error bar in ^{13}C/^{12}C that goes below zero (infinite ^{12}C/^{13}C). If the 15 nm thick deposition layer is also removed, leaving only the Pt matrix, the C isotopic ratios are 8^{+2}_{-1} (1^+), and undefined (2^+), after background corrections. The low concentration of C contamination to measure in the IBS-deposited Pt leads to a low signal-to-background, such that the 2^+ ratio does not have any ^{13}C counts after correction. Note that the 1^+ ratio of 8 is *more* anomalous than the measurements in the nanodiamonds and deposition layer.

The carbon isotopic contents of the overall matrix and deposition layer in 19354 – extremely enriched in ^{13}C for 1^+ vs. extremely depleted for 2^+ – suggest that $^{12}CH^+$ hydride interference on $^{13}C^+$ is contributing to or entirely responsible for the apparent ^{13}C enrichment. The carbon-hydrogen molecule, methylidyne, is a radical with an odd number of unpaired electrons – one, when in its ground state – such that formation of the singly ionized form, CH^+ is electronically favored over doubly ionized CH^{++} (Brooks and Schaefer III 1977). This could explain the apparently ^{13}C-enriched outliers in the DND and ADM data sets, for 1^+ but not necessarily for 2^+. This interpretation requires that some microtips are affected more by hydride interference

than others. Finally it must be remembered that the C contamination in the IBS-deposited Pt is not entirely comparable to that in the acid residues, as it has different bonds and different evaporation conditions.

ADM R06 20159

The deposition layer in this reconstructed microtip takes up a large fraction of the volume and is not limited to a narrow layer (Figure 7.19). It is composed not only of C but also Na. PtOC is actually higher in concentration *outside* of this clear deposition layer than inside of it. The pancake-shaped C depositions and streaks of Na suggest this microtip did not run stably. The C in these regions may be from nanodiamonds or nanodiamonds embedded in disordered C. There is no clear demarcation of the deposition layer, so we are not able to assess the isotopic ratio of the matrix as well as we are for data sets such as ADM 19354. The deposition ratios are 62^{+11}_{-8} (1^+) and 38^{+19}_{-9} (2^+). The matrix ratios of 37^{+5}_{-4} (1^+) and 34^{+19}_{-9} (2^+) are in good agreement with each other and are *more* ^{13}C-enriched than the deposition layer ratios, indicating the anomalous ratios in this data set are probably the result of instrumental artifacts.

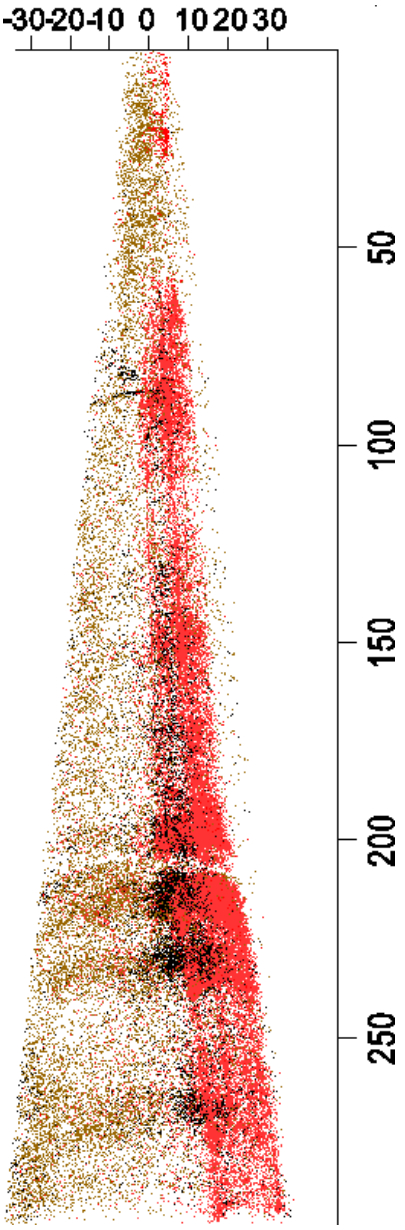

Figure 7.18 Reconstruction of ADM R06 20159. C_1 ions (black) are oriented in a splotchy deposition layer edge-on to the point of view, surrounded by streaks of Na ions (red) on one side, and PtOC ions (brown) on the other.

ADM R06 15005

This microtip reconstruction is a statistical outlier with un-normalized ratios of 55^{+11}_{-22} (1^+), and 33^{+20}_{-11} (2^+). After normalization, the 2^+ acid residue ratio is no longer anomalous, but the 1^+ ratio still is. The isotopic ratios of the Pt matrix outside of the 15 nm deposition layer subvolume from this microtip reconstruction are 7^{+2}_{-1} (1^+), and undefined (2^+) due to vanishingly low ^{13}C signal-

to-noise, similar to the pattern observed in 19354, again suggesting hydride interference at $^{13}C^{+}$, which also explains the anomalous 1^{+} isotopic ratio inside the deposition layer. There is no significant evidence of disordered C in the deposition layer; the acid residue in this data set appears to be composed primarily of diamond.

ADM R06 23612

This data set contains a mixture of C-rich and PtOC-rich clusters, with larger C clusters (Figure 7.20). Inside the 10 nm wide deposition layer, the isotopic ratios are 30^{+19}_{-8} (1^{+}) and 55^{UND}_{-34}. No $^{12}C^{++}$ was detected outside the deposition layer for this data set. It is therefore impossible to tell if the ratios at the two charge states differ, only that the matrix ratio of C^{+} ions (7^{+10}_{-3}) is even more enriched in ^{13}C than both deposition layer ratios – self-standardization shows the acid residue in this microtip shows no evidence for isotopic heterogeneity.

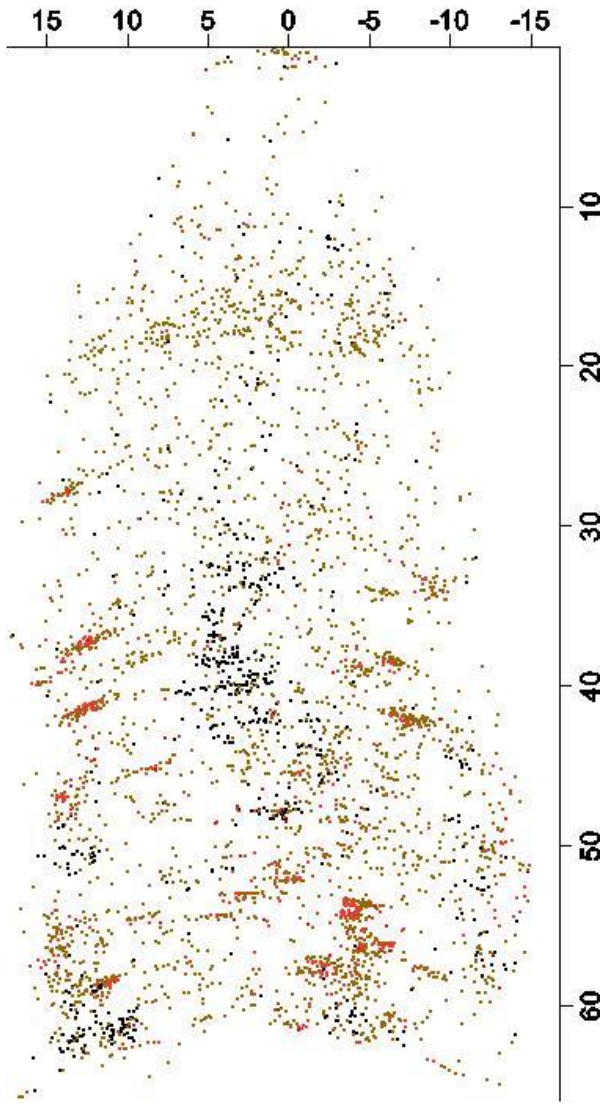

Figure 7.19 Reconstructions of ADM R06 23612. C (black), PtOC (brown), and Na and NaO (red) ions are displayed. Scale bars are in nm.

ADM R06 23617

The deposition layer in this microtip reconstruction lies along the edge of the field of view. Again the 1^+ ratio (21^{+11}_{-5}) is more enriched in ^{13}C than the 2^+ ratio (65^{UND}_{-33}), suggesting that hydride interference is at work. The matrix has lower $^{12}C/^{13}C$ ratios than the deposition layer, 9^{+5}_{-2} (1^+) and 23^{UND}_{-14}(2^+). Clearly, self-standardization demonstrates that the acid residue in this microtip is not evidence for isotopic heterogeneity.

ADM R06 19568

This data set from Allende is not a >4σ outlier, but it is discussed here because it has the highest $^{12}C/^{13}C$ ratio of all the ADM data sets. The acid residue ROI selected by a 5% atomic C isoconcentration surface has C isotopic ratios of 110^{+18}_{-14} (1^+) and 53^{+9}_{-7} (2^+), while the region outside of the 5% C isoconcentration surface, including the Pt matrix and the edge of the deposition layer, has C isotopic ratios of 69^{+35}_{-17} (1^+) and 66^{+91}_{-24} (2^+). These matrix ratios are the closest to the total bulk C isotopic ratios of the Allende data sets of any of the ROIs discussed in this section (see Table 7.3), with deviations of only -0.05σ (1^+) and -0.09σ (2^+). The 1^+ ratio in the acid residue is enriched compared to the 1^+ ratio in the matrix, and the 2^+ ratio is slightly depleted, but the uncertainties on the ratios are large enough that these anomalies are not significant if based solely on self-standardization.

DND R06 21905

This detonation nanodiamond standard microtip is marked by unusual levels of contaminants, including clusters rich in Ni, Ga, and PtOC (Figure 7.21), with some F but no significant Na or Cl. C is spread throughout the reconstructed volume and does not resemble a deposition layer. These lines of evidence lead us to believe this region of the microtip is either composed of a large chunk of acid residue and laboratory contamination with a significantly different pedigree from most of our samples, or else the sample fractured in the atom-probe and the region we are observing is not from the deposition layer at all. The C isotopic ratios in the acid residue ROI are $97^{+5}_{-0.4}$ (1^+) and 37^{+2}_{-2} (2^+). In the ADM outliers there is generally more ^{13}C-enrichment in 1^+ than in 2^+; the inverse is true here. The acid residue ROI was selected using a 10 C atom/nm^3 isodensity surface. The matrix subvolume was selected using a 5 C atom/nm^3 isodensity surface, and has C isotopic ratios of 91^{+12}_{-10} (1^+) and 122^{UND}_{-65} (2^+). The 1^+ ratios from the matrix and acid residue are in good agreement with each other; the 2^+ ratios are not in

agreement within 1σ, in spite of high uncertainties for the ratio measured in the Pt matrix. The presence of a highly ^{13}C-depleted 2^{+} isotopic ratio in the acid residue of one of the DND standards, even under self-standardization, means that even if the same were the case for an ADM data set further evidence would be required to demonstrate that Allende data set carried inherent isotopic anomalies.

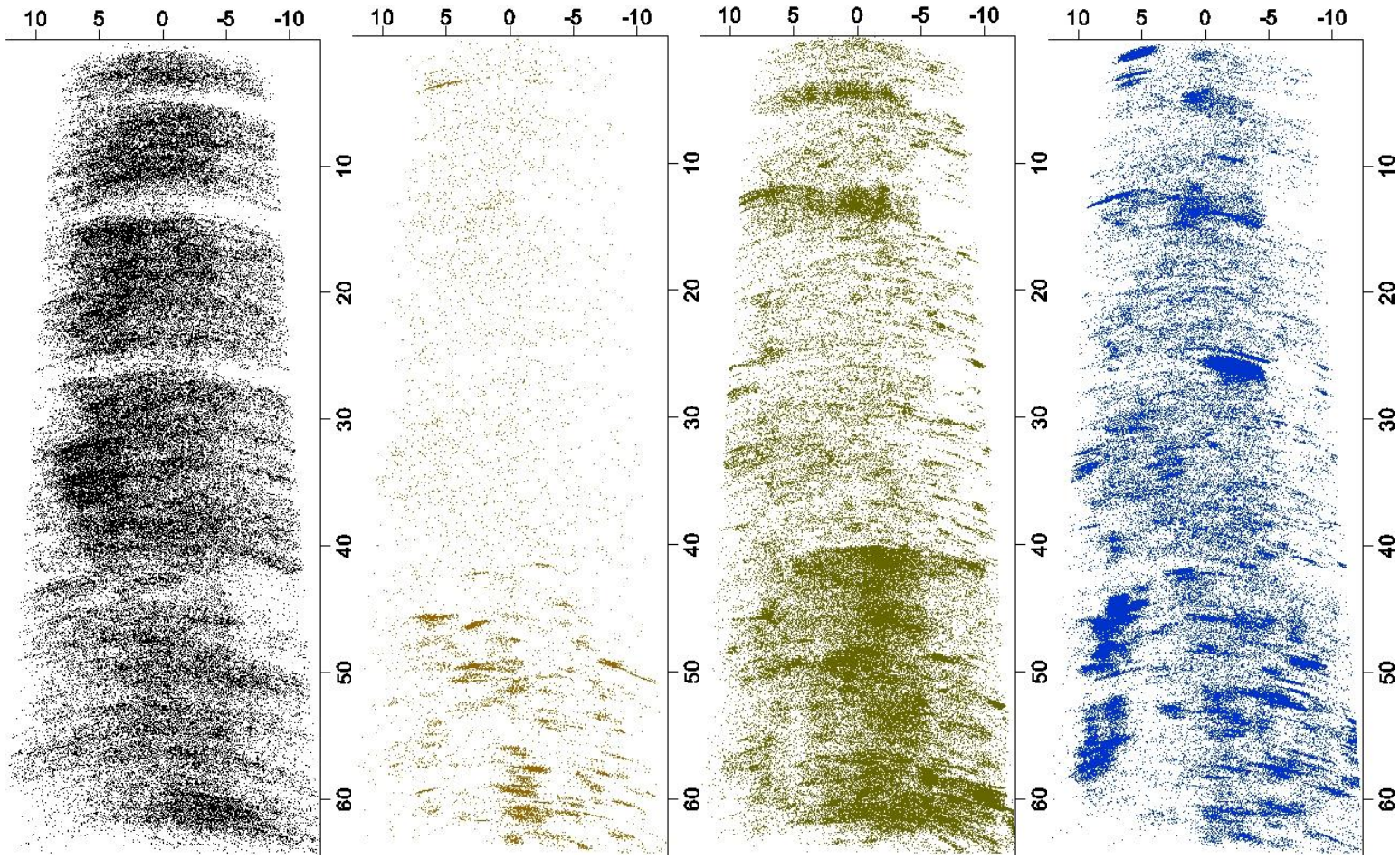

Figure 7.20 Reconstructions of data set DND R06 21905 with C (black), PtOC (brown), Ga (green), and Ni (blue) ions. Scale bars are in nm.

DND R06 17621

The deposition layer runs along the edge of the field of view in this microtip reconstruction. The background level fluctuates at different masses, such that the fit to the background is not a good estimate, especially for C^{++}. Therefore we used the local background window method instead of the whole-spectrum fit to estimate the background for the peaks used in the ratios for this microtip. After corrections, there were not enough counts of $^{13}C^{++}$ from the acid residue to assess the $^{12}C^{++}/^{13}C^{++}$ ratio. The 1^+ acid residue ratio (19^{+3}_{2}) is less ^{13}C-enriched than the ratios measured at both charge states in the Pt matrix (12^{+2}_{-2} (1^+) and 6^{+24}_{-3} (2^+)). This indicates that the ^{13}C enrichment in the deposition layer is probably an instrumental artifact. The 2^+ ratio from the Pt matrix is lower than the 1^+ ratio, opposite what is expected if hydride interference is the major instrumental artifact at work, but large uncertainties make this part of the result unclear.

DND R06 17629

Only the top of this microtip reconstruction contained the deposition layer, so the top region is used as the region of interest for the nanodiamond isotopic ratio. The matrix ratio is calculated from the remainder of the data set farther down the shank. This microtip was also background corrected using noise windows due to a poor estimate from the background fit to the whole mass spectrum. The acid residue ratios are 62^{UND}_{-43} (2^+) and 14^{+2}_{-2} (1^+) and the matrix ratios are 21^{UND}_{-18} (2^+) and 10^{+1}_{-1} (1^+). The 1^+ ratio from the matrix is even more ^{13}C-enriched than the 1^+ ratio from the acid residue, indicating this outlier is the result of an instrumental anomaly. The 2^+ matrix and acid residue ratios are both ^{13}C-enriched, but not as much as the 1^+ ratios, but the counting statistics are too low for us to assess finite uncertainties on either value.

7.3.5 TEM

TEM and STEM imaging, EELS, and TEM diffraction pattern analysis show evidence for nanodiamonds and graphitic C in several of the microtips (Table 7.4).

Table 7.4 Yes/No matrix of TEM and associated observations made on microtips.[a]

Sample[b]	Acid residue near apex: SEM	Diamond: TEM image[c]	Diamond: FFT[d]	Diamond: Diffraction	C: EELS[e]	low-density features: STEM[f]
HG01-B (first region)	N	--	--	N	--	N
HG01-B (resharpened)	Y	--	--	?	N	Y
HG01-C	Y	--	--	--	--	Y
HG04-C	N	Y, and graphite	--	--	N	N
HG06-A	? One faint cluster	N	N	--	--	N
HG06-B	Y	N	N	--	--	Y
HG06-C	Y	N	?	--	--	Y
HG06-D	Y	N	Y	?	--	Y
HG06-E	?	N	N	?	--	?
HG05-A	Y	Y	Y	Y	Y	Y
HG05-B	N	N	N	--	--	N
HG05-C	N	Y	Y	--	--	Y, few
HG05-D	--	N	N	--	--	Y
HG05-E	--	N	N	--	N	Y, few

[a] '--' represents no data for the given category and sample. '?' represents possible but inconclusive observation for the given category and sample. All samples are from Allende acid residue multilayer pND3.

[b] Samples are arranged in the order of TEM analysis, first to last.

[c] 'Y' in this column means that TEM images of this microtip have atomic planes with spacings within uncertainty of the 2.06 nm of diamond (111) planes. An 'N' means the TEM image does not have diamond (111) planes.

[d] 'Y' in this column means that FFTs of TEM images have spots for diamond (111) spacing, and

no un-indexed spots, which would suggest the presence of Moiré fringes and call into question the identification of diamond spots.

[e] 'Y' in this column means the C k-edge was resolved from an EELS map of an image feature.

[f] 'Y' in this column means that STEM imaging shows chains or a few isolated ~1 nm-sized circular regions of lower Z-contrast than the surroundings.

While EDXS maps were collected, low count rates and instrument drift prohibited us from obtaining enough counts to distinguish C hot spots from the background. Probably for this reason, there were no clear regions of C enrichment in any of the microtips under EDXS analysis.

Low-density features are present in TEM and STEM HAADF and BF imaging for each microtip in which SEM observation suggests the presence of acid residue in the top 50 nm of the microtip. These features are often evenly spaced with little clumping. Some even appear to be laid out in a linear or curved chain of non-touching particles. For half grid HG01, the data presented, with low-density features and the presence of diamond and graphite spacing, is taken from microtips that are resharpened. Prior to resharpening, SEM and TEM showed no resolvable acid residue at the apex, and no low-density features, respectively.

In traditional TEM, atomic planes with spacings corresponding to Pt(111) and (200) are frequently present (e.g., Figure 7.22; Table 7.5 gives common planar spacings for Pt, diamond, and graphite). Moiré fringes, resulting from overlapping crystals, are also visible in many samples.

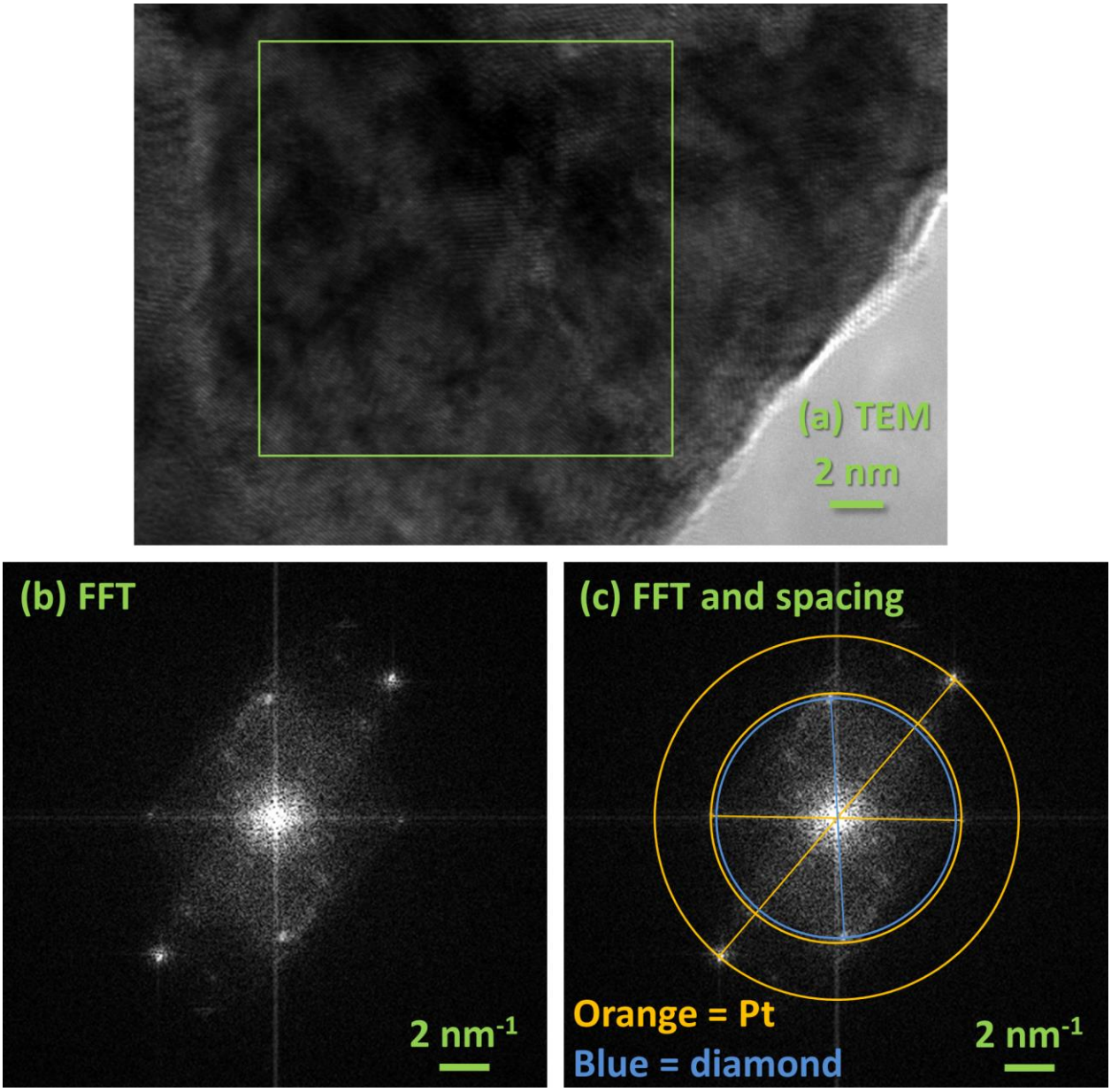

Figure 7.21 TEM and FFT checks for microtip contents from a region of HG05-A. (a) shows the TEM image with a target FFT region denoted with a square. The microtip apex is in the down-left direction. (b) shows the FFT, with several spot pairs. (c) shows lines connecting 3 pairs, each with different spacings. From largest to smallest diameter, the pairs correspond to Pt(220), Pt(200), and diamond(111).

Table 7.5 Interplanar spacings (d-spacings).

3C Diamond	Pt metal	2H Graphite	3R Graphite
a=3.566 Å	*a*=3.923 Å	*a*=2.470 Å *c*=6.724 Å[a]	*a*=2.456 Å *c*=10.044 Å[a]
Fd3m (227)	*F m-3m* (225)	*P63/mmc* (194)	*R3* (146)
		(001) 6.72 Å[a]	
(111) 2.06 Å	(111) 2.24 Å	(002) 3.36 Å[a]	(003) 3.35 Å[a]
	(200) 1.94 Å	(003) 2.24 Å[a]	(101) 2.08 Å[a]
(220) 1.26 Å	(220) 1.37 Å	(100) 2.14 Å	(012) 1.96 Å[a]
(311) 1.08 Å	(311) 1.17 Å	(101) 2.04 Å[a]	(006) 1.67 Å[a]
	(222) 1.12 Å	(102) 1.80 Å[a]	(104) 1.62 Å[a]
(400) 0.892 Å	(400) 0.970 Å	(004) 1.68 Å[a]	(015) 1.46 Å[a]
(331) 0.818 Å	(331) 0.890 Å	(103) 1.55 Å[a]	(110) 1.23 Å
	(420) 0.867 Å	(005) 1.34 Å[a]	(107) 1.19 Å[a]

Graphene planar hexagonal sheets
(100) 2.13 Å
(110) 1.23 Å
(200) 1.07 Å
(120) 0.805 Å

[a] The c-axis intersheet distance is variable For examples see Kellett and Richards (1971) and Zhou et al. (2014).

Even in the beam-normal orientation (Figure 7.1b), TEM often corroborates SE imaging of the deposition layer placement, showing that the two layers of Pt in the multilayer were milled unevenly during sharpening, leading to one thin layer at the apex of the microtip, and a sudden broadening of the microtip and increase in diffraction complexity and Moiré fringes slightly

farther down. Likewise, STEM-HAADF imaging often shows Z-contrast changes consistent with one Pt layer extending to the apex of the microtip (e.g., Figure 7.23a), a layer of acid residue material exposed on the surface slightly farther from the microtip (e.g., the higher-Z layer that begins in Figure 7.23b, along with low-Z spheres), and an added layer of Pt farther down (e.g. Figure 7.23c).

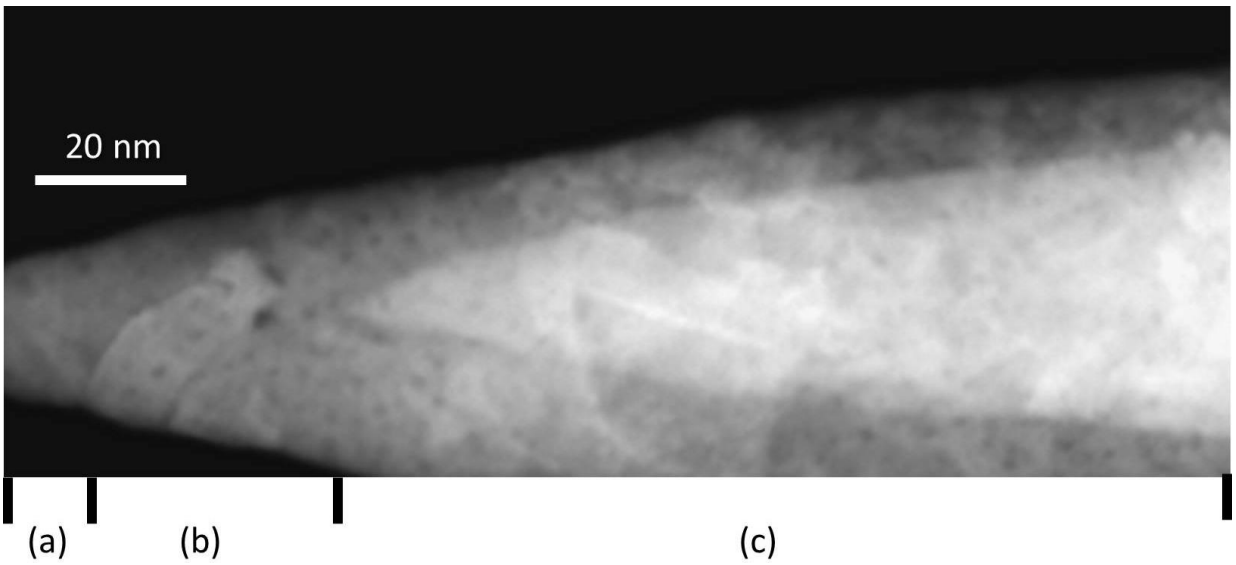

Figure 7.22 STEM HAADF image of the apex region of microtip HG05-A, excluding the last few nm of the apex. The regions denoted (a), (b), and (c) are dominated by progressively higher Z-contrast features, suggesting the addition of layers of material.

7.3.6 Detailed Discussion of TEM Data from Individual Microtips

HG01-B

This microtip is unique among our data in that it was characterized by TEM before and after FIB resharpening, that is, two different regions of the same sample have been studied. Secondary electron imaging of the first region does show an acid residue deposit in the deposition layer. TEM and STEM-HAADF and -BF images are free of features the size and density of nanodiamonds. The second region, brought to the apex of the microtip by FIB milling, does have a thick acid residue deposition layer, visible in SEM, TEM, STEM-HAADF, and STEM-BF images as 1 nm-diameter low-density features.

Electron diffraction images were captured from both of these regions. Spacings consistent with Pt are identified and used to calibrate the spacings in each image. For the deposition-free first region, there are no isolated spots at the innermost diamond spacing (diamond(111), Table 7.5) (Figure 7.24a,b), and the first two peaks of Pt are resolved from each other (Figure 7.24c), but for the deposition-rich second region there are clear diamond(111) spots (Figure 7.25a,b), and a shoulder between the two innermost Pt peaks, at the spacing for diamond (111) (Figure 7.25c). As demonstrated in the case of this microtip, we find it is a general rule that if we observe large chunks of acid residue in the deposition layer by SEM, we will also observe 1 nm low-density features in STEM-HAADF, and some sign of diamond material based on electron diffraction. The second, acid-residue containing region in this microtip was also studied by APT (see Section 7.3.7).

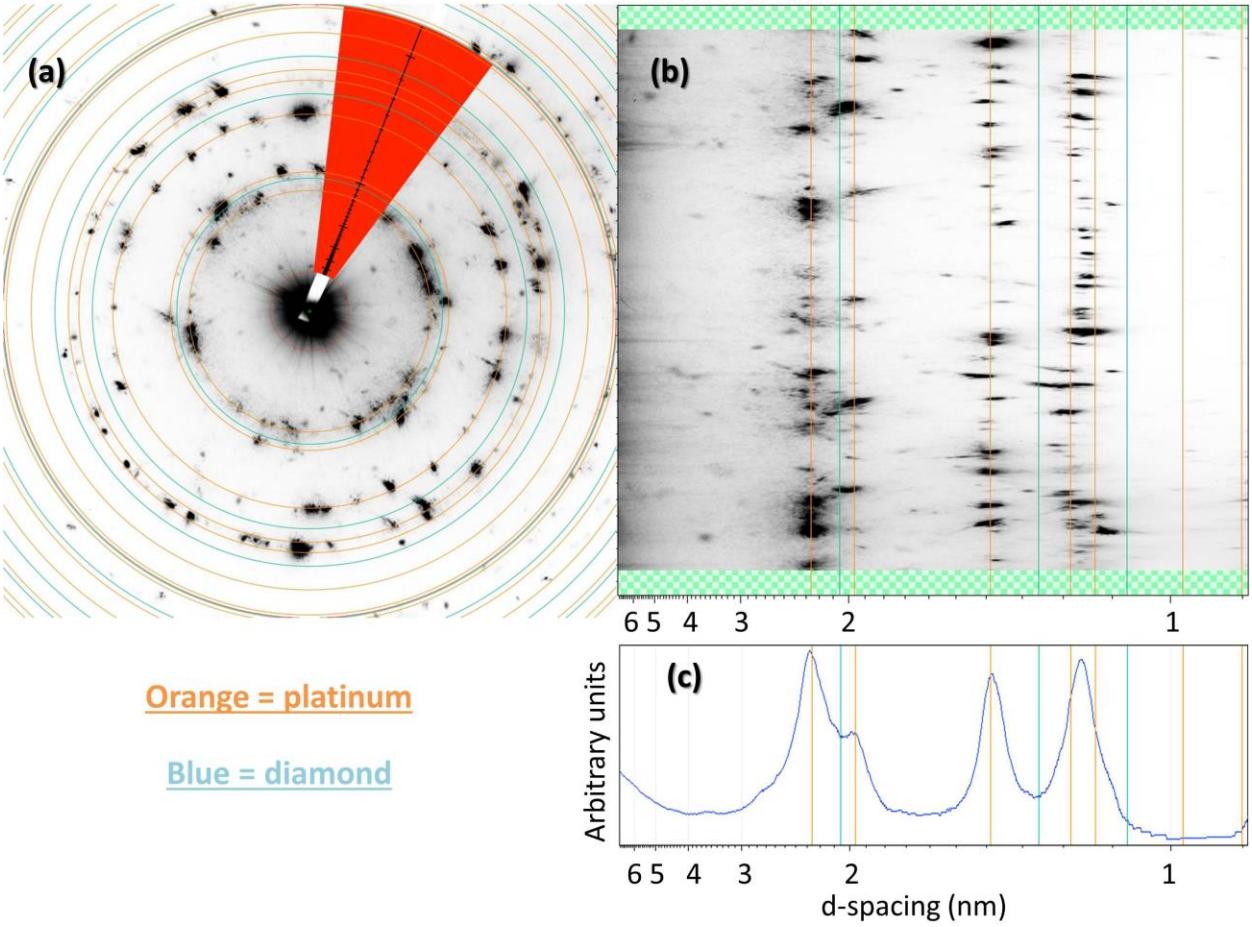

Figure 7.23 Electron diffraction pattern taken of microtip HG01-B (first region, prior to resharpening). (a) is the original diffraction image, where the red arc was excluded from the data used to calculate the integrated radial signal. (b) is the digitally unwrapped diffraction image, where green hashed areas are the arc of the circle that was not included in calculating the radial signal, and (c) is the integrated signal from smaller to larger radius in q-space, with the x-axis converted to d-spacing for ease of reading. The image was calibrated using Pt peaks (orange). The diamond peaks (blue) were then projected onto the patterns.

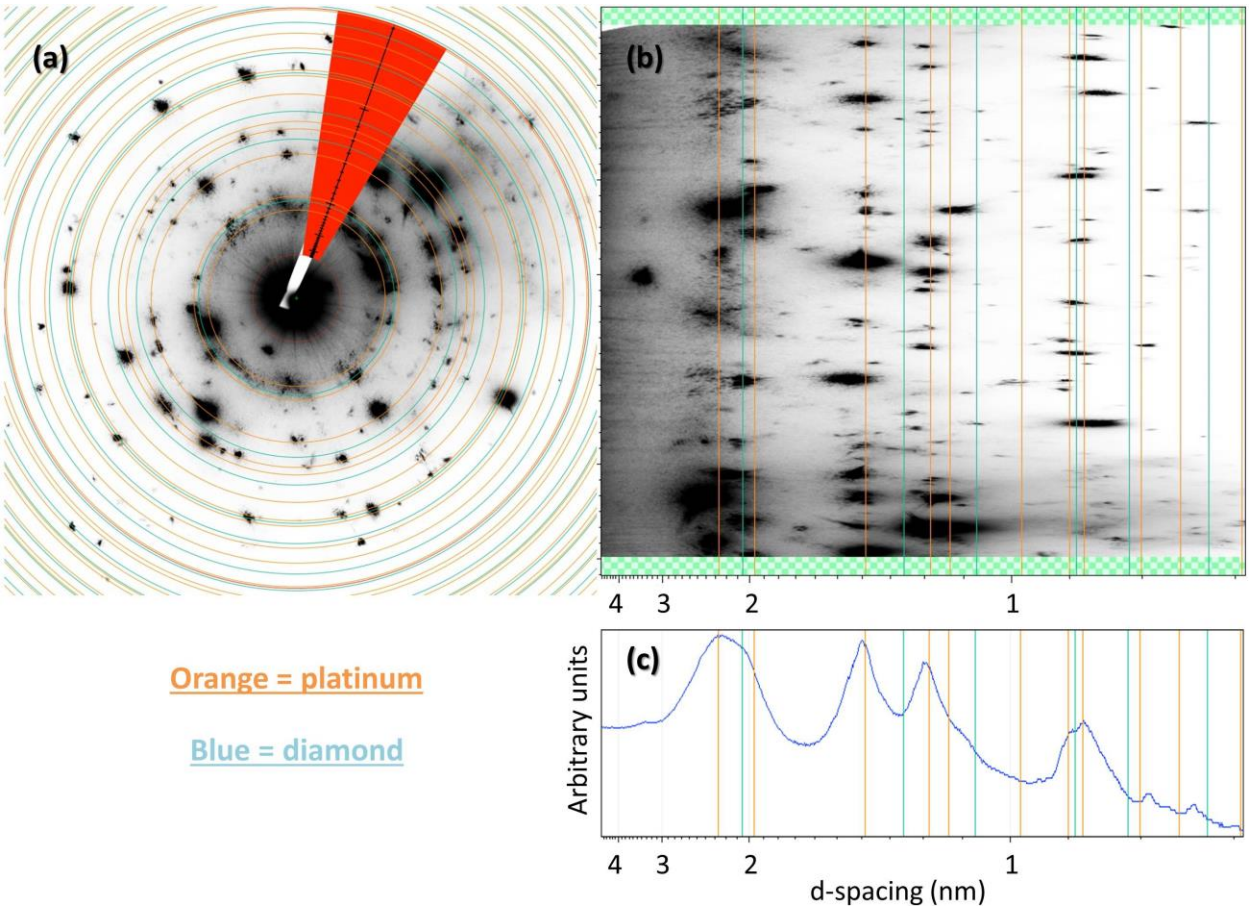

Figure 7.24 Electron diffraction pattern taken of microtip HG01-B (second region, after resharpening). (a) is the original diffraction image, (b) is the digitally unwrapped diffraction image, and (c) is the integrated signal from smaller to larger radius.

HG05-A

An EELS C-edge is present in a 3 nm diameter low-density feature observed in HG05-A. This is probably a nanodiamond, in which case it is the largest nanodiamond visible in the microtip, and one of the largest observed in any microtip. The TEM electron beam was not scanned over this microtip extensively prior to collection of the EELS map, and an EELS search over the rest of the apex of the microtip did not record any other C; therefore, hydrocarbon growth on the microtip surface is not a viable explanation for the C signal. The EELS map has a clear dip in O signal and increase in C signal from the large feature and a small adjacent feature that corresponds to a 1 nm low-density feature observed in STEM imaging (Figure 7.26).

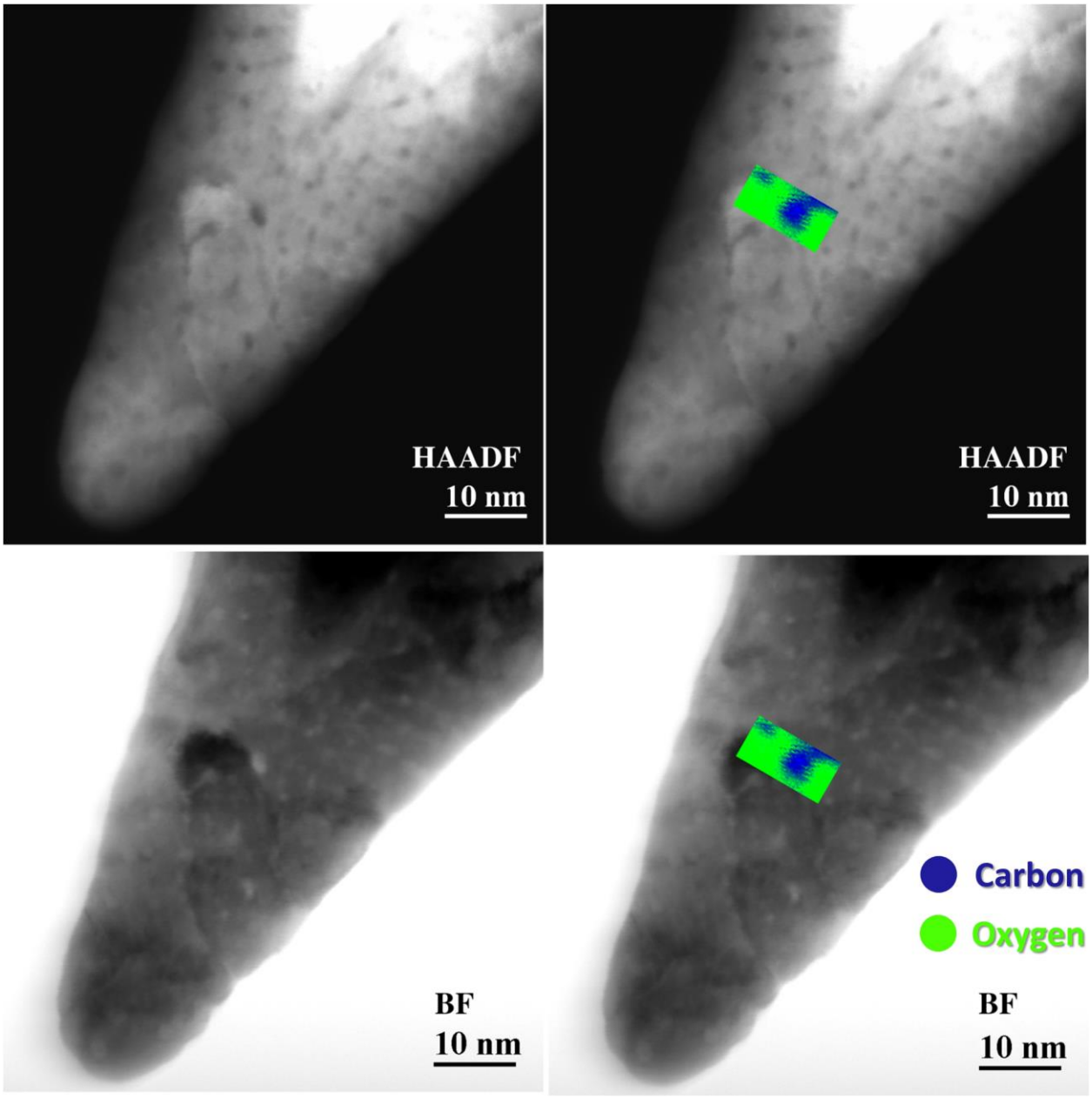

Figure 7.25 The nanodiamond-containing Pt multilayer microtip HG05-A (left) with EELS maps of C k-edge (blue) and O (green) overlayed (right). One axis of the EELS map lies along the axis of rotation of the microtip; it is 33 pixels long. The perpendicular axis is 63 pixels long, with a step size of 2 Å. The map spans roughly 13 nm across and 7 nm along the microtip axis of rotation in STEM HAADF Z-contrast imaging.

However, we returned to this sample a day later and re-found the large, low-density feature, but this time we could find no EELS C signal. This is not consistent with an internal nanodiamond, which could not have moved. It is also not consistent with a nanodiamond adhered to and

protruding from the surface, because this would have produced slightly higher contrast due to the increased thickness (and HAADF signal) from the surface diamond plus the column of microtip material as opposed to just the column of microtip material. It is consistent, however, with a nanodiamond partially embedded in the Pt and partially exposed at the surface. A disordered carbon layer surrounding the diamond would have left it loosely secured in the Pt. The electron beam may have dislodged the diamond, leaving a crater void which would continue to produce a dark feature in STEM HAADF imaging, while the C-K edge EELS signal disappeared (Figure 7.27).

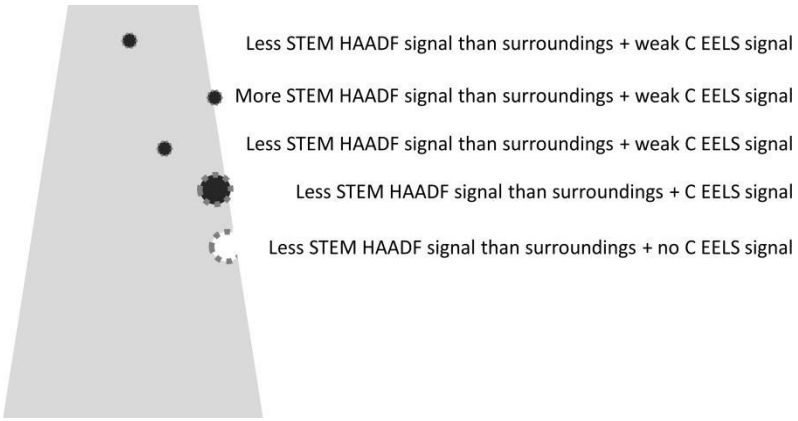

Figure 7.26 Various ways nanodiamonds can be incorporated in a Pt microtip. Small nanodiamonds give EELS signals too weak to detect over the background signal from the Pt matrix. Nanodiamonds adhering to the surface do not decrease the column of Pt that the imaging electrons must pass through, and thus do not create observable dips in Z-contrast in STEM. A large grain, partially exposed at the surface, but recessed, should be detected as a void-like feature with an EELS C signal. Weak bonds to the disordered sp^2-bonded C with which the nanodiamond is surrounded allow it to be removed from the sample, causing a drop in the EELS signal while the void continues to be observed in STEM.

Furthermore, electron diffraction images captured from HG05-A in the TEM show spacings consistent with diamond, graphite, and Pt (Table 7.5, Figure 7.28). Diamond spots are clearly visible at the two innermost diamond peak radii in (Figure 7.28a and b), consistent with several nanodiamonds. A diamond peak is visible in (Figure 7.26c) at the diamond 111 line, over the

background from the two bracketing Pt peaks. We also observed strong diamond (111), Pt (111), Pt (200), and Pt (222), in FFTs of more than one region of HG05-A (e.g., Figure 7.22).

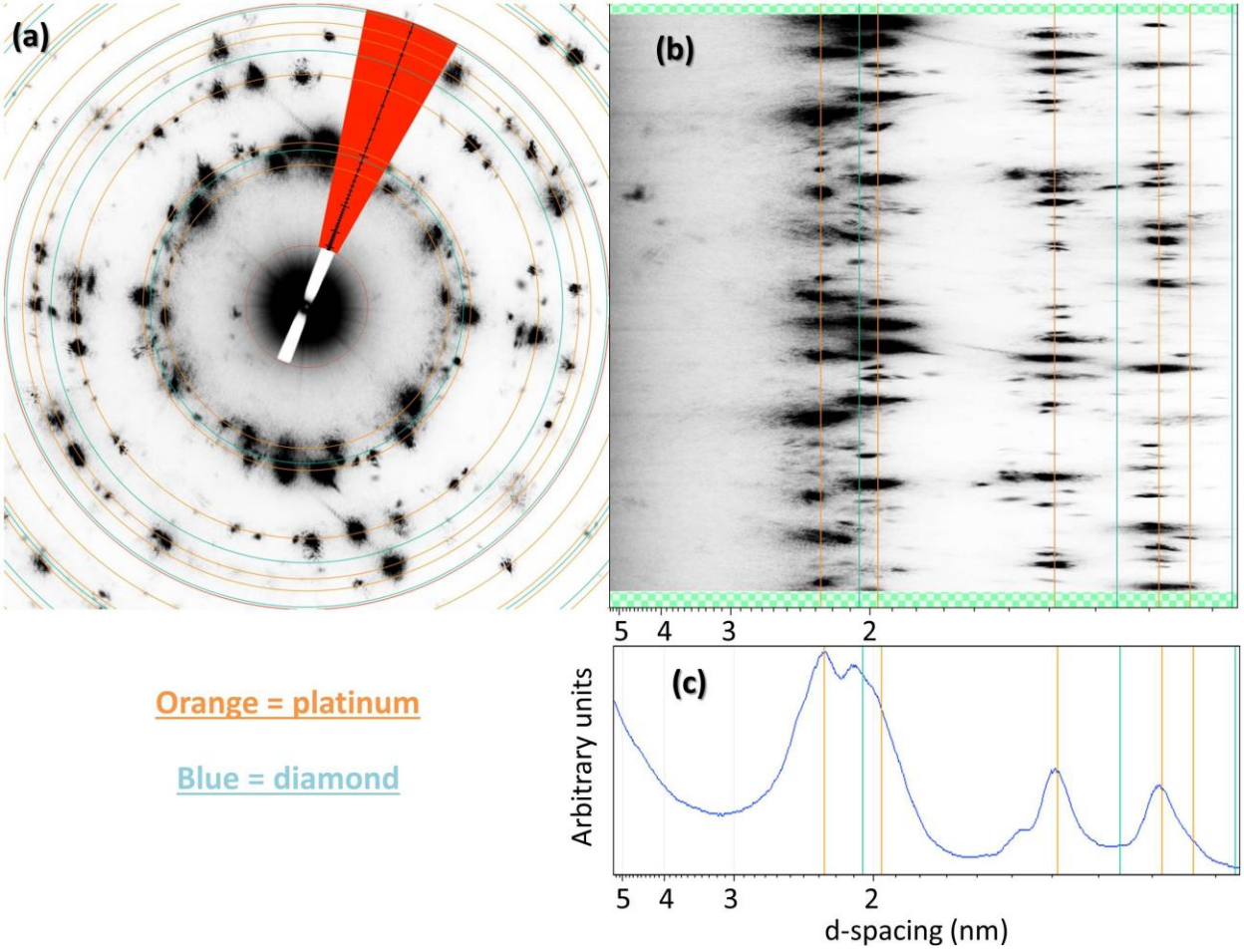

Figure 7.27 Electron diffraction pattern taken of microtip HG05-A. (a) is the original diffraction image, (b) is the digitally unwrapped diffraction image, and (c) is the integrated signal from smaller to larger radius.

HG04-C

Half-grid HG04 was oriented such that the electron beam was parallel to the plane of the deposition layer (Figure 7.1a), rather than normal. SEM and TEM imaging do not give evidence of acid residue at the apex of the microtip. But more than 300 nm down from the apex there is an electron transparent layer, containing atomic spacing for diamond in a 3 nm roughly circular region, covered by several layers with variable spacing consistent with graphene sheets (Figure

7.29). On both sides of the layer there are atomic planes with Pt spacing. This is fully consistent with acid residue-containing nanodiamonds embedded in graphene sheets. An EELS spot analysis of this region did not detect a clear C signal. The samples on HG04 were damaged in handling before APT could be conducted.

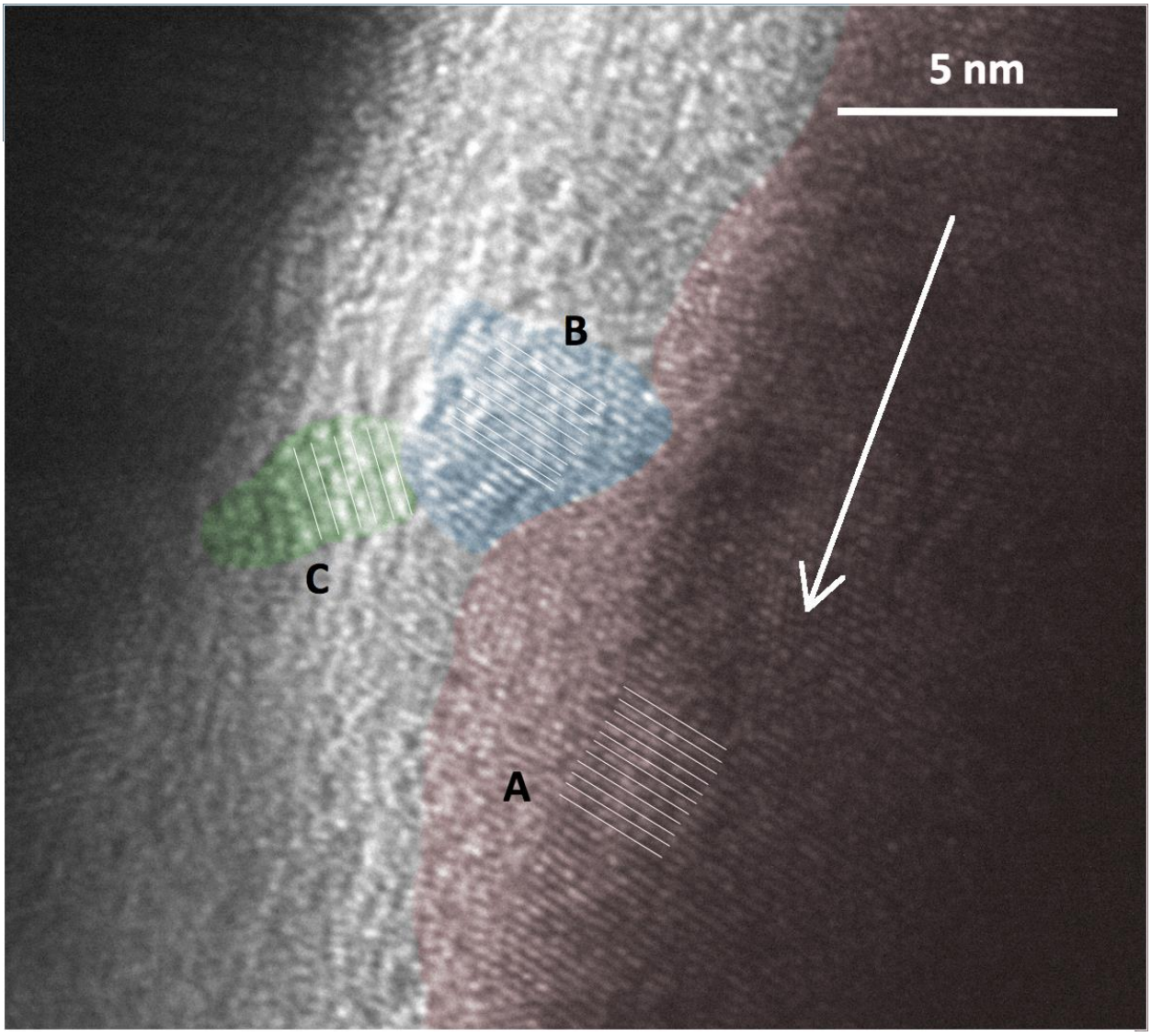

Figure 7.28 TEM image along the deposition layer of microtip HG04-C. White arrow indicates the direction to the microtip apex. Region (a), in red, is dominated by Pt 111 spacings. Region (b), in blue, is roughly the size of an average nanodiamond, and has 10–15 planes with diamond 111 spacing. Region (c), in green, has at least 6 planes with spacings consistent with graphene sheets, which wrap around the left-hand side of the diamond region.

HG06-D

This microtip appears to contain some nanodiamonds, but the interpretation is a borderline case, with some indicator, including diffraction patterns (Figure 7.30), not showing clear evidence of acid residue contents. The best interpretation is that this microtip contains only small amounts of carbonaceous acid residue material. As such, the indicators that do detect signs of acid residue are probably the most sensitive – they include SEM imaging of acid residue in the vicinity of the microtip apex and STEM HAADF imaging of ~1 nm-diameter low Z-density features.

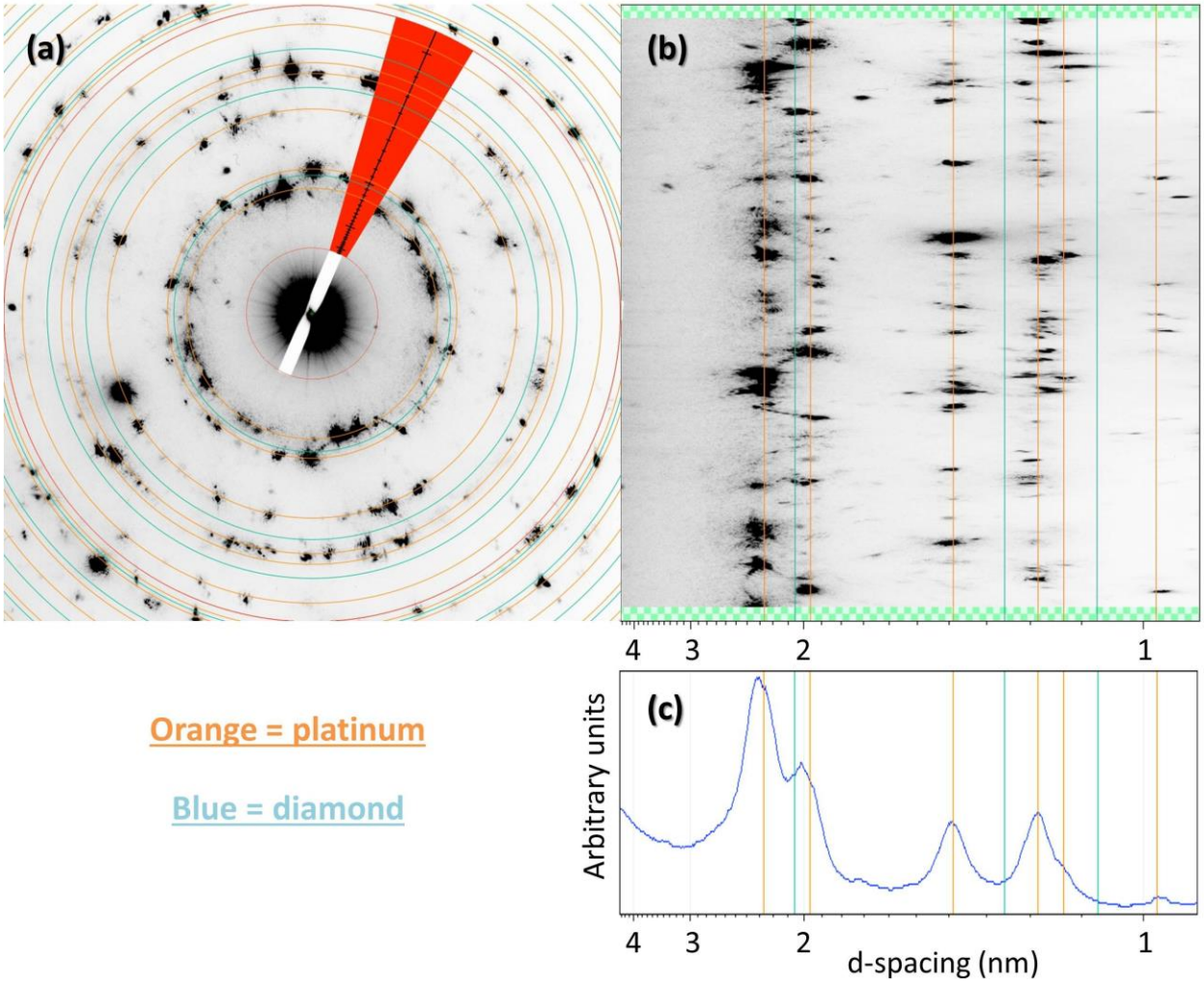

Figure 7.29 Electron diffraction pattern taken of microtip HG06-D. (a) is the original diffraction image, (b) is the digitally unwrapped diffraction image, and (c) is the integrated signal from smaller to larger radius.

HG06-E

Diamond spacing is observed in FFTS, but not all spots in the FFTs from this could be successfully identified as corresponding to planes of expected material, and thus Moiré fringes may be present. In addition, a 1.8 Å spot is observed, which is consistent with a (002) plane, but (002) is a forbidden spot for diamond, suggesting we are detecting some other material, or else are simply observing Moiré fringes.

In two spots, however, we were able to locate the source of the diamond signal in TEM imaging and measure the fringe spacing to be 2.07±1 nm, in agreement with the known value of 2.06 nm for diamond (Table 7.5).

All the regions of this sample where these features were evident in FFT contained ~2 nm void-like features in the middle of chains of low-z features possibly corresponding to nanodiamonds embedded in disordered sp^2-bonded carbon. Taken together with the low-density features, there is good evidence that there are nanodiamonds in this microtip.

7.3.7 Correlated TEM/APT

HG01-B and HG01-C

These two microtips were analyzed by TEM followed by APT. HG01-C is an exception to our practice of conducting a beam shower on the half-grid to fix hydrocarbons prior to analysis, and exhibits a significant hydrocarbon cap in both TEM and APT data sets. TEM and STEM imaging shows ~1 nm low-density features consistent with nanodiamonds (Figure 7.31). These are not randomly spaced, or else some features would have closer neighbors than others. Instead, they are roughly the same distance apart. Atom-probe reconstructions of these microtips do not reproduce evenly-spaced carbonaceous features, or ~1 nm features. Rather, in each of the microtips there is a deposition layer composed of C contaminated with Na. The C is low in

density compared to deposition layers observed in many other samples, and forms a shell-like structure of lower density on the inside of the layer (the outside of the layer is outside the field of view, and was possibly even milled away from the microtip by FIB sharpening. Taken together, these features suggest that these two samples of acid residue contain nanodiamonds associated with loosely-packed carbonaceous material. When deposited on a Pt substrate in suspension, the nanodiamonds were spread evenly across the surface by the retreating edge of the evaporating liquid droplet, along with small amounts of disordered, presumably sp^2-bonded C. The nanodiamonds are detected by STEM HAADF imaging as low-density features. They are surrounded by disordered, porous material, resulting in poor bonding, which results in them being plucked from the acid residue whole under field evaporation conditions in the atom-probe and lost, while some of the disordered C is detected, giving the observed low-density, hollow deposition layer.

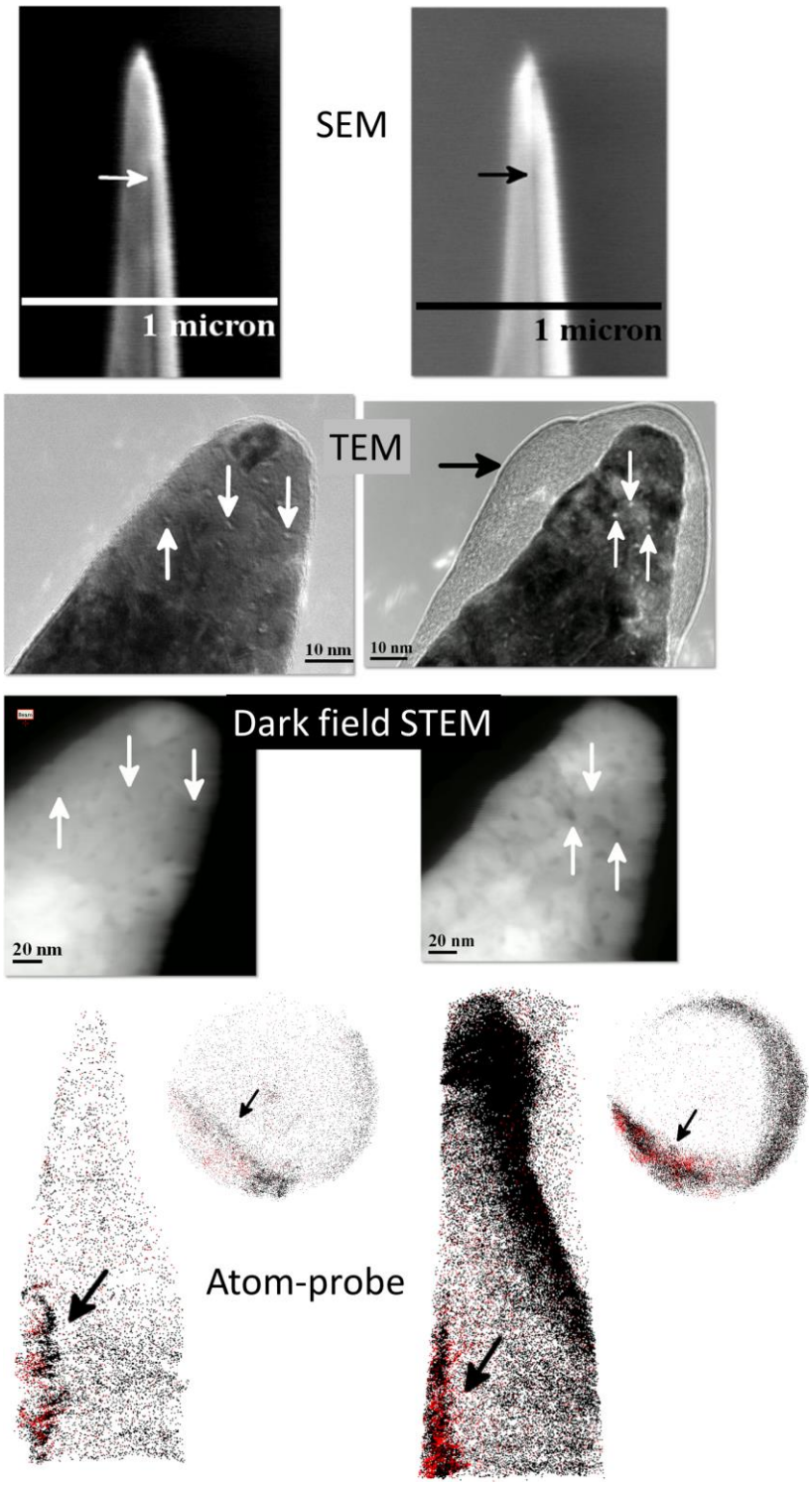

Figure 7.30 Correlated SE/APT/TEM of two microtips containing carbonaceous acid residue, HG01-B (left) and HG01-C (right). For each, SE and APT data show that a layer of acid residue is present in the microtips off-center. TEM and dark field STEM images are oriented such that the beam passes through the deposition layer at a normal angle, such that the contents lie in the plane of the image, showing a number of low-Z contrast features.

HG06-C

In microtip HG06-C, signals from overlapping lattices make the spacing measurements uncertain, but the FFTs appear to contain spots for diamond (111), graphite (111), Pt (111), Pt (002), and no unidentified spots. Atom-probe tomography of this microtip (atom-probe data set R5079 168357, collected on the LEAP 5000X Si) collected under a million Pt ions before fracturing. This represents the top few nanometers of the microtip. There is no evidence of a deposition layer, acid residue, or nanodiamonds, but these features could all have been farther down the microtip in regions from which no APT data was collected. The Pt multilayer contains only a few hundred C atoms, which are homogeneously distributed, probably contamination from the IBS-deposited Ni coating layer.

HG05-E

The LEAP 5000X Si atom-probe data set from this sample, R5079 168252, contains only ~2 million Pt ions. There is no evidence of a deposition layer, acid residue, or nanodiamonds. The Pt multilayer contains only a few hundred C atoms, which are homogeneously distributed contamination from the IBS-deposited Ni-capping layer, as well as laboratory contamination. C does not rise above 5% concentration anywhere in the sputter deposited Pt, or above a density of ~3 C atoms/nm^3. This is consistent with the non-observation of a deposition layer or diamond spacings in TEM and FFT, and the observation of only a few low-density features, but we did not collect data from far enough down the microtip to confirm the TEM non-detection of acid residue.

7.4 Discussion

7.4.1 Implications of Bulk Isotopic Ratios of Nanodiamonds and Disordered C

The bulk C isotopic ratios for our nanodiamond data sets are within 2σ of the terrestrial ratios, albeit with low precision. Potential experimental artifacts affect the normalization of the ADM 2^+ data sets. The counting statistics uncertainty on the bulk ratios is significantly smaller than σ, the standard deviation of the data points, suggesting large uncorrected or undercorrected instrumental artifacts.

Although self-standardization shows similar or more extreme ^{13}C-enrichment in the Pt matrix of each data set with a large ^{13}C-enrichment in the acid residue, it is possible to interpret the anomalies in the ADM data sets as due to intrinsic isotopic anomalies. In principle, the ^{13}C-enriched material observed in the matrices of the ADM outlier data sets could also be from isotopically heavy nanodiamonds, with C signal being projected into the Pt matrix volume due to trajectory aberrations (see Section 2.3.8). However, we do not see the expected gradient in ^{13}C-concentration with increasing radial distance from the nanodiamonds in the reconstructions.

Alternatively, a combination of statistical fluctuations, hydride interference, and potentially unidentified experimental artifacts may be invoked to explain the >4σ ^{12}C/^{13}C isotopic ratio anomalies in the direction of ^{13}C enrichment. Indeed, such effects *must* be invoked to explain similar anomalies in the terrestrial detonation nanodiamond data sets. The large anomalies observed in the Pt matrices of the outlier data sets are good evidence that field evaporation conditions and/or levels of hydride contamination are unusual for these data sets. Thus, we conclude that there is not compelling evidence of isotopic outliers in the APT data, and the ratios

measured therein are consistent with solar system values. Of course, given our sensitivity, our results are also consistent with small isotopic anomalies.

7.4.2 Disordered C in the Acid Residue

For the first time, nanodiamonds on the order of 1 nm in diameter are observed embedded in between the Pt multilayers of microtips, identified in STEM HAADF imaging and diffraction patterns. Low-density C was detected by atom-probe tomography in two of the microtips for which tentative TEM evidence exists for the presence of nanodiamonds. The best explanation is that what we detect in APT reconstructions are ions from disordered sp^2-bonded C surrounding the nanodiamonds in the acid residue that could not be detected by TEM, but that some or all of each nanodiamond fell out after being exposed at the microtip edge or apex. This is consistent with many other cases in which the measured density of C detected by APT is too low to be explained by other known APT effects. Indeed, we observed an instance of a 5 nm carbonaceous grain embedded in the surface, presumably a nanodiamond, disappearing, leaving a hole behind, after it was identified by EELS and STEM HAADF Z-contrast imaging. The above interpretation is that more signal is lost from nanodiamonds than from disordered C. A carbon atom on the surface of a roughly spherical nanodiamond is bonded with three C–C bonds when it is first exposed on the surface. If, on the other hand, a C atom is exposed on the edge of a graphene sheet, it only has two C–C bonds. Prediction of field-evaporation behavior based on this difference is nuanced: If chunks of disordered C are bonded to the Pt matrix or to other chunks of disordered C, it will be easier to tear these chunks from their bonds than to remove a chunk from a nanodiamond. On the other hand, individual disordered C atoms should field evaporate more readily than nanodiamond atoms, so it is less likely the local field will increase enough to remove entire chunks of disordered C; rather, C ions will field evaporate as they are exposed,

"unraveling" the sheets of sp^2-bonded material. The nanodiamond atoms, or sp^2-bonded closed volumes (such as C_{60} buckyballs or concentric graphene shells, potentially present around the nanodiamonds) will not field evaporate as easily. This implies that the degree of damage done to the different phases in the acid residue is important to understanding how they will field evaporate. Compared to nanodiamonds surrounded by disordered sp^2-bonded C, isolated nanodiamonds may have more bonds to the sputter deposited Pt, strong enough to prevent loss of the diamond for some time, creating holes in the reconstruction (e.g., cross sections of APT data sets R06 18430 (Figure 7.16) and R06 19354 (Figure 7.17)). But nanodiamonds embedded in disordered C, laid down together in solution, are much more likely to be removed quickly from the sample by the electric field and laser pulsing due to weak bonds to the surrounding low-density material (e.g., HG01-B, HG01-C, and likely many others).

Comparing these competing factors, the higher field required for the field evaporation of diamond compared to disordered C probably dominates cluster loss behavior, making it more likely to lose signal from nanodiamonds than from disordered C.

In many cases, even without correlated TEM data, we have distinguished between the two phases of acid residue material, one consistent with disordered C, the other with nanodiamonds. Many data sets contain fractions of each phase, with the disordered phase often located around the periphery of the nanodiamonds (e.g., Figures 7.8 and 7.20). This appears to vary based on variations in how the acid residue deposit for the multilayer is made, and what regions of the multilayer are selected for FIB liftout.

Analysis of the isotopic ratios of data sets dominated by one phase or the other does not indicate a large difference in the isotopic ratios of the two phases; however, our sensitivity to anomalies in ^{13}C content is on the order of 10s of %, not single % or ‰.

7.4.3 Isotopic Assessment of Data Sets with 1–10 Nanodiamonds

Normalization to the bulk isotopic ratio of the terrestrial detonation nanodiamond standards eliminated much but not all of the effects of instrumental artifacts (Sections 7.3.1 and 7.3.2). The remaining effects were detected by data-set by data-set self-standardization of the acid residue using the low-level terrestrial C contamination in the IBS-deposited Pt matrix (Section 7.3.4). None of the 36 APT data sets, each containing 1–10 nanodiamonds and unknown amounts of disordered C, showed signs of major (100s of ‰) ^{13}C enrichment, or extreme (1000s of ‰.) ^{13}C depletion. Smaller isotopic anomalies could have been present below the sensitivity of the technique.

In light of the results from each of these two methods for standardization against instrumental artifacts in APT isotope ratio measurements, one cannot be entirely discarded in favor of the other; rather, it remains useful, even necessary, to take advantage of the benefits of each to help correct for the weaknesses of the other. The first method leverages larger numbers of counts and data sets for better statistics and comparisons of various samples, while the second method minimizes the effects of sample preparation and different analysis conditions on the standardization process.

7.4.4 Isotopic Ratios of Nanodiamonds vs. Disordered C

SEM, TEM, and APT evidence allow for qualitative distinctions to be made between APT reconstructions that are dominated by disordered C or nanodiamond. Trends, albeit weak ones,

exist between decreasing O/residuals and increasing $^{12}C^{+}/^{13}C^{+}$ ratio, and between increasing $C_1+(2\times C_2)+(3\times C_3)$/residuals and increasing $^{12}C^{+}/^{13}C^{+}$ ratio. Several interpretations are available:

(1) $^{12}CH^{+}$ hydride formation goes up with increasing O and decreasing fraction of C, causing lower measured C^{+} ratios but not lower C^{++} ions.

(2) Higher O counts and lower C counts relative to total acid residue counts are not a sign of a larger fraction of disordered C, but of a higher fraction of Pt matrix contamination. This is a doubtful interpretation because Figure 7.13 indicates no trend for the C counts with increasing Pt counts, and only a small trend towards higher O counts with increasing Pt counts, with a poor linear fit. But if this interpretation is correct, increased Pt matrix contamination in a data set corresponds to more isotopically heavy C^{+} ions (Figure 7.12), suggesting that either the acid residue has higher isotopic ratios than the matrix, or else different field evaporation conditions or experimental artifacts such as hydride interference are resulting in different ratio measurements. This could imply the presence of a few data sets with isotopically light C^{+} in the acid residue, but does not explain why we do not measure similar trends for C^{++}.

(3) It is possible the observed trends are produced by the random scatter of the ratio data and do not have any implications for the sample or experimental artifacts. The fits to a trend line do not have high enough R^2 values to rule out this possibility with a high degree of confidence.

(4) Decreasing O and increasing C counts correlate with decreasing disordered C and increasing nanodiamond content in a data set. In this interpretation, our results indicate that the nanodiamonds have higher isotopic ratios than the disordered C, and that these two phases form from two different reservoirs of carbonaceous material. However, it must be remembered that the trends were only apparent for the 1^{+} ratios.

Interpretations (1) and (2) call for further work to understand and control factors for sample preparation, and to correct for various instrumental artifacts. Interpretation (3) calls for the collection of more data points with higher atomic detection efficiency to improve statistics, and is consistent with any scenario in which the disordered C and nanodiamonds have similar mean isotopic ratios for aggregates on the order of thousands of C atoms. This includes most explanations for the formation of the disordered C and nanodiamonds: That one phase formed from the other; that they originated from the same stars; that they formed together in the ISM; or that both formed from an isotopically homogenized reservoir such as the early solar system. Interpretation (4), that the nanodiamonds have slightly higher $^{12}C/^{13}C$ ratios than the disordered C in the acid residue, has the most implications for the origins of presolar nanodiamonds, which are discussed in Section 7.4.6.

7.4.5 Summary of Experimental Findings on Nanodiamonds

(1) APT findings are consistent with bulk studies by stepped heating and small-bulk studies by NanoSIMS. Aggregates of various numbers of nanodiamonds (1–10 by APT, ~1000 and ~10^6 by NanoSIMS (Lewis et al. 2017) show mostly insignificant deviation from solar system isotopic ratios.

(2) ^{13}C-enriched outlier data sets observed by APT are best explained as the result of instrumental artifacts such as $^{12}CH^+$ hydride interference affecting some data sets more than others. This non-detection of strong isotopic anomalies in a data set of about 100 nanodiamonds is consistent with the four to five probable ^{13}C-enriched aggregates out of 72,103 NanoSIMS measurements of ~1000 nanodiamonds at a time (less than one anomaly per ten thousand measurements), in that strongly ^{13}C-enriched material appears to be present in the acid residue, but only in concentrations less than 1/1000.

(3) There is inconclusive evidence that the disordered C has isotopic compositions that are ^{13}C-enriched relative to the nanodiamonds.

(4) The sensitivity of APT measurements and the amount of material analyzed to date is insufficient to provide additional insight into the evidence from broadening of distributions of C isotopic ratio measurements by NanoSIMS that the acid residues are composed of material from at least two reservoirs with different ratios of $^{12}C/^{13}C$.

7.4.6 Implications for Nanodiamond Origins

Supposing, based on these findings, that a small minority of nanodiamonds are extremely enriched in ^{13}C, that some potentially larger fraction have varied (but not extremely anomalous) isotopic ratios, and that different fractions of the nanodiamonds could be from different presolar and solar sources, additional discussion is warranted concerning the locations and processes where and by which meteoritic nanodiamonds may have formed.

Supernova: Type II, He/C Shell

Nanodiamond formation by chemical vapor deposition (CVD) requires free C, and under equilibrium conditions a ratio of carbon to oxygen > 1 is required for the presence of C not trapped in CO. The He/C shell in Type II supernovae provides C >> O, as well as abundant ^{12}C through the triple-alpha process (Figure 1.2). Mixing of material from the adjacent ^{13}C-rich He/N zone during and after the explosion can provide a broad range of C isotopic ratios. No estimate exists for the mean$^{12}C/^{13}C$ ratio one might expect from He/C shell nanodiamonds from a variety of supernovae. Quantitative modeling has so far not been sufficient to conclude confidently what the average $^{12}C/^{13}C$ ratio would be in the He/C shell with mixed-in He/N shell material of a supernova of a given mass. And if nanodiamonds form in the He/C shells of many supernovae of different masses, a better understanding of the distribution of masses in Type II supernovae is

also required before such an estimation could be made. However, Type II supernovae produce a minority of the total carbon in the interstellar medium (Meyer 1997), so it is unlikely that the average supernova $^{12}C/^{13}C$ ratio is the same as the solar system ratio. This implies that only a minority of meteoritic nanodiamonds could come from Type II supernovae, unless some mechanism is found that allows for nanodiamond formation only within a narrow range of $^{12}C/^{13}C$ ratios in a mix between the He/C and He/N zones, *and* that, by chance, that narrow range of ratios happens to be close to the solar system C isotopic ratio.

One significant difficulty in reconciling supernova formation with data on presolar grains is that only nanodiamonds have been found to carry Xe-HL, but a significant fraction of presolar graphite grains and a small fraction of presolar SiC grains have been identified as coming from supernovae. If the nanodiamonds and Xe-HL come from supernovae, these other supernova grains should also contain a Xe-HL component. However, nanodiamonds are the most abundant type of presolar grain by mass. If a large fraction of the nanodiamonds are from supernovae, it implies that only a very small fraction of supernova grains are implanted with Xe-HL (fewer than 1 in a million nanodiamonds are required to carry an atom drawn from a reservoir of Xe-HL isotopes). The mass concentrations of *supernova* SiC and graphite in carbonaceous chondrites are factors of roughly 1000 times smaller than that of nanodiamond, so if most of the nanodiamonds are from supernovae, we would expect the concentration of Xe-HL that is from supernova SiC and graphite to be 1000 times smaller (Zinner 2014), possibly below the sensitivity of the stepped heating and gas mass spectrometry originally used to trace and isolate the carrier of Xe-HL.

But again, if a large fraction of nanodiamonds formed in the He shell, a mechanism is needed to explain why they have, on average, solar system C and N isotopic ratios and no dramatic C isotopic heterogeneity; to date, none exists.

If, on the other hand, only a *small* fraction of nanodiamonds are from supernovae, the C and N isotopes are no longer an issue, but a mechanism must be found to explain the absence of Xe-HL in supernova SiC and graphite. If, for example, only 1 in 10,000 nanodiamonds are from supernovae, and about 1 in 10^6 nanodiamonds carries an atom of Xe from the Xe-HL reservoir, then about 1 in 1000 *supernova* nanodiamonds is required to carry the Xe-HL, and one would expect the same amount of Xe-HL to be carried by SiC and graphite by mass in carbonaceous chondrites, but this is clearly counterindicated by experiments. The conclusion is that either a large fraction of meteoritic nanodiamonds formed in the He shell with solar C and N isotopic ratios, or else the Xe-HL is not carried by He-shell nanodiamonds.

Another difficulty with nanodiamond formation in the He shell is the lack of evidence for ^{26}Al incorporation into the nanodiamonds, as ^{26}Al is known to have been produced in this shell (Woosley and Weaver 1995; Zinner 2014). But measurements of nanodiamond-containing meteoritic acid residues from Murchison and Allende did not find such evidence (Besmehn, Hoppe, and Ott 2011).

Supernova: Type II, H Shell

There may be transient free C in C/O < 1 regions of supernovae for the first few years after the explosion due to ultraviolet radiation from short-lived radionuclide ^{56}Ni dissociating CO. Simulations of C grain formation competing with CO suggests that free C may be able to nucleate carbonaceous grains in spite of a C/O ratio less than 1 (Clayton et al. 1999; Deneault et al. 2006). However, there are several lines of evidence that SiC and graphite grains did not form

in regions where C/O < 1 (Zinner 2014, and references therein), meaning there is no evidence that carbonaceous grains are forming there. Under most circumstances, graphite is thermodynamically favored to form over diamond, so it would not seem likely that nanodiamonds formed in these regions if graphite could not. However, in laboratory environments, CVD of diamond occurs much more readily in the presence of hydrogen (Angus and Hayman 1988; Frenklach and Spear 1988), which makes the H-rich shell attractive for nanodiamond formation, if O does not bind up all the free C. Lower C/O ratios increase the probability of diamond vs. graphite products from CVD processes (assuming formation of carbonaceous grains proceeds at all). There are two mechanisms that may contribute to this. First, O introduced into laboratory CVD environments has been shown to destroy graphite by oxidation, leaving only the nanodiamonds behind. Second, O may serve a similar role as H in catalyzing diamond formation preferentially to graphite (Michael Frenklach, personal communication). Most studies of CVD have laboratory conditions in mind; even in that context modeling of the exact kinetic and chemical processes is complex (e.g., Frenklach and Wang 1991), so there remains considerable uncertainty as to exactly what conditions would foster nanodiamond growth in supernovae environments.

Instead of forming by CVD, small carbonaceous grains may be annealed into nanodiamonds by absorption of ultraviolet photons from radioactive decay of ^{56}Ni (Nuth and Allen 1992). Again, this requires either the appropriate concentration of H, or the appropriately low C/O ratio to prevent the grains from forming graphite instead of nanodiamond. One argument against this, and any formation condition other than CVD, is that the frequency of occurrence of twin boundaries in meteoritic nanodiamonds is consistent with that expected from CVD nanodiamond formation (Daulton et al. 1996).

For nanodiamonds to form in the H shell, mixing in of material from the next two lower shells: He/N (^{13}C-rich) and He/C (^{12}C-rich) is required to provide C, and, indeed, significant mixing during and after the explosion is expected (e.g., Fedkin et al. 2010). This would create a wide range of ^{12}C, ^{13}C, and H concentrations. It is possible that a mixture of ^{13}C- and ^{12}C-rich zones could correlate with the appropriate concentrations of C and H for CVD growth of nanodiamonds to be favored over graphite formation.

Such specific formation requirements for CVD nanodiamond growth, including not only the presence of H and some form of C, but also low C/O ratio and a source of UV photons, offer explanatory power to explain why nanodiamonds have trace element signatures that are only consistent with supernovae, not AGB stars, whereas most other presolar grain types have large populations that originated from AGB stars. That is, diamond may not form around AGB stars because it is a metastable state of C while graphite is a stable state, but might form in Type II supernova H shells because of precise formation conditions being met. This also separates the nanodiamond formation conditions from those of supernova graphite and SiC, both in location and possibly in time, leaving open the possibility of a scenario in which the Xe-HL implants into just the nanodiamonds. This would resolve several issues, allowing a small fraction of the nanodiamonds to be from supernovae and carriers of Xe-HL, some with the observed non-solar isotopic ratios, while not requiring non-existent Xe-HL in presolar SiC and graphite.

Supernova: Type Ia

Binary star systems that undergo Type Ia supernova explosions have been suggested as a formation location for the meteoritic nanodiamonds (Jorgensen 1988). Particularly, a red giant with C/O>1, that is, a C star, could produce the nanodiamonds, and a companion white dwarf experiencing a Type Ia supernova could implant Xe-HL. Similar difficulties with reconciling the

data are present for this formation environment as for Type II supernovae, but it offers the same explanatory advantages by forming the nanodiamonds in conditions hostile to SiC and graphite formation.

If one takes the position that nanodiamonds are formed in C/O < 1 material through ^{56}Ni-driven UV photodissociation of CO, red dwarfs other than carbon stars (i.e., oxygen stars with C/O < 1) could create the C for the nanodiamonds instead of C stars, but only *after* the supernova explosion. As in Type II supernovae, the explanatory advantage of this aspect of the model is that it explains why we do not find significant numbers of nanodiamonds from AGB stars – it is because CVD processes typically form *either* graphite *or* nanodiamonds, and it is only in supernovae that the proper conditions are met for nanodiamond formation on a large scale.

Interstellar Medium

Supernova shock waves traveling through the interstellar medium might convert carbonaceous organics into nanodiamonds and disordered carbon (Stroud et al. 2011) with the low concentration of Xe-HL and other supernova trace element phases, as observed in meteorites. This scenario predicts the same carbon isotopic ratios for the two carbonaceous phases, so more conclusive atom-probe measurements of the isotopic ratios of the two phases, or a different experimental approach to separating and measuring the isotopes in the two phases, would be helpful in testing this explanation for the nanodiamond origin.

The solar system C isotopic ratio in the bulk nanodiamonds may be consistent with this formation mechanism, assuming the carbonaceous material is similar to that of the well-mixed protosolar nebula. If the nanodiamonds formed in the protostellar nebula, the question is raised as to why other, orders-of-magnitude larger presolar grains were not also implanted with Xe-HL.

If they were, one must argue that the lower concentration of these grains and the presence of other components have so far prevented the Xe-HL components from being detected in those grains.

Condensation of a handful of grains in supernovae would account for ^{13}C-enriched grains in this scenario.

Solar System: Evidence

Nanodiamonds are strongly depleted in non-cluster IDPs (Dai et al. 2002), a puzzling observation if the nanodiamonds are presolar and thus were present in the early solar system when the IDPs formed. In order to explain the absence of nanodiamonds one must either posit a heterogeneous presolar grain distribution, with lower grain abundances in the outer solar system, or else a different formation location for non-cluster IDPs than currently believed – outer solar system material such as IDPs could be material that was processed by the sun, reducing dust content, and then circulated into the outer solar system (Dai et al. 2002). Either scenario would be a striking revision to our understanding of early solar system processes. IDP parent-bodies are theorized to form in the same regions as comets, for which some presolar grain data exists due to the Stardust mission's return of material from the comet Wild II (Brownlee 2014). Very few presolar grains have been detected from this comet, none of them nanodiamonds. However, comparison to test shots using well-characterized meteoritic material showed that most of the apparent depletion was the result of sorting, alteration, and destruction of grains during collection (Floss et al. 2013).

Signals from nanodiamonds may have been observed in the circumstellar disks of young stars, suggesting that the conditions for their formation can and do exist in protostellar environments, and therefore may have existed in our own young solar system. Infrared emission lines from C-H

bulk-terminated stretch modes have been observed in the circumstellar disks around some young stars. These signatures could be from hydrogenated nanodiamond surfaces (Van Kerckhoven, Tielens, and Waelkens 2002). However, they could also be from diamondoids, carbonaceous structures smaller than 1 nm (Pirali et al. 2007).

Bulk-termination bonding occurs on diamond-bonded structures, but not sp^2-bonded structures, indicating that if these signals are from nanodiamonds, the grains are not covered in sp^2-bonded shells. Bulk-termination bonding is thermodynamically favored above 800 K, but excluded above 1300 K, as dehydrogenation and conversion of nanodiamond surfaces to a graphite shell begins above this temperature. This establishes a temperature range for the formation of these potential nanodiamonds.

The vast majority of spectroscopically observed protostellar disks do not, however, bear the distinctive signature of these diamonds. Perhaps in many environments nanodiamonds form but are surrounded by sp^2-bonded carbon shells. Or perhaps there are as-yet-undetermined requirements for their formation that are not met by most protostellar environments.

Solar System: Formation Mechanisms

Whether or not nanodiamonds form in protostellar or young solar environments has yet to be conclusively demonstrated. Given the presence of free atomic C in a low-pressure environment, graphite formation is typically favored over C. Hydrogen overabundance can, however, make the formation of diamond favorable over graphite (Angus and Hayman 1988; Frenklach and Spear 1988), and the presence of O may serve a similar role; however, for $C/O < 1$, CO formation dominates easily over graphite or diamond. Fischer-Tropsch reactions on a substrate such as Fe can catalyze CO dissociation, and iron grains are believed to be present in the early solar system (Meibom et al. 1999). Alternatively, diamond might have been formed indirectly, by

transformation of presolar graphitic, sp^2-bonded C to sp3-bonded diamond. Shock transformation of sp^2-bonded C "onion shell" fullerene structures is an example of a potentially viable process (Marks et al. 2012) that could have taken place through collisions with early solar system solids.

Whether the precise conditions for condensation of nanodiamond are commonly, or ever, provided by circumstellar disk environments remains unknown. It is therefore difficult to assess the likelihood that such conditions existed in our solar system. However, most of the nanodiamonds have solar system $^{12}C/^{13}C$ isotopic ratios, down to small clusters, evidence that such conditions can and did exist.

Conclusions

In conclusion the presence of Xe-HL and a small (<1/1000) fraction of greatly ^{13}C-enriched nanodiamonds, along with evidence that the nanodiamonds are composed of a mixture of C isotopic material, strongly implies the presence of supernova material in the nanodiamonds.

But unless one can produce a mechanism to put Xe-HL in a large fraction of supernova nanodiamonds while not putting it into supernova SiC and graphite, one must assume a large fraction of nanodiamonds are from supernovae, in order to posit that the fraction of supernova grains with Xe-HL implantation is low, and this leads to irreconcilable problems with the C and N ratios in the nanodiamonds.

Condensation of nanodiamonds in the H shells of Type II supernovae, where supernova SiC and graphite do not form, is not a complete explanation for this phenomenon, but would be a step in the right direction, as this mechanism separates the formation conditions and environment for supernova nanodiamonds from other types of presolar grains.

Co-formation of nanodiamonds and disordered C by supernova shock in the interstellar medium, given plenteous carbonaceous precursor material and effective transformation, implies the same isotopic contents in the two phases of C and a low level of Xe-HL in other presolar grains, both of which implications are likely to be experimentally testable in the near future.

7.4.7 Outlook of Investigations into the Origins of Meteoritic Nanodiamonds

(1) APT remains the only viable technique for isotopic studies of individual nanodiamonds.

(2) Quantitative assessment of C isotopes from nanodiamond-containing acid residue still poses significant analytical challenges. Carbonaceous materials are prone to correlated evaporation in the atom-probe and are difficult to match to a matrix with a similar evaporation field. The acid residue has two phases, making it impossible to avoid aberrations in data collection due to mismatched field evaporation behavior. Given the high field required for acid residue field evaporation, the bonding between IBS-deposited Pt and the acid residue is likely insufficient to prevent particles from falling out when they are subjected to high fields and thermal pulsing while exposed on the microtip surface. Advances in field evaporation theory regarding correlated evaporation and estimation of evaporation fields of various materials may offer insights useful in overcoming these challenges.

(3) Careful control and characterization of acid-residue deposits in multilayers is important for future projects. For acid residue deposits in multilayers, a study of deposits using different concentrations of acid residue in suspension, different substrate temperatures, and different ultrasonication parameters may identify a technique that reproducibly creates deposits favorable for FIB liftout of targeted acid residue regions and TEM and APT analysis. Preparation steps should be carried out identically for nanodiamond samples and DND standards to minimize the differences between the samples. Methods to subdivide the acid residue based on some

distinguishing feature (Gilmour et al. 2005; Pravdivtseva et al. 2016; Shatoff et al. 2015; Stroud et al. 2016; Verchovsky et al. 1998) are invaluable, because even qualitatively distinguishing the phases in APT reconstructions is difficult.

7.5 References

Angus J. C., and Hayman C. C. 1988. Low-pressure, metastable growth of diamond and "diamondlike" phases. *Science* 241:913–921.

Anisichkin V. F. 2007. Isotope studies of detonation mechanisms of TNT, RDX, and HMX. *Combustion, Explosion, and Shock Waves* 43:580–586.

Bernatowicz T. J., Gibbons P. C., and Lewis R. S. 1990. Electron energy loss spectrometry of interstellar diamonds. *The Astrophysical Journal* 359:246–255.

Besmehn A., Hoppe P., and Ott U. 2011. Search for extinct aluminum-26 and titanium-44 in nanodiamonds from the Allende CV3 and Murchison CM2 meteorites: Aluminum-26 and titanium-44 in meteoritic diamonds. *Meteoritics & Planetary Science* 46:1265–1275.

Brooks B. R., and Schaefer III H. F. 1977. Reactions of carbynes. Potential energy surfaces for the doublet and quartet methylidyne (CH) reactions with molecular hydrogen. *The Journal of Chemical Physics* 67:5146–5151.

Brownlee D. 2014. The Stardust mission: Analyzing samples from the edge of the solar system. *Annual Review of Earth and Planetary Sciences* 42:179–205.

Clayton D. D., Liu W., and Dalgarno A. 1999. Condensation of carbon in radioactive supernova gas. *Science* 283:1290–1292.

Coffin R. B., Miyares P. H., Kelley C. A., Cifuentes L. A., and Reynolds C. M. 2001. Stable carbon and nitrogen isotope analysis of TNT: Two-dimensional source identification. *Environmental Toxicology and Chemistry* 20:2676–2680.

Coplen T. B. et al. 2002. Isotope-abundance variations of selected elements (IUPAC Technical Report). *Pure and Applied Chemistry* 74:1987–2017.

Dai Z. R., Bradley J. P., Joswiak D. J., Brownlee D. E., Hill H. G. M., and Genge M. J. 2002. Possible in situ formation of meteoritic nanodiamonds in the early Solar System. *Nature* 418:157–159.

Daulton T. L., Bondi K. S., and Kelton K. F. 2010. Nanobeam diffraction fluctuation electron microscopy technique for structural characterization of disordered materials—Application to Al88−xY7Fe5Tix metallic glasses. *Ultramicroscopy* 10:1279–1289.

Daulton T. L., Eisenhour D. D., Bernatowicz T. J., Lewis R. S., and Buseck P. R. 1996. Genesis of presolar diamonds: Comparative high-resolution transmission electron microscopy study of meteoritic and terrestrial nano-diamonds. *Geochimica et Cosmochimica Acta* 60:4853–4872.

Deneault E. A.-N., Clayton D. D., and Meyer B. S. 2006. Growth of carbon grains in supernova ejecta. *The Astrophysical Journal* 638:234–240.

Fedkin A. V., Meyer B. S., and Grossman L. 2010. Condensation and mixing in supernova ejecta. *Geochimica et Cosmochimica Acta* 74:3642–3658.

Floss C., Stadermann F. J., Kearsley A. T., Burchell M. J., and Ong W. J. 2013. The abundance of presolar grains in comet 81P/Wild 2. *The Astrophysical Journal* 763:140 (11pp).

Frenklach M., and Spear K. E. 1988. Growth mechanism of vapor-deposited diamond. *Journal of Materials Research* 3:133–140.

Frenklach M., and Wang H. 1991. Detailed surface and gas-phase chemical kinetics of diamond deposition. *Physical Review B* 43:1520–1545.

Gilmour J. D., Verchovsky A. B., Fisenko A. V., Holland G., and Turner G. 2005. Xenon isotopes in size separated nanodiamonds from Efremovka: 129Xe*, Xe-P3, and Xe-P6. *Geochimica et Cosmochimica Acta* 69:4133–4148.

Greiner N. R., Phillips D. S., Johnson J. D., and Volk F. 1988. Diamonds in detonation soot. *Nature* 333:440–442.

Harris P. J. F. 2004. Fullerene-related structure of commercial glassy carbons. *Philosophical Magazine* 84:3159–3167.

Heck P. R. et al. 2014. Atom-probe analyses of nanodiamonds from Allende. *Meteoritics & Planetary Science* 49:453–467.

Howa J. D., Lott M. J., Chesson L. A., and Ehleringer J. R. 2014. Carbon and nitrogen isotope ratios of factory-produced RDX and HMX. *Forensic Science International* 240:80–87.

Jorgensen U. G. 1988. Formation of Xe-HL-enriched diamond grains in stellar environments. *Nature* 332:702–705.

Kellett E. A., and Richards B. P. 1971. The c-axis thermal expansion of carbons and graphites. *Journal of Applied Crystallography* 4:1–8.

Kunicki T. C., Beerman D., Geiser B. G., Oltman E., O'Neill R. W., and Larson D. J. 2006. Atom probe data reconstruction, visualization and analysis with the Imago Visualization and Analysis System (IVAS). *19th International Vacuum Nanoelectronics Conference & 50th International Field Emission Symposium*. pp. 535–536.

Lewis J. B., Isheim D., Floss C., and Seidman D. N. 2015. 12C/13C-ratio determination in nanodiamonds by atom-probe tomography. *Ultramicroscopy* 159:248–254.

Lewis J. B., Isheim D., Floss C., Daulton T. L., and Seidman D. N. 2016. Analysis of Allende nanodiamond residue by correlated transmission electron microscopy and atom-probe tomography. *Lunar and Planetary Science Conference XLVII*. Abstract #2248.

Lewis J. B., Floss C., and Gyngard F. 2017. Origin of nanodiamonds from Allende constrained by statistical analysis of C isotopes from small clusters of acid residue by NanoSIMS. *Geochimica et Cosmochimica Acta* (Submitted).

Marks N. A., Lattemann M., and McKenzie D. R. 2012. Nonequilibrium route to nanodiamond with astrophysical implications. *Physical Review Letters* 108:075503.

Meibom A., Petaev M. L., and Krot A. N. 1999. Primitive FeNi metal grains in CH carbonaceous chondrites formed by condensation from a gas of solar composition. *Journal of Geophysical Research* 104:22053.

Meyer B. S. 1997. Supernova nucleosynthesis. *AIP Conference Proceedings* 402:155–178.

Nuth J. A., and Allen J. E. 1992. Supernovae as sources of interstellar diamonds. *Astrophysics and Space Science* 196:117–123.

Ogliore R. C., Huss G. R., and Nagashima K. 2011. Ratio estimation in SIMS analysis. *Nuclear Instruments and Methods in Physics Research Section B: Beam Interactions with Materials and Atoms* 269:1910–1918.

Pirali O., Vervloet M., Dahl J. D., Carlson R. M. K., Tielens A. G. G. M., and Oomens J. 2007. Infrared spectroscopy of diamondoid molecules: New insights into the presence of nanodiamonds in the interstellar medium. *The Astrophysical Journal* 661:919–925.

Pravdivtseva O., Shatoff E. A., Meshik A. P., and Stroud R. M. 2016. Separation of Allende nanodiamonds by electrophoresis. *Lunar and Planetary Science Conference XLVII*. Abstract #2996.

Russell S. S., Arden J. W., and Pillinger C. T. 1991. Evidence for multiple sources of diamond from primitive chondrites. *Science* 254:1188–1191.

Russell S. S., Arden J. W., and Pillinger C. T. 1996. A carbon and nitrogen isotope study of diamond from primitive chondrites. *Meteoritics & Planetary Science* 31:343–355.

Shatoff E. A., Meshik A. P., and Pravdivtseva O. V. 2015. Electrophoresis of Allende nanodiamonds in colloidal solution. *Lunar and Planetary Science Conference XLVI*. Abstract #2688.

Stephan T., Heck P. R., Isheim D., and Lewis J. B. 2015. Correction of dead time effects in laser-induced desorption time-of-flight mass spectrometry: Applications in atom probe tomography. *International Journal of Mass Spectrometry* 379:46–51.

Stroud R. M., Chisholm M. F., Heck P. R., Alexander C. M. O., and Nittler L. R. 2011. Supernova shock-wave-induced co-formation of glassy carbon and nanodiamond. *The Astrophysical Journal Letters* 738:L27 (5pp).

Stroud R. M., Pravdivtseva O. V., Meshik A. P., and Shatoff E. A. 2016. Aberration-corrected STEM analysis of electrophoresis separates of Allende nanodiamond. *Lunar and Planetary Science Conference XLVII*. Abstract #2311.

Swart P. K., Grady M. M., Pillinger C. T., Lewis R. S., and Anders E. 1983. Interstellar carbon in meteorites. *Science* 220:406–410.

Van Kerckhoven C., A. G. G. M Tielens, and Waelkens C. 2002. Nanodiamonds around HD 97048 and Elias 1. *Astronomy & Astrophysics* 384:568–584.

Verchovsky A. B., Fisenko A. V., Semjonova L. F., Wright I. P., Lee M. R., and Pillinger C. T. 1998. C, N, and noble gas isotopes in grain size separates of presolar diamonds from Efremovka. *Science* 281:1165–1168.

Woosley S. E., and Weaver T. A. 1995. The evolution and explosion of massive stars. II. Explosive hydrodynamics and nucleosynthesis. *The Astrophysical Journal Supplement Series* 101:181–285.

Zhou Z., Bouwman W. G., Schut H., and Pappas C. 2014. Interpretation of X-ray diffraction patterns of (nuclear) graphite. *Carbon* 69:17–24.

Zinner E. 2014. Presolar Grains. In *Treatise on Geochemistry*, 2nd ed. Elsevier. pp. 181–213.

Appendix 1

Python Script to Process Atom-Probe Data, Including Iterative Proportional Fitting of All C Peaks

```
#%%

# -*- coding: utf-8 -*-
"""
Created on Mon Aug 19 14:41:13 2013

@author: jblewis
"""
"""
From working directory reads in all .EPOS, .RRNG or .RNG files and ignores all others.
.EPOS files are generated by the Cameca IVAS software.
Searches for matches between .EPOS file names and .RRNG file names and uses ranges with that
EPOS file.
Writes to list 'a' the multiple data for the n(n-1)/2 multiple hit pairs in each multiple
event.
-Prepares and saves a .csv and .txt summary of the dataset with multiple hit data.
-Saves 2d histograms of various mass-to-charge regions of interest: uncomment figures you
want.
Memory errors are common. This will vary by dataset but takes up more than 1Gb RAM

New to version '*ExhaustiveC':
-reads in .rng or .rrng file and parses each range as one to deadtime correct and report on.
Deadtime correction deviations are relative
to the other ions in the matrix, so only include essential, independent ions (e.g., all C
ions) in the range file.
-deadtime correction can accept any square (n*n) matrix and deadtime correct.

NOTE on deadtime correction: Uses Iterative proportional fitting as in Saxey 2011. The
algorithm is prevented from subtracting counts from the original value detected,
even at the expense of proper correlation.

NOTE on plots: 2d histogram bins where mass1 > mass2 should be empty to first order because
mass ~ time-of-flight ~ arrival order...
...heavier mass/charge should always arrive later. you could just reflect the data across the
axis, p_{ij}= p_{ji} (e.g. Saxey), but why plot data that isn't there?
Still, if we plot every p_{ij} except i = j we're including many ions multiple times -- ion
count information is not contained in the historgram, only PAIR count information.
NOTE2 on plots: 1d histogram plots all the ions from the matrix a, which repeats ions, so it
is not an accurate mass spectrum -- just for quick comparison

NOTE: written for python 3.3 compatibility. input() replaces raw_input(). pre-python3
interprets input() differently
Also, 3.3 requires print() rather than print

Based on v18 of IO-for-EPOS-files

"""
import math
import struct
import numpy as np
import matplotlib.pyplot as plt
from matplotlib.colors import LogNorm
```

```
import gc
import os
from matplotlib.ticker import LogFormatter
from matplotlib.ticker import LogLocator
import sys
import pandas as pd
import datetime

#Choose parameters for 2dhistogram (consider making this interactive where these are
defaults).
bpd = 20 #TODO was 20bins per daulton. Must be an integer. bins 5000 or higher in
np.histogram2d may result in a MemoryError
dpb = 0.05 #daultons per bin. Using different variables to avoid division problems
if bpd != 1/dpb:
    sys.exit("bpd != 1/dpb! Please revise parameters to make sense")
dpi=480 #default 80 in matplotlibrc
sizex = 16
sizey = 12 # (8,6) default in matplotlibrc
xlabel = 'Ion 2 mass-to-charge-state ratio\n(amu)'
ylabel = 'Ion 1 mass-to-charge-state ratio\n(amu)'

#The leftmost and rightmost edges of the bins along each dimension (if not specified
explicitly in the bins parameters): [[xmin, xmax], [ymin, ymax]].
#...All values outside of this range will be considered outliers and not tallied in the
histogram.
#extent using edges is different from extent defined here.
#imshow(aspect = 'equal') plots bins, not masses
#imshow(asepect = 'auto') plots bins, not masses
rangeov = [[0,250],[0,250]]
rangec12 = [[5,14],[5,14]]
rangept200 = [[185,200],[185,200]]
rangelowmass = [[0,50],[0,50]]
rangech = [[0,14],[5,14]]
rangeh = [[0,2],[5,14]]
#range = [[,],[,]]#range = [[xmin, xmax],[ymin,ymax]]

rangeSi =  [[11, 27], [11, 27]]

binsov = (rangeov[0][1] - rangeov[0][0])*bpd
binsc12 = (rangec12[0][1] - rangec12[0][0])*bpd
binspt200 = (rangept200[0][1] - rangept200[0][0])*bpd
binslowmass = (rangelowmass[0][1] - rangelowmass[0][0])*bpd
binsch = [np.arange(rangech[0][0] + dpb, rangech[0][1] + dpb/2,dpb/2),
np.arange(rangech[1][0]+dpb,rangech[1][1] + dpb/2,dpb/2)]
binsh = [np.arange(rangeh[0][0] + dpb, rangeh[0][1] + dpb/2,dpb/2),
np.arange(rangeh[1][0]+dpb,rangeh[1][1] + dpb/2,dpb/2)]
#bins = [np.arange(range[0][0] + dpb, range[0][1] + dpb,dpb),
np.arange(range[1][0]+dpb,range[1][1] + dpb,dpb)]

binsSi = (rangeSi[0][1] - rangeSi[0][0])*2*bpd

sizeov = (sizex, sizey)
sizeov1d = (16,12)
sizec12 = (sizex/2, sizey/2)
sizept200 = (sizex/2, sizey/2)
sizelowmass = (sizex, sizey)
sizeh = (sizex, sizey/3)
sizech = (sizex, sizey)

sizeSi = (sizex, sizey)
```

```
#%%
def ion_ops( m, ran, ion ): #Run these operations identically for every ion in the EPOS data
set
    for r in range(len(ran)):
        if(m>ran[r][0] and m<ran[r][1]):
            ion[r] += 1
    return ion;

#%%
def deadtime_correction( c0 ):

    dslist = []#list to hold deviation sums. Length of this list will be the number of
iterations.

    #cp0 will hold original matrix values for comparison.
    cp = c0.copy()
    ctest = c0.copy()

    ds = 1.0 #sum d's
    ds0=1000.0 #previous iteration d's sum
    ds_test = 1.0#decrease in d's sum this iteration compared to last, set loop end condition
to some small value.

    dim = c0.shape[0] #NOTE previously d, but that is 1) what is used for matrix of deviations
2) is a debugger command
    #we know we'll have a square matrix. Dimension is unknown prior to method call.
    #symmetrize
    for i in range(dim):
        for j in range(dim):
            if i != j:
                cp[i,j] = (c0[i,j] + c0 [j,i])/2
            #if i = j do nothing

    #expectation values. Initializing matrices for 4*4 case. Other isotope systems will
require different matrix sizes.
    e = np.ones([dim,dim])

    #Carbon Pairs Sum. Sum ion pairs in matrix
    cps = cp.sum()
    #Carbon Pairs Column Sums. Equal to sums of rows.
    cpcs = np.zeros(dim)#NOTE np.zeros([1,d]) = array([[0., 0., 0., 0.,]]) which will cause
problems because of nesting. This is not an issue with np.array([entry a, entry b, entry c])
obviously
    for i in range(dim):
        cpcs[i] = cp[i].sum()

    #probabilities for each column.
    pr = cpcs/cps
    #update e's here
    for i in range(dim):
        for j in range(dim):
            e[i,j] = pr[i]*pr[j]*cps

    dinit = (cp-e)/np.sqrt(e)
    dsinit = abs(dinit).sum()
    dslist.append(0)#fill entry 0 -- will not plot on a log axis. 0 so it won't mess up
average, sum of list
    dslist.append(dsinit)#fill entry 1 -- the first that will plot on a log axis. Notice the
extra entry will change n, dsinit if not properly handled
```

```
    while (ds_test > 0.0000000000000000001):

        #print("Iteration: ");

        for k in range(dim):
            #Only needs to be run on one dimension because the matrix is diagonally symmetric.
            e[k,k] = e[k,k]*(cpcs[k])/(e[k].sum())

        for k in range(dim):
            #Prevent diagonal counts from dropping below counts (off-diagonal counts are
fixed).
            if e[k,k] > c0[k,k]:
                cp[k,k] = e[k,k]
                ctest[k,k] = e[k,k]

        cps = cp.sum()
        #cp column sums
        cpcs = np.zeros(dim)
        for k in range(dim):
            cpcs[k] = cp[k].sum()

        #probabilities for each column
        pr = cpcs/cps

        #calculate eijs for next round
        for i in range(e.shape[0]):
            for j in range(e.shape[0]):
                e[i,j] = pr[i]*pr[j]*cps

        d = (cp-e)/np.sqrt(e)
        ds = abs(d).sum()

        ds_test = ds0 - ds
        dslist.append(ds)
        ds0 = ds

    cres = c0.copy()#get back original off-diagonal values
    for i in range(dim):
        cres[i,i] = cp[i,i]

    return cres, dslist, d

#%%
#make date string to attach to output filenames and prevent over-writing
now = datetime.datetime.now()
date = now.strftime("%y-%m-%d")

results_path = '..' + os.sep + 'Results' + os.sep + date + os.sep
"""
set path string that will be appended to the front of filenames
#(if empty '' you will create files in the working directory.
Trying to run the script again in the same working directory
will cause errors since the data structure of the new files is not IVAS csv output
"""
dirname = os.path.dirname(results_path)
if not os.path.exists(dirname):
    os.makedirs(results_path)

table = pd.DataFrame()
```

```
cwd = os.getcwd()
files = os.listdir(cwd) #get list of files in working directory.
epos = []
rrng = []
filepairs = []

for file in files:
    if file.lower()[-5:] == '.epos':
        epos.append(file)
    elif file.lower()[-5:] == '.rrng':
        rrng.append(file)
    else:
        print(file + ' is not an .epos or .rrng file. Skipping')
        #files.remove(file)

for i in range(len(epos)):
    for j in range(len(rrng)):
        if rrng[j].lower().startswith(epos[i].lower()[:-5]): #see if there's a range file for
this EPOS file
            filepairs.append([epos[i],rrng[j]])
    else:
        print(epos[i] + ' does not have a .rrng file of the same name included in the working
directory. Skipping')

#%%
for i in range(len(filepairs)):

    #
    #Read in Ranges
    #

    rrng = filepairs[i][1]
    inrrng = open(rrng, 'r')
    line =  inrrng.readline()
    while(line != '[Ranges]\n'):
        line = inrrng.readline()
    n = int(inrrng.readline().rpartition('=')[2])#the line after [Ranges] must be Number=###,
so we take everything after the '='. rpartition splits into stuff before and after '=', with
indices [0] = before [1] = during ('=') and after [2]
    ranges = []

    for j in range(n):
        line = inrrng.readline()
        stuff = (line.partition('=')[2]).split(' ' )#list of strings of everything after the
range number, separated by spaces
        ranges.append([float(stuff[0]), float(stuff[1])])#first two stuff are range start and
stop. Molecule name is in there but not so useful -- just print out the actual ranges

    #
    #Initialize variables
    #

    maxmass = 0
    cntmax = 0
    ion_count = 0
    ions = np.zeros(n)
    mult = 0
    c = 0
    cpairs = np.zeros((n,n))
```

```
    c13 = 0
    cmult = 0
    c12Hmult = 0
    c6Hmult = 0
    rangedmultions = 0

    si = 0
    si14 = 0
    si28 = 0
    simult = 0
    simultions = 0

    # Initialize nested 2d lists with [[mass1], [mass2]] format. Dynamically expanded using
list.append().
    a = [[],[]]

    epos = filepairs[i][0]
    fname = rrng[:-5]#use range file to distinguish, not epos, since you can run multiple rrng
files at a time on one epos.

    fnameov = fname+ '_' + str(binsov) + 'bins'
    fnamec12 =  fname + '_C_singly_charged_' + str(binsc12) + 'bins'
    fnamept200 = fname + '_Pt_singly_charged_' + str(binspt200) + 'bins'
    fnamelowmass = fname + '_lowmass' + '_' + str(binslowmass) + 'bins'
    #fnamech = fname + '_C&H_' + str((rangech[0][1] - rangech[0][0])*bpd*2)+ 'by' +
str((rangech[1][1] - rangech[1][0])*bpd*2) + 'bins'
    fnameh = fname + '_Hydrogen_' + str((rangeh[0][1] - rangeh[0][0])*bpd*2)+ 'by' +
str((rangeh[1][1] - rangeh[1][0])*bpd*2) + 'bins'
    #fname = fname + '_NAME_' + str((range[0][1] - range[0][0])*bpd)+ 'by' + str((range[1][0]
- range[1][1])*bpd) + 'bins'
    fnamedev = fname + '_' + 'Deviation_Reduction'

    fnameSi = fname + '_SiC_' + str(binsSi) + 'bins'

    print("The EPOS file you chose is " + fname)

    #
    #Reading EPOS file
    #

    # open .EPOS file as a binary file
    infile = open(epos,"rb")

    path = results_path + os.sep + fnameov
    if not os.path.exists(path): #If the code has been run before for this fname, avoid an
error
        os.mkdir(path)

    outfilepath =  path + os.sep + fname + "_multiples.txt"
    outfile = open(outfilepath, "w")
    outfile.write('Created by ' + os.path.basename(__file__) + '\n')
    outfile.write('The EPOS file you chose is: ' + '\n' + fname + '\n\n')

    # read the first 44 bytes (x, y, z, mass-to-charge ratio,
    # time-of-flight, standing voltage, pulsed voltage,
    # detector-impact-x, detector-impact-y, pulses-since-last-ion,
    # hit multiplicity)
    atom = infile.read(44)
```

```
    while len(atom) == 44:
        # '>f' signifies that the format of the data is
        # big-endian float. Each float is 4 bytes long.
        # "The first 9 values are in floating-point format,
        # whereas the last two values are in unsigned-integer
        # format" Atom probe Microscopy. Gault et al 2012)
        (x,y,z,mass, tof, vdc, vp, xdet, ydet, deltap, nm) =
struct.unpack('>fffffffffII',atom)
        cnt = nm
        ion_count = ion_count + cnt
        """
        if count is one, this takes care of adding one for this ion. If cnt > 1,
        we're going to skip the next cnt ions including this one, so the operation is correct
for both.
        """
        ions = ion_ops(mass, ranges, ions)

        if cnt > 1: #this is the first in a set of multiple hits nm long
            mult = mult + cnt
            if cnt > cntmax:#check for a new highest # counts in a single pulse
                cntmax = cnt
            if mass > maxmass:#check for a new highest mass in a multiple
                maxmass = mass
            masses = [] #list of masses in this multiple
            masses.append(mass)
            for i in range(0, cnt-1):
                atom = infile.read(44)
                (x,y,z,mass, tof, vdc, vp, xdet, ydet, deltap, nm) =
struct.unpack('>fffffffffII',atom)

                if mass > maxmass: #check for maxmass. We've already checked for cntmax for
this entire multiple event.
                    maxmass = mass
                masses.append(mass)
                ions = ion_ops(mass, ranges, ions)

            addcmult=False
            for m in masses:
                for bound in ranges:
                    if (m > bound[0] and m < bound[1]):#huge savings in code by looping
through a list of ranges, rather than writing them out individually
                        rangedmultions += 1
                        addcmult = True

            if addcmult:
                cmult+=1

            #n(n-1)/2 unique p_{ij} combinations of n multiples added to data set
            for i in range(0, cnt-1):
                for j in range(i+1, cnt-1):
                    a[0].append(masses[i])
                    a[1].append(masses[j])
                    for r in range(len(ranges)):
                        for s in range(len(ranges)):
                            if ((masses[i] > ranges[r][0] and masses[i] < ranges[r][1]) and
(masses[j] > ranges[s][0] and masses[j] < ranges[s][1])):
                                cpairs[r,s] += 1

        atom = infile.read(44)
```

```
    infile.close()

    ccorrected, dslist, d_final = deadtime_correction(cpairs)

    diff = ccorrected - cpairs
    sumdiff = diff.sum()

    dsinit = dslist[1]#initial deviation absolute sum (1 not 0 because first entry arbitrarily
filled with a 0)
    it = len(dslist) - 1#number of iterations (-1 because first entry was arbitrarily filled
with a 0, see NOTE above)
    dsfinal = dslist[it]#final deviation absolute sum (len - 1 because of index starting at 0)

    ion_count = ion_count + sumdiff
    mult = mult + sumdiff
    c = c + sumdiff
    rangedmultions = rangedmultions + sumdiff

    index = []
    for i in range(len(ranges)):
        index.append(str(ranges[i]))

    d_df = pd.DataFrame(data = d_final, index = index, columns = index)
    d_df.sort_index(axis=0, inplace=True)
    d_df.sort_index(axis=1, inplace=True)
    d_df.to_csv(path + os.sep + fname + '_devations_final.csv')

    p_df = pd.DataFrame(data = ccorrected, index = index, columns = index)
    p_df.sort_index(axis=0, inplace=True)
    p_df.sort_index(axis=1, inplace=True)
    p_df.to_csv(path + os.sep + fname + '_corrected_counts.csv')

    output = {}

    outfile.write('C counts correction' + str(sumdiff) + '\n\n')
    output['C counts correction'] = sumdiff

    print('maximum counts detected in one multiple event:')
    outfile.write('maximum counts detected in one multiple event: ' + '\n')
    print(cntmax)
    outfile.write(str(cntmax) + '\n\n')
    output['cntmax'] = cntmax

    print('maximum mass detected in a multiple event:')
    outfile.write('maximum mass detected in a multiple event: ' + '\n')
    print(maxmass)
    outfile.write(str(maxmass) + '\n\n')
    output['Max Mass'] = maxmass

    print('total ions in dataset:')
    outfile.write('total ions in dataset: ' + '\n')
    print( ions)
    outfile.write(str(ion_count) + '\n\n')
    output['Total Ions'] = ion_count

    print( 'ions that were part of a multiple event:')
    outfile.write('ions that were part of a multiple event: ' + '\n')
    print( mult)
    outfile.write(str(mult) + '\n\n')
    output['Mult. Ions'] = mult
```

```
    print( '% total ions detected that were part of a multiple event detection:')
    outfile.write('% total ions detected that were part of a multiple event detection: ' +
'\n')
    print( float(mult)/float(ion_count)*100)
    outfile.write(str(float(mult)/float(ion_count)*100) + '\n\n')
    output['Mult. %'] = float(mult)/float(ion_count)*100

    for i in range(0,n) :
        for j in range(i,n) :
            print(ccorrected[i,j])
            outfile.write('(' + str(ranges[i][0]) + '-' + str(ranges[i][1]) + ',' +
str(ranges[j][0]) + '-' + str(ranges[j][1]) + ')' + '(' + str(i) + ',' + str(j) + ') corrected
pairs ' + str(ccorrected[i,j]) + '\n\n')
            output['(' + str(ranges[i][0]) + '-' + str(ranges[i][1]) + ',' + str(ranges[j][0])
+ '-' + str(ranges[j][1]) + ')' + ' deadtime_corrected pairs '] = ccorrected[i,j]

            print(diff[i,j])
            outfile.write('(' + str(ranges[i][0]) + '-' + str(ranges[i][1]) + ',' +
str(ranges[j][0]) + '-' + str(ranges[j][1]) + ') correction' + str(diff[i,j]) + '\n\n')
            output['(' + str(ranges[i][0]) + '-' + str(ranges[i][1]) + ',' + str(ranges[j][0])
+ '-' + str(ranges[j][1]) + ') correction'] = diff[i,j]

    #print(str(diff[0,0] + diff[2,2]))
    #outfile.write('12C counts correction' + str(diff[0,0] + diff[2,2]) + '\n\n')
    #output['12C counts correction'] = diff[0,0] + diff[2,2]

    #print(str(diff[1,1] + diff[3,3]))
    #outfile.write('13C counts correction' + str(diff[1,1] + diff[3,3]) + '\n\n')
    #output['13C counts correction'] = diff[1,1] + diff[3,3]


    for r in range(len(ranges)):
        print( 'Number of ions that are between ' + str(ranges[r][0]) + ' and ' +
str(ranges[r][1]) + ':')
        outfile.write('Number of ions that are between ' + str(ranges[r][0]) + ' and ' +
str(ranges[r][1]) + ':' + '\n')
        print(ions[r])
        outfile.write(str(ions[r]) + '\n\n')
        output['Ion Count ' + str(ranges[r][0]) + '-' + str(ranges[r][1]) + ' amu'] =
int(ions[r])

    print( '% total Si ions detected that were part of a multiple event detection:')
    outfile.write('% total Si ions detected that were part of a multiple event detection: ' +
'\n')
    if(si14 + si28 > 0 ):
        print( float(simultions)/float(si14 + si28)*100)
        outfile.write(str(float(simultions)/float(si14+si28)*100) + '\n\n')
        output['Si Mult. %'] = float(simultions)/float(si14+si28)*100
    else:
        print('No silicon')
        outfile.write('no silicon' + '\n\n')
        output['Si Mult. %'] = 'NA'
        #    print( 'Number of ions that are in a multiple event and are between ' +
str(c6Includes[0]) + ' and ' + str(c6pt5Includes[1]) + ' or between ' + str(c12Includes[0]) +
' and ' + str(c13Includes[1]) + ' Da (better to use IVAS values from careful IVAS ranging):')
        #    outfile.write('Number of ions that are in a multiple event and are between ' +
str(c6Includes[0]) + ' and ' + str(c6pt5Includes[1]) + ' or between ' + str(c12Includes[0]) +
' and ' + str(c13Includes[1]) + ' Da (better to use IVAS values from careful IVAS ranging):' +
'\n')
```

```
        #    print( cmultions)
        #    outfile.write(str(cmultions) + '\n\n')
        #    output['C-mult-ions-DC'] = cmultions

    print( '% total C ions detected that were part of a multiple event detection:')
    outfile.write('% total C ions detected that were part of a multiple event detection: ' +
'\n')
    if c > sumdiff:
        print( float(rangedmultions)/float(c)*100)
        outfile.write(str(float(rangedmultions)/float(c)*100) + '\n\n')
        output['C Mult. % DC'] = float(rangedmultions)/float(c)*100
    else:
        print('No C')
        outfile.write('No C' + '\n\n')
        output['C Mult. % DC'] = 'NA'

    #    print( 'pairs of ions in a multiple (e.g. a triple event counts as three pairs) that
are between ' + str(c6Includes[0]) + ' and ' + str(c6pt5Includes[1]) + ' or between ' +
str(c12Includes[0]) + ' and ' + str(c13Includes[1]) + ' Da:')
    #    outfile.write('pairs of ions in a multiple (e.g. a triple event counts as three
pairs) that are between ' + str(c6Includes[0]) + ' and ' + str(c6pt5Includes[1]) + ' or
between ' + str(c12Includes[0]) + ' and ' + str(c13Includes[1]) + ' Da:' + '\n')
    #    print(cmult)
    #    outfile.write(str(cmult) + '\n\n')
    #    output['C multiple events'] = cmult
    #

    #    print( 'Number of H pairs between ' + str(c12Includes[0]) + ' and ' +
str(c13Includes[1]) + ' Da in a multiple event:')
    #    outfile.write('Number of H pairs between ' + str(c12Includes[0]) + ' and ' +
str(c13Includes[1]) + ' Da in a multiple event:' + '\n')
    #    print( c12Hmult)
    #    outfile.write(str(c12Hmult) + '\n\n')
    #    output['(12C+, H+) pairs'] = c12Hmult

    print( 'Ratio (12C+, H+) events to total C events, deadtime corrected:')
    outfile.write('Ratio (12C+, H+) events to total C events, deadtime corrected:' + '\n')
    if c > 0:
        print( float(c12Hmult)/float(c))
        outfile.write(str(float(c12Hmult)/float(c)) + '\n\n')
        output['(12C+, H+)/C_tot_DC'] = float(c12Hmult)/float(c)
    else:
        print( 'no c' )
        outfile.write('no c' + '\n\n')
        output['(12C+, H+)/C_tot_DC'] = 'NA'


    print( 'Ratio (12C+, H+) events to 13C+ events')
    outfile.write('Ratio (12C+, H+) events to 13C+ events' + '\n')
    if c13 > 0:
        print( float(c12Hmult)/float(c13))
        outfile.write(str(float(c12Hmult)/float(c13)) + '\n\n')
        output['(12C+, H+)/(13C)+'] = float(c12Hmult)/float(c13)
    else:
        print('no c13')
        outfile.write('no c13' + '\n\n')
        output['(12C+, H+)/(13C)+'] = 'NA'
        #    print('Divergent?')
        #    outfile.write('Divergent?' + '\n')
        #    print(divergent)
```

```
        #    outfile.write(str(divergent) + '\n\n')
        #    output['divergent'] = str(divergent)

    print('Iterations to Deadtime correct')
    outfile.write('Iterations to Deadtime correct' + '\n')
    print(it)
    outfile.write(str(it) + '\n\n')
    output['PF Iterations'] = str(it)

    print('Initial correlation sum')
    outfile.write('Initial correlation sum' + '\n')
    print(dsinit)
    outfile.write(str(dsinit) + '\n\n')
    output['d sum init'] = str(dsinit)

    print('Final Correlation sum')
    outfile.write('Final Correlation sum' + '\n')
    print(dsfinal)
    outfile.write(str(dsfinal) + '\n\n')
    output['d sum final'] = str(dsfinal)

    out = pd.Series(output)
    out.name = fname
    out.to_csv(path + os.sep + fnameov + "_multiples.csv")

    column = pd.Series(out.values.flatten(), index=out.index)
    column.name = fname
    table = table.join(column, how='outer')

    l_f = LogFormatter(labelOnlyBase=False)
    l_l = LogLocator(subs=np.arange(1,9,1))
    l_l2 = LogLocator(subs=np.arange(1,9,2))

    """
    #Here are various figures. Uncomment the ones you want. They take the majority of the run-
time.

    """
    #FIGURE 1: OVERVIEW
    plt.figure(num=1, figsize=sizeov)

    H, xedges, yedges = np.histogram2d(a[0], a[1], bins=binsov, range=rangeov)
    extentov = [xedges[0], xedges[-1], yedges[0], yedges[-1]]

    plt.imshow(H, origin='lower', extent=extentov, interpolation='nearest', norm=LogNorm())
#interpolation! Remember the image isn't pixel-for-pixel your data. Do any analysis using a or
H, not the image.
    plt.xticks(np.arange(xedges[0], xedges[-1], 10))
    plt.yticks(np.arange(yedges[0], yedges[-1], 10))
    plt.tick_params(axis='both',which='both', direction='out', labelsize='small')
    plt.xlabel(xlabel, fontsize ='small', multialignment='center')
    plt.ylabel(ylabel, fontsize ='small', multialignment='center')
    plt.colorbar(ticks = l_l, format=l_f)
    plt.title('Overview of ' + fname + ' ' + str(binsov) + 'bins', y=1.01, fontsize = 'small')
    plt.grid(alpha=0.25, linewidth=0.5)

    plt.savefig(path + os.sep + fnameov, dpi=dpi)

    del H
    gc.collect()
```

```
    plt.close()#free up memory
    """
    #FIGURE 5: 1D HISTOGRAM FOR COMPARISON
    plt.hist(a, bins = binsov, range=(rangeov[0][0],rangeov[0][1]), log=True)
    plt.xticks(np.arange(xedges[0], xedges[-1], 20))
    plt.tick_params(axis = 'both', which ='both', direction='out', width=1, length=6,
labelsize='small')
    plt.ylim(ymin = 1)
    plt.ylabel('number', fontsize='small')
    plt.xlabel('mass-to-charge-state ratio\n(Da)', fontsize = 'small',
multialignment='center')
    plt.title(fnameov + '_1D', y=1.03, fontsize = 'small')
    plt.grid(alpha=0.25, linewidth=0.5, axis='y')

    plt.savefig(path + os.sep + fnameov + '_1D', dpi=dpi)

    gc.collect()
    plt.close()#free up memory

    """
    # FIGURE 2: ZOOM IN ON SINGLY-CHARGED C
    plt.figure(num=2, figsize=sizec12)

    Hc12, xedgesc12, yedgesc12 = np.histogram2d(a[0], a[1], bins = binsc12, range=rangec12)
    extentc12 = [xedgesc12[0], xedgesc12[-1], yedgesc12[0], yedgesc12[-1]]

    plt.imshow(Hc12, origin='lower', extent=extentc12, interpolation = 'nearest',
norm=LogNorm())
    plt.colorbar(ticks = l_l, format=l_f)
    #plt.xlabel(xlabel, fontsize ='small', multialignment='center')
    #plt.ylabel(ylabel, fontsize ='small', multialignment='center')
    plt.xlabel(xlabel, fontsize ='medium', multialignment='center')
    plt.ylabel(ylabel, fontsize ='medium', multialignment='center')
    plt.tick_params(axis = 'both', which ='both', direction='in', width=1, length=8,
labelsize='small')
    plt.xticks(np.arange(xedgesc12[0], xedgesc12[-1], 1))
    plt.yticks(np.arange(yedgesc12[0], yedgesc12[-1], 1))
    #plt.title(', y=1, fontsize = 'small')
    #plt.title(fnamec12, y=1, fontsize = 'small')
    plt.grid(alpha=0.25, linewidth=0.5)

    plt.savefig(path + os.sep + fnamec12, dpi=dpi)

    plt.close() #free up memory
    del Hc12
    gc.collect()
    """
    # FIGURE 9: ZOOM IN ON Si++ through Si+
    plt.figure(num=9, figsize=sizeSi)

    HSi, xedgesSi, yedgesSi = np.histogram2d(a[0], a[1], bins = binsSi, range=rangeSi)
    extentSi = [xedgesSi[0], xedgesSi[-1], yedgesSi[0], yedgesSi[-1]]

    plt.imshow(HSi, origin='lower', extent=extentSi, interpolation = 'nearest',
norm=LogNorm())
    plt.colorbar(ticks = l_l, format=l_f)
    plt.xlabel(xlabel, fontsize ='medium', multialignment='center')
    plt.ylabel(ylabel, fontsize ='medium', multialignment='center')
    plt.tick_params(axis = 'both', which ='both', direction='in', width=1, length=8,
labelsize='small')
```

```
    plt.xticks(np.arange(xedgesSi[0], xedgesSi[-1], 1))
    plt.yticks(np.arange(yedgesSi[0], yedgesSi[-1], 1))
    plt.title(fnameSi, y=1, fontsize = 'small')
    plt.grid(alpha=0.25, linewidth=0.5)

    plt.savefig(path + os.sep + fnameSi, dpi=dpi)

    plt.close() #free up memory
    del HSi
    gc.collect()

    #FIGURE 7: ZOOM IN ON C and H
    plt.figure(num=7, figsize=sizech)

    Hch, xedgesch, yedgesch = np.histogram2d(a[0], a[1], bins = binsch, range = rangech)
    extentch = [yedgesch[0], yedgesch[-1], xedgesch[0], xedgesch[-1]]

    plt.imshow(Hch, origin='lower', extent=extentch, interpolation = 'nearest',
norm=LogNorm())
    cb = plt.colorbar(ticks = l_l2, format=l_f)
    plt.xlabel(xlabel, fontsize ='medium', multialignment='center')
    plt.ylabel(ylabel, fontsize ='medium', multialignment='center')
    plt.tick_params(axis='both',which='both', direction='in', width =1, length=8,
labelsize='medium')
    plt.xticks(np.arange(yedgesch[0], yedgesch[-1], 1))
    plt.yticks(np.arange(xedgesch[0], xedgesch[-1], 1))
    plt.title(fnamech, y=1, fontsize='medium')
    plt.grid(alpha=0.25, linewidth=0.5)

    plt.savefig(path + os.sep + fnamech, dpi=dpi)

    plt.close() #free up memory
    del Hch
    gc.collect()

    #FIGURE 8: ZOOM IN ON HYDROGEN
    plt.figure(num=8, figsize=sizeh)

    Hh, xedgesh, yedgesh = np.histogram2d(a[0], a[1], bins = binsh, range = rangeh)
    extenth = [yedgesh[0], yedgesh[-1], xedgesh[0], xedgesh[-1]]

    plt.imshow(Hh, origin='lower', extent=extenth, interpolation = 'nearest', norm=LogNorm())
    plt.colorbar(ticks = l_l2, format=l_f, shrink = 1)
    plt.xlabel(xlabel, fontsize ='small', multialignment='center')
    plt.ylabel(ylabel, fontsize ='small', multialignment='center')
    plt.tick_params(axis='both',which='both', direction='in', width=1, length=6,
labelsize='medium')
    plt.xticks(np.arange(yedgesh[0]-dpb, yedgesh[-1]-dpb, 1))
    plt.yticks(np.arange(xedgesh[0]-dpb, xedgesh[-1]-dpb, 1))
    plt.title(fnameh, y = 1.1, fontsize='small')
    plt.grid(alpha=0.25, linewidth=0.5)

    plt.savefig(path + os.sep + fnameh, dpi=dpi)

    plt.close() #free up memory
    del Hh
    gc.collect()


    #end figures removed just for sending short out to Thomas
```

```
    """
    """
    #FIGURE 8: ZOOM IN ON HYDROGEN
    ######################################################
    ### Scaling and labels for 2014 LPSC Abstract ###
    ######################################################

    plt.figure(num=8, figsize=sizeh)

    Hh, xedgesh, yedgesh = np.histogram2d(a[0], a[1], bins = binsh, range = rangeh)
    print( Hh.shape, xedgesh.shape, yedgesh.shape)
    extenth = [yedgesh[0], yedgesh[-1], xedgesh[0], xedgesh[-1]]

    plt.imshow(Hh, origin='lower', extent=extenth, interpolation = 'nearest', norm=LogNorm())
    plt.colorbar(ticks = l_l2, format=l_f, shrink = 1)#was shrink = 0.75
    plt.xlabel('Ion 2 mass-to-charge-state ratio\n(Da)', fontsize ='large',
multialignment='center')
    plt.ylabel('Ion 1 mass-to-charge-state ratio\n(Da)', fontsize ='large',
multialignment='center')
    plt.tick_params(axis='both',which='both', direction='in', width=1, length=8,
labelsize='large')#was labelsize='small'
    plt.xticks(np.arange(yedgesh[0]-dpb, yedgesh[-1]-dpb, 1))# was
plt.xticks(np.arange(yedgesh[0], yedgesh[-1], 1))
    plt.yticks(np.arange(xedgesh[0]-dpb, xedgesh[-1]-dpb, 1))
    plt.title(fnamec12, y=1, fontsize = 'small')#plt.title('Allende Microtip R06 18430v01,
50X225 bins', y = 1.1)plt.title(fnameh, y = 1.1)
    plt.grid(alpha=0.25, linewidth=0.5)

    plt.savefig(path + os.sep + fnameh, dpi=dpi)

    plt.close() #free up memory
    del Hh
    gc.collect()
    """

    """
    #FIGURE 6: 1D C12 HISTOGRAM FOR COMPARISON
    plt.hist(a, bins = binsc12, range=(rangec12[0][0],rangec12[0][1]), log=True)
    plt.xticks(np.arange(xedgesc12[0], xedgesc12[-1], 1))
    plt.tick_params(axis='both',which='both', direction='out', width=1, length=6,
labelsize='small')
    plt.ylim(ymin = 1)
    plt.ylabel('number', fontsize='small')
    plt.xlabel('mass-to-charge-state ratio\n(Da)', fontsize = 'small',
multialignment='center')
    plt.title(fnamec12 + '1D', y = 1.03, fontsize='small')

    plt.grid(alpha=0.25, linewidth=0.5, axis='y')

    plt.savefig(path + os.sep + fnamec12 + '_1D', dpi=dpi)

    gc.collect()
    plt.close()#free up memory
    """

    """
    #FIGURE 3: ZOOM IN ON SINGLY-CHARGED PT NEAR 200
    plt.figure(num=3, figsize=sizept200)
```

```
    Hpt200, xedgespt200, yedgespt200= np.histogram2d(a[0], a[1], bins = binspt200,
range=rangept200)
    extentpt200 = [xedgespt200[0], xedgespt200[-1], yedgespt200[0], yedgespt200[-1]]

    plt.imshow(Hpt200, origin='lower', extent=extentpt200, interpolation = 'nearest',
norm=LogNorm())
    plt.colorbar()
    plt.xlabel(xlabel, fontsize ='medium', multialignment='center')
    plt.ylabel(ylabel, fontsize ='medium', multialignment='center')
    plt.xticks(np.arange(xedgespt200[0], xedgespt200[-1], 1))
    plt.yticks(np.arange(yedgespt200[0], yedgespt200[-1], 1))
    plt.tick_params(axis='both',which='both', direction='in', width=1, length=8,
labelsize='medium')
    plt.title(fnamept200, y=1.1, fontsize='medium')

    plt.savefig(path + os.sep + fnamept200, dpi=dpi)

    plt.close() #free up memory
    del Hpt200
    gc.collect()
    """

    #ZOOM IN ON LOW M/C RATIOS
    plt.figure(num=4, figsize=sizelowmass)

    Hlowmass, xedgeslowmass, yedgeslowmass= np.histogram2d(a[0], a[1], bins = binslowmass,
range=rangelowmass)
    extentlowmass = [xedgeslowmass[0], xedgeslowmass[-1], yedgeslowmass[0], yedgeslowmass[-1]]

    plt.imshow(Hlowmass, origin='lower', extent=extentlowmass, interpolation = 'nearest',
norm=LogNorm())
    plt.colorbar(ticks = l_l, format=l_f)
    plt.xlabel(xlabel, fontsize ='small', multialignment='center')
    plt.ylabel(ylabel, fontsize ='small', multialignment='center')
    plt.xticks(np.arange(xedgeslowmass[0], xedgeslowmass[-1], 5))
    plt.yticks(np.arange(yedgeslowmass[0], yedgeslowmass[-1], 5))
    plt.tick_params(axis='both',which='both', direction='in', width=1, length=6,
labelsize='small')
    plt.title(fnamelowmass, y=1, fontsize='small')
    plt.grid(alpha=0.25, linewidth=0.5)

    plt.savefig(path + os.sep + fnamelowmass, dpi=dpi)

    del Hlowmass
    plt.close() #free up memory
    gc.collect()

    #FIGURE 6: 1D LOWMASS HISTOGRAM FOR COMPARISON
    plt.hist(a, bins = binslowmass, range=(rangelowmass[0][0],rangelowmass[0][1]), log=True)
    plt.xticks(np.arange(xedgeslowmass[0], xedgeslowmass[-1], 5))
    plt.tick_params(axis='both',which='both', direction='out', width=1, length=6,
labelsize='small')
    plt.ylim(ymin = 1)
    plt.ylabel('number', fontsize='small')
    plt.xlabel('mass-to-charge-state ratio\n(Da)', fontsize = 'small',
multialignment='center')
    plt.title(fnamelowmass + '_1D', y=1.03, fontsize='small')
    plt.grid(alpha=0.25, linewidth=0.5, axis='y')

    plt.savefig(path + os.sep + fnamelowmass + '_1D', dpi=dpi)
```

```
    plt.close()#free up memory
    gc.collect()



    #FIGURE 10: DEVIATION REDUCTION DURING IPF
    if math.isnan(dslist[len(dslist)-1]):
        print("nan as last entry in dslist, not plotting")
    else:
        plt.loglog(dslist)
        plt.ylabel('ds')
        plt.xlabel('Iteration')
        plt.title(fnamedev)

        plt.savefig(path + os.sep + fnamedev)

        plt.close()#free up memory
    gc.collect()

    outfile.write('\n' + 'end of file')
    outfile.close()

outcsv = results_path + date + '.csv'

#mode = 'a' appends new column as new rows. Need to read in as a new dataframe and add table
by column
if os.path.exists(outcsv): #don't write over old csv file, append to it
    data = pd.read_csv(outcsv)
    output = pd.concat([data, table], axis = 1, join = 'outer')
    output.to_csv(outcsv, mode='w')

else:
    table.to_csv(outcsv, mode='w')

bla = input("You've reached the end!")


"""
following from Elizaveta Plotnikov at NUCAPT
#! /usr/bin/env python

# Converts input.pos to input-rotated.pos
# Rotates .pos file on xy, xz, and yz planes

import struct
import math

pos = raw_input('What POS file? ')
theta1 = input('Rotation on X-Y plane (degrees): ')
theta2 = input('Rotation on X-Z plane (degrees): ')
theta3 = input('Rotation on Y-Z plane (degrees): ')

fname = pos
print "The pos file you chose is " + fname

# open .pos file as a binary file
infile = open(fname,"rb")

# this will create a new file
```

```
outfile = open(fname[:-4] + "-rotated.pos","wb")

# read the first 16 bytes (x, y, z, mass-to-charge ratio)
atom = infile.read(16)

thetarad1 = math.radians(theta1)
thetarad2 = math.radians(theta2)
thetarad3 = math.radians(theta3)

while len(atom) == 16:
    # '>f' signifies that the format of the data is
    # big-endian float. Each float is 4 bytes long.
    (x,y,z,mass) = struct.unpack('>ffff',atom)

    # X-Y plane rotation
    if thetarad1 != 0:
        x1 = math.sqrt(x*x+y*y)*math.cos(math.atan2(y,x)+thetarad1)
        y1 = math.sqrt(x*x+y*y)*math.sin(math.atan2(y,x)+thetarad1)
    else:
        x1 = x
        y1 = y

    # X-Z plane rotation
    if thetarad2 != 0:
        x2 = math.sqrt(x1*x1+z*z)*math.cos(math.atan2(z,x1)+thetarad2)
        z1 = math.sqrt(x1*x1+z*z)*math.sin(math.atan2(z,x1)+thetarad2)
    else:
        x2 = x1
        z1 = z

    # Y-Z plane rotation
    if thetarad3 != 0:
        y2 = math.sqrt(y1*y1+z1*z1)*math.cos(math.atan2(z1,y1)+thetarad3)
        z2 = math.sqrt(y1*y1+z1*z1)*math.sin(math.atan2(z1,y1)+thetarad3)
    else:
        y2 = y1
        z2 = z1

    outfile.write(struct.pack('>ffff',x2,y2,z2,mass))
    atom = infile.read(16)

infile.close()
outfile.close()
bla = input("You've reached the end!")
"""
```

Appendix 2

Python Script to Convert Binary NanoSIMS .IM Files into Text and Spreadsheets, and to Conduct Basic and Smallbeam Analyses

```
#%%

# -*- coding: utf-8 -*-
"""
Created on Mon Aug 19 14:41:13 2013

@author: jblewis
"""
"""

Specifications(NOT YET FULFILLED):
From working directory reads in an *.IM file.
*.IM files are generated by CAMECA NanoSIMS 50 image analyses.
-User friendly command line interface:
ISSUE: ipython and stdin don't play nice?
-Extracts data and metadata.
-Prints a text version of the *.IM file sans data (for size concerns)
TODO: not all data correctly parsed. Compare to the text files generated by Cameca for
improvement
-Prints images of the summed counts for each element to the file format of your choice.
-Prints an xlsx of the image data itself, and of the summed data. This file can be easily read
in via Pandas or another spreadsheet library.

NOTE: endianess may be tricky. Written on Windows 10 and tested against data from WashU
NanoSIMS 50 Nano 101

NOTE: written for python3.3 compatibility. input() replaces python2 raw_input(). pre-python3
interprets input() differently
Also, 3.3 requires print() rather than print

TODO ISSUE running without defaults, and target_cnts set to 1000 isn't hitting the expected
loops?

"""
import struct
import numpy as np
import matplotlib.pyplot as plt
import matplotlib.mlab as mlab
import gc
import os
import pandas as pd
import datetime
import scipy.stats as sts
import traceback
import sys

#
####Parameters####
#%%

default = ''#change to 'y' and this script can be run as an executable
```

```
txt = ''
el_xlsx = ''
sum_xlsx = ''
images = ''
sb = ''
sb_images = ''
target_cts=None
im_format=None
sigma_devs_level = 4 #Any 12C/13C ratio this many sigmas or more from the average will be
reported in smallbeam analysis
siC_level = 0.5 #Any Si/C ratio above this value will be reported in smallbeam analysis
min_c_counts = 1 #Any C counts below this value will be excluded from calculations
bpu = 1 #bins per unit, how many bins there will be per step (1 unit of 12C/13C) in the
histogram).
#%%

DEFAULT = True
TXT = True
EL_XLSX = True
SUM_XLSX = True
IMAGES = True
IM_FORMAT = 'png'
SB = True
TARGET_CTS=10000
SB_IMAGES = False

#%%

while default != 'y' and default!= 'n':
    default = input('Use default settings? (no means you have to make more choices) y/n')
    if default == 'y':
        DEFAULT = True
    if default == 'n':
        DEFAULT = False

if DEFAULT:
    pass
else:
    while txt != 'y' and txt != 'n' :
        txt = input('Create text file of experiment metadata? y/n')
        if txt == 'y' :
            TXT = True
        if txt == 'n' :
            TXT = False

    while el_xlsx != 'y' and el_xlsx != 'n' :
        el_xlsx = input('Create XLSX spreadsheet file for each element/SE containing image
data for each layer? y/n' )
        if el_xlsx == 'y' :
            EL_XLSX = True
        if el_xlsx == 'n' :
            EL_XLSX = False

    while sum_xlsx != 'y' and sum_xlsx != 'n' :
        sum_xlsx = input('Create XLSX spreadsheet file for with a sheet of summed pixels for
each of the elements/SE? y/n')
        if sum_xlsx == 'y' :
            SUM_XLSX = True
        if sum_xlsx == 'n' :
            SUM_XLSX = False
```

```
    while sb != 'y' and sb != 'n' :
        sb = input('Run Smallbeam data analysis module? y/n')
        if sb == 'y' :
            SB = True
            while target_cts == None:
                try:
                    target_cts = float(input('specify integer average C counts per pixel to
target with plane summation. 0 to sum all planes. If you dont know what this means enter 0'))
                    if abs(target_cts) != target_cts:
                        print('youve entered a negative number. Please enter a positive
number')
                        target_cts = None
                    if target_cts%1 != 0:
                        print('Youve entered a non-integer. Please enter an integer.')
                        target_cts = None
                except TypeError:
                    print('Python TypeError. Please enter an integer.')
                    target_cts = None
            TARGET_CTS = int(target_cts)
            while sb_images != 'y' and sb_images != 'n' :
                sb_images = input('Save high-res images from the small beam analysis? (may use
lots of hard drive space) y/n')
                if sb_images == 'y':
                    SB_IMAGES = True
                if sb_images == 'n' :
                    SB_IMAGES = False
        if sb == 'n' :
            SB = False

    while images != 'y' and images != 'n' :
        images = input('Create an image file of summed counts for each element? y/n')
        if images == 'y' :
            IMAGES = True
            while im_format == None:
                im_format = input('OK. What image format do you want to save to? e.g., jpg png
bmp pdf eps gif tiff')
                IM_FORMAT = im_format

        if images == 'n' :
            IMAGES = False

#
####endParameters ####
#

#
####Functions####
#

#%%
def clean_string( s ):
    """Cleans a string after reading in."""
    #This partition operation removes the 00 bytes padding found at the end of strings in the
.im files.
    s = s.partition(b'\x00')[0]
    #.decode('ascii') gets rid of pesky b in front of a string by translating into an ascii
string.
    s = s.decode('ascii')
```

```
    #string.strip() gets rid of the empty space in front (or after the characters) but does
not get rid of any remaining padding bytes.
    s = s.strip()

    return s;

def summed_pixel_by_pixel( planes ):
    """
    Sums the counts at a pixel over multiple planes to most closely match
    the cts/px of the input target. Repeats the process until it's out of
    planes.
    Returns a numpy array of cycles or none (if caught exception)
    old function summed_over_planes summed until the average counts/pix for an entire 256
pixel image hit the mean -- this one is going to sum at each pixel.
    The result will be the same number of pixels as in the data set originally, each one now
summed over following pixels.
    For this reason only outliers are meaningful here, and a little harder to definte.
    """

    if TARGET_CTS == 0:
        summed_pixels = np.zeros(planes.shape)
        for j in range(len(planes[0,:,0,0])):
            for k in range(len(planes[0,0,:,0])):
                for l in range(len(planes[0,0,0,:])):
                    summed_pixels[0,j,k,l] = planes[:,j,k,l].sum()
    else:
        summed_pixels = planes.copy()#Copy rather than zeros in case the first cycle is
already the closest to the target.
        skip_list = np.zeros(summed_pixels[0,0].shape, dtype='bool')
        delete_from=-1#skip list may take care of the delete_from functionality.
        for i in range(len(summed_pixels[:,0,0,0])):#cycle
            empty=True
            for j in range(len(summed_pixels[0,0,:,0])):#row
                for k in range(len(summed_pixels[0,0,0,:])):#column
                    if skip_list[j,k]==True:#'Weve summed to the end of this profile before,
do nothing'
                        print('pixel ' + str(j) + ',' + str(k) + 'ran out of cycles when it
started summing from cycle ' + str(i) + ', skipping')
                    else:
                        planes_summed = 0#keep track of how many planes were summed into this
pixel
                        net_c_cnt = 0
                        prev_c_cnt = 0
                        for l in range(len(summed_pixels)-i):
                            net_c_cnt = prev_c_cnt + planes[i+l,0,j,k] + planes[i+l,1,j,k]
                            if net_c_cnt >= TARGET_CTS:
                                if abs(net_c_cnt-TARGET_CTS) > abs(prev_c_cnt-TARGET_CTS):
                                    #done, stop sum with previous, save, and move to next
pixel
                                    summed_pixels[i,:,j,k] = planes[i:i+l,:,j,k].sum(axis=0)
                                    empty=False
                                    break
                                else:
                                    #done, go ahead and sum this cycle, save, and move to next
pixel
                                    summed_pixels[i,:,j,k] = planes[i:i+l+1,:,j,k].sum(axis=0)
                                    planes_summed += 1
                                    prev_c_cnt = net_c_cnt
                                    empty = False
```

```
                                    if i+l+1 == len(summed_pixels):#last index, next sum won't
make it and will just oversample.
                                        skip_list[j,k] = True#and do what? all the rest of the
values are in there... They'll fail the 1/2.5 of the max, though.
                                    break
                            else:
                                planes_summed += 1
                                prev_c_cnt = net_c_cnt
                            if i+l+1 == len(summed_pixels):#last index and we didn't get a
sum. No point summing over this again.
                                skip_list[j,k]=True # and do what? All the values are still in
there. Could zero them ...
            if empty:
                delete_from=i
                print('set #' + str(i) + ' this whole cycle was empty, done summing for this
data set and moving on without checking further cycles')
                break




            if delete_from !=-1:
                summed_pixels=summed_pixels[:delete_from]

    return summed_pixels

def bootstrap( data, num_samples, statistic, alpha ):
    """
    Sample with replacement to estimate and return as a tuple the 100.0*(1-alpha) confidence
interval for statistic. Adapted from http://people.duke.edu/~ccc14/pcfb/analysis.html
retrieved March 30, 2016
    num_samples of 10,000,000 has been known to crash a 16 GB RAM Windows 10 system
    num_samples of 1,000,000 has been observed to use over 5 GB RAM Windows 10 system
    """
    n = len(data)
    try:
        idx = np.random.randint(0, n, (num_samples, n))
    except ValueError as ve:
        print('ValueError')
        print(ve)
    samples = data[idx]
    stat = np.sort(statistic(samples, 1))
    return ( stat[int((alpha/2.0)*num_samples)] , stat[int((1-alpha/2.0)*num_samples)] )


def ratio_ops( elements, p, num = 1, den = 0 , min_count = 1, siC_level = 0.5, images=False,
bs=False ):
    """
    Execute ratio operations pertaining to small beam analysis:
    take a ratio, save the ratio image, save the ratio excel file, and,
    most importantly, calculate mean, standard deviation, uncertainty in
    standard deviation (and median, mode, anything else we can think of)
    and output these to a text file.
    Returns a lot of things. Read the return statement.
    Currently accepts only shape (elements, row, column) but probably should shift to
accepting (cycle or summed layer, elements, row, column)
    I use this surrounded by a try except Index_Error in case none of the pixels have enough
counts to avoid being zeroed, in which case mode will throw an Index_Error
    Set up for 13C/12C (num = 1, den = 0)
    """
```

```
    try:
        crit_relsig = 0.5#have to have half the average significance to get in

        lyrs = len(elements)
        rows = len(elements[0,0,:])
        cols = len(elements[0,0,0,:])

        numstring = '13C'
        denstring = '12C'
        nums = []
        dens = []

        siC_high = []
        rat_image = elements[:,num]/elements[:,den]#for image only; allows divide by zero for
den counts=0, but will replace the inf with 0 later
        ccounts = elements[:,num] + elements[:,den]
        numcounts = elements[:,num].sum()
        dencounts = elements[:,den].sum()
        #TODO remove hardwiring of Si isotope index
        siC_image = elements[:,4]/(ccounts)#for image, not flattened
        siC = siC_image#previously had this flattened -- not seeing the utility in that move
anymore
        e1 = elements[:,num]
        e2 = elements[:,den]
        nums_im = np.zeros(e1.shape, dtype='float')
        dens_im = np.zeros(e2.shape, dtype='float')
        mean_ccounts = ccounts[:-1].mean()#Removed last slice before running
        if len(ccounts[:-1]) == 0 :
            max_ccount = ccounts.max()#unfortunately this lets all the individual slices pass.
        else:
            max_ccount = ccounts[:-1].max()

        if issubclass(elements[:,num].dtype.type, np.integer) or
issubclass(elements[:,den].dtype.type, np.integer):
            print('counts are stored as integers, ratios are going to have rounding errors!',
flush=True)

        siC_check = False
        if siC.max() > siC_level :
            siC_check = True

        for i in range(lyrs):
            for j in range(rows):
                for k in range(cols):
                    if siC_check and siC[i,j,k] > siC_level:
                        siC_high.append(siC[i,j,k])#for processing

                    if e1[i,j,k] >= min_count and e2[i,j,k] >= min_count and e1[i,j,k] +
e2[i,j,k] > max_ccount/2.5:
                        nums.append(e1[i,j,k])
                        dens.append(e2[i,j,k])
                        nums_im[i,j,k] = e1[i,j,k]
                        dens_im[i,j,k] = e2[i,j,k]
                    else:
                        nums_im[i,j,k] = 0
                        dens_im[i,j,k] = 0#Ratios for image zero out bad counts pixels -- TODO
need to remove these from calculations as well? No -- already does with nums, dens.append

        nums = np.array(nums, dtype='float64')#dtype just to be careful
        dens = np.array(dens, dtype='float64')
```

```
        rats = nums/dens#ratios for pixels with above-minimum counts for both num and den.
Good for math.
        rat_image = nums_im/dens_im
        for n in np.nditer(rat_image, op_flags=['readwrite']):
            if np.isnan(n) or np.isinf(n):
                n[...]=0
        pix = rats.size
        if pix == 0:
            print('no ratios survived min_count; skipping this layer')
            return pix, mean_ccounts, numcounts, dencounts, 0, 0, 0, 0, 0, 0, 0, 0, 0, 0

        #
        #Basic math
        #
        raterrs = np.sqrt( 1/nums + 1/dens )#fractional
        raterrs_im = np.sqrt(  1/nums_im + 1/dens_im )#fractional
        for n in np.nditer(raterrs_im, op_flags=['readwrite']):
            if np.isnan(n) or np.isinf(n):
                n[...]=0
        #weights_raw = 1/np.power(raterrs, 2)
        #weights_raw_im = 1/np.power(raterrs_im, 2)
        raterrs_abs = rats*raterrs
        raterrs_abs_im = rat_image*raterrs_im
        weights_raw = 1/np.power((raterrs_abs), 2)#modified to be based on absolute rather
than fractional error
        weights_raw_im = 1/np.power((raterrs_abs_im*raterrs_im), 2)#modified to be based on
absolute rather than fractional error
        for n in np.nditer(weights_raw_im, op_flags=['readwrite']):
            if np.isnan(n) or np.isinf(n):
                n[...]=0
        sum_weights = weights_raw.sum()
        sum_weights_im = weights_raw_im.sum()
        weights = weights_raw*pix/sum_weights
        weights_im = weights_raw_im*pix/sum_weights_im#using pix here because we want to
explude the pixels that were zeroed out -- they don't count in our weighting normalization
        wmean = weights.mean()
        comparison_mean = (weights*rats).sum()/(weights.sum())#considerable skew in ratio due
to lots of low counts ratios
        mean = numcounts/dencounts
        #median = np.median(rats)
        #mode = sts.mode(rats, axis=None)[0][0]
        w = weights.sum()/( np.power(weights.sum(), 2) - (np.power(weights, 2)).sum() )
        ns = weights/wmean#relative significance of this data point. could also use the number
of counts, not the weights. hmmm.
        ns_im = weights_im/wmean
        stddev = np.sqrt(w*(weights*np.power(rats - mean, 2)).sum())
        seom = stddev/np.sqrt(pix)
        #old_errstddev = ((2*w)/(stddev))*np.sqrt((np.power(rats,2)).sum() +
np.power(rats.sum(),2))

        try:
            errstddev = np.sqrt(1/(2*(pix-1)))#fractional!
        except ZeroDivisionError as zde:
               print(zde)
               #trace = traceback.format_exc(sys.exc_info())
               #print(trace)
               errstddev = 0#Obviously you can't do a real distribution with one pixel

        devfrac_im = abs(rat_image-mean)/stddev
        devfrac_flat = abs(rats - mean)/stddev
```

```
        outliers = []
        prof_size=(4.6,2.3)#w, h for figsize attribute
        for i in range(lyrs):
            for j in range(rows):
                for k in range(cols):
                    if devfrac_im[i,j,k] >= sigma_devs_level and rat_image[i,j,k] !=
0:#checking for zeros -- this means this is a bad data point and should not be included
                        outliers.append((i,j,k, devfrac_im[i,j,k], ns_im[i,j,k],
rat_image[i,j,k], e1[i,j,k], e2[i,j,k], elements[i,2,j,k], elements[i,3,j,k],
elements[i,4,j,k], elements[i,5,j,k]))#Quick and dirty storage using tuples with format:
CYCLE, ROW, COLUMN, SIGMAS DEVIATION, REL-SIGNIFICANCE, RATIO, 12C COUNTS, 13C COUNTS, 16O,
12C14N, 28SI, SE.

        #Using imdata structure of pixels that haven't been summed to a target, plot depth
profiles of outliers above crit_relsig relative significance (usually set to 1).
        labels = ['12C counts', '13C counts', '16O counts','12C14N counts', '28Si counts', 'SE
counts']
        to_plot = []
        for i in range(len(outliers)):#select only outliers of at or above critical relative
significance to plot depth profiles for
            if(outliers[i][4] >= crit_relsig):
                to_plot.append(outliers[i])
        #This block plots depth profiles for each ion and SE.

        frames = np.empty(len(to_plot), len(labels)+1)
        for i in range(len(labels)):
            #plt.figure(i)
            for j in range(len(to_plot)):
                plt.figure(figsize=prof_size)
                #plt.subplot(len(to_plot),1,j+1)
                frames[j,i] = imdata[:,i,to_plot[j][1], to_plot[j][2]]
                plt.plot(frames[j,i])
                prof_title = str(to_plot[j][0]) + '-' + str(to_plot[j][1]) + '-' +
str(to_plot[j][2])
                plt.title(prof_title)
                plt.savefig(str(p) + str(labels[i]) + '_'+ prof_title + '.' + IM_FORMAT,
format = IM_FORMAT, bbox_inches='tight')
                plt.close()

            #plt.xlabel('cycle')
            #plt.ylabel('profile trace ' + labels[i])
            #prof_title = filename + 'outlier_profiles_for' + labels[i]

                """

                pd.DataFrame(data=(imdata[:,i, to_plot[j][1], to_plot[j][2]]),
columns=(prof_title))
                frames[i,j].to_excel(writer, prof_title)

                      outfile_ratio_flat_xlsx = p + 'ratios_flat.xlsx'
        output = np.array([rats, nums, dens, devfrac_flat])
        writer = pd.ExcelWriter(outfile_ratio_flat_xlsx)
        df = pd.DataFrame(output).transpose()
        df.columns = [numstring + '/' + denstring + ' ratio', numstring + ' counts', denstring
+ ' counts', 'deviation (sigmas)']
        df.to_excel(writer)
        writer.close()"""

        #This block plots 13C/12C
        #plt.figure(len(labels))
```

```
        for i in range(len(to_plot)):
            #plt.subplot(len(to_plot),1,i+1)
            plt.figure(figsize=prof_size)
            plt.plot(imdata[:,num,to_plot[i][1], to_plot[i][2]] / imdata[:,den,to_plot[i][1],
to_plot[i][2]])
            prof_title = str(to_plot[i][0]) + '-' + str(to_plot[i][1]) + '-' +
str(to_plot[i][2])
            plt.title(prof_title)
            plt.savefig(str(p) + str(to_plot[i][0]) + '_' + prof_title + '.' + IM_FORMAT,
format = IM_FORMAT, bbox_inches='tight')
            plt.close()
        #plt.xlabel('cycle')
        #plt.ylabel('13C/12C ratio')
        #prof_title = filename + '13Cto12C_ratio_depth_profile'
        #plt.title(prof_title)


        #This time using summed pixels, plot depth profiles of outliers above crit_relsig
relative significance (usually set to 1).
        labels = ['12C counts', '13C counts', '16O counts','12C14N counts', '28Si counts', 'SE
counts']
        to_plot = []
        for i in range(len(outliers)):#select only outliers of at or above critical relative
significance to plot depth profiles for
            if(outliers[i][4] >= crit_relsig):
                to_plot.append(outliers[i])
        #Using summed pixels, this block plots depth profiles for each ion and SE.
        for i in range(len(labels)):
            #plt.figure(i)
            for j in range(len(to_plot)):
                #plt.subplot(len(plot),1,j+1)
                plt.figure(figsize=prof_size)
                plt.plot(elements[:,i,to_plot[j][1], to_plot[j][2]])
                #plt.xlabel('cycle')
                #plt.ylabel('profile trace summed pixels ' + labels[i])
                prof_title = str(to_plot[j][0]) + '-' + str(to_plot[j][1]) + '-' +
str(to_plot[j][2])
                plt.title(prof_title)
                plt.savefig(str(p) + str(labels[i]) + '_' + prof_title + '_sum.' + IM_FORMAT,
format = IM_FORMAT, bbox_inches='tight')
                plt.close()
        #Using summed pixels, this block plots 13C/12C
        plt.figure(len(labels))
        for i in range(len(to_plot)):
            plt.figure(figsize=prof_size)
            #plt.subplot(len(to_plot),1,i+1)
            plt.plot(rat_image[:,to_plot[i][1], to_plot[i][2]])
            #plt.xlabel('cycle')
            #plt.ylabel('13C/12C ratio (pixels are summed to a target)')
            prof_title = str(to_plot[i][0]) + '-' + str(to_plot[i][1]) + '-' +
str(to_plot[i][2])
            plt.title(prof_title)
            plt.savefig(str(p) + str(to_plot[i][0]) + '_' + prof_title + '_sum.' + IM_FORMAT,
format = IM_FORMAT, bbox_inches='tight')
            plt.close()

        """
        #This was a chunk of code I was working on to save off the actual data for the
profiles so I could mess with the images later. It is unfinished and untested, use at your own
risk.
```

```
        writer = pd.ExcelWriter(p+'profiles_to_plot.xlsx')
        for j in range(len(to_plot)):
            df = pd.DataFrame(data=(frames[:,j]), columns=(labels.extend(['12C/13C', labels,
'12C/13C summed'])))
            df.to_excel(writer, str(to_plot[j][0]) + '-' + str(to_plot[j][1]) + '-' +
str(to_plot[j][2]))
        """



        if bs:#flattened images pile a lot of pixels into bootstrap at once, overwhelming 16
GB RAM on my system. This option allows one to bypass running bootstrap functions
            #
            #Bootstrap
            #
            stddev_interval= bootstrap(rats, 1000000, np.std, 0.317)#10,000,000 crashes 16 GB
RAM windows 10, 1,000,000 uses 5GB briefly. Changes stddev less than a % going from 100,000 to
1,000,000
            mean_interval = bootstrap(rats, 1000000, np.mean, 0.317)#Using 1 sigma exclusion.
Half of the returned interval is the standard deviation of the returned statistic)
            err_bsstddev = (stddev_interval[1]-stddev_interval[0])/2
            err_bsmean = (mean_interval[1]-mean_interval[0])/2
            bsstddev = (stddev_interval[0] + stddev_interval[1])/2
            bsmean = (mean_interval[0] + mean_interval[1])/2
        else:
            stddev_interval=0
            mean_interval=0
            bsstddev=0
            bsmean=0
            err_bsstddev = 0
            err_bsmean = 0

        #
        #Xi-squared fitting
        #
        dof =  pix - 1#number of pixels - 1(mean value) - (additional fitted parameters)
        observed = rats #observed = 1/flat
        expected = mean #expected = 1/mean
        err_counts = observed*raterrs#12C/13C uncertainty based on counts, absolute units,
just for graph
        xi_squared = sum(pow((observed - expected)/stddev,2))
        reduced_xi = xi_squared/dof#In standards, we know the uncertainties that
        #prevent this from being xi-squared = 1 are all the result of
        #systematic error. Therefore, we increase a Err_syst term that adds onto
        #the errors until reduced_xi_squared converges to 1.
        #print(reduced_xi)
        stddev_syst = 0
        residual = reduced_xi - 1

        cnt = 0
        while abs(residual) > 0.00000001 and cnt < 10000 :#n is a safety valve against
infinite loops
            stddev_syst = stddev_syst + residual*0.1*stddev#stddev_syst is the error added to
the standard deviation to make the xi-squared equal to 1.
            stddev_fit = stddev + stddev_syst#could do adding, or multiplying of the error.
Assuming the errors are in some form dependent. This results in the calculation of a smaller
systematic error. Note also this is absolute, not fractional
            xi_squared = sum(pow((observed - expected)/stddev_fit,2))
            reduced_xi = xi_squared/dof
            residual = reduced_xi - 1
```

```
            cnt = cnt+1
            if cnt==10000:
                print('WARNING: HIT SAFETY VALVE ON XI-SQUARED FIT, CHECK GOODNESS OF FIT')
        #print(reduced_xi)
        broadening = stddev_syst/stddev

        #
        #Xi-squared fitting bootstrap
        #
        dof =  pix - 1#number of pixels - 1(mean value) - (additional fitted parameters)
        observed = rats #observed = 1/flat
        expected = bsmean #expected = 1/mean
        #err_counts = observed*raterrs#12C/13C uncertainty based on counts, absolute units
        xi_squared = sum(pow((observed - expected)/bsstddev,2))
        bsreduced_xi = xi_squared/dof#In standards, we know the uncertainties that
        #prevent this from being xi-squared = 1 are all the result of
        #systematic error. Therefore, we increase a Err_syst term that adds onto
        #the errors until reduced_xi_squared converges to 1.
        #print(reduced_xi)n
        bsstddev_syst = 0
        residual = bsreduced_xi - 1

        cnt = 0
        while abs(residual) > 0.00000001 and cnt < 10000 :#n is a safety valve against
infinite loops
            bsstddev_syst = bsstddev_syst + residual*0.1*bsstddev#err_syst is the error added
to each error bar to make the xi-squared equal to 1.
            bsstddev_fit = bsstddev + bsstddev_syst#could do adding, or multiplying of the
error. Assuming the errors are in some form dependent. This results in the calculation of a
smaller systematic error. Note also this is absolute, not fractional
            xi_squared = sum(pow((observed - expected)/bsstddev_fit,2))
            bsreduced_xi = xi_squared/dof
            residual = bsreduced_xi - 1
            cnt = cnt+1
            if cnt==10000:
                print('WARNING: HIT SAFETY VALVE ON XI-SQUARED FIT, CHECK GOODNESS OF FIT')
        #print(reduced_xi)
        if bsstddev != 0:
            bs_broadening = bsstddev_syst/bsstddev
        else:
            print('setting bs_broadening to 0 because bsstddev = 0 and would cause a divide by
zero error')
            bs_broadening = 0


        outfile_ratio_flat_xlsx = p + 'ratios_flat.xlsx'
        output = np.array([rats, nums, dens, devfrac_flat])
        writer = pd.ExcelWriter(outfile_ratio_flat_xlsx)
        df = pd.DataFrame(output).transpose()
        df.columns = [numstring + '/' + denstring + ' ratio', numstring + ' counts', denstring
+ ' counts', 'deviation (sigmas)']
        df.to_excel(writer)
        writer.close()

        outfile_ratio_xlsx = p + 'ratio_im_format.xlsx'
        writer = pd.ExcelWriter(outfile_ratio_xlsx)
        num_sheet = pd.DataFrame(elements[:,num].reshape(-1,16))
        num_sheet.to_excel(writer, 'numerator (' + numstring + ')')
        den_sheet = pd.DataFrame(elements[:,den].reshape(-1,16))
        den_sheet.to_excel(writer, 'denominator (' + denstring + ')')
```

```
        ratios_sheet = pd.DataFrame(rat_image.reshape(-1,16))
        ratios_sheet.to_excel(writer, 'ratios')
        deviations_sheet = pd.DataFrame(devfrac_im.reshape(-1,16))
        deviations_sheet.to_excel(writer, 'standard deviations')
        writer.close()

        outlier_xlsx = p + 'outliers.xlsx'
        writer = pd.ExcelWriter(outlier_xlsx)
        df = pd.DataFrame(outliers)
        if df.empty == False:
            df.columns = ['cycle', 'row', 'column', 'deviation (sigmas)', 'rel. sig. d.p.',
numstring + '/' + denstring + ' ratio', numstring + ' counts', denstring + ' counts', '16O
counts', '12C14N counts', '28Si counts', 'SE counts' ]
            df.to_excel(writer)
        writer.close()

        outfile_ratio_txt =  str(p) + 'info'+ '.rat_txt'
        outfile = open(outfile_ratio_txt, "w")
        outfile.write('Created by ' + os.path.basename(__file__) + '\n')
        outfile.write('The IM file you chose is: ' + '\n' + fname + '\n\n')
        outfile.write('Number of pixels: ' + str(pix) + '\n\n')
        outfile.write('Mean C counts per pixel: ' + str(mean_ccounts) +'\n\n')

        outfile.write('Mean ratio (statistical): ' + str(mean) + '\n\n')
        outfile.write('For comparison: mean using weighted average of ratios (statistical): '
+ str(comparison_mean) + '\n\n')
        outfile.write('SEOM (statistical): ' + str(seom) + '\n\n')
        outfile.write('Standard deviation of ratio (statistical): ' + str(stddev) + '\n\n')
        outfile.write('Fractional error in standard deviation of ratio: ' + str(errstddev) +
'\n\n')
        outfile.write('Xi-squared estimate of systematic error, fraction of sigma: ' +
str(broadening) + '\n\n')
        outfile.write('reduced_xi: ' + str(reduced_xi) + '\n\n')

        outfile.write('Mean ratio (bootstrap): ' + str(bsmean) + '\n\n')
        outfile.write('Err in mean (bootstrap): ' + str(err_bsmean) + '\n\n')
        outfile.write('Standard deviation of ratio (bootstrap): ' + str(bsstddev) + '\n\n')
        outfile.write('Fractional error in standard deviation of ratio (bootstrap): ' +
str(err_bsstddev) + '\n\n')
        outfile.write('Xi-squared estimate of average bootstrap systematic error, fraction of
sigma: ' + str(bs_broadening) + '\n\n')
        outfile.write('reduced_xi bs: ' + str(bsreduced_xi) + '\n\n')

        outfile.write('# pixels with Si/C > ' + str(siC_level) + ' : ' + str(len(siC_high)) +
'\n\n')
        outfile.write('max Si/C ratio: ' + str(siC.max()) + '\n\n')
        outfile.write(numstring + ' counts total: ' + str(numcounts) +'\n\n')
        outfile.write(denstring + ' counts total: ' + str(dencounts) +'\n\n')
        for o in outliers:
            outfile.write(str(o[3]) + ' sigma outlier at cycle=' + str(o[0])
                + ', row=' + str(o[1]) + ', column=' + str(o[2]) + ' significance of datapoint
=  ' + str(o[4])
                + ' ratio=' + str(o[5]) + ' ' + numstring + ' counts=' + str(o[6])
                + ' ' + denstring + ' counts=' + str(o[7]) + ' 16O counts=' + str(o[8])
                + ' 12C14N counts=' + str(o[9]) + ' 28Si counts=' + str(o[10]) + ' SE counts'
+ str(o[11]) + '\n\n')
            #outfile.write('outlier with sigmas:  ' + str(d))
        outfile.write('\n' + 'end of file')
        outfile.close()
```

```
        if images:

            plt.imshow(siC, interpolation='none')
            plt.colorbar()
            plt.tick_params(axis='both',
            which='both',
            top='off',
            bottom='off',
            left='off',
            right='off',
            labelbottom='off',
            labeltop='off',
            labelleft='off',
            labelright='off')
            plt.title('SiC ratio')
            plt.savefig(str(p) + 'SiC_ratio.' + IM_FORMAT, format=IM_FORMAT)
            plt.close()

            plt.errorbar(range(0,len(observed),1), observed, yerr=err, fmt='.', color='m',
ecolor='g', elinewidth = '0.5')
            plt.ylabel(numstring +'/'+ denstring + ' ratio')
            plt.xlabel('pixel')
            plt.tick_params(
            axis='x',          # changes apply to the x-axis
            which='both',      # both major and minor ticks are affected
            bottom='off',      # ticks along the bottom edge are off
            top='off',         # ticks along the top edge are off
            labelbottom='off',
            labeltop='off')
            plt.title('pixel ratios with errors adjusted to achieve a reduced xi-squared of
1')
            plt.savefig(str(p) + numstring + denstring + '_fit.jpg',
format='jpg',dpi=1800)#for quick looks
            plt.savefig(str(p) + numstring + denstring + '_fit.' + IM_FORMAT,
format=IM_FORMAT, dpi=1800)#for publication
            plt.close()

            n, b, patches = plt.hist(rats, bins=(int(rats.max()-rats.min()+1))*bpu,
color=None, normed=True)
            y = mlab.normpdf(b, mean, stddev)
            z = mlab.normpdf(b, bsmean, bsstddev)
            plt.plot(b, y, 'k--', linewidth=1.5)
            plt.plot(b, z, 'r--', linewidth=1.5)
            ax = plt.axes()
            plt.axvline(x=(mean + 2*stddev), color='b', linestyle='--')
            plt.axvline(x=(mean - 2*stddev), color='b', linestyle='--')
            plt.xlabel(numstring +'/'+ denstring + ' ratio')
            plt.ylabel('Arbitrary units')
            #plt.grid(False)
            plt.text(0.2,0.9, 'C counts/pixel = ' + str(int(mean_ccounts)),
horizontalalignment='center', verticalalignment ='center', transform=ax.transAxes)
            plt.savefig(str(p) + 'ratio_histogram.' + IM_FORMAT, format=IM_FORMAT)#for
publication
            plt.savefig(str(p) + 'ratio_histogram.jpg', format='jpg', dpi=1200)#for quick
looks
            plt.close()

            n, b, patches = plt.hist(rats, bins = (int(rats.max()-rats.min()+1))*bpu,
color=None, normed=True, weights=weights)
            y = mlab.normpdf(b, mean, stddev)
```

```
            z = mlab.normpdf(b, bsmean, bsstddev)
            plt.plot(b, y, 'k--', linewidth=1.5)
            plt.plot(b, z, 'r--', linewidth=1.5)
            ax = plt.axes()
            plt.axvline(x=(mean + 2*stddev), color='b', linestyle='--')
            plt.axvline(x=(mean - 2*stddev), color='b', linestyle='--')
            plt.xlabel(numstring +'/'+ denstring + ' ratio (weighted pixels)')
            plt.ylabel('Arbitrary units')
            #plt.grid(False)
            plt.text(0.2,0.9, 'C counts/pixel = ' + str(int(mean_ccounts)),
horizontalalignment='center', verticalalignment ='center', transform=ax.transAxes)
            plt.savefig(str(p) + 'ratio_histogram_weighted.' + IM_FORMAT, format= IM_FORMAT,
dpi=1200)#for publication
            plt.savefig(str(p) + 'ratio_histogram_weighted.jpg', format='jpg', dpi=1200)#for
quick looks
            plt.close()

            outfile_ratio_im = str(p) + str(int(mean_ccounts)) + '-counts_ratios-image.' +
IM_FORMAT
            plt.imshow(rat_image, interpolation='none')
            plt.colorbar()
            plt.tick_params(axis='both', which='both', top='off', bottom='off', left = 'off',
right='off', labelbottom='off', labeltop='off', labelleft='off', labelright='off')
            plt.title(numstring +'/'+ denstring + ' Ratio')
            plt.savefig(outfile_ratio_im, format=IM_FORMAT, dpi=1200)
            plt.close()

            outfile_devs_im= str(p) + 'deviation_image.' + IM_FORMAT
            plt.imshow(devfrac_im, interpolation="none")
            plt.colorbar()
            #plt.xlabel('12C/13C ratio')
            #plt.ylabel('Arbitrary units')
            plt.tick_params(axis='both', which='both', top='off', bottom='off', left = 'off',
right='off', labelbottom='off', labeltop='off', labelleft='off', labelright='off')
            plt.title('Absolutized number of standard deviations from mean')
            plt.savefig(outfile_devs_im, format=IM_FORMAT, dpi=1200)
            plt.close()
    except IndexError as ie:
        print(ie)
        trace = traceback.format_exc(sys.exc_info())
        print(trace)
    return pix, mean_ccounts, numcounts, dencounts, mean, seom, stddev, errstddev, broadening,
bsmean, err_bsmean, bsstddev, err_bsstddev, bs_broadening

#
#_END_FUNCTIONS_#
#

#%%
#make date string to attach to output filenames and prevent over-writing
#
now = datetime.datetime.now()
now_string = now.strftime("%y-%m-%d")

cwd = os.getcwd()
files = os.listdir(cwd) #get list of files in working directory.

im = [] #list of image files read in from working directory

for file in files:
```

```
    if file.lower()[-3:] == '.im':
        im.append(file)
        print('Added ' + file + ' to the list of .im files for processing.', flush=True)
    else:
        print(file + ' is not an .im file. Skipping', flush=True)

#%%
for i in range(len(im)):

    print('Processing ' + im[i] + ' ...', flush=True)

    #
    #Read in Header
    #

    infilename = im[i]
    infile = open(infilename, 'rb')

    fname = infilename[:-3]

    path = fname + '_ANAL_'  + now_string + os.sep
    """
    Set path string that will be appended to the front of filenames
    #(if empty '' you will create files in the working directory.
    """

    if not os.path.exists(path): #If the code has been run before for this fname, avoid an
error.
        os.mkdir(path)

    # '<' signifies that the format of the data is little-endian.
    # 'I' is an unsigned integer, 4 bytes long.
    # 'H' is an unsigned short, 2 bytes long.
    # 's' is a character (string) # bytes long.
    # 'x' is padding bytes, # bytes long and not assigned to a variable in the struct tuple.

    #Unpack the def_analysis structure, known to be 124 bytes:x
    def_analysis = infile.read(124)
    (release, analysis_type, hdr_usr, sample_type, data_present, sple_pos_x, sple_pos_y,
analysis_name, username, unused, date, hour) =
struct.unpack('<IIIIIII32s16s16s16s16s',def_analysis)
    if data_present == 0:
        print('No data present. Will continue analyis but will probably just produce a text
summary of the file header')

    mask_im = infile.read(528)
    (filename, anal_duration, cycle_number, scantype, magnification, sizetype, size_detector,
no_used, beam_blanking, pulverisation, pulve_duration, auto_cal_in_anal, sig_reference,
nb_mass) = struct.unpack('<16sIIIHHHHIIII72xI156xI240x', mask_im)
    filename = clean_string(filename)

    #set up variables for the mass tables, of which there will be nb_mass
    #TODO Not sure these are the right variables or if these are all the variables in the
nb_mass structure
    mass_index = [None]*nb_mass
    n1 = [None]*nb_mass
    n2 = [None]*nb_mass
    n3 = [None]*nb_mass
    n4 = [None]*nb_mass
    n5 = [None]*nb_mass
```

```
    num_elements = [None]*nb_mass
    element_name = [None]*nb_mass

    for j in range(nb_mass) :

        tab_mass = infile.read(192)
        (mass_index[j], n1[j], n2[j], n3[j], n4[j], n5[j], num_elements[j], element_name[j]) =
struct.unpack('<I4xHHHH22xH16xI5x8s119x', tab_mass)
        element_name[j] = clean_string(element_name[j])
        #saves SE without an element name. This statement will incorrectly label any unlabeled
ions as SE, but should correctly label Secondary electrons.
        if element_name[j] == '':
            element_name[j] = 'SE'

    len_cal_cond = 96 * nb_mass
    cal_cond = infile.read(len_cal_cond)

    poly_list = infile.read(24)#read poly_list
    (structname, nb_poly) = struct.unpack('<16sI4x', poly_list)#unpack poly_list
    structname = clean_string(structname)

    polyatomique = infile.read(144*nb_poly)

    mask_nano = infile.read(1552)#read mask_nano
    (m_nNbBField) = struct.unpack('<96xI1452x', mask_nano)#unpack mask_nano
    len_tab_Bfield_nano = 2840*m_nNbBField[0]
    tab_Bfield_nano = infile.read(len_tab_Bfield_nano)#read past Tab_Bfield_nano

    anal_param_nano = infile.read(1840)#read past anal_param_nano

    def_analysis_bis = infile.read(2048)#read past def_analysis_bis

    anal_param_nano_bis = infile.read(15264)#read past anal_param_nano_bis

    filler = infile.read(792)#read past unused fill

    header_image = infile.read(84)#read header_image
    (size_self, imtype, width, height, px_size, n_images, n_planes, raster, nickname) =
struct.unpack('<IHHHHHHI64s', header_image)#unpack header_image
    nickname = clean_string(nickname)

    #set up variables for the images, of which there will be n_images
    imdata = [None]*n_images
    imsum = [None]*n_images

    imdata = np.fromfile(infile, dtype='<I4', count = width * height * n_planes *n_images)
    if imdata.size == 0:
        print('Length of imdata is 0. No, or corrupt data in ' + infilename + ' Skipping
analysis.', flush=True)
        continue#skips the rest of the analysis for this .im file

    #try:
    imdata = imdata.reshape((n_planes, n_images, height, width), order = 'C')

    for j in range(n_images) :

        planes = [None]*n_planes

        if EL_XLSX :
            outfile_el_xlsx = path + element_name[j] + '_px.xlsx'
```

```
            writer = pd.ExcelWriter(outfile_el_xlsx)
            for k in range(n_planes) :
                planes[k] = pd.DataFrame(imdata[k,j,:,:])
                planes[k].to_excel(writer, 'plane # ' + str(k))
            writer.close()
        del planes
        #
        #summed planes
        #
        imsum[j] = np.empty((width, height))

        for k in range(height):
            for l in range(width):
                imsum[j][k,l] = imdata[:,j,k,l].sum()

        #correct for NanoSIMS software indexing issues
        #TODO not sure if this is fixing the problem, if the problem always occurs, or why it
occurs
        oldsum = imsum[j].copy()
        imsum[j][:,0] = oldsum[:,height-1]
        imsum[j][:,1:] = oldsum[:,:height-1]

        oldsum = imsum[j].copy()
        imsum[j][0,:] = oldsum[height-1,:]
        imsum[j][1:,:] = oldsum[:height-1,:]

        profile = np.zeros((imdata[:,:,0,0].shape))
        for k in range(len(imdata[:,0,0,0])) :
            for l in range(len(imdata[0,:,0,0])) :
                profile[k,l] = imdata[k,l,:,:].sum()/len(imdata[0,0])*len(imdata[0,0,0])

        #save summed data image #electron image comes out un-named
        if IMAGES :

            outfile_depth_profile = path + 'depth_profile.' + IM_FORMAT
            x = range(len(profile[:,0]))
            for k in range(len(profile[0,:])) :
                plt.plot(x, profile[:,k])
            plt.xlabel('cycle')
            plt.ylabel('mean counts/pixel')
            plt.title('Depth profile')
            plt.savefig(outfile_depth_profile, format=IM_FORMAT)
            plt.close()

            outfile_el_im = path + element_name[j] + '_sum_image.' + IM_FORMAT
            plt.imshow(imsum[j], interpolation='none')
            plt.colorbar()
            plt.tick_params(axis='both', which='both', top='off', bottom='off', left = 'off',
right='off', labelbottom='off', labeltop='off', labelleft='off', labelright='off')
            plt.title(element_name[j] + ' counts')
            plt.savefig(outfile_el_im, format=IM_FORMAT)
            plt.close()

    #save summed pixel counts to xlsx
    if SUM_XLSX :
        sum_el_px = [None]*n_images
        outfile_sum_xlsx = path + 'sum_el_px.xlsx'
        writer = pd.ExcelWriter(outfile_sum_xlsx)
        for k in range(len(sum_el_px)) :
            sum_el_px[k]= pd.DataFrame(imsum[k])
```

```
            sum_el_px[k].to_excel(writer, element_name[k] + ' summed planes')
        writer.close()

        outfile_depth_prof_xlsx = path + 'depth_prof.xlsx'
        writer = pd.ExcelWriter(outfile_depth_prof_xlsx)
        depth_prof = [None]*n_images
        for k in range(len(profile[0,:])) :
            depth_prof[k] = pd.DataFrame(profile[:,k])
            depth_prof[k].to_excel(writer, element_name[k] + ' mean counts per pixel')
        writer.close()
    try:
        if SB :#TODO are ALL uses of range(len()) going to index n+1 and throwing index errors
I'm not noticing?
            ratio_path = path + str(int(TARGET_CTS)) + '-counts_ratios' + os.sep
            if not os.path.exists(ratio_path): #If the code has been run before for this
folder, avoid an error
                    os.mkdir(ratio_path)
            writer1 = pd.ExcelWriter(ratio_path + 'pixel_ratios.xlsx')
            writer2 = pd.ExcelWriter(ratio_path + 'experiment_statistics.xlsx')
            num = 1#running 13C/12C
            den = 0#running 13C/12C

            data_sets = summed_pixel_by_pixel(imdata)
            pix_ratio_path = ratio_path + 'all_pix' + os.sep
            if not os.path.exists(pix_ratio_path):#If the code has been run before for this
folder, avoid an error
                os.mkdir(pix_ratio_path)
            try:
                all_pix_ops = ratio_ops(data_sets, pix_ratio_path, num, den, min_c_counts,
siC_level, images=False, bs=False)#store results as a tuple
            except IndexError:
                print('ratio operations failed due to an IndexError. Are all pixels below
minimum counts (usually 10)? In ' + infilename + ' skipping', flush=True)

            stats = np.zeros((len(data_sets),),
                             dtype=[('pixels', 'f4'),
                                    ('counts', 'f4'),
                                    ('13C counts', 'f4'),
                                    ('12C counts', 'f4'),
                                    ('mean', 'f4'),
                                    ('seom', 'f4'),
                                    ('stddev', 'f4'),
                                    ('errstddev', 'f4'),
                                    ('exp_xi2_broadening', 'f4'),
                                    ('bsmean', 'f4'), ('err_bsmean', 'f4'),
                                    ('bsstddev', 'f4'),
                                    ('err_bsstddev', 'f4'),
                                    ('bs_xi2_broadening', 'f4')])
            for k in range(len(data_sets)):
                cts_ratio_path = ratio_path + 'number' + str(k) + os.sep
                if not os.path.exists(cts_ratio_path): #If the code has been run before for
this folder, avoid an error
                    os.mkdir(cts_ratio_path)
                try:
                    layer = np.empty((1, len(data_sets[k]), len(data_sets[k,0]),
len(data_sets[k,0,0])))
                    layer[0] = data_sets[k]
                    stats[k] = ratio_ops(layer, cts_ratio_path, num, den, min_c_counts,
siC_level, images=SB_IMAGES, bs=True )#store results as a tuple
                except IndexError:
```

```
                    print('ratio operations on segment ' + str(k) + ' failed due to an
IndexError. Are all pixels below minimum counts (usually 10)? In ' + infilename + 'skipping
that segment', flush=True)

            stats_frame = pd.DataFrame(stats[0:-1])#drops the last entry as it will have
imperfectly summed cycles
            N = len(stats_frame.index)

            stats_frame['stddev/mean'] = stats_frame['stddev']/stats_frame['mean']

            stats_frame['bsstddev/bsmean'] = stats_frame['bsstddev']/stats_frame['bsmean']

            stats_frame['ratio_error_stat'] = stats_frame['mean']*np.sqrt( 1/stats_frame['12C
counts'] + 1/stats_frame['13C counts'] )#TODO better to have this fractional, since it really
applies best to the ratio of the sums, not the mean or bsmean.

            mean_pix = stats_frame['pixels'].mean()
            mean_counts = (stats_frame['12C counts']+stats_frame['13C counts']).mean()
            mean_mean = stats_frame['mean'].mean()
            mean_seom = stats_frame['seom'].mean()
            mean_bsmean = stats_frame['bsmean'].mean()
            mean_stddev = stats_frame['stddev'].mean()
            mean_errstddev = stats_frame['errstddev'].mean()
            mean_bsstddev = stats_frame['bsstddev'].mean()

            stds = []
            for k in range(len(stats_frame.columns)):
                stds.append(stats_frame.ix[:,k].std())

            #stats_frame.loc[len(stats_frame.index)+1] = (stds)
            stats_frame.loc['standard deviations'] = (stds)

#[mean_pix,mean_counts,mean_mean,mean_seom,mean_bsmean,mean_stddev,mean_errstddev,mean_errsyst
]
            stats_frame.to_excel(writer2)#(pdb) ??
            writer2.close()

    except IndexError as ie:
        print('no or corrupt image data in ' + infilename + 'skipping Smallbeam analyses',
flush=True)
        print(ie)

    if TXT :
        outfile_im_txt =  path + fname + ".im_txt"
        outfile = open(outfile_im_txt, "w")
        outfile.write('Created by ' + os.path.basename(__file__) + '\n')
        outfile.write('The IM file you chose is: ' + '\n' + fname + '\n\n')

        outfile.write('data_present: ' + str(data_present) + '\n\n')
        outfile.write('nickname: ' + str(nickname) + '\n\n')

        outfile.write('anal_duration: ' + str(anal_duration) + '\n\n')
        outfile.write('analysis_type: ' + str(analysis_type) + '\n\n')
        outfile.write('auto_cal_in_anal: ' + str(auto_cal_in_anal) + '\n\n')
        outfile.write('beam_blanking: ' + str(beam_blanking) + '\n\n')

        outfile.write('release: ' + str(release) + '\n\n')
        outfile.write('sample_type: ' + str(sample_type) + '\n\n')
        for j in range(len(element_name)) :
            outfile.write('element: ' + str(element_name[j]) + '\n\n')
```

```
        for j in range(len(num_elements)) :
            outfile.write('num_element: ' + str(num_elements[j]) + '\n\n')

        outfile.write('scantype: ' + str(scantype) + '\n\n')
        outfile.write('sig_reference: ' + str(sig_reference) + '\n\n')
        outfile.write('size_detector: ' + str(size_detector) + '\n\n')
        outfile.write('sizetype: ' + str(sizetype) + '\n\n')

        outfile.write('sple_pos_x: ' + str(sple_pos_x) + '\n\n')
        outfile.write('sple_pos_y: ' + str(sple_pos_y) + '\n\n')

        outfile.write('height: ' + str(height) + '\n\n')
        outfile.write('width: ' + str(width) + '\n\n')
        outfile.write('n_cycles: ' + str(n_planes) + '\n\n')

        outfile.write('px_size: ' + str(px_size) + '\n\n')
        outfile.write('raster: ' + str(raster) + '\n\n')

        outfile.write('cycle_number: ' + str(cycle_number) + '\n\n')

        outfile.write('hdr_usr: ' + str(hdr_usr) + '\n\n')
        outfile.write('len_cal_cond: ' + str(len_cal_cond) + '\n\n')
        outfile.write('len_tab_Bfield_nano: ' + str(len_tab_Bfield_nano) + '\n\n')
        outfile.write('m_nNbBField: ' + str(m_nNbBField) + '\n\n')
        outfile.write('nb_mass: ' + str(nb_mass) + '\n\n')
        outfile.write('nb_poly: ' + str(nb_poly) + '\n\n')

        outfile.write('pulve_duration: ' + str(pulve_duration) + '\n\n')
        outfile.write('pulverisation: ' + str(pulverisation) + '\n\n')

        outfile.write('\n' + 'end of file')
        outfile.close()

    #del sum_el_px
    gc.collect()

print('script completed')
```

Appendix 3

Python Script to Compile a Counts Report from Multiple Atom-probe Data Sets

```
# -*- coding: utf-8 -*-
"""
Created on Wed Sep 11 12:09:25 2013

@author: jblewis

Imports all files from the working directory and combines various slices of those files.
Intended for use on IVAS bulk counts output data for large numbers of atom-probe runs.

Takes each column and joins it with the same column from each data file, outputting as a .csv
with ion type as index and dataset as column

This script must be run w a working directory full of .csv files formatted as IVAS data
outputs and nothing else -- it cannot parse out other folders or file types. Attempts to save
output files to the path
results_path

DO NOT put other files or folders in the directory from which you plan to run.

2014-01-16 updated with os.sep so it's platform independent and added () to print so it runs
in python 3
"""

import pandas as pd
import os
import datetime

#Set which operations you want saved to csv files
print_ion_fraction_corrected = True
print_counts_corrected = True
print_counts_decomposed_corrected = True
print_counts = True
print_ion_fraction = True
print_counts_decomposed = True

#make date string to attach to output filesnames and prevent over-writing
now = datetime.datetime.now()
date = now.strftime("%y-%m-%d")

results_path = '..' + os.sep + 'Results' + os.sep + date + os.sep #set path string that will
be appended to the front of filenames (if empty '' you will create files in the working
directory. Trying to run the script again in the same working directory will cause errors
since the data structure of the new files is not IVAS csv output
d = os.path.dirname(results_path)
if not os.path.exists(d):
    os.makedirs(results_path)
corrected_str = ' Corrected' #string to append to row/column that has corrected counts

#get list of files in working directory.
cwd = os.getcwd()
files = os.listdir(cwd)
```

```
outtables = {}# initialize a dictionary to hold our growing and key-unknown list of output
files
intables = {}

#read_csv each file in files, trim, label, and put in intables
for i in range(len(files)):
    d = pd.read_csv(files[i])
    d.columns = d.ix[0:0].values.flatten()
    d = d.ix[1:]#remove empty first row
    d.index = d['Ion Type'].values.flatten()
    intables[files[i]] = d

#Initialize DataFrame object using first file in list

d = intables[files[0]]
#d = list(intables.values())[0] is a random number generator #edited 12/10/2014 for Python 3
dict.values() returns a view now, rather than a list.
for j in range(len(d.columns.values)-1):
    #Select column of interest and initilize DataFrame to store these columns
    c = d.ix[:,j+1:j+2]
    name = c.columns.values[0]

    #Way of renaming the column with the file name -- there's some issue with renaming the
column in a 1-column DataFrame?
    c = pd.Series(c.values.flatten(), index=c.index)
    c.name = files[0]

    if name in outtables: #edited 12/10/2014 to not use has_key, not used in Python 3.
        outtables[name + corrected_str] = pd.DataFrame(c)
    else:
        outtables[name] = pd.DataFrame(c);

#loop through remaining files in list and add column of interest from each as column of joined
DataFrame
for k in range(len(intables)-1):#skipping first file as it has already been handled so need to
go one fewer than length
    d = intables[files[k+1]]#d = list(intables.values())[k+1] is a random number generator
    corrected = False
    for l in range(len(d.columns.values)-1):

        c = d.ix[:,l+1:l+2]##select column

        name = c.columns.values[0]
        print(name)
        print(corrected)
        c = pd.Series(c.values.flatten(), index=c.index)
        c.name = files[k+1]
        print(c.name)
        if corrected:
            outtables[name + corrected_str] = outtables[name + corrected_str].join(c,
how='outer')
        else:
            outtables[name] = outtables[name].join(c, how='outer')

        if name == 'Background Count':#Way of seeing if we're about to start repeating row
names. Might be better if you change those the first time through?
            corrected = True

#do operations on joined DataFrames here:
#sample operation: add a row of Pt/C for each dataset
```

```
#Working correctly, math agrees with calculator out to ~10 decimal places
"""
countsc = outtables['Ion Count' + corrected_str] #This is a deep copy, not a pointer, so the
append at the end must reference outtables[key] explicitly.
icc_pt = countsc.loc['Pt']#get row by index
icc_c = countsc.loc['C']
icc_pt = pd.Series(icc_pt, dtype='float')#as series w dtype cast to avoid puzzling string
operation exceptions
icc_c = pd.Series(icc_c, dtype='float')
icc_cdivpt = icc_pt.div(icc_c) #operate
icc_cdivpt.name = 'Pt/C Ratio' #name new row
outtables['Ion Count' + corrected_str] = outtables['Ion Count' +
corrected_str].append(icc_cdivpt)#append returns a copy so the assignment is necessary. Plus,
countsc is a copy of the dictionary entry in outtables, so explicit reference to the outtables
dictionary is required
"""
#write all csv files
for key, table in outtables.items():
    table.to_csv(results_path + str(key) + date + '.csv')

print('finished')
```

Appendix 4

Python Script to Find the Union of Detected Ions in a .POS File of a Subvolume and an .EPOS File of the Whole Data Set, and Save as an .EPOS of the Subvolume

```
# -*- coding: utf-8 -*-
"""
Created on Mon Jan 13 16:21:50 2014

@author: jblewis

Command line utility to convert .POS file of a region of interest into an .EPOS by filtering
the .EPOS for the whole data set for just the .POS-included ions
Reads in an .EPOS file generated by the Cameca IVAS software, filename to be input from
command line.
Reads in a .POS file that is a subvolume of the same set from the .EPOS file (from the same
.ROOT file!)

Writes .POS to list b and converts to a set of tuples, one tuple per atom
Compares .EPOS atom by atom to set, writes out full .EPOS data to a file of the same title as
.POS file but with .EPOS extension

Using list or another non-hashable data structure would yield prohibitive computing time due
to ~1e6 searches through ~1e6 element list.

Memory errors are common on python 32-bit. Use 64 bit python. This will vary by dataset but
takes up more than 1Gb RAM
A 15 Matom dataset, 18430-v01_20nm_dep-layer, takes roughly 2.5 gb ram to run in linux mint.
Garbage collection is important. rois that are most of the dataset will crash!

Ran 19572-v01-roi_C_C2_PtOC_5%Iso_Outside overnight on linux mint virtual w 5 gib RAM and 8
GiB swap. Used all RAM, 2.3 Gib swap and completed.

using input -- Python 3 replacement for Python 2's raw_input
"""

import struct
import os
import gc

b = []
ions_in_pos = 0
ions_not_in_pos = 0

epos = input('What EPOS file? ')
fname = epos
#if fname[-5:] != '.epos'
   # sys.exit('not an epos file')
pos = input('What POS file for ROI ?')
fname2 = pos

print("The EPOS file you chose is " + fname)
print("The POS file you chose for roi selection is " + fname2)

# open .epos file as a binary file
infile = open(fname,"rb")
```

```
infile2 = open(fname2,"rb")

path = os.getcwd() + os.sep + 'Converted_Files' + os.sep
if not os.path.exists(path): #If the code has been run before for this fname, avoid an error
    os.mkdir(path)

outfile = open(path + os.sep + fname2[:-4] + '.epos', "wb") #create a file to write out the
.pos "filtered" epos file with the same title at the pos but .epos typ (could really do this
as a seperate converter utility code)
#"wb" is necessary for python 3. "w" worked for Python 2 but not Python 3. "wb" has not been
tested for python 2!

def in_pos( x, y, z, mass ):
    "see if .epos position and mass is included in supplied .pos data"

    mylist = [x,y, z, mass]

    if tuple(mylist) in s:
        return True
    else:
        return False

# read the first 16 bytes (x, y, z, mass-to-charge ratio)
atom = infile2.read(16)

while len(atom) == 16:
    # '>f' signifies that the format of the data is
    # big-endian float. Each float is 4 bytes long.

    (x,y,z,mass) = struct.unpack('>ffff',atom)
    b.append([x, y, z, mass])
    atom = infile2.read(16)

infile2.close()
print('to tuple')
s=set(tuple(map(tuple,b)))#Set should have O(1) lookup instead of List's O(n), obviously a big
deal with n~1e6. Memory errors using this in 32 bit python
del b
gc.collect()

# read the first 44 bytes (x, y, z, mass-to-charge ratio,
# time-of-flight, standing voltage, pulsed voltage,
# detector-impact-x, detector-impact-y, pulses-since-last-ion,
# hit multiplicity)
atom = infile.read(44)
cnt = 0
print('break')

while len(atom) == 44:
    # '>f' signifies that the format of the data is

    # big-endian float. Each float is 4 bytes long.
    # "The first 9 values are in floating-point format,
    # whereas the last two values are in unsigned-integer
    # format" Atom probe Microscopy. Gault et al 2012)

    (x,y,z,mass, tof, vdc, vp, xdet, ydet, deltap, nm) = struct.unpack('>fffffffffII',atom)

    if in_pos(x, y, z, mass):
```

```
        outfile.write(struct.pack('>fffffffffII',x,y,z,mass, tof, vdc, vp, xdet, ydet, deltap,
nm))
        ions_in_pos += 1
    else:
        ions_not_in_pos += 1
    cnt += 1
    atom = infile.read(44)

print(str(ions_not_in_pos) + ' ions in original .epos not found in .pos')
print(str(ions_in_pos) + ' ions in original .epos were found in .pos and written to file')
infile.close()
outfile.close()
print('wrote intersection of ions to ' + outfile.name)
bla = input("You've reached the end!")
```

Appendix 5

Table of Uncorrected Atom-Probe Data

Table A5.1 Counts from APT ROIs.

Sample[a]	$^{12}C^{+}$ raw	noise	tail	multi	$^{13}C^{+}$ raw	noise	tail	multi	$^{12}C^{++}$ raw	noise	tail	multi	$^{13}C^{++}$ raw	noise	tail	multi	T (K)	E (pJ)
Synthetic nanodiamonds																		
DND R06 17619 A61 M35[b,c,d]	644	3	0	--	19	3	0	--	*349*	3	0	--	*2*	3	0	--	80	40
DND R06 17620 A61 M35[d]	4959	3	0	63	107	3	0	0	3053	2	0	15	62	3	0	0	80	40
DND R06 17621 A61 M34[c,d]	1243	46	0	--	109	45	0	--	*188*	21	0	--	*27*	19	13	--	80	40
DND R06 17626 A62 M4[d]	4758	1	0	0	75	1	0	0	1053	1	0	17	27	1	0	0	55	80–100
DND R06 17629 A61 M3[c,d]	452	45	0	--	77	43	5	--	338	53	0	--	56	46	5	--	55	70–90
DND R06 17967 A62 M35[c,d]	1058	72	0	--	102	69	6	--	*807*	34	0	--	*34*	33	0	--	54	40
DND R06 17969 A62 M28[d]	2709	2	0	3	61	2	0	0	2382	3	0	100	59	3	0	0	54	40
DND R06 17978	904	26	0	--	58	26	0	--	*178*	9	0	--	*12*	8	0	--	95	40

Sample[a]	$^{12}C^{+}_{raw}$	noise	tail	multi	$^{13}C^{+}_{raw}$	noise	tail	multi	$^{12}C^{++}_{raw}$	noise	tail	multi	$^{13}C^{++}_{raw}$	noise	tail	multi	T (K)	E (pJ)
A62 M34[c,d]																		
DND R06 18428 A64a M34[b,c,d]	1273	1	0	--	16	1	0	--	*418*	1	0	--	*5*	1	0	--	95	40–80
DND R06 19586 A69 M12[b,c,e]	2318	1	0	--	33	1	0	--	*410*	2	0	--	*9*	2	0	--	95	80
DND R06 19587 A69 M11[b,c,e]	979	1	0	--	25	1	0	--	*270*	0	0	--	*8*	0	0	--	95	80
DND R06 19589 A69 M12[c,e]	2643	4	0	--	41	4	0	--	580	25	0	--	47	24	0	--	95	80
DND R06 21153 A77 M33[c,e]	3763	1	0	--	65	1	5	--	589	1	0	--	11	1	0	--	95	80
DND R06 21155v02 A77 M35[b,c,e]	460	1	0	--	13	1	0	--	*234*	1	0	--	*5*	1	0	--	95	80
DND R06 21155v03 A77 M35[c,e]	40754	11	0	55	529	11	25	0	7807	8	0	416	155	7	5	0	95	80
DND R06 21157 A77 M30[c,e]	6544	2	0	--	85	2	0	--	1367	2	0	--	19	2	0	--	95	80
DND R06 21888 A83 M29	13028	3	0	6	187	3	6	0	1747	3	0	210	31	3	0	0	95	80
DND R06 21889	20721	2	0	6	255	2	24	0	6174	2	0	351	151	2	8	0	60	80

Sample[a]	$^{12}C^{+}$ raw	noise	tail	multi	$^{13}C^{+}$ raw	noise	tail	multi	$^{12}C^{++}$ raw	noise	tail	multi	$^{13}C^{++}$ raw	noise	tail	multi	T (K)	E (pJ)
A83 M30																		
DND R06 21893 A83 M35[b]	627	1	0	0	11	1	0	0	*243*	1	0	0	*10*	1	0	0	60	40
DND R06 21895 A83 M32	10131	5	0	17	169	5	3	0	2788	4	0	66	57	4	0	0	60	40
DND R06 21899 A83 M36	2111	1	0	3	27	1	0	0	893	1	0	3	23	1	0	0	60	80
DND R06 21905 A83 M06	51120	6	0	32	595	5	75	0	1947	6	0	61	133	6	75	0	60	80
DND R06 21896 A83 M32	5920	5	0	4	108	5	0	0	3160	5	0	394	69	7	0	0	60	80
DND R06 21906 A83 M05	10829	1	0	10	126	1	2	0	2403	1	0	365	52	1	2	0	60	80
DND R06 21907 A83 M04	1538	1	0	2	34	1	0	0	1176	1	0	2	23	1	0	0	60	80
DND R06 21909 A83 M01	620	0	0	1	13	0	0	0	957	1	0	6	19	0	0	1	60	80
Allende nanodiamonds																		
ADM R06 15004 A36 M01[d]	1711	1	0	3	35	1	0	0	972	1	0	3	15	1	0	0	95	150

Sample[a]	$^{12}C^{+}$ raw	noise	tail	multi	$^{13}C^{+}$ raw	noise	tail	multi	$^{12}C^{++}$ raw	noise	tail	multi	$^{13}C^{++}$ raw	noise	tail	multi	T (K)	E (pJ)
ADM R06 15005 A36 M01[d]	574	1	0	1	18	1	0	0	834	2	0	13	18	2	0	0	95	150
ADM R06 16096 A47 M10[d]	1854	1	0	3	40	1	0	0	1261	1	0	3	18	1	0	0	103	150
ADM R06 16097v03 A47 M11[c,d]	655	1	0	--	11	1	0	--	459	0	0	--	10	0	0	--	102	150
ADM R06 16098 A47 M12[b,d]	905	1	0	2	11	1	0	0	565	1	0	2	6	1	0	0	103	150
ADM R06 16119 A47 M12[b,d]	825	1	0	1	10	1	0	0	355	1	0	1	5	1	0	0	103	150
ADM R06 16120 A47 M13[b,d]	3382	1	0	4	58	1	0	0	1668	1	0	4	20	1	0	0	102	250
ADM R06 18430 A65a M06[d]	5198	21	0	5	121	21	0	0	3000	22	0	76	68	21	0	0	95	40–100
ADM R06 18436 A65a M05[c,d]	1164	1	0	--	18	1	0	--	914	1	0	--	19	1	0	--	95	40

Sample[a]	$^{12}C^{+}_{raw}$	noise	tail	multi	$^{13}C^{+}_{raw}$	noise	tail	multi	$^{12}C^{++}_{raw}$	noise	tail	multi	$^{13}C^{++}_{raw}$	noise	tail	multi	T (K)	E (pJ)
ADM R06 18437 A65a M04[d]	8747	13	0	15	155	13	4	0	4487	12	0	93	82	12	3	0	95	40–80
ADM R06 19314 A62 M07[b,c,e]	1022	1	0	--	15	1	0	--	*461*	1	0	--	*9*	1	1	--	95	60
ADM R06 19315 A62 M08[c,e]	1286	4	0	--	27	4	3	--	*942*	6	0	--	*13*	6	1	--	95	80
ADM R06 19354 A62 M010[c,e]	479	50	0	--	80	50	0	--	625	94	0	--	106	90	0	--	95	60
ADM R06 19557 A70 M25[e]	8595	10	0	10	113	10	5	0	4791	11	0	88	83	10	3	0	95	60
ADM R06 19559 A70 M25[e]	18625	14	0	10	271	13	8	0	9622	13	0	386	147	12	10	0	95	60–80
ADM R06 19565 A70 M32[e]	6045	4	0	4	94	3	3	0	2376	5	0	152	53	5	3	0	60	80
ADM R06 19566 A70 M33[e]	2064	1	0	2	31	1	1	0	1418	1	0	18	23	1	0	0	60	80
ADM R06 19567 A70 M33[e]	24915	25	0	10	312	24	6	0	8689	24	0	558	161	23	3	0	60	80
ADM R06 19568 A70	5810	2	0	--	55	2	3	--	2891	2	0	--	56	2	0	--	60	60

Sample[a]	$^{12}C^{+}_{raw}$	noise	tail	multi	$^{13}C^{+}_{raw}$	noise	tail	multi	$^{12}C^{++}_{raw}$	noise	tail	multi	$^{13}C^{++}_{raw}$	noise	tail	multi	T (K)	E (pJ)
M34[c,e]																		
ADM R06 19572 A70 M35[e]	4892	1	0	0	61	1	2	0	2377	1	0	109	39	1	0	0	95	80
ADM R06 20159 A78 M05[c,e]	3001	1	0	--	49	1	3	--	393	1	0	--	11	1	0	--	95	80
ADM R06 20163 A78 M12[c,e]	4130	4	0	--	67	3	6	--	719	7	0	--	19	7	0	--	95	80
ADM R06 21164 A78 M25[e]	26154	5	0	5	426	5	25	0	2887	6	0	889	55	6	1	0	95	80
ADM R06 21179 A78 M30[c,e]	8774	3	0	--	120	3	5	--	2072	4	0	--	40	4	1	--	95	80
ADM R06 21180 A78 M29[b,c,e]	1255	0	0	--	14	0	0	---	307	0	0	--	4	0	0	--	95	80
ADM R06 21886 A84 M10	7363	1	0	210	108	1	0	0	2172	2	0	9	45	2	0	0	95	80
ADM R06 21903 A84 M04	8571	9	0	39	277	12	50	0	2487	12	0	75	85	22	0	0	60	80
ADM R06 22577 A94	815	0	0	0	18	0	0	0	64	0	0	0	0	0	0	0	60	80–120[f]

Sample[a]	$^{12}C^{+}_{raw}$	noise	tail	multi	$^{13}C^{+}_{raw}$	noise	tail	multi	$^{12}C^{++}_{raw}$	noise	tail	multi	$^{13}C^{++}_{raw}$	noise	tail	multi	T (K)	E (pJ)
M04[b]																		
ADM R06 22582 A94 M18	14420	4	0	1	194	4	5	0	2017	3	0	2	39	3	0	0	60	120
ADM R06 22595 A94 M18[b]	1510	1	0	--	28	1	0	--	*197*	1	0	--	*3*	1	0	--	60	120–80[f]
ADM R06 22596 A94 M18	12972	3	0	6	180	3	0	0	1055	4	0	8	14	3	0	0	60	105
ADM R06 22597 A94 M13[b]	5667	1	0	0	112	1	0	0	*636*	0	0	31	*8*	0	0	0	60	120
ADM R06 22598 A94 M13[b]	769	0	0	--	13	0	0	--	*113*	0	--	0	*3*	0	0	--	60	120
ADM R06 23612 A98 M21[b]	451	9	0	1	23	8	0	0	*115*	4	0	1	*6*	4	0	0	60	80
ADM R06 23617 A94 M19[b]	314	5	0	1	19	5	0	0	*209*	4	0	1	*7*	4	0	0	64	80
ADM R06 23619 A94 M20	2964	1	0	4	36	1	0	0	788	0	0	5	16	0	0	0	60	80

[a] ADM stands for Allende nanodiamonds. DND stands for detonation nanodiamonds. R06 indicates a data set was collected using the LEAP 4000X Si instrument at Northwestern University. A## M## indicates the microtip analyzed.

[b] Insignificant $^{13}C^{++}$ counts (<10). $^{12}C^{++}$ and $^{13}C^{++}$ counts are reported in italics and not used in calculating the mean ratio or the weighted standard deviation, nor are these ratios recorded on the figures in this chapter.

[c] Too few multi-hits to deadtime correct.

[d] Data set was first published in (Heck et al. 2014), here presented with updated ROIs and deadtime corrections.

[e] Data set was first published in (Lewis et al. 2015), here presented with updated ROIs and deadtime corrections.

[f] Laser energy was adjusted up in 5–10 pJ steps during the run to observe its effect on charge-state ratio, which corresponds to field evaporation conditions.